Cost-Effective Green Catalysts for Sustainable Hydrolysis of Waste Lignocellulosic Biomass for Platform Chemicals and Drop-in-Biofuel Production

Thesis submitted by

Sourav Barman

Doctor of Philosophy (Engineering)

Department of Chemical Engineering,

Faculty Council of Engineering & Technology

Jadavpur University

Kolkata, India

2024

To my Family for their unconditional support

JADAVPUR UNIVERSITY

KOLKATA – 700032, INDIA

INDEX NO. 191/17/E

1. **Title of Thesis**: Cost-Effective Green Catalysts for Sustainable Hydrolysis of Waste Lignocellulosic Biomass for Platform Chemicals and Drop-in-Biofuel Production.

2. **Name, Designation & Institution of the Supervisor**:

Prof. (Dr.) Rajat Chakraborty

Professor

Department of Chemical Engineering

Jadavpur University

3. **List of Publications**:

Journal Papers

1. **Barman**, S., & Chakraborty, R. (2018). Printed circuit board-derived glass fiber-epoxy resin-supported Mo–Cu bimetallic catalyst for glucose synthesis. *ACS omega*, 3(12), 18499-18509.
2. **Barman**, S., & Chakraborty, R. (2019). Kinetics of combined noncatalytic and catalytic hydrolysis of jute fiber under ultrasonic–far infrared energy synergy. *AIChE Journal*, 65(10), e16677.
3. **Barman**, S., & Chakraborty, R. (2021). Sustainable HMF synthesis from waste cooked rice water using fly-ash based Al2SiO5 supported nano-photocatalyst under halogen-ultrasound synergistic-energy: LCA and DFT based simulation. *Journal of Environmental Chemical Engineering*, 9(6), 106736.
4. **Barman**, S., & Chakraborty, R. (2024). Energy-efficient and eco-friendly continuous production of 5-CMF in a UV-ultrasound irradiated catalytic packed bed reactor: heterogeneous kinetics, reactor simulation and LCA analysis. *Reaction Chemistry & Engineering*, 9(1), 160-171.
5. **Barman**, S., Roy Choudhury, S., & Chakraborty, R. (2024). Environmentally sustainable ethyl levulinate synthesis from delignified sugarcane bagasse using ternary eutectic solvent under MW-xenon irradiation: engine performance and emission assessment. *Environmental Science and Pollution Research*, 1-14.

Submitted paper in journal

1. **Barman**, S., & Chakraborty, R. Continuous ethyl levulinate production from pretreated sugarcane bagasse in Microwave-Visible irradiated continuous stirred slurry reactor:

Reaction kinetics, Techno-economic & environmental sustainability analyses. *RSC Sustainability* (Manuscript ID: SU-ART-05-2024-000250)

4. **List of Presentations in National/International Conferences**:

1. **Barman**, S., & Chakraborty, R. Oral presentation on "sustainable ethyl levulinate synthesis from delignified sugarcane bagasse using ternary eutectic solvent under MW-xenon irradiation: engine performance and emission assessment" in ICEIS-2023 held during 26-27th February, 2023 at Jadavpur University, Kolkata, India.

5. **List of Presentations in National/International Seminars**:

1. **Barman**, S., & Chakraborty, R. Poster presentation on "Energy efficient far infrared radiated ammonia fiber expansion pretreatment process for sustainable extraction of cellulose from lignocellulosic biomass" in national seminar on innovative process technology for sustainable development (IPTSD) held during held during 23-24th February, 2018 at Jadavpur University, Kolkata, India.

2. **Barman**, S., & Chakraborty, R. Oral presentation on "Intensified glucose production through starch hydrolysis in hybrid electromagnetic radiation assisted catalytic packed bed reactor" in international seminar on sustainable 2-G biorefinery platforms (Sponsor: Rusa-2.0) held at chemical engineering department, Jadavpur University.

"Statement of Originality"

I **Sourav Barman** registered on **08/08/2017** do hereby declare that this thesis entitled" **"Cost-Effective Green Catalysts for Sustainable Hydrolysis of Waste Lignocellulosic Biomass for Platform Chemicals and Drop-in-Biofuel Production"** contains literature survey and original research work done by the undersigned candidate as part of Doctoral studies.

All information in this thesis have been obtained and presented in accordance with existing academic rules and ethical conduct. I declare that, as required by these rules and conduct, I have fully cited and referred all materials and results that are not original to this work.

I also declare that I have checked this thesis as per the "Policy on Anti Plagiarism, Jadavpur University, 2019", and the level of similarity as checked by iThenticate software is 5 %.

Sourav Barman.

Signature of Candidate:

Date: 27.05.2024.

27.05.24

Certified by Supervisor

(Signature with date, seal)

Prof. Rajat Chakraborty
Chemical Engineering Department
Jadavpur University
Kolkata-700032

Certificate from the Supervisor

This is to certify that the thesis entitled **"Cost-Effective Green Catalysts for Sustainable Hydrolysis of Waste Lignocellulosic Biomass for Platform Chemicals and Drop-in-Biofuel Production"** submitted by **Sourav Barman** who got his name registered on **08/08/2017** for the award of Ph. D. (Engg.) degree of Jadavpur University, is absolutely based upon his own work under the supervision of **Prof. Rajat Chakraborty**, that neither her thesis nor any part of the thesis has been submitted for any degree or any other academic award anywhere before.

27.05.24,

Signature of the supervisor and date with Office Seal

Prof. Rajat Chakraborty
Chemical Engineering Department
Jadavpur University
Kolkata-700032

Acknowledgements

First and foremost, I would like to show my sincere and utmost gratitude to my supervisor, Prof. Rajat Chakraborty, Department of Chemical Engineering, Jadavpur University, Kolkata, India for his kind and valuable advices during the completion of this research work. I sincerely appreciate invaluable academic and personal support I received from him throughout this PhD tenure.

I am also grateful to Prof. Papita Das, Head of the Department, Department of Chemical Engineering, Jadavpur University for her untiring cooperation during my PhD submission.

This long journey wouldn't have been as exciting as it was without the avid support of my lab mates and all their names couldn't be enlisted in such a short space. We brainstormed and exchanged our ideas, solved problems together, and they stayed by my side as support during my unsuccessful attempts.

My special recognition goes out to the excellent non-teaching staff of the Chemical Engineering Department, Jadavpur University who were extremely helpful and made every official process easier to navigate.

I would also like to thank the Department of Chemical Engineering, Jadavpur University for providing the essential facilities required for my PhD completion.

Finally, I would like to dedicate this work to my family members, especially my father mother and brother who has inspired me to dream big and achieve my goals.

Sourav Barman

Sourav Barman 27.05.2024.

Abbreviations

5-CMF	5-(Chloromethyl) furfural
5-HMF	5-Hydroxymethyl furfural
A-15	Amberlyst-15
BET	Brunauer-Emmett-Teller
CRW	Cooked rice water
CTS	Conventional thermal system
DFT	Density functional theory
DES	Deep eutectic solvent
EIA	Environmental impact assessment
EL	Ethyl levulinate
FA	Fly ash
FIRW	Far-infrared wave
FTIR	Furrier-transform infrared spectroscopy
GF	Glass fiber
GFER	Glass fiber-epoxy resin
HPLC	High performance liquid chromatography
LA	Levulinic acid
LB	Lignocellulosic biomass
LCA	Life cycle assessment
LCI	Life cycle inventory
MW	Microwave
NIRR	Near infrared radiation
NZF	Nickel zinc ferrite
PSCB	Pretreated sugarcane bagasse
PWJF	Pretreated waste jute fiber
RPBR	Rectangular packed bed reactor
RS	Reducing sugar
SCB	Sugarcane bagasse
SEM	Scanning electron microscope
SS	Soluble starch
TADES	Ternary acidic deep eutectic solvent
TEM	Transmission electron spectroscopy
THUS	Tungsten halogen radiation and ultrasound
TOD	Taguchi orthogonal design
US	Ultrasound
VIS	Visible
WJF	Waste jute fiber
WPCB	Waste printed circuit board
XPS	x-ray photoelectron spectroscopy
XRD	x-ray diffraction

Table of Contents

6.1.3.8. TEM analyses
6.1.3.9. X-ray Photoelectron Spectroscopic (XPS) analysis
6.1.4. *Possible reaction Mechanism of pretreated WJF hydrolysis using* NCu-Mo$^{1.0}$
6.1.5. *Catalytic performance of NCu-Mo$^{1.0}$ catalyst on pretreated WJF hydrolysis process*
6.1.6. *Pretreated WJF hydrolysate characterization*
6.1.6.1. FTIR analyses of hydrolysate
6.1.6.2. High performance liquid chromatography (HPLC) analyses of hydrolysates
6.1.7. *Catalyst reusability test*
6.2. **Activity 2:**
6.2.1. Effects of process parameters on PWJF hydrolysis process
6.2.2. Interactive effects of process parameters on PWJF hydrolysis process
6.2.3. Performance comparison among US-FIRW, FIRW, US and CTS
6.2.4. Hydrolysis Kinetics of PWJF
6.2.5. Analyses of product hydrolysate through FTIR
6.2.6. FTIR analyses of WJF, PWJF and optimally hydrolysed PWJF
6.2.7. HPLC analyses of hydrolysates
6.2.8. XRD analysis
6.2.9. Mechanism of A-15 catalysed hydrolysis
6.3. Activity 3:
6.3.1. Influences of process factors and ANOVA
6.3.2. Catalyst characterization
6.3.2.1. XRD analysis
6.3.2.2. FTIR Spectra
6.3.2.3. BET-BJH analyses
6.2.3.4. HR-TEM analysis
6.3.2.5. Acidity of FA_NPC and FA_NPC^{CO}*
6.3.2.6. TGA analysis
6.3.2.8. UV-Vis DRS analysis of FA_NPC^{O} and FA_NPC^{CO}*
6.3.2.7. XPS analysis
6.3.3. Performance assessment of prepared photo-catalysts in CRW conversion
6.3.5. Reusability of the optimal FA_NPC^{O}*
6.3.6. *Plausible reaction mechanism of HMF formation on FA_NPC*^{O}*
6.3.7. *LCA of photocatalytic conversion of CRW*
6.4. Activity 4:
6.4.1. Optimization of 5-CMF synthesis process parameters in UVUS-BR
6.4.2. Effect of process parameters on Y_{CMF}
6.4.3. Effect of extracting solvents on 5-CMF yield
6.4.4. *Kinetics parameters evaluation for 5-CMF synthesis process*
6.4.5. 5-CMF synthesis in UVUS-RPBR system
6.4.6. Effect of US and UV on RPBR performance
6.4.7. Simulation study of UVUS-RPBR using ANSYS Fluent software
6.4.8. Environmental impacts of SS to 5-CMF synthesis process
6.4.9. Comparative study with previously reported relevant works on 5-CMF synthesis process
6.5. Activity 5:
6.5.1. Optimization of EL synthesis process
6.5.2. Individual parametric effects on EL synthesis process
6.5.3. Property of synthesized TADES
6.5.4. Comparative study with previous work on one pot EL synthesis process
6.5.5. EL-Biodiesel-Diesel blending fuel properties
6.5.6. Engine performance and exhaust analysis
6.5.7. Life cycle environmental impact analysis
6.6. Activity 6:
6.6.1. Screening of DES
6.6.2. Optimization of EL synthesis process

List of Tables

List of Figures

CHAPTER I: INTRODUCTION

1.1.Overview

Waste lignocellulosic biomass is abundantly available worldwide, generated in large quantities from organic materials such as agricultural crops and their residues, forestry residues and daily household wastes. The primary components of lignocellulosic biomass (LB) such as cellulose and hemicellulose are hydrolysed to produce reducing sugars which can be further converted into extensive range of key platform chemicals such as furan derivatives (furfurals, 5-hydroxymethyle furfural, 5-chloromethoxy furfural), levulinic acid and drop-in-biofuels like levulinate esters [1-3]. Harnessing LB for the sustainable production of high-value platform chemicals and drop-in biofuels has the potential to bolster rural economies while promoting environmental sustainability.

Due to the intrinsic structural complexity of LB, hydrolysis of LB is challenging, making the process both energy and cost-intensive. To enhance product yield and reduce process energy requirements, various efficient homogeneous and heterogeneous solid acid catalysts have been employed. However, heterogeneous solid acid catalysts offer several advantages over homogeneous catalysts, including easier product separation, reduced corrosiveness, and minimal waste stream generation [4,5]. While heterogeneous catalysts such as sulfonated solid acid catalysts, metal oxides, supported metal oxides, and acidic ion exchange resins are effective for LB conversion [6], the use of these commercially expensive catalysts significantly increases the overall cost of the process. In this context, utilization of metal-rich wastes like coal-based fly ash (FA) and waste printed circuit board (WPCB) for production of catalysts and catalyst supports presents a cost-effective alternative, enhancing the practicality and efficiency of the LB conversion process while reducing overall expenses. `

In India, millions of tons of solid waste, stemming from both e-waste and industrial sources, are generated daily due to a lack of awareness regarding solid waste disposal thus rendering environmental and ecological disturbances. Printed Circuit Board (PCB) is the integral component of any electronic equipment as it electrically connects and mechanically supports the other electronic components. According to Global E-waste Monitor–2017, globally 44.7 million metric tonnes of e-waste was generated [7], fuelling concerns about the growing threats to the environment and public health. WPCB is still being chiefly disposed in open air or in landfills that pose grave threat to the environment. Accumulation of waste PCB is not only a crisis of quantity but also an alarming environmental concern due to presence of toxic ingredients that results in occupational, environmental and human health threats. On the other

hand, India, being the third-largest coal-based power generator country, co-produces large quantities of coal-based fly ash (FA) throughout the year. According to central electricity authority of India (2018-19) report, a staggering 217.04 million tons FA was generated. Both WPCB and FA are rich sources of various precious and valuable metallic components like copper, nickel, iron, along with non-metallic components such as silica and alumina [8-10]. These resources hold significant potential for the development of both cost-effective green catalysts and catalyst supports, enhancing the efficiency of the hydrolytic conversion process of LB.

Thus, in this thesis, efforts have been made to synthesize cost-effective, efficient solid acid catalysts or catalyst supports using WPCB and FA for the sustainable conversion of LB into value-added platform chemicals and drop-in biofuels. Other than catalysts, various other important factors including different process parameters such as reaction time, temperature, solvents also affects the overall process economic feasibility. In this context, various non-ionizing and ionizing electromagnetic irradiation systems have been employed either alone or combinedly to enhance the LB conversion rate at mild reaction conditions. Moreover, optimization of process parameters employing efficient statistical methodologies has also been done to minimize energy consumption while maximizing product yield. Besides process optimization, effort has been made to develop of realistic reaction kinetic model as this can help in reactor design and possible industrial scaleup of the process. The present study also investigated the LB conversion process in continuous reactors and discussed the techno-economic feasibility of the process. Additionally, the engine performance and exhaust emissions of the synthesized drop-in biofuel (ethyl levulinate) blended with diesel-biodiesel were analysed in a diesel engine. Notably, environmental sustainability analysis of the LB conversion processes was also performed in the present study.

1.2. Lignocellulosic biomass and its sources

LB primarily consists of cellulose, hemicellulose, and lignin, forming the structural framework of plant cell walls. This biomass can be sourced from various materials, including agricultural residues (such as straw, corn stover, and sugarcane bagasse), forestry residues (including sawdust and wood chips), dedicated energy crops (like switchgrass and miscanthus), and even organic municipal solid waste. These diverse resources offer significant potential for sustainable bioenergy and bioproducts production, driven by their widespread availability and

lower environmental impact compared to fossil fuels. Table 1.1 demonstrated various sources of LB and their respective cellulose, hemicellulose and lignin content.

Table 1. 1. Various sources of LB

Sources	LB	Lignin (%)	Hemicellulose (%)	Cellulose (%)
Agricultural waste [11]	Wheat straw	12-16	23-29	35-40
	Barley straw	6.4-9.7	24-33	36-44
	Rice straw	17-20	23-25	29-34
	Sugarcane bagasse	15-25	28-30	25-40
Forestry waste [12]	Poplar	15-16	26-28	50-53
	Eucalyptus	21-22	18-19	52-54
	Pine	20-21	24-27	42-45
Municipal waste [13]	Banana peel	0.93	3.85	1.5
	Tomato peel	5.5	11	9.5
	Paper	1-15	0	85-99

1.3.Value-added platform chemicals and drop-in-biofuels from LB

As previously indicated, LB stands out as a highly promising renewable resource which offers significant potential for the production of valuable platform chemicals and drop-in-biofuels. LB feedstocks can be initially transformed into a wide array of platform chemicals, including hexoses like glucose, fructose derived from cellulose, mixed pentoses or hexoses like xylose, arabinose and mannose originating from hemicellulose, lignin-derived aromatic compounds. These primary platform chemicals can further convert to a diverse array of commercially viable products through a combination of thermal, chemical, and biological processes.

The sugars derived from cellulose and hemicellulose can further converted into valuable chemicals viz. lactic acid, succinic acid, acetone, furans and drop-in-biofuels viz., ethanol, propanol, butanol and levulinate esters [14]. Besides polysaccharides, conversion of lignin also has promising potential and it can be considered as most abundant component in the LB for production of aromatic compounds. Currently lignin is used as road binder, dye dispersant, raw material for vanillin production, animal feed pellets, pesticide dispersant and solid fuel for combustions [15].

Some LB derived furans such as 5-Hydroxymethyl furfural (5-HMF) and 5-(Chloromethyl) furfural (5-CMF), derived from the dehydration of hexoses like glucose or fructose, hold significant promise as platform chemicals for producing various value-added products (Figure 1.1). Their unique chemical properties enable a wide range of industrial applications. Both 5-HMF and 5-CMF can be hydrogenated to produce 2,5-dimethylfuran, a biofuel with high energy density and compatibility with existing infrastructure. Additionally, these compounds serve as precursors for synthesizing fine chemicals such as levulinic acid, formic acid, and furan derivatives, which are used in pharmaceuticals, agrochemicals, and polymer synthesis. Moreover, solvents derived from 5-HMF or 5-CMF exhibit favourable properties, making them suitable for extraction and reaction processes across various industries [16].

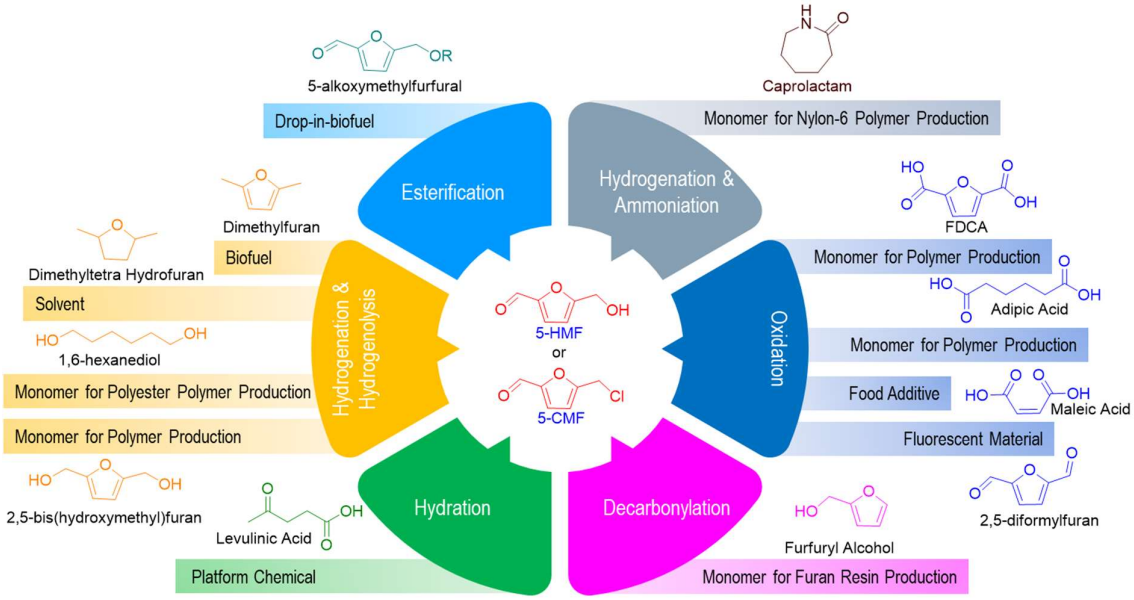

Figure 1. 1. 5-HMF to value-added chemicals

Levulinic acid (LA), another crucial platform chemical derived from LB, is a versatile starting material for the production of numerous value-added chemicals (Figure 1.2). These include γ-valerolactone, succinic acid, α-angelica lactone, alkyl levulinates, 1,4-pentanediol, 2-butanone, 2-methyl tetrahydrofuran, and glycerol ketal ester oligomer, which can be synthesized through various pathways. Among all these products, alkyl levulinates, particularly ethyl levulinate (EL), have gained significant attention due to their similar physicochemical properties to fatty acid methyl esters (FAME) used in biodiesel. Ethyl levulinate is produced through esterification of levulinic acid with ethanol and can serves as an oxygenated drop-in biofuel [17]. It can be blended with conventional fuels like diesel or gasoline to improve combustion efficiency and reduce emissions, offering a renewable alternative for partially

replacing fossil fuels and helping to secure future energy demands. Additionally, EL finds applications in the flavour and fragrance industry, serving as a flavour enhancer and fragrance precursor in food and cosmetic formulations [18-19]. Moreover, EL exhibits solvent properties and serves as a versatile chemical intermediate for the synthesis of specialty chemicals, plasticizers, and lubricants.

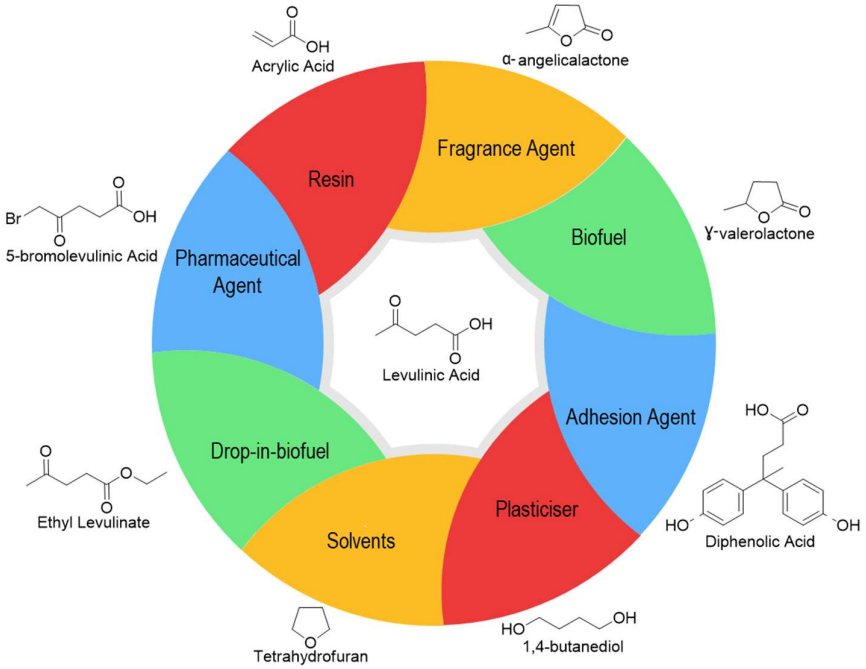

Figure 1. 2. LA to value-added chemicals

Thus, the utilization of lignocellulosic biomass for the production of these key platform chemicals and drop-in-biofuels, offers promising pathways towards sustainable and economically viable solutions in various industries. These renewable chemicals not only reduce dependence on fossil resources but also contribute to mitigating environmental impacts associated with traditional chemical synthesis processes. Continued research and development in this field are crucial for unlocking the full potential of lignocellulosic biomass as a valuable resource for the production of high-value chemicals and drop-in biofuels.

1.4. E-waste and Fly ash generation and utilization

The Global E-waste Monitor 2020 reported that India produced 3.2 million metric tonnes of e-waste in 2019, with an annual growth rate of around 13% [20]. Additionally, the Central Electricity Board of the Government of India indicated that 4.05% of the fly ash generated by thermal power plants remained unutilized that year (Figure 1.3). The

accumulation of these solid wastes presents a significant environmental threat unless they are sustainably reused or recycled [21].

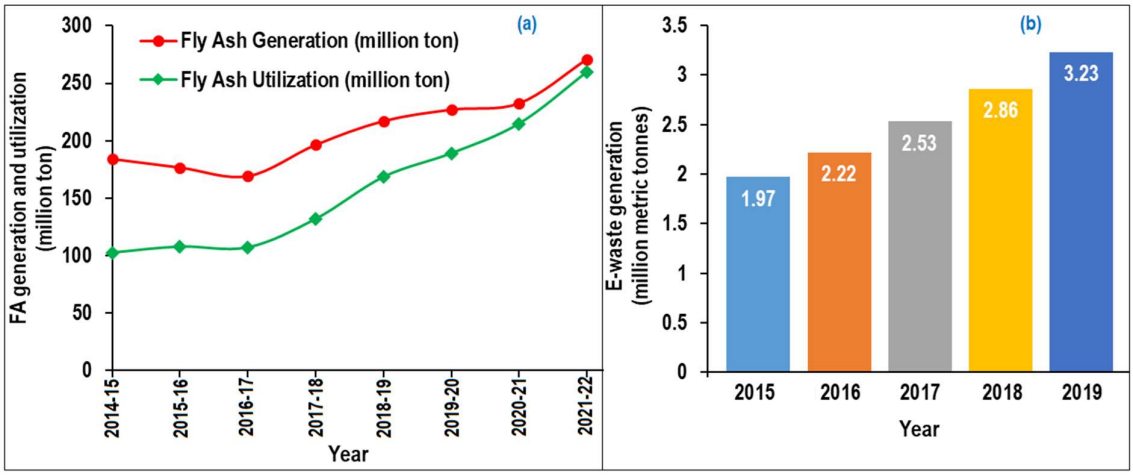

Figure 1. 3. (a) FA generation and utilization (b) E-waste generation

As PCB an integral part of e-waste it also generated along with e-waste and waste PCB (WPCB) contains various metallic compound including iron, copper, aluminium, zinc, lead (Figure 1.4 (a)) and non-metallic compound like glass fiber, epoxy resin (Figure 1.4 (b)). Although no research has been conducted on catalysts derived from WPCB or glass fiber (GF) supported catalysts from WPCB, some studies have reported the preparation and application of GF supported catalysts in various other reactions. For instance, Kiwi-Minsker et al. [22] prepared Pt and Pd doped GF as a combustion catalyst for use in the temperature range of 200–500°C. The work reported the prepared catalyst showed high thermal stability, excellent specific surface area (275 m^2/g) and the Pt doped GF demonstrate highest activity when modified with titania. In another work, Bal'zhinimaev et al. [23] prepared GF supported vanadium catalyst for the SO_2 oxidation process in the temperature range of 420–700°C. Both the work reported that high activity and good thermal resistance of the prepared catalyst. Thus, GF can be used as an effective catalyst support for preparation of both heterogenous solid catalyst as well as photocatalyst, and recycling of WPCB to extract GF for catalyst preparation can reduce costs and mitigate e-waste disposal issues.

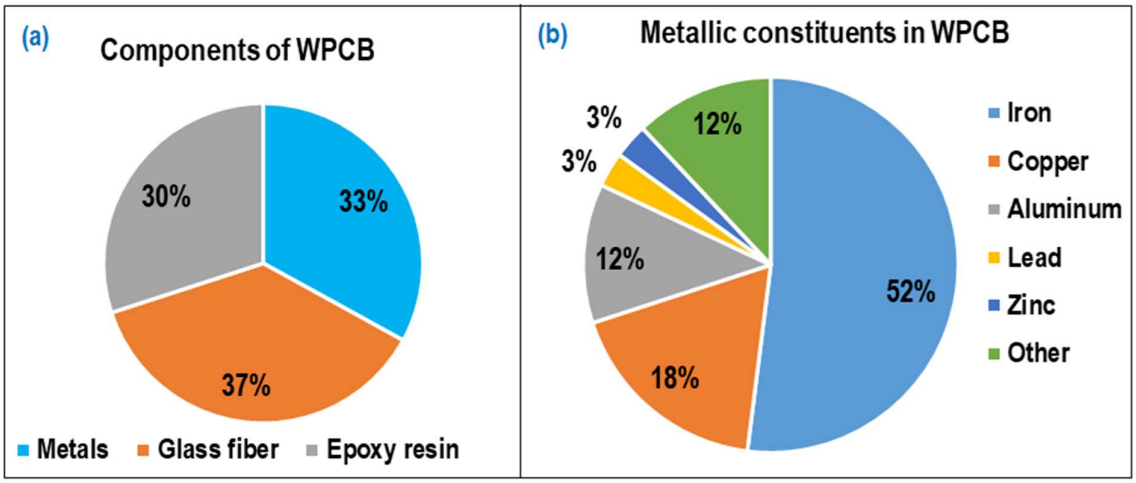

Figure 1. 4. (a) components of WPCB (b) metallic components of WPCB

FA also contains various metallic (34 % Al_2O_3, 2 % Fe_2O_3) and non-metallic compounds (60 % SiO2, 0.2 % CaO). Synthesis of catalyst or catalyst support from coal-based fly ash (FA) for the valorisation of LB or LB derived platform chemicals into value-added chemicals has been reported by several researchers. For instance, Chatterjee et al., [24, 25] utilized FA from Durgapur steel plant, India to produce two types of catalysts viz., H_2SO_4 treated FA [24] and MIL-101 (Cr) based MOF-FA-composite [25] and produced catalysts efficacy was investigated in xylose dehydration process in toluene/aqueous NaCl biphasic medium. The reported studies showed that the H_2SO_4 treated FA could produce 68 mol % of furfurals from xylose at 170°C and 210 min, whereas the MIL-101 (Cr) based MOF-FA-composite could render maximum 78 mol % of furfural at 150°C and 3h. Thus, the reported work suggest that Fly ash can be effectively utilized in the cost-effective catalyst or catalyst support preparation process for sustainable hydrolysis of LB.

1.5.Optimization of LB conversion process parameters

Conventional single-factor optimization techniques often necessitate numerous experimental trials, particularly when dealing with a multitude of process factors, rendering optimization analyses time-consuming and inefficient. To address this issue, efficient statistical methodologies such as Taguchi orthogonal designs and Box-Behnken have been employed for optimization studies, systematically identifying the optimal factorial combinations for chemical processes with precision. Among these approaches, the Taguchi optimization design (TOD) stands out as particularly suitable when the ranges and levels of the variables to be optimized are predetermined. The Taguchi orthogonal design (TOD) also assesses the variance between experimental values and model predictions through the signal-to-noise (S/N) ratio.

Three key criteria are employed for optimizing the S/N ratio: "larger is better" for maximizing the response variable, "lower is better" for minimizing the response variable, and "nominal is better". The widespread use of Taguchi orthogonal design (TOD) in optimizing the lignocellulosic biomass conversion process parameters, as documented in prior research, underscores the effectiveness of this approach.

1.6.Techno-enviro-economic sustainability analysis

1.6.1. Techno-economic analysis

Techno-economic analysis is an effective method for assessing both the technical performance and economic viability of the LB conversion process. Aspen Plus software has been extensively used to scale up and simulate the laboratory processes to industrial scale operations for detailed techno-economic analysis [33]. This analysis involves evaluation of overall process capital and annual operating costs by examining costs associated with LB procurement, processing technologies, and product distribution, as well as the potential revenue from the sale of these products. By identifying economic bottlenecks and optimization opportunities, Techno-economic analysis helps in making informed decisions for scaling up and commercializing LB conversion technologies.

1.6.2. Application of electromagnetic irradiations in process intensification

Electromagnetic energy serves as an effective intensification technique for catalyst preparation and lignocellulosic biomass (LB) conversion process, offering targeted energy delivery to enhance reaction efficiency, reduce processing times, and improve product quality. Both ionizing and non-ionizing irradiation systems play crucial roles in these processes.

Non-ionizing irradiations like microwave (MW) energy accelerate reactions via dipolar rotation and ionic conduction, facilitating rapid heating to enhance active site formation in catalysts and lower activation energy barriers in LB conversion, thereby improving depolymerization rates of LB and product yields. Whereas Infrared (IR) radiation promotes uniform temperature distribution, minimizing thermal gradients and unwanted side reactions through molecular stretching and bending vibrations. Ultrasound energy operates through acoustic cavitation, generating localized high-energy zones. This enables uniform dispersion of active components in catalyst synthesis and disrupts biomass structures in LB conversion by breaking hydrogen bonds and enhancing solvent penetration, improving cellulose and hemicellulose accessibility.

Ionizing electromagnetic energy, such as UV irradiation promote electron excitation and bond cleavage, driving photochemical reactions and enhancing photocatalytic processes by creating active sites and reactive intermediates, making it a powerful tool in catalyst development and biomass conversion.

Thus, integration of these electromagnetic energy techniques offers innovative pathways for achieving efficient and sustainable chemical processes, transforming traditional methods into high-performance, energy-efficient systems.

1.6.3. Life cycle assessment (LCA) analysis

LCA analysis is an essential technique for assessing the environmental impacts associated with any products or processes, which helps in identifying opportunities to minimize environmental burdens and improve the overall sustainability of products or processes. It is a systematic approach that involves four key steps viz., goal and scope delineation which involves establishment of system boundaries and objectives for the analysis, preparation of life cycle inventory (LCI) database, environmental impacts assessment (EIA), and interpretation of the results and evaluating alternative scenarios or strategies for the reduction of environmental burdens (Figure 1.5). Comprehensive LCA analysis provides the necessary knowledge and tools to make informed decisions that minimize environmental burdens, enhance resource efficiency, and foster sustainable practices throughout the lifecycle of products and processes. Over the past decade, researchers have employed various computational software such as SimaPro, GaBi and OpenLCA to conduct LCA analyses.

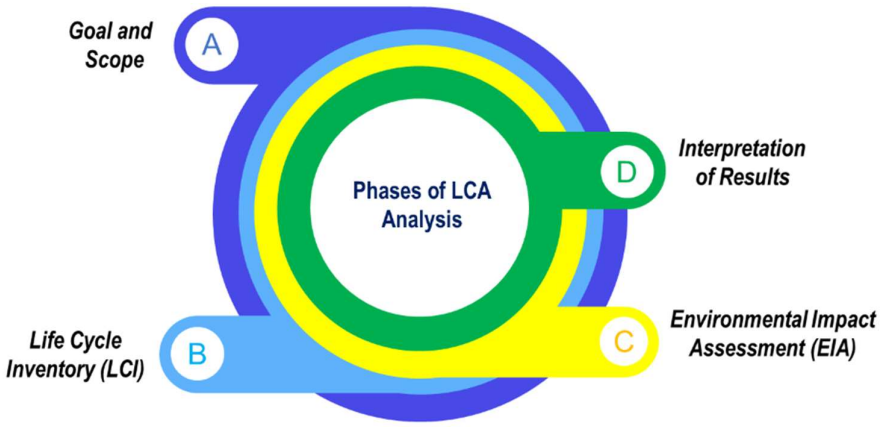

Figure 1. 5. steps of LCA analysis

1.7. Summary

From Chapter 1 (Introduction), it is understandably clear that utilizing industrial solid wastes like FA and E-waste like WPCB for the production of cost-effective efficient green catalysts presents an opportunity to synthesize valuable platform chemicals, including reducing sugars, furfurals and drop-in biofuels from lignocellulosic biomass. Such an approach not only promotes sustainability but also offers an economically advantageous pathway for value-added chemical synthesis.

Therefore, in Chapter 2 (Literature Survey), prior studies on the synthesis of platform chemicals and drop-in biofuels from lignocellulosic biomass through the hydrolytic pathway are reviewed. Additionally, various methodologies discussed in these studies are examined, including the use of inexpensive catalyst supports for developing efficient, cost-effective, and highly recyclable catalysts, the employment of non-conventional energy sources to accelerate lignocellulosic biomass conversion reactions, continuous flow reactor design and the selection of optimal process conditions to maximize desired product selectivity and yield. These approaches are considered for their potential to improve the efficiency of converting lignocellulosic biomass into platform chemicals and drop-in biofuels. Furthermore, a detailed analysis of previously published works on LB hydrolytic conversion reaction kinetics and techno-enviro-economic analysis has also been summarized in the Literature Survey section to understand the complexities and implications of these processes.

1.8. References

1. Onda A, Ochi T, Yanagisawa K. Selective hydrolysis of cellulose into glucose over solid acid catalysts. Green Chemistry. 2008;10(10):1033-7.
2. Qi X, Watanabe M, Aida TM, Smith RL. Catalytic conversion of cellulose into 5-hydroxymethylfurfural in high yields via a two-step process. Cellulose. 2011 Oct;18:1327-33.
3. Pileidis FD, Tabassum M, Coutts S, Titirici MM. Esterification of levulinic acid into ethyl levulinate catalysed by sulfonated hydrothermal carbons. Chinese Journal of Catalysis. 2014 Jun 1;35(6):929-36.
4. Pang J, Wang A, Zheng M, Zhang T. Hydrolysis of cellulose into glucose over carbons sulfonated at elevated temperatures. Chemical Communications. 2010;46(37):6935-7.
5. Takagaki A, Tagusagawa C, Domen K. Glucose production from saccharides using layered transition metal oxide and exfoliated nanosheets as a water-tolerant solid acid catalyst. Chemical communications. 2008(42):5363-5.
6. Wang J, Xi J, Wang Y. Recent advances in the catalytic production of glucose from lignocellulosic biomass. Green Chemistry. 2015;17(2):737-51.
7. Balde, C.P.; Forti, V.; Gray, V.; Kuehr, R.; Stegmann, P. The global e-waste monitor 2017: Quantities, flows and resources. United Nations University, International Telecommunication Union, and International Solid Waste Association; **2017**.
8. Bhattacharjee A, Mandal H, Roy M, Kusz J, Hofmeister W. Microstructural and magnetic characterization of fly ash from Kolaghat Thermal Power Plant in West Bengal, India. J. Magn. Magn. Mater. 2011; 323(23):3007-12.
9. Ahmaruzzaman M. A review on the utilization of fly ash. Progress in energy and combustion science. 2010 Jun 1;36(3):327-63.
10. Wang C, Wang H, Cao Y. Waste printed circuit boards as novel potential engineered catalyst for catalytic degradation of orange II. Journal of cleaner production. 2019 Jun 1;221:234-41.
11. Werpy, T. A., Petersen, G., 2004. Top Value Added Chemicals from Biomass: I. Results of Screening for Potential Candidates from Sugars and Synthesis Gas, U.S. Department of Energy (DOE)
12. Mood SH, Golfeshan AH, Tabatabaei M, Jouzani GS, Najafi GH, Gholami M, Ardjmand M. Lignocellulosic biomass to bioethanol, a comprehensive review with a focus on pretreatment. Renewable and sustainable energy reviews. 2013 Nov 1;27:77-93.
13. Hadar Y. Sources for lignocellulosic raw materials for the production of ethanol. InLignocellulose conversion: enzymatic and microbial tools for bioethanol production 2013 Jun 12 (pp. 21-38). Berlin, Heidelberg: Springer Berlin Heidelberg.
14. Das H, Singh SK. Useful byproducts from cellulosic wastes of agriculture and food industry—a critical appraisal. Critical reviews in food science and nutrition. 2004 Mar 1;44(2):77-89.

15. Bozell, J.J., G.R. Petersen. 2010. Technology development for the production of biobased products from biorefinery carbohydrates- the US department of energy's "TOP 10" revisited,Green Chemistry, 12, 539-554
16. Yoshida N, Kasuya N, Haga N, Fukuda K. Brand-new biomass-based vinyl polymers from 5-hydroxymethylfurfural. Polymer journal. 2008 Dec;40(12):1164-9.
17. Windom BC, Lovestead TM, Mascal M, Nikitin EB, Bruno TJ. Advanced distillation curve analysis on ethyl levulinate as a diesel fuel oxygenate and a hybrid biodiesel fuel. Energ. Fuel. 2011;25(4):1878-90.
18. Leibig C, Mullen B, Mullen T, Rieth L, Badarinarayana V. Cellulosic-derived levulinic ketal esters: a new building block. InRenewable and Sustainable Polymers 2011 (pp. 111-116). American Chemical Society.
19. Ertl J, Cerri E, Rizzuto M, Caretti D. Natural derivatives of diphenolic acid as substitutes for bisphenol-A. InAIP Conference Proceedings 2014 May 15 (Vol. 1599, No. 1, pp. 326-329). American Institute of Physics.
20. Anon 2014. ASSOCHAM India. Available at https://www.assocham.org/ newsdetail.php?id=4351
21. Report on fly ash generation at coal / lignite based thermal power stations and its utilization in the country for the year 2021 – 22, ministry of power, government of India, available at https://cea.nic.in
22. Chatterjee A, Xijun HU, Lam FL. Modified coal fly ash waste as an efficient heterogeneous catalyst for dehydration of xylose to furfural in biphasic medium. Fuel. 2019 Mar 1; 239:726-36.
23. Chatterjee A, Hu X, Lam FL. Catalytic activity of an economically sustainable fly-ash-metal-organic-framework composite towards biomass valorization. Catalysis Today. 2018 Sep 15; 314:137-46.
24. Kiwi-Minsker L, Yuranov I, Slavinskaia E, Zaikovskii V, Renken A. Pt and Pd supported on glass fibers as effective combustion catalysts. Catalysis Today. 2000 Jun 10;59(1-2):61-8.
25. Bal'zhinimaev BS, Simonova LG, Barelko VV, Toktarev AV, Zaikovskii VI, Chumachenko VA. Pt-containing catalysts on a base of woven glass fiber support: a new alternative for traditional vanadium catalysts in SO2 oxidation process. Chemical Engineering Journal. 2003 Mar 15;91(2-3):175-9.

CHAPTER II: LITERATURE SURVEY

Chapter 2 presents a comprehensive literature review on various sulfonic acid and metal oxide-based solid acid catalysts used in the hydrolytic conversion of lignocellulosic biomass (LB) to produce key platform chemicals such as glucose, 5-HMF, 5-CMF, levulinic acid (LA), and drop-in-biofuel (ethyl levulinate). Additionally, previous literature on the effectiveness of waste fly ash (FA) and waste printed circuit boards (WPCB) (as mentioned in Chapter 1) in various chemical reactions as catalysts or catalyst supports has been reviewed to uncover the underlying concepts behind their successful application in the synthesis of value-added chemicals. Furthermore, to perform reactions under milder conditions and save energy, the focus has shifted towards utilizing electromagnetic energy sources instead of conventional energy. Consequently, relevant articles were reviewed to demonstrate the effectiveness of electromagnetic energy sources in accelerating LB conversion reactions. The chapter also presents reported kinetic models related to the conversion of LB into the aforementioned key platform chemicals and ethyl levulinate.

2.1. Hydrolytic conversion of LB employing Sulfonated and metal oxide based solid acid catalyst

2.1.1. Sulfonated solid acid catalyst for hydrolytic conversion of LB into glucose or RS synthesis

Among the various solid acid catalysts used for glucose production from cellulose or LB, sulfonated carbonaceous solid acid catalysts stand out as a promising alternative to the highly corrosive liquid acid catalysts as these catalysts offer superior catalytic activity and excellent reusability. Suganuma et al. [1] prepared a mesoporous carbonaceous material supported catalysts, $CH_{0.62}O_{0.54}S_{0.05}$ which contains Bronsted acidic sites of $-SO_3H$, -COOH and -OH group. Their study reported that, due to these Brønsted acidic sites, the catalyst could convert 68% of cellulose at 100°C in 3 hours (Table 2.1), achieving a maximum yield of 64 mol% reducing sugars (RS). In another work, Onda et al. [2] prepared nitric acid treated activated carbon doped sulfonated acid catalyst ($AC-SO_3H$) and utilised in ball milled cellulose hydrolysis process. The work demonstrated that the prepared catalyst could render maximum 40.5 mol % of glucose from balled milled cellulose at 150°C in 24 h. Moreover, the work also reported that compared to the H form zeolite, it exhibited superior glucose yield, owing to its high hydrothermal stability and excellent catalytic properties attributed to the presence of $-SO_3H$ functional groups and hydrophobic activated carbon support.

Apart from these sulfonated carbonaceous solid acid catalysts, sulfonic acid functionalized ion-exchange resin solid acid catalysts also work very well in the hydrolysis of LB at low temperature. While a variety of cation exchange resins have found extensive application in LB hydrolysis, Amberlyst-15 stands out as one of the most frequently employed catalysts in this process. For instance, Kitano et al. [4] employed Amberlyst-15 and hydrolyse cellobiose into glucose with 62 mol % yield at 90°C in 24 h. another work reported by Dhepe et al. [5] demonstrated that sucrose could hydrolysed to glucose in presence of Amberlyst-15 and gives 88 mol % of glucose yield at 80°C in 4 h. Interestingly, among other previously reported work on sulfonated ion exchange resins, Zajšek et al. [7] utilized Amberlite IR-120H to hydrolyse sucrose, achieving complete conversion into glucose at 79°C within 1.5 hours under a nitrogen atmosphere. Despite exhibiting good catalytic activity, sulfonated ion exchange resins suffer from certain drawbacks, including poor temperature stability (< 130°C) and the tendency to leach active sites in aqueous media.

Table 2. 1. Sulfonated solid acid catalyst for hydrolytic conversion of LB in glucose or RS

Catalyst	Substrate	Reaction conditions	Glucose / RS yield (mol %)	Reference
$CH_{0.62}O_{0.54}S_{0.05}$	Cellulose	100°C; 3h	64	[1]
AC-SO_3H[a]	Ball milled cellulose	150°C; 24h	40.5	[2]
AC-N-SO_3H-250[b]	Ball milled cellulose	150°C; 24h	62.6	[3]
CMK-3-SO_3H[c]	Ball milled cellulose	150°C; 24h	74.5	[3]
Amberlyst-15	Cellobiose	90°C, 24 h	62	[4]
Amberlyst-15	Sucrose	80°C, 4 h	88	[5]
Amberlite IR-120H	Sucrose	170°C, 1h	85	[6]
Amberlite IR-120H	Sucrose	79°C, 1.5 h, N_2	100	[7]
Amberlite 200C	Sucrose	80°C, 3 h	98	[8]
Amberlyst-35W	Cellobiose	130°C, 2h	70	[9]
Nafion NR50	Cellobiose	100°C, 4 h	6.7	[10]

[a: activated carbon-sulfonic acid, b: nitric acid treated activated carbon-sulfonic acid, c: mesoporous CMK-3 doped sulfonic acid]

2.1.1. Metal oxide based solid acid catalyst for hydrolytic conversion of LB into glucose or RS synthesis

Metal oxides serve as solid catalysts rich in Lewis acid sites, often characterized by high specific surface areas and large pore sizes. These properties facilitate the easy access and interaction of reactants with the active sites within the pores of the metal oxides. A range of catalysts, including single, bi-metallic, and even trimetallic oxides, have been employed for the hydrolysis of lignocellulosic biomass (LB) and its derived disaccharides, such as sucrose and cellobiose (Table 2.2). For instance, Marzo et al. [11] used Nb_2O_5 catalyst for the hydrolysis of sucrose and achieved 10 mol % RS yield at 80°C, 24 h. Takagaki et al. [12] investigated a layered transition-metal oxide, $HNbMoO_6$, which demonstrated exceptional catalytic performance in the hydrolysis of disaccharides like sucrose, cellobiose and polysaccharides such as starch, and cellulose. Notably, the $HNbMoO_6$ catalyst demonstrated superior activity in the hydrolysis of sucrose and cellobiose, producing glucose at more than twice the rate of the commercially available -SO_3H functionalized ion exchange resin, Amberlyst-15. The remarkable activity of $HNbMoO_6$ in these reactions was attributed to its strong acidity, water tolerance, and intercalation capability although the specific surface area of the catalyst was very low (5 m^2/g). In another work, Lai et al. [13] used magnetic solid acid catalyst, $CoFe_2O_4$-SBA15-SO_3H to hydrolyse the cellobiose into glucose and demonstrated that maximum 96 mol % of glucose can be achieved at 120°C and 1 h due to the presence of both Bronsted and Lewis acidic sites in the prepared catalyst.

Table 2. 2. Metal oxide catalysts for hydrolytic conversion of LB in glucose or RS

Catalyst	Substrate	Operating conditions	Glucose / RS yield (mol %)	Reference
Nb_2O_5	Sucrose	80°C, 24 h	10	[11]
Nb_2O_5-PO_4	Sucrose	80°C, 24 h	62	[11]
SiO_2-ZrO_2	Sucrose	80°C, 24 h	5	[11]
SiO_2-Al_2O_3	Sucrose	80°C, 24 h	9	[11]
Layered $HNbMoO_6$	Sucrose	100°C, 70 min	100	[12]
	Cellobiose	100°C, 70 min	100	

	Starch	100°C, 15 h	21	
	cellulose	100°C, 12 h	8.5	
$CoFe_2O_4$-SiO_2-SO_3H	cellobiose	175°C, 1 h	50	[13]
$H_4SiW_{10}O_{40}$	cellobiose	150°C, 24 h	53	[14]
$H_4PMo_{12}O_{40}$	cellobiose	150°C, 24 h	48	[14]
$H_4SiMo_{12}O_{40}$	cellobiose	150°C, 24 h	42	[14]
$CoFe_2O_4$-SBA15-SO_3H	cellobiose	120°C, 1 h	96	[15]
WO_3/ZrO_2	cellobiose	97°C, 32 h	7.5	[16]

2.1.2. Sulfonic acid and metal oxide based solid acid catalyst for synthesis of furanic compounds from LB

Various sulfonic acid and metal oxide based solid acid catalysts have been used for synthesis of furanic compounds like 5-HMF from LB or LB derived carbohydrates. Table 2.3 demonstrated the 5-HMF production employing various sulfonic acid and metal oxide based solid acid catalysts. Qi et al. [17] used a sulfonated ion exchange resin catalyst, Dowex 50wx8 for the dehydration of fructose substrate in acetone/water biphasic medium under microwave heating and achieved 70.30 mol % of 5-HMF at 150°C in 10 min. In another work, Wang et al. [18] prepared superhydrophobic mesoporous solid acid catalyst (P-SO_3H-154), which could prevent 5-HMF from hydration during reaction and reported that maximum 95.4 mol % of 5-HMF could be achieved from glucose in presence of tetrahydrofuran (THF) /dimethyl sulfoxide (DMSO) biphasic medium at 100°C in 10 h. Notably, Xing et al. [19] investigated efficacy of β-SO_3H-zeolite catalyst in LB (Wheat straw and Moso bamboo) to 5-HMF hydrolytic conversion process, and achieved 18.7 and 25.1 mol % of 5-HMF at 210°C in 2h from Wheat straw and Moso bamboo, respectively.

Dutta et al. [20] employed TiO_2 to convert fructose into 5-HMF in DMSO under microwave heating, achieving a 54.10 mol% yield of 5-HMF within a short reaction time of 5 minutes, albeit at a high reaction temperature of 140°C. Interestingly, Hirano et al. [23] employed both ion-exchange resin and metal oxide catalyst [Table 2.3] to dehydrate glucose into 5-HMF in Water/MIBK/$CaCl_2$ medium under microwave heating. The work reported that maximum 85.9 mol % of 5-HMF yield could achieved at 175°C in 3 h, due to presence of both Lewis and Bronsted acid functional group in TiO_2-ZrO_2/Amberlyst-70 catalytic systems.

Table 2. 3. 5-HMF production using sulfonic acid and metal oxide-based catalyst

Catalyst	Substrate	Solvent	Operating conditions	5-HMF yield (mol%)	Reference
Dowex 50wx8	Fructose	Acetone/water	150°C, 10 min	70.30	[17]
P-SO_3H-154	glucose	THF/DMSO	100°C, 10 h	95.4	[18]
β-SO_3H-zeolite	Fructose	THF/NaCl-water	150°C, 2h	95.5	[19]
	Glucose		170°C, 3h	86.5	
	Sucrose		180°C, 3h	76.8	
	Starch		190°C, 2h	68.1	
	Cellulose		200°C, 3h	59.4	
	Wheat straw		210°C, 2h	18.7	
	Moso bamboo		210°C, 2h	25.1	
TiO_2	Fructose	DMSO	140°C, 5min, microwave heating	54.10	[20]
SiO_2-ZrO_2	Fructose	DMSO	140°C, 20 min	72.80	[21]
ɣ-Al_2O_3	Glucose	Water/MIBK/$CaCl_2$	175°C, 15 min	52.0	[22]
TiO_2-ZrO_2/Amberlyst-70	Glucose	THF/water	175°C, 3 h, Microwave heating	85.9	[23]

2.1.3. Sulfonic acid and metal oxide-based catalysts for Levulinic acid (LA) production

Few works on LA production employing sulfonic acid and metal oxide-based catalyst were also reported (Table 2.4). For instance, Upare et al. [24] investigated graphene oxide, activated carbon and methoxy triethyl silane/graphene oxide based sulfonated catalysts in glucose to LA conversion process. The work demonstrated that sulfonated graphene oxide (GO-SO_3H) showed higher catalytic activity compared to the other two prepared catalyst, yielding 78 mol % of LA yield at 200°C in 2 h. LA was also prepared from municipal LB waste, kiwifruit waste residue employing Nb/Al oxide [26], although the reported LA yield was low (9.8 %) even at high reaction temperature (190°C).

Table 2. 4. LA production using sulfonic acid and metal oxide-based catalyst

Catalyst	Substrate	Operating conditions	LA yield (mol%)	Reference
GO-SO_3H^a	Glucose	200°C, 2h	78	[24]

AC-SO_3H	Glucose	200°C, 2h	4.2	[24]
MTS/GO-SO_3H[b]	Glucose	200°C, 2h	11	[24]
CP-SO_3H-1.69[c]	Glucose	170°C, 10 h	44.2	[25]
CP-SO_3H-1.69 [b]	Sucrose	170°C, 10 h	48.5	[25]
CP-SO_3H-1.69 [b]	cellulose	170°C, 10 h; GVL/water medium	65.5	[25]
Nb/Al oxide	kiwifruit waste residue	190°C, 15 min	9.8	[26]
Ga_2O_3-UiO-66	Cellulose	240°C, 360 min	32	[27]
CeO_2-UiO-66	Cellulose	240°C, 360 min	14	[27]
CoO-UiO-66	Cellulose	240°C, 360 min	7	[27]

[a: sulfonated graphene, b: methoxy triethyl silane, c: sulfonated chloromethyl polystyrene resin]

2.1.4. EL production using sulfonic acid and metal oxide-based catalyst

The synthesis of EL employing sulfonic acid and metal oxide-based catalysts have primarily been reported through two main routes: the esterification process of LA derived from LB or the dehydration and esterification of furanic compounds such as 5-HMF, furfural alcohol in ethanol. However, there is no reported work on one-pot EL production directly from LB. various carbonaceous solid acid catalysts such as CNT-SO_3H-210, BoiC-S3 have been employed for esterify LA into EL (Table 2.5). Interestingly Pileidis et al. [30] employed hydrothermal treated lignocellulosic biomass, rice husk and LB derived cellulose and glucose to synthesize sulphated carbonaceous catalysts viz., HTC-RS-S, HTC-Cell-S and HTC-Glu-S. Among the prepared catalysts, HTC-Glu-S showed superior catalytic activity in LA esterification reaction and rendered 97 mol % of EL at mild reaction temperature of 60°C over a prolonged reaction time of 3 hours.

Metal oxide catalysts were also employed in LA esterification reaction by some researchers (Table 2.5). For instance, Fernandes et al. [31] employed various SO_4^{2-} doped metal oxides in LA esterification reaction, and reported that SO_4/SnO_2 catalyst showed superior activity in terms of EL yield (44 mol %). Quereshi et al. [32] utilised silicotungstic acid-zirconium oxide catalyst (HPS/ZrO_2) and the work reported that maximum 90 mol % of EL yield could be achieved at 110°C in 30 min under microwave heating.

Table 2. 5. EL production using sulfonic acid and metal oxide-based catalyst

Catalyst	Substrate	Operating conditions	EL yield (mol %)	Reference
CNT-SO_3H-210	LA	70°C, 5 h	55	[28]
BoiC-S3[a]	5-HMF	130°C, 6 h	84	[29]
HTC-Glu-S[b]	LA	60°C, 3 h	97	[30]
HTC-Cell-S[c]	LA	60°C, 3 h	89	[30]
HTC-RS-S[d]	LA	60°C, 3 h	92.2	[30]
SO_4/SnO_2	LA	70°C, 5 h	44	[31]
SO_4/TiO_2	LA	70°C, 5 h	40	[31]
SO_4/Nb_2O_5	LA	70°C, 5 h	14	[31]
SO_4/ZrO_2	LA	70°C, 5 h	9	[31]
HPS/ZrO_2[e]	LA	110°C, 30 min, microwave heating	90	[32]
Sulfated-TiO_2	LA	160°C, 100 min	72	[33]
Sulfated-SnO_2	LA	160°C, 100 min	75	[33]
Sulfated-ZrO_2	LA	160°C, 100 min	69	[33]
Ni-TiO_2	Furfural alcohol	190°C, 1 h	75	[34]

[a: biochar-sulfonic acid (S content: 4.95 wt%), b: sulfonated-hydrothermally treated glucose, c: sulfonated-hydrothermally treated cellulose, d: sulfonated-hydrothermally treated rice straw, e: silicotungstic acid-zirconium oxide]

2.2. Applications of FA and WPCB as catalyst or catalyst support

Synthesis of catalyst or catalyst support from coal-based fly ash (FA) for the valorisation of LB or LB derived platform chemicals into value-added chemicals has been reported by several researchers (Table 2.6). For instance, Chatterjee et al., [35,36] utilized FA from Durgapur steel plant, India to produce two types of catalysts viz., H_2SO_4 treated FA [35] and MIL-101 (Cr) based MOF-FA-composite [36] and produced catalysts efficacy was investigated in xylose dehydration process in toluene/aqueous NaCl biphasic medium. The reported studies showed that the H_2SO_4 treated FA could produce 68 mol % of furfurals from xylose at 170°C and 210 min, whereas the MIL-101 (Cr) based MOF-FA-composite could render maximum 78 mol % of furfural at 150°C and 3h. Gong et al. [37] utilized FA as catalyst support to produce SO_4^{2-}/SnO_2-Al_2O_3-FA catalyst and utilized in xylose rich corn stover hydrolysate dehydration

reaction. The study described that the produced SO_4^{2-}/SnO_2-Al_2O_3-FA catalyst possess high specific surface area (27.141 m^2/g) and pore size (3.093 nm) which render maximum 84.7 mol % of furfural at 180°C for 30 min in a NH_4Cl-toluene biphasic reaction medium.

Table 2. 6. Reported works on FA derived catalysts

Reference	Catalyst	FA source	Catalyst preparation method	Catalyst's recyclability	Catalyst's application process	Product yield (mol%)
[35]	Activated FA	FA source (Durgapur steel plant, India)	H_2SO_4 treated fly-ash	6 cycles	Xylose Dehydration in toluene/aqueous NaCl biphasic medium (170°C and 210 min)	Furfural (68 %)
[36]	MOF- FA-composite	FA source (Durgapur steel plant, India)	hydrothermal method	10 cycles	Xylose Dehydration toluene/aqueous NaCl biphasic medium (150°C and 3 h)	Furfural (78 %)
[37]	SO_4^{2-}/SnO_2-Al_2O_3-FA	Henan Borun Casting Material Co., Ltd. Chaina	Co-condensation and precipitation	5 cycles	Xylose rich corn stover hydrolysate (NH4Cl-toluene biphasic system at 180°C for 30 min)	Furfural (84.7 %)
[38]	Ni/FA	Not mentioned	Incipient wetness impregnation	4 cycles	Sorbitol hydrogenation in aqueous medium (60 bar, 200°C, 6 h)	1,2-propanediol (10.1), Glycerol (7.56), ethylene glycol (3.6)
[39]	Cellulase immobilized magnetic FA-Chitosan	Guodian Yongfu Power Generation Co., Ltd. Chaina	Precipitation (catalyst-1) emulsification in oil phase (catalyst-2)	Activity 69.9% (catalyst-1) and 75.5% (catalyst-2) of the original after 10 cycles	Cellulose hydrolysis (70°C, 5 h)	Glucose (19.8, for catalyst-1) (22.2, for catalyst-2)

Although no research has been conducted on catalysts derived from WPCB or glass fiber (GF) supported catalysts from WPCB, some studies have reported the preparation and application of GF supported catalysts in various other reactions. For instance, Kiwi-Minsker et al. [40] prepared Pt and Pd doped GF as a combustion catalyst for use in the temperature range of 200–500°C. The work reported the prepared catalyst showed high thermal stability, excellent specific surface area (275 m^2/g) and the Pt doped GF demonstrate highest activity when modified with titania. In another work, You et al. [41] employed GF as effect transparent support to prepare TiO_2 doped GF photocatalyst. Bal'zhinimaev et al. [42] prepared GF supported vanadium catalyst for the SO_2 oxidation process in the temperature range of 420–700°C. Similarly, Mikenin et al. [43] prepared GF supported Fe catalyst for the oxidation of

H_2S. Both the work reported that high activity and good thermal resistance of the prepared catalyst. Thus, GF can be used as an effective catalyst support for preparation of both heterogenous solid catalyst as well as photocatalyst, and recycling of WPCB to extract GF for catalyst preparation can reduce costs and mitigate e-waste disposal issues.

2.3. Intensification of LB conversion process employing electromagnetic irradiation

Electromagnetic irradiation techniques, such as microwave (MW) and ultrasound (US), have been extensively used to intensify the LB conversion process and enhance conversion yields. Several research studies have investigated the efficacy of these auxiliary techniques, which are discussed in more detail in the following sections.

US energy is primarily utilized in the pretreatment of LB, where it disrupts intermolecular hydrogen bonds between lignocellulosic components, enhancing LB dissolution [44,45]. Additionally, US energy promotes solvent penetration into cellulosic materials, thereby increasing the mass transfer rate. Velmurugan et al. [46] studied the effect of ultrasound pretreatment on sugarcane bagasse with 10% NaOH for 1 h in an autoclave. The results indicated a 95% reduction in lignin, along with a recovery of 79% cellulose and 99% hemicellulose. Lan et al. [47] reported that using 30 W ultrasound energy for 20 minutes reduced the complete dissolution time of cellulose in 1-butyl-3-methylimidazolium chloride ($[C_4mim]Cl$) from 190 min to 60 min. Ultrasonic treatment also modified the cellulose structure, improving its accessibility to catalysts [48].

2.3.1. *Intensification of LB conversion process employing microwave irradiation*

Over the last decades, MW irradiation has been extensively employed LB conversion process. MW-induced heating primarily occurs through dipolar rotation and ionic conduction [49], enhancing reaction rates by lowering activation energies through internal energy modification in reacting molecules. Table 2.7 demonstrated MW assisted glucose production through hydrolytic conversion of cellulose. Li et al. [52] investigated MW irradiation effect in ball milled cellulose hydrolysis process in presence of a poly(acrylic acid)-random-poly(styrene sulfonic acid) catalyst. The work reported that 35 mol % of glucose can be achieved under MW irradiation at 120°C in 2 h.

Table 2. 7. Reported works on MW assisted glucose production

Substrate	Catalyst	Reaction conditions	Glucose/RS yield (mol %)	Reference
Cellulose	BC-SO_3H-2[a]	90°C; 1h	19.8	50
Ball milled cellulose	BC-CSA-SO_3H[b]	130°C; 2h	34.6	51
Ball milled cellulose	PAA-r-PSSH[c]	120°C; 2 h	35	52

[a: biomass char-sulfonic acid; b: biomass char-carbonaceous solid acid c: poly(acrylic acid)-random-poly(styrene sulfonic acid)]

Production of 5-HMF employing MW induced heating have also been investigated by some researchers. For instance, Wang et al. [53] investigated various metal oxide catalysts under MW irradiation system to produce 5-HMF from fructose. Among various utilized catalysts in this work, SO_4^{2-}/WOx-ZrO_2 catalyst showed superior activity in terms of 5-HMF yield (70.88 mol %) in presence of DMSO solvent (Table 2.8). In another work, Hirano et al. [55] employed metal doped reduced graphene oxide (rGO) to convert glucose into 5-HMF in THF-water biphasic medium under MW heating and reported that the nickel doped rGO (Ni-rGO) catalyst showed great thermal stability and rendered highest 5-HMF yield at 200°C in 30 min under MW heating.

Table 2. 8. Reported works on MW assisted 5-HMF synthesis

Substrate	Catalyst	Solvent	Reaction conditions	HMF yield (mol %)	Reference
Fructose	ZrO_2	DMSO	140°C; 5min	31.02	[53]
Fructose	WOx-ZrO_2	DMSO	140°C; 5min	53.03	[53]
Fructose	MoOx-ZrO_2	DMSO	140°C; 5min	47.26	[53]
Fructose	SO_4^{2-}/WOx-ZrO_2	DMSO	140°C; 5min	70.88	[53]
Fructose	SO_4^{2-}/MoOx-ZrO_2	DMSO	140°C; 5min	67.11	[53]
Fructose	Niobium phosphate	Water	190°C; 8 min	33.9	[54]
Fructose	Zirconium phosphate	Water	190°C; 8 min	40	[54]
Glucose	Blank	Water-THF	200°C; 30 min	12.5	[55]
Glucose	GO	Water-THF	200°C; 30 min	4.3	[55]

Glucose	rGO	Water-THF	200°C; 30 min	7.4	[55]
Glucose	Pt-rGO	Water-THF	200°C; 30 min	9.8	[55]
Glucose	Ni-rGO	Water-THF	200°C; 30 min	28.1	[55]
Glucose	Co-rGO	Water-THF	200°C; 30 min	17.8	[55]

[THF: Tetrahydrofuran; rGO: reduced graphene oxide]

Table 2.9 and Table 2.10 outline published studies on microwave-assisted production of LA and EL, respectively. These processes predominantly utilize homogeneous acid catalysts for the production of LA and EL from LB or cellulose under MW irradiation. For instance, Lappalainen et al. [56] employed H_2SO_4 and $CrCl_3$ catalyst in potato peel to LA production process (Table 2.9) whereas Zhang et al. [63] and Liu et al. [64] employed H_2SO_4 for the production of EL from corn stover (Table 2.10). A work done by Aliko et al. reported that employing homogenous Maleic acid and $Al_2(SO_4)_3$ catalyst in aqueous medium can render 86.7 mol % LA yield under MW irradiation at 180°C in 38 min. Interestingly, Ahmad et al. [66] investigated LA esterification reaction under MW without catalyst and reported that 85 mol % of EL could be achieved at 80°C in 90 min.

While numerous studies have effectively converted LB into value-added platform chemicals and drop-in biofuels like EL using MW irradiation, it's crucial to consider factors such as MW penetration depth, solvent selection, and MW power when employing MW in LB conversion processes.

Table 2. 9. Reported works on MW assisted LA production

Substrate	Catalyst	Solvent	Reaction conditions	LA yield (mol %)	Reference
Potato peel	H_2SO_4 and $CrCl_3$	Water	180°C; 15 min	49	[56]
Orange peel	H_2SO_4	Water	170°C; 30 min	71	[57]
Wheat straw	HCl	Water	200°C; 60 min	49.3	[58]
cellulose	$Al_2(SO_4)_3$	Water	180°C; 40 min	70.6	[59]
cellulose	H_3PO_4 and NaCl	Water	170°C; 60 min	67	[60]
Glucose	Maleic acid and $AlCl_3$	Water	180°C; 6 min	41	[61]
Mandarin peel	Maleic acid and $Al_2(SO_4)_3$	Water	180°C; 38 min	86.7	[62]

Table 2. 10. Reported works on MW assisted EL production

Substrate	Catalyst	Reaction conditions	EL yield (mol %)	Reference
Corn stover	H_2SO_4	190°C; 30 min	58.1	[63]
Corn stover	H_2SO_4	160°C; 30 min	31.23	[64]
Fructose	WS_2	160°C; 30 min	62 % EMF and 7 % EL	[65]
LA	Non-catalytic	80°C; 90 min	85 %	[66]

2.3.2. Application of electromagnetic irradiation in catalyst synthesis process

Electromagnetic irradiation especially MW and US have been employed to enhance the catalysts properties. For instance, Zhang et al. [67] investigated impregnation of CoO doped on a carbon support employing US energy. This study reported that utilization of US energy could reduce the impregnation time to one-third of that required by conventional methods, while ensuring a uniform distribution of active sites. In a separate study, Mahboob et al. [68] demonstrated the benefits of using US energy (90 W), achieving impregnation of Co onto γ-Al_2O_3 and ZrO_2 supports within 80 minutes. Additionally, Yin et al. [69] reported preparation of a Co-Fe-P-O electrocatalyst in presence of US and MW energy, within a total impregnation time of only 36 minutes with 30 minutes of US energy followed by 6 minutes of MW irradiation time. Notably, applying MW energy during the calcination step of MgAlO-supported, Sn-Pt catalysts preparation led to an approximate 11% improvement in the surface area of the prepared catalyst compared to conventional calcination method [70]. Interestingly, Motshekga et al. [71] reported that the use of MW (500 W) can reduced the impregnation time for SnO_2 catalyst on carbon nano tube support to 10 minutes, although it resulted in a decrease in specific surface area compared to the conventional method.

The literature survey clearly indicates that microwave radiation requires more power than ultrasonic energy. In many studies, the surface properties of catalysts deteriorated after 2-3 cycles or resulted in inferior properties compared to conventional preparation methods. However, the significantly reduced wet-impregnation times underscore the benefits of electromagnetic energy. Therefore, the judicious application of electromagnetic radiation in the catalyst preparation step can help reduce energy consumption while enhancing surface properties and catalyst stability in chemical reactions.

2.4. LB depolymerization kinetics

Pseudo homogeneous kinetic model had been extensively employed to describe the reaction kinetics of hydrolytic conversion of LB into glucose and furanic compounds like 5-HMF, 5-CMF conversion processes. The Pseudo homogeneous hydrolytic conversion kinetics for LB to glucose or reducing sugar was mainly described in the following form

$$cellulose \overset{k_1}{\rightarrow} glucose \overset{k_2}{\rightarrow} undesired\ products \quad (2.1)$$

$$\frac{dC_{cellulose}}{dt} = -k_1 C_{cellulose} \quad (2.2)$$

$$\frac{dC_{glucose}}{dt} = k_1 C_{cellulose} - k_2 C_{glucose} \quad (2.3)$$

Where $C_{cellulose}$ and $C_{glucose}$ represent the cellulose and glucose concentration and are the rate constants. Notably, Arrhenius equation was used to calculate the activation energies associated with each rate equations. The reported activation energies for various LB to glucose depolymerization process at different temperature range (110-240°C) and acid concentrations (0.2-12.2 %) were tabulated in Table 2.11.

Table 2. 11. Reported activation energies for LB to glucose conversion kinetics

Substrate	Temperature (°C)	Acid concentration (%)	Activation energy (kJ/mol)	Reference
Douglas fir	170-190	0.4-1	179	[72]
Municipal solid waste	200-240	1.4-4.4	171	[73]
Kraft paper	180-240	0.2-1	188	[74]
Paper refuse	180-240	0.2-1	137	[75]
Solka-floc	180-240	0.5-2	177	[75]
Filter paper	200-240	0.4-1.5	178	[76]
Sunflower residues	110-140	0.5-6	101	[77]
Hardwood	170-190	4.41-12.2	165	[78]

Detailed literature survey on LB to 5-HMF conversion kinetic models and corresponding activation energies were tabulated in Table 2.12. Some research works were also reported on reaction kinetics of 5-CMF synthesis process in homogeneous catalytic system. Antonyraj et al. [79] presented the first homogeneous kinetic models for consecutive reaction steps in 5-CMF synthesis from glucose in homogeneous catalytic (HCl) system. Another study by Rojahn et al. [80] developed homogeneous kinetic models for consecutive reaction steps in 5-CMF synthesis from D-fructose.

Kinetic studies conducted on LB to ethyl levulinate (drop-in-biofuel) synthesis processes have so far also extensively employed simplified pseudo-homogeneous kinetic models to describe such multiphase reactions [81,82]. For instance, Tao et al [83] employed simplified pseudo-homogeneous first order kinetic model to understand the EL synthesis process from cellulose in presence of solid $Al_{2/3}H_2SiW_{12}O_{40}$ catalyst.

However, development a realistic reaction kinetic model for such complex multiphase reactions is crucial to understanding the reaction mechanisms and scaling up industrial processes. Various important factors like internal and external mass transfer limitations, molecular simulation to understand the reaction mechanism, leaching of heterogeneous catalysts active sites and heterogeneous reaction kinetic models such as Eley-Rideal and Langmuir-Hinshelwood kinetic models and efficient solvers like non-linear regression method needs to be considered when develop the reaction kinetic model for lignocellulosic biomass to platform chemicals and drop-in biofuel conversion process.

Table 2. 12. Reported activation energies for LB derived substrates to 5-HMF and LA synthesis process

Proposed model	Solvent	Catalyst	Temperature (°C)	Activation energy (kJ/mol)	Reference
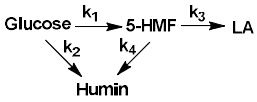	Water	HCl	140-180	E_1 = 160 E_2 =51 E_3 =95 E_4 =142	[84]
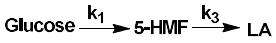	Water	Fe/HY Zeolite	120-220	E_1 = 64 E_2 =76 E_3 =61	[85]
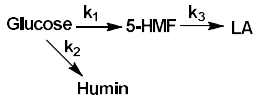	Water	H_3PO_4 + $CrCl_3$	150-180	E_1 = 65.4 E_2 =85.6 E_3 =60.6 E_4 =82.1	[86]
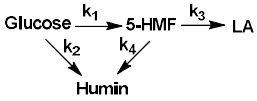	Water + Sulfonate	H_2SO_4	140-200	E_1 = 134 E_2 =131 E_3 =94.4 E_4 =94.7	[87]
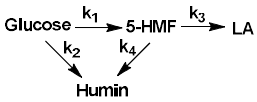	Water	H_2SO_4	140-200	E_1 = 152.2 E_3 =164.7	[88]

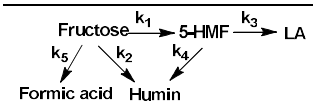	Water	Cr/HZSM-5		E_1 = 69.1 E_3 =54.0	[89]
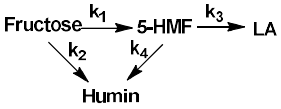	Water	$FeCl_3$	160-200	E_1 = 93.25 E_2 =94.04 E_3 =42.86	[90]
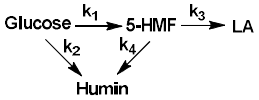	Water	$SnCl_4$	170-190	E_1 = 45.99 E_2 =76.3 E_3 =57.04 E_4 =67.25	[91]
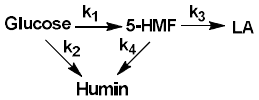	Water	NiSO4. 6H2O in {IL-SO3H][Cl]	145-175	E_1 = 47.45 E_2 =68.86 E_3 =34.28 E_4 =99.02	[92]
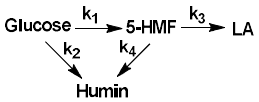	Water	No catalyst	180-220	E_1 = 108 E_2 =136 E_3 =89 E_4 =109	[93]
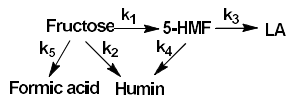	Water	HCl	70-150	E_1 = 126 E_2 =135 E_3 =97 E_4 =62 E_5=130	[94]
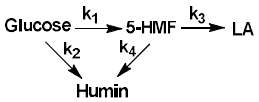	Water	$LiCl. 3H_2O$	120-170	E_1 = 160.96 E_2 =23.45 E_3 =71.81 E_4 =42.15	[95]
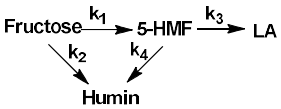	Water	$LiCl. 3H_2O$	120-170	E_1 = 139.20 E_2 =49.54 E_3 =72.72 E_4 =54.38	[95]

2.5. Engine performance of levulinate esters

Levulinate esters, recognized as promising oxygenated drop-in biofuels for biodiesel and diesel, have gained attention for their dual role as cold flow enhancers [96] and clean-burning fuels. Despite their potential, studies on engine performance and exhaust emissions of levulinate esters remain limited. Christensen et al. [97] reported that large reductions in the engine-out smoke number of a horizontal, single cylinder, four stroke diesel engine (41.3% and 55 %, respectively) were observed when 10 % EL (EL10) and 20 % butyl levulinate (BL20) blended diesel due to the presence of high oxygen content in levulinate esters. Although, the

author also reported that the lower energy density of the blended fuels resulted in increased brake-specific fuel consumption: 5.1% for EL10, and 7.6% for BL20 whereas EL10 had no effect on nitrogen oxides (NOx) emission and BL20 increased NOx by 4.6%. In contrast, Wang et al. [98] observed a different trend, reporting that NOx emissions decreased with higher power when ethyl levulinate (EL) was blended with diesel in concentrations ranging from 5 to 10 vol%. Lei et al. [99] blended EL-biodiesel-diesel in different proportions and investigate performance of blended fuels in a horizontal, single cylinder, four stroke diesel engine and reported that Nox emission similar or slightly lower when diesel blended with 2.5 % EL and 2.5 % biodiesel. The author also reported that the HC and CO emission is significantly low compared to diesel for all the blended flues. This highlights the variability in results across studies and the need for further investigation into the engine performance and emission characteristics of levulinate ester blends.

2.6. Reference

1. Suganuma S, Nakajima K, Kitano M, Yamaguchi D, Kato H, Hayashi S, Hara M. Hydrolysis of cellulose by amorphous carbon bearing SO3H, COOH, and OH groups. Journal of the American Chemical Society. 2008 Sep 24;130(38):12787-93.
2. Onda A, Ochi T, Yanagisawa K. Selective hydrolysis of cellulose into glucose over solid acid catalysts. Green Chemistry. 2008;10(10):1033-7.
3. Pang J, Wang A, Zheng M, Zhang T. Hydrolysis of cellulose into glucose over carbons sulfonated at elevated temperatures. Chemical Communications. 2010;46(37):6935-7.
4. Kitano M, Yamaguchi D, Suganuma S, Nakajima K, Kato H, Hayashi S, Hara M. Adsorption-enhanced hydrolysis of β-1, 4-glucan on graphene-based amorphous carbon bearing SO3H, COOH, and OH groups. Langmuir. 2009 May 5;25(9):5068-75.
5. Dhepe PL, Ohashi M, Inagaki S, Ichikawa M, Fukuoka A. Hydrolysis of sugars catalyzed by water-tolerant sulfonated mesoporous silicas. Catalysis Letters. 2005 Aug;102:163-9.
6. Adnadjevic BK, Jovanovic JD. A comparative kinetics study on the isothermal heterogeneous acid-catalyzed hydrolysis of sucrose under conventional and microwave heating. Journal of Molecular Catalysis A: Chemical. 2012 Apr 1;356:70-7.
7. Zajšek K, Goršek A. A kinetic study of sucrose hydrolysis over Amberlite IR-120 as a heterogeneous catalyst using in situ FTIR spectroscopy. Reaction Kinetics, Mechanisms and Catalysis. 2010 Aug;100:265-76.
8. Plazl I, Leskovšek S, Koloini T. Hydrolysis of sucrose by conventional and microwave heating in stirred tank reactor. The Chemical Engineering Journal and the Biochemical Engineering Journal. 1995 Nov 1;59(3):253-7.

9. Kim Y, Hendrickson R, Mosier N, Ladisch MR. Plug-flow reactor for continuous hydrolysis of glucans and xylans from pretreated corn fiber. Energy & fuels. 2005 Sep 21;19(5):2189-200.
10. Suganuma S, Nakajima K, Kitano M, Hayashi S, Hara M. sp3-Linked Amorphous Carbon with Sulfonic Acid Groups as a Heterogeneous Acid Catalyst. ChemSusChem. 2012 Sep;5(9):1841-6.
11. Marzo M, Gervasini A, Carniti P. Hydrolysis of disaccharides over solid acid catalysts under green conditions. Carbohydrate research. 2012 Jan 10;347(1):23-31.
12. Takagaki A, Tagusagawa C, Domen K. Glucose production from saccharides using layered transition metal oxide and exfoliated nanosheets as a water-tolerant solid acid catalyst. Chemical communications. 2008(42):5363-5.
13. Peña L, Ikenberry M, Ware B, Hohn KL, Boyle D, Sun XS, Wang D. Cellobiose hydrolysis using acid-functionalized nanoparticles. Biotechnology and bioprocess engineering. 2011 Dec;16:1214-22.
14. Shimizu KI, Furukawa H, Kobayashi N, Itaya Y, Satsuma A. Effects of Brønsted and Lewis acidities on activity and selectivity of heteropolyacid-based catalysts for hydrolysis of cellobiose and cellulose. Green Chemistry. 2009;11(10):1627-32.
15. Lai DM, Deng L, Li J, Liao B, Guo QX, Fu Y. Hydrolysis of cellulose into glucose by magnetic solid acid. ChemSusChem. 2011 Jan 17;4(1):55-8.
16. Kourieh R, Bennici S, Marzo M, Gervasini A, Auroux A. Investigation of the WO3/ZrO2 surface acidic properties for the aqueous hydrolysis of cellobiose. Catalysis Communications. 2012 Mar 1;19:119-26.
17. Qi X, Watanabe M, Aida TM, Smith Jr RL. Catalytic dehydration of fructose into 5-hydroxymethylfurfural by ion-exchange resin in mixed-aqueous system by microwave heating. Green Chemistry. 2008;10(7):799-805.
18. Wang L, Wang H, Liu F, Zheng A, Zhang J, Sun Q, Lewis JP, Zhu L, Meng X, Xiao FS. Selective catalytic production of 5-hydroxymethylfurfural from glucose by adjusting catalyst wettability. ChemSusChem. 2014 Feb;7(2):402-6.
19. Xing X, Shi X, Ruan M, Wei Q, Guan Y, Gao H, Xu S. Sulfonic acid functionalized β zeolite as efficient bifunctional solid acid catalysts for the synthesis of 5-hydroxymethylfurfural from cellulose. International Journal of Biological Macromolecules. 2023 Jul 1; 242:125037.
20. Dutta S, De S, Patra AK, Sasidharan M, Bhaumik A, Saha B. Microwave assisted rapid conversion of carbohydrates into 5-hydroxymethylfurfural catalyzed by mesoporous TiO2 nanoparticles. Applied Catalysis A: General. 2011 Dec 15;409:133-9.
21. Qi X, Watanabe M, Aida TM, Smith Jr RL. Sulfated zirconia as a solid acid catalyst for the dehydration of fructose to 5-hydroxymethylfurfural. Catalysis Communications. 2009 Jul 25;10(13):1771-5.

22. García-Sancho C, Fúnez-Núñez I, Moreno-Tost R, Santamaría-González J, Pérez-Inestrosa E, Fierro JL, Maireles-Torres P. Beneficial effects of calcium chloride on glucose dehydration to 5-hydroxymethylfurfural in the presence of alumina as catalyst. Applied Catalysis B: Environmental. 2017 Jun 5;206:617-25.
23. Hirano Y, Beltramini JN, Mori A, Nakamura M, Karim MR, Kim Y, Nakamura M, Hayami S. Microwave-assisted catalytic conversion of glucose to 5-hydroxymethylfurfural using "three dimensional" graphene oxide hybrid catalysts. RSC advances. 2020;10(20):11727-36.
24. Upare PP, Yoon JW, Kim MY, Kang HY, Hwang DW, Hwang YK, Kung HH, Chang JS. Chemical conversion of biomass-derived hexose sugars to levulinic acid over sulfonic acid-functionalized graphene oxide catalysts. Green chemistry. 2013;15(10):2935-43.
25. Zuo Y, Zhang Y, Fu Y. Catalytic conversion of cellulose into levulinic acid by a sulfonated chloromethyl polystyrene solid acid catalyst. ChemCatChem. 2014 Mar;6(3):753-7.
26. Wang R, Xie X, Liu Y, Liu Z, Xie G, Ji N, Ma L, Tang M. Facile and low-cost preparation of Nb/Al oxide catalyst with high performance for the conversion of kiwifruit waste residue to levulinic acid. Catalysts. 2015 Sep 25;5(4):1636-48.
27. Wang K, Liu Y, Wu W, Chen Y, Fang L, Li W, Ji H. Production of levulinic acid via cellulose conversion over metal oxide-loaded MOF catalysts in aqueous medium. Catalysis Letters. 2020 Feb;150:322-31.
28. Oliveira BL, da Silva VT. Sulfonated carbon nanotubes as catalysts for the conversion of levulinic acid into ethyl levulinate. Catalysis Today. 2014 Oct 1;234:257-63.
29. Peixoto AF, Ramos R, Moreira MM, Soares OS, Ribeiro LS, Pereira MF, Delerue-Matos C, Freire C. Production of ethyl levulinate fuel bioadditive from 5-hydroxymethylfurfural over sulfonic acid functionalized biochar catalysts. Fuel. 2021 Nov 1;303:121227.
30. Pileidis FD, Tabassum M, Coutts S, Titirici MM. Esterification of levulinic acid into ethyl levulinate catalysed by sulfonated hydrothermal carbons. Chinese Journal of Catalysis. 2014 Jun 1;35(6):929-36.
31. Fernandes DR, Rocha AS, Mai EF, Mota CJ, Da Silva VT. Levulinic acid esterification with ethanol to ethyl levulinate production over solid acid catalysts. Applied Catalysis A: General. 2012 May 28;425:199-204.
32. Quereshi S, Ahmad E, Pant KK, Dutta S. Synthesis and characterization of zirconia supported silicotungstic acid for ethyl levulinate production. Industrial & Engineering Chemistry Research. 2019 May 22;58(35):16045-54.
33. Yadav GD, Yadav AR. Synthesis of ethyl levulinate as fuel additives using heterogeneous solid superacidic catalysts: Efficacy and kinetic modeling. Chemical Engineering Journal. 2014 May 1;243:556-63.

34. Zhao D, Li X, Liu Q, Xie J, Tang F, Su T, Zhao J, Yang Z. Effective synthesis of ethyl levulinate via alcoholysis of furfuryl alcohol over simple nickel-titanium dioxide. Applied Catalysis A: General. 2022 Nov 25;648:118921.
35. Chatterjee A, Xijun HU, Lam FL. Modified coal fly ash waste as an efficient heterogeneous catalyst for dehydration of xylose to furfural in biphasic medium. Fuel. 2019 Mar 1; 239:726-36.
36. Chatterjee A, Hu X, Lam FL. Catalytic activity of an economically sustainable fly-ash-metal-organic-framework composite towards biomass valorization. Catalysis Today. 2018 Sep 15; 314:137-46.
37. Gong L, Xu ZY, Dong JJ, Li H, Han RZ, Xu GC, Ni Y. Composite coal fly ash solid acid catalyst in synergy with chloride for biphasic preparation of furfural from corn stover hydrolysate. Bioresource technology. 2019 Dec 1; 293:122065.
38. Shanthi RV, Sankaranarayanan TM, Mahalakshmy R, Sivasanker S. Fly ash based Ni catalyst for conversion of sorbitol into glycols. Journal of environmental chemical engineering. 2015 Sep 1; 3(3):1752-7.
39. Zang L, Qiao X, Hu L, Yang C, Liu Q, Wei C, Qiu J, Mo H, Song G, Yang J, Liu C. Preparation and evaluation of coal fly ash/chitosan composites as magnetic supports for highly efficient cellulase immobilization and cellulose bioconversion. Polymers. 2018 May 14;10(5):523.
40. Kiwi-Minsker L, Yuranov I, Slavinskaia E, Zaikovskii V, Renken A. Pt and Pd supported on glass fibers as effective combustion catalysts. Catalysis Today. 2000 Jun 10;59(1-2):61-8.
41. You YS, Chung KH, Kim YM, Kim JH, Seo G. Deactivation and regeneration of titania catalyst supported on glass fiber in the photocatalytic degradation of toluene. Korean Journal of Chemical Engineering. 2003 Jan; 20:58-64.
42. Bal'zhinimaev BS, Simonova LG, Barelko VV, Toktarev AV, Zaikovskii VI, Chumachenko VA. Pt-containing catalysts on a base of woven glass fiber support: a new alternative for traditional vanadium catalysts in SO_2 oxidation process. Chemical Engineering Journal. 2003 Mar 15;91(2-3):175-9.
43. Mikenin P, Zazhigalov S, Elyshev A, Lopatin S, Larina T, Cherepanova S, Pisarev D, Baranov D, Zagoruiko A. Iron oxide catalyst at the modified glass fiber support for selective oxidation of H2S. Catalysis Communications. 2016 Dec 5;87:36-40.
44. Tang, A., Zhang, H., Chen, G., Xie, G., Liang, W., 2005. Influence of ultrasound treatment on accessibility and regioselective oxidation reactivity of cellulose. Ultrason. Sonochem., 12, 467-72.
45. Gasparotto, J.M., Werle, L.B., Mainardi, M.A., Foletto, E.L., Kuhn, R.C., Jahn, S.Z., Mazutti, M.A., 2015. Ultrasound-assisted acid hydrolysis of palm leaves (Roystoneaoleracea) for production of fermentable sugars. Biocatalysis and Agricultural Biotechnology, 4, 480–485
46. Velmurugan, R., Muthukumar, K., 2011. Utilization of sugarcane bagasse for bioethanol production: Sono-assisted acid hydrolysis approach. Bioresource Technology, 102, 7119–7123

47. Lan, W., Liu, C.F., Yue, F.X., 2011. Ultrasound-assisted dissolution of cellulose in ionic liquid. Carbohyd. Polym., 86, 672-7
48. Mikkola, J.P., Kirilin, A., Tuuf, J.C., Pranovich, A., Holmbom, B., Kustov, L.M., 2007. Ultrasound enhancement of cellulose processing in ionic liquids: from dissolution towards functionalization. Green Chem., 9, 1229-37.
49. Mannhold R, Kubinyi H, Folkers G (2006) Molecular interaction fields: applications in drug discovery and ADME prediction. John Wiley & Sons
50. Wu Y, Fu Z, Yin D, Xu Q, Liu F, Lu C, Mao L. Microwave-assisted hydrolysis of crystalline cellulose catalyzed by biomass char sulfonic acids. Green Chemistry. 2010;12(4):696-700.
51. Jiang Y, Li X, Wang X, Meng L, Wang H, Peng G, Wang X, Mu X. Effective saccharification of lignocellulosic biomass over hydrolysis residue derived solid acid under microwave irradiation. Green Chemistry. 2012;14(8):2162-7.
52. Li X, Jiang Y, Shuai L, Wang L, Meng L, Mu X. Sulfonated copolymers with SO_3H and COOH groups for the hydrolysis of polysaccharides. Journal of Materials Chemistry. 2012;22(4):1283-9.
53. Wang J, Qu T, Liang M, Zhao Z. Microwave assisted rapid conversion of fructose into 5-HMF over solid acid catalysts. RSC advances. 2015;5(128):106053-60.
54. Antonetti C, Melloni M, Licursi D, Fulignati S, Ribechini E, Rivas S, Parajó JC, Cavani F, Galletti AM. Microwave-assisted dehydration of fructose and inulin to HMF catalyzed by niobium and zirconium phosphate catalysts. Applied Catalysis B: Environmental. 2017 Jun 5;206:364-77.
55. Hirano Y, Beltramini JN, Mori A, Nakamura M, Karim MR, Kim Y, Nakamura M, Hayami S. Microwave-assisted catalytic conversion of glucose to 5-hydroxymethylfurfural using “three dimensional” graphene oxide hybrid catalysts. RSC advances. 2020;10(20):11727-36.
56. Lappalainen K, Vogeler N, Kärkkäinen J, Dong Y, Niemelä M, Rusanen A, Ruotsalainen AL, Wäli P, Markkola A, Lassi U. Microwave-assisted conversion of novel biomass materials into levulinic acid. Biomass Conversion and Biorefinery. 2018 Dec;8:965-70.
57. Tukacs JM, Hollo AT, Retfalvi N, Csefalvay E, Dibó G, Havasi D, Mika LT. Microwave-assisted valorization of biowastes to levulinic acid. ChemistrySelect. 2017 Feb 1;2(4):1375-80.
58. Galletti AM, Antonetti C, De Luise V, Licursi D, Nassi N. Levulinic acid production from waste biomass. BioResources. 2012 Feb 28;7(2):1824-35.
59. Huang YB, Yang T, Lin YT, Zhu YZ, Li LC, Pan H. Facile and high-yield synthesis of methyl levulinate from cellulose. Green chemistry. 2018;20(6):1323-34.
60. Qin K, Yan Y, Zhang Y, Tang Y. Direct production of levulinic acid in high yield from cellulose: joint effect of high ion strength and microwave field. RSC advances. 2016;6(45):39131-6.
61. Zhang X, Hewetson BB, Mosier NS. Kinetics of maleic acid and aluminum chloride catalyzed dehydration and degradation of glucose. Energy & Fuels. 2015 Apr 16;29(4):2387-93.

62. Aliko K, Doudin K, Osatiashtiani A, Wang J, Topham PD, Theodosiou E. Microwave-assisted synthesis of levulinic acid from low-cost, sustainable feedstocks using organic acids as green catalysts. Journal of Chemical Technology & Biotechnology. 2020 Aug;95(8):2110-9.
63. Zhang Y, Wang X, Hou T, Liu H, Han L, Xiao W. Efficient microwave-assisted production of biofuel ethyl levulinate from corn stover in ethanol medium. Journal of energy chemistry. 2018 May 1;27(3):890-7.
64. Liu H, Zhang Y, Hou T, Chen X, Gao C, Han L, Xiao W. Mechanical deconstruction of corn stover as an entry process to facilitate the microwave-assisted production of ethyl levulinate. Fuel processing technology. 2018 Jun 1;174:53-60.
65. Quereshi S, Ahmad E, Pant KK, Dutta S. Insights into microwave-assisted synthesis of 5-ethoxymethylfurfural and ethyl levulinate using tungsten disulfide as a catalyst. ACS sustainable chemistry & engineering. 2019 Nov 11;8(4):1721-9.
66. Ahmad E, Alam MI, Pant KK, Haider MA. Insights into the synthesis of ethyl levulinate under microwave and nonmicrowave heating conditions. Industrial & Engineering Chemistry Research. 2019 May 6;58(35):16055-64.
67. Zhang, G., Du, Y., Xu, Y., & Zhang, Y. (2014). Effects of preparation methods on the properties of cobalt/carbon catalyst for methane reforming with carbon dioxide to syngas. *Journal of Industrial and Engineering Chemistry*, *20*(4), 1677-1683.
68. Mahboob S, Haghighi M, Rahmani F. Sonochemically preparation and characterization of bimetallic Ni-Co/Al2O3-ZrO2 nanocatalyst: Effects of ultrasound irradiation time and power on catalytic properties and activity in dry reforming of CH4. Ultrasonics Sonochemistry. 2017 Sep 1;38:38-49.
69. Yin, D., Jin, Z., Liu, M., Gao, T., Yuan, H., & Xiao, D. (2018). Microwave-assisted synthesis of the cobalt-iron phosphates nanosheets as an efficient electrocatalyst for water oxidation. *Electrochimica Acta*, *260*, 420-429.
70. Wang, Z., & Yu, S. (2016). Synthesis of high-stability acidic Ce^{3+}(La^{3+} or Sm^{3+})~ β/Al-MCM-41 and the catalytic performance for the esterification of oleic acid. *Catalysis Communications*, *84*, 108-111.
71. Motshekga SC, Kesavan Pillai S, Ray SS, Jalama K, Krause RW. An easy two-step microwave assisted synthesis of SnO2/CNT hybrids. John Wiley & Sons.
72. Camacho F, González-Tello P, Jurado E, Robles A. Microcrystalline-cellulose hydrolysis with concentrated sulphuric acid. Journal of Chemical Technology & Biotechnology: International Research in Process, Environmental AND Clean Technology. 1996 Dec;67(4):350-6.
73. Malester IA, Green M, Shelef G. Kinetics of dilute acid hydrolysis of cellulose originating from municipal solid wastes. Industrial & engineering chemistry research. 1992 Aug;31(8):1998-2003.

74. Abatzoglov N, Bouchard J, Chornet E, Overend RP. Dilute acid depolymerization of cellulose in aqueous phase: experimental evidence of the significant presence of soluble oligomeric intermediates. The Canadian Journal of Chemical Engineering. 1986 Oct;64(5):781-6.
75. Thompson DR, Grethlein HE. Design and evaluation of a plug flow reactor for acid hydrolysis of cellulose. Industrial & Engineering Chemistry Product Research and Development. 1979 Sep;18(3):166-9.
76. Franzidis JP, Porteous A, Anderson J. The acid hydrolysis of cellulose in refuse in a continuous reactor. Conservation & Recycling. 1982 Jan 1;5(4):215-25.
77. Jimenez L, Bonilla JL. Acid hydrolysis of sunflower residue biomass. Process biochemistry. 1993 Jan 1;28(4):243-7.
78. Song SK, Lee YY. Acid hydrolysis of wood cellulose under low water condition. Biomass. 1984 Jan 1;6(1-2):93-100.
79. Antonyraj CA, Chennattussery AJ, Haridas A. 5-(Chloromethyl) furfural production from glucose: A pioneer kinetic model development exploring the mechanism. International Journal of Chemical Kinetics. 2021 Jul;53(7):825-33.
80. Rojahn P, Nigam KD, Schael F. Experimental study and kinetic modeling of continuous flow conversion of fructose to 5-(chloromethyl) furfural using micro-and millistructured coiled flow inverter. Chemical Engineering Journal. 2022 Dec 15;450:138243.
81. Flannelly T, Dooley S, Leahy JJ. Reaction pathway analysis of ethyl levulinate and 5-ethoxymethylfurfural from D-fructose acid hydrolysis in ethanol. Energ. Fuel. 2015; 29(11):7554-65.
82. Weina ZH, CHANG C, Chen MA, Fengguang DU. Kinetics of glucose ethanolysis catalyzed by extremely low sulfuric acid in ethanol medium. Chinese, J. Chem. Eng. 2014; 22(2):238-42.
83. Tao C, Peng L, Zhang J, He L. Al-modified heteropolyacid facilitates alkyl levulinate production from cellulose and lignocellulosic biomass: Kinetics and mechanism studies. Fuel. Process. Technol. 2021; 213:106709.
84. R. Weingarten, J. Cho, R. Xing, W.C. Conner Jr., G.W. Huber, Kinetics and reaction engineering of levulinic acid production from aqueous glucose solutions, ChemSusChem 5 (7) (2012) 1280–1290.
85. N.A.S. Ramli, N.A.S. Amin, Kinetic study of glucose conversion to levulinic acid over Fe/HY zeolite catalyst, Chem. Eng. J. 283 (2016) 150–159.
86. W. Weiqi, W. Shubin, Experimental and kinetic study of glucose conversion to levulinic acid catalyzed by synergy of Lewis and Brønsted acids, Chem. Eng. J. 307 (2017) 389–398.
87. J.A. Marja Mikola, Ju.ha. Tanskanen, Production of levulinic acid from glucose in sulfolane water mixtures, Chem. Eng. Res. Des. 148 (2019) 291–297.

88. B. Girisuta, L.P.B.M. Janssen, H.J. Heeres, Green chemicals, Chem. Eng. Res. Des. 84 (5) (2006) 339–349.
89. W. Wei, S. Wu, Experimental and kinetic study of glucose conversion to levulinic acid in aqueous medium over Cr/HZSM-5 catalyst, Fuel 225 (2018) 311–321.
90. X. Zheng, Z. Zhi, X. Gu, X. Li, R. Zhang, X. Lu, Kinetic study of levulinic acid production from corn stalk at mild temperature using FeCl 3 as catalyst, Fuel 187 (2017) 261–267.
91. Q.G. Qing Qing, Pengbo Wang, Hongjia Qian, Xiaohang Gao, Yue Zhang, Kinetics study of levulinic acid production from corncobs by tin tetrachloride as catalyst, Bioresour. Technol. 260 (2018) 150–156.
92. K. Kumar, S. Pathak, S. Upadhyayula, 2nd generation biomass derived glucose conversion to 5-hydroxymethylfurfural and levulinic acid catalyzed by ionic liquid and transition metal sulfate: elucidation of kinetics and mechanism, J. Clean. Process 256 (2020), 120292.
93. L.X. Jing Qi, Kinetics of non-catalyzed decomposition of glucose in high- temperature liquid waterain, Chin. J. Chem. Eng. 16 (6) (2008) 890–894.
94. C.B.T. Dallas Swift, Vinit Choudhary, George Peklaris, Vladimiros Nikolakis, Dionisios G. Vlachos, Kinetics of homogeneous brønsted acid catalyzed fructose dehydration and 5-hydroxymethyl furfural rehydration a combined experimental and computational study, ACS Catal. 4 (2014) 259–267.
95. Wang J, Cui H, Wang J, Li Z, Wang M, Yi W. Kinetic insight into glucose conversion to 5-hydroxymethyl furfural and levulinic acid in LiCl· 3H2O without additional catalyst. Chemical Engineering Journal. 2021 Jul 1;415:128922.
96. Windom BC, Lovestead TM, Mascal M, Nikitin EB, Bruno TJ. Advanced distillation curve analysis on ethyl levulinate as a diesel fuel oxygenate and a hybrid biodiesel fuel. Energ. Fuel. 2011;25(4):1878-90.
97. Christensen E, Williams A, Paul S, Burton S, McCormick RL. Properties and performance of levulinate esters as diesel blend components. Energy & fuels. 2011 Nov 17;25(11):5422-8.
98. Wang ZhiWei WZ, Lei TingZhou LT, Liu Liang LL, Zhu JinLing ZJ, He XiaoFeng HX, Li ZaiFeng LZ. Performance investigations of a diesel engine using ethyl levulinate-diesel blends.
99. Lei TingZhou LT, Wang ZhiWei WZ, Chang Xia CX, Lin Lu LL, Yan XiaoYu YX, Sun YinCong SY, Shi XinGuang SX, He XiaoFeng HX, Zhu JinLing ZJ. Performance and emission characteristics of a diesel engine running on optimized ethyl levulinate-biodiesel-diesel blends.

CHAPTER III: RESEARCH GAP

- Globally huge amounts of naturally occurring waste lignocellulosic biomass (LB) are produced every year and still, researchers are facing several challenges to convert this waste into valuable industrially important chemicals and other products through an energy-efficient green process.
- There is a scarcity of scientific literature exploring the utilization of e-waste, such as printed circuit boards, and industrial waste like fly ash, in the development of solid acid catalysts and photocatalysts for LB conversion.
- There exists limited research regarding the utilization of cost-effective acidic deep eutectic solvents for the conversion of lignocellulosic biomass (LB) into drop-in biofuels such as ethyl levulinate.
- Limited scientific research has investigated the combined application of various electromagnetic irradiation energy sources in the conversion of LB.
- The prevailing trend in the literature favours pseudo-homogeneous kinetic models for LB conversion, leaving a gap in understanding heterogeneous reaction kinetics and pathways relevant to LB conversion processes.
- Very few scientific literatures were published on continuous LB conversion process.
- The literature lacks systematic and comprehensive investigations into the economic and environmental sustainability of LB biorefineries.

CHAPTER IV: AIMS & OBJECTIVES

- **Development of cost-effective green catalyst and its characterization**

Key Activities:

- Utilization of cost-effective catalyst supports sourced from E-waste viz., waste printed circuit board (WPCB) and industrial waste viz., fly ash (FA) for the synthesis of heterogeneous cost-effective green acidic photocatalysts.
- Utilization of various characterization techniques to analyse the properties of the prepared heterogeneous catalysts.
- Enhancement of catalyst properties to facilitate the synthesis of desired products under milder conditions compared to those reported in existing literature.
- Synthesis and characterization of cost-effective acidic deep eutectic solvents.

- **Assessment of catalyst performance in lignocellulosic biomass valorisation process**

Key Activities:

- Comparative investigations on catalytic performance at different metal precursor loadings in lignocellulosic biomass conversion process to verify the plausible improvement on the incorporation of active metal in the support framework
- Catalyst recyclability test to identify catalyst life in several consecutive reaction cycles.
- Characterization of spent catalyst to evaluate the consistency in spent catalyst's properties compared to fresh catalyst.

- **Reaction mechanism and kinetic study**

  To investigate possible reaction pathways involved in the heterogeneous catalytic LB conversion process, DFT (density functional theory) analysis employing molecular simulation software such as Amsterdam Modeling Suite (AMS) and BIOVIA Materials Studio® is utilized. Additionally, to evaluate kinetic parameters, several kinetic models including Langmuir-Hinshelwood, Eley Rideal, and pseudo-homogeneous models are applied to fit experimental LB conversion data gathered at specific reaction time intervals, with the goal of identifying the most appropriate kinetic model.

- **Minimization of energy consumption**

Key activities:

- Intensification of LB conversion process employing electromagnetic energy individually and combinedly for reduction of reaction time, temperature, catalyst requirement.

- Minimization of energy consumption and chemical usage through strategic optimization vis-à-vis conforming to environmental sustainability.

➢ **Continuous reactor design and reactor performance study**

Continuous reactor design and reactor performance study in LB to platform chemical such as 5-HMF, 5-CMF and drop-in-biofuel (ethyl levulinate) production process

➢ **Process economic and environmental sustainability**

Key Activities:

- Techno-economic analysis of the continuous LB conversion process employing ASPEN PLUS software.
- Setting of goal and scope depending on system boundaries, objectives, and the functional unit for the environmental sustainability assessment.
- Data collection and compilation of life cycle inventories for the overall process

➢ **Drop-in-biofuel property estimation and diesel engine testing**

Blending of lignocellulosic biomass derived ethyl levulinate with diesel-biodiesel mix at different proportion and blended fuels property estimation. Performance and exhaust emission analysis of the blended fuels in single cylinder 4 stroke diesel engine.

➢ **Novelty Statement**

This thesis contributes to the "waste-to-wealth" paradigm by converting lignocellulosic biomass (LB) into valuable platform chemicals and biofuels through innovative and sustainable approaches. It utilizes unconventional waste materials, such as e-waste (e.g., waste printed circuit boards) and industrial by-products (e.g., fly ash), as catalyst supports for the development of green heterogeneous acidic photocatalysts, demonstrating a circular economy framework.

A key novel aspect of this research lies in the synergistic application of hybrid radiation sources, including microwave, infrared, and ultrasound energy and waste derived cost-effective photocatalyst to intensify the LB conversion process. This innovative approach reduces energy consumption, reaction times, and catalyst requirements, while significantly improving product yields under milder reaction conditions.

Additionally, the study incorporates a comprehensive heterogeneous kinetic analysis to design and scale up continuous reactor systems for LB valorisations. This aspect ensures the efficient production of ethyl levulinate and other high-value biofuels by integrating detailed reaction kinetics with reactor design principles. The thesis further employs process simulation tools to

evaluate and optimize LB biorefinery operations, integrating techno-economic and life cycle assessments to establish the economic feasibility and environmental sustainability of the proposed processes.

Finally, the innovative blending of ethyl levulinate with diesel-biodiesel mixtures and its performance evaluation in diesel engines highlights the practical application and emission reduction potential of this green process. By bridging gaps in waste valorisations, hybrid energy utilization, catalytic process enhancement, reactor design, and sustainability assessments, this research provides a transformative framework for the green and efficient conversion of lignocellulosic biomass.

CHAPTER V: MATERIALS AND METHODS

5.1. Activity 1:

PRINTED CIRCUIT BOARD DERIVED GLASS FIBER-EPOXY RESIN-SUPPORTED MO−CU BIMETALLIC CATALYST FOR GLUCOSE SYNTHESIS

This activity primarily envisages the preparation of waste printed circuit board (WPCB) derived glass fiber-epoxy resin (GFER) supported Mo-Cu doped solid acid catalyst through energy-efficient near infrared radiation (NIRR; wavelength: 0.75-1.4 μm) activated hydrothermal treatment. Various characterization techniques, including XRD, FTIR, BET, NH_3-TPD, TGA, SEM, and HRTEM, were employed to investigate the physicochemical properties of the prepared catalysts. The efficacy of prepared NIRR activated novel catalyst was estimated in the pretreated waste jute fiber (WJF) hydrolysis process and compared with conventionally prepared catalyst which was activated through conventional hydrothermal treatment. Besides, the process was optimized using Taguchi orthogonal design (TOD) to maximize glucose selectivity.

5.1.1. Materials

Bis (acetylacetonato) dioxomolybdenum (VI) [$CH_3COCH=C(O-)CH_3]_2MoO_2$], acetic acid, hydrogen peroxide, acetone, DNS (di-nitro salicylic acid), aqueous NH_4OH (25%) etc. were purchased from Merck and all the chemicals used were of analytical reagent (AR) grade. The mixed wastes PCBs (WPCB) were collected from the local scrap market at Kolkata, India. The waste Jute fiber (WJF) was also purchased from local market.

5.1.2. WPCB processing and GFER Extraction

The attached parts, viz. RAM, PCI slot, and chip slots were removed manually from collected WPCB (computer, TV, other electrical and electronics component) and the WPCB was grinded into fine powder (150 μm mesh size) using drum sander (Figure 5.1(a)) and laboratory ball mill. Afterwards, the ferrous materials were removed using magnetic stirrer. Subsequently, 1 M NaOH solution was added for removal of tin, aluminium, lead through sedimentation. 5g of powder WPCB was stirred with 100 ml of 1 M NaOH solution for 4h at 50°C for complete removal of tin, aluminium, lead. Then glass fiber, epoxy resin and copper mixture were separated and collected and sent it for oven drying. Afterwards, copper was removed by stirring the NaOH treated WPCB with 100 ml of 1 M acetic acid and 10 ml H_20_2

solution for 4 h. Finally, the non-metallic part; namely glass fiber-epoxy resin (GFER) was collected (Figure 5.1(b)) and oven dried (105°C) and eventually sent it for catalyst preparation.

The composition of ground WPCB is presented in Fig 5.1(c). The iron content in the ground WPCB was determined after separating it using a magnetic separator. The percentages of other metallic components were measured using microwave digestion followed by ICP-OES analysis. The percentage of non-metallic components (GFER) in WPCB was calculated by drying the residue obtained after treating the WPCB with peracetic acid and NaOH.

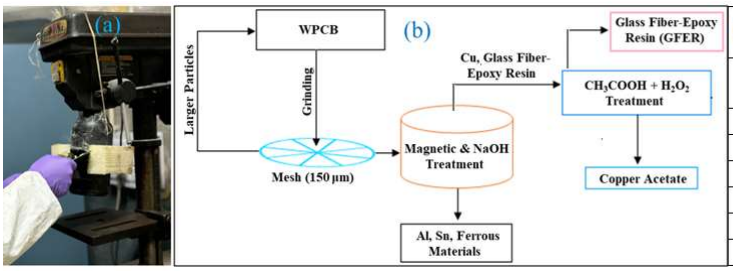

(C)

Grinded WPCB compositions	Weight Percentage
Non-metallic components (Glass fiber, epoxy resin)	72 %
Copper	15 %
Iron	4 %
Solder	4 %
Tin	3 %
Nickel	1 %
Other metals	1 %

Figure 5. 1. (a) WPCB grinding in drum sander (b) Flow Chart for WPCB processing (c) Grinded WPCB compositions

5.1.3. GFER supported Mo-Cu catalyst preparation

Following the extraction of GFER (containing 0.65 wt.% Cu as measured by ICP) from WPCB, the extracted GFER was utilized for the preparation of various GFER-supported Mo-Cu doped solid acid catalysts by varying precursor loading of Molybdenum salt [$CH_3COCH=C(O-)CH_3]_2MoO_2$] according to Table 5.1. The GFER and $CH_3COCH=C(O-)CH_3]_2MoO_2$ mixture was stirred vigorously in acetone for 4 h at 60°C under NIRR (100 W; near infrared wavelength: 0.75-1.4 µm) (Figure 5.2). Subsequently, the mixture was ripened for 24 h and eventually oven dried (105°C). Afterwards, Mo dispersed GFER was calcined at 240°C for 3h and accordingly, different GFER supported Cu-Mo catalysts prepared under NIRR were designated as NCu-$Mo^{0.75}$ (Mo precursor loading 0.75wt.%), NCu-$Mo^{1.0}$ (Mo precursor loading 1.0 wt.%) and NCu-$Mo^{1.25}$ (Mo precursor loading 1.25 wt.%) respectively.

5.1.4. Characterization of GFER and prepared catalyst

Thermo-gravimetric analysis (TGA) of the WPCB, oven dried GFER powder, calcined GFER and the prepared Mo-Cu catalyst was performed with a Perkin-Elmer TGA analyser (Pyris Diamond TG/DTA) in nitrogen atmosphere (20 mL/ min) from 30 °C to 500 °C with a temperature increasing rate of 15.0 °C/min. The infrared spectra of the WPCB, GFER powder,

calcined GFER and the prepared Mo-Cu catalyst were detected with a FTIR, SHIMADZU (Alpha), from 400 to 4000 cm^{-1} while XRD (X-ray diffraction) patterns of were analysed using a Cu Kα source equipped with an Intel CPS 120 hemispherical detector. XRD Analysis was performed at 2θ ranging from 10° to 90° at a scanning speed of 1° min^{-1}. The specific surface area, pore volume and pore size distribution were measured by BET (Brunner–Emmett–Teller) and DFT methods using Quantachrome Instruments, Nova 4000e. Before BET-DFT analysis the samples were pretreated and degassed at 150°C to remove surface moisture. The acidity of the catalysts and calcined GFER was determined through NH_3-TPD experiments using Quantachrome Instruments, TPR win v2.1. Furthermore, the Bronsted and Lewis acidic sites of the optimum catalyst and calcined GFER was evaluated by Fourier transform infrared spectrometry (FTIR) [1]. Samples (30 mg) were pressed into self-supporting discs (diameter 1.2 cm) and outgassed under vacuum (10^{-5} mbar) at 200 ° C for 2 h. Adsorption of pyridine on the outgassed samples was saturated at a pressure of 5 mbar for 10 min and after adsorption of pyridine, the samples were further outgassed under vacuum at 100 °C for 30 min to remove the physiosorbed pyridine. The binding energy of Mo 3d and Cu 2p of the optimum catalyst was measured by XPS (X-ray photoelectron spectroscopy) while surface morphology of the optimum catalyst was determined using scanning electron microscope (SEM) at 15kV (JEOL Ltd., JSM-6360). Additionally, Transmission electron microscope (TEM), high-angle annular dark-field scanning TEM (HAADF-STEM) analysis were carried out also on a FEI Titan G260-300 transmission electron microscope at an accelerating voltage of 300 kV. Lattice spacing of the crystallites were calculated using 'GATAN digital micrograph' through processing the micrographs. Photo-catalytic property of the optimum NCu-$Mo^{1.0}$ catalyst and calcined GFER was verified with Parkin Elmer Lamda-365UV–visible spectrophotometer in the range 200–900 nm [2].

5.1.5. Reactor configurations and hydrolysis procedure

The performance of the prepared NCu-Mo catalyst was evaluated in jute hydrolysis process. One pot pretreatment-hydrolysis of WJF was performed in a batch reactor assisted with near infrared radiation (NIRR) (100 W; 0.75-1.4 μm) system (Figure 5.2). For pretreatment, a measured amount of WJF was taken in the three-neck flask, followed by addition of measured amount of aqueous NH_4OH (2.5 ml/g of WJF) and deionized water (20ml/g of WJF) at a pre-set controlled temperature of 70°C. Over the specified time span of 20 min, the mix was stirred at 400 rpm. After pretreatment, the purging of N_2 through one neck

of the three-neck flask was carried out to remove remaining ammonia. Afterwards, a measured amount of prepared catalyst and water (10 ml/g of WJF) were added to the pretreated WJF present in the reactor mix and stirred at 400 rpm for the subsequent hydrolysis over a specified time (Table 5.1). Subsequently, vacuum filtration was conducted to separate the pretreated WJF residue and the catalyst. Afterward, the filtrate was processed for measurement of glucose concentration by standard DNS method.

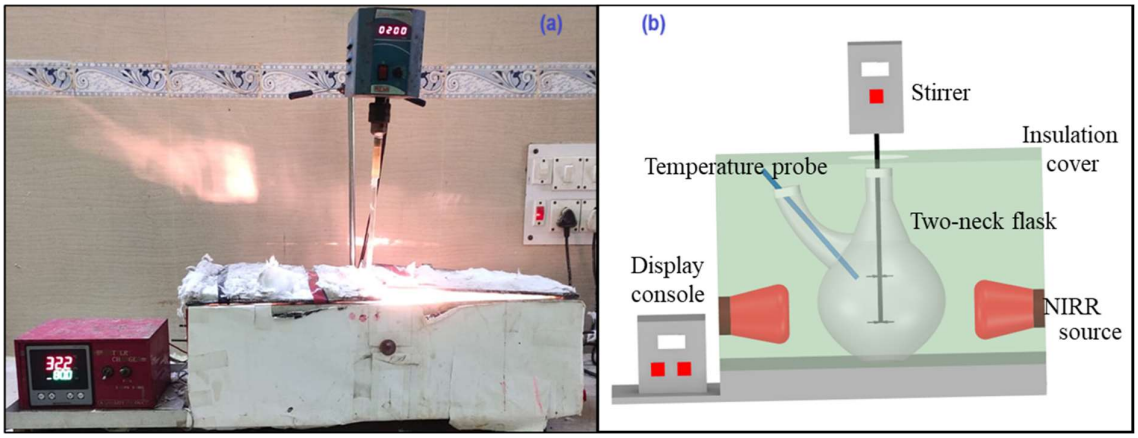

Figure 5. 2. NIRR-assisted batch reactor: (a) experimental setup and (b) schematic representation

5.1.5.1. Design of experiment

The pretreated WJF hydrolysis reaction under NIRR activated NCu-Mo catalyst was optimized deploying the following four independent process parameters viz., Mo loading (ϕ_{NIRRMo}), catalyst concentration (ϕ_{MoC}), hydrolysis temperature ($\phi_{T_{NIRR}}$) and hydrolysis time ($\phi_{t_{NIRR}}$). The levels of each process parameter were selected based on single parametric experiments (Table 5.1).

Using L9 Taguchi orthogonal design (TOD) (Minitab Inc. USA for Windows 7), nine experimental runs (Table 5.2) were conducted to assess and optimize the effects of independent process parameters on the response variable (glucose yield, G_{NIRR}). The optimal process parameters corresponding to maximum G_{NIRR} were determined through evaluation of signal to noise (S/N) ratios (employing the 'larger is better' criterion) (Equation 5.1) and analysis of variance (ANOVA).

$$S/N\ ratio = -10\ log(\frac{1}{n}\sum_{i=1}^{n}\frac{1}{G_{NIRR,i}^2}) \qquad (5.1)$$

Where, n: number of experimental runs performed at a particular set condition (Table 5.2); i: number of replications; $G_{NIRR,i}$: G_{NIRR} corresponding to run n.

Table 5. 1. Process variable for pretreated WJF hydrolysis using NCu-Mo catalysts

Process parameters	ϕ_{NIRRMo} (wt. %)	ϕ_{MoC} (wt. %)	$\phi_{T_{NIRR}}$ (°C)	$\phi_{t_{NIRR}}$ (min)
L_{-1}	0.75	2.5	60	10
L_0	1.0	5	70	15
L_1	1.25	7.5	80	20

L_{-1}: lower level; L_0: middle level; L_1: upper level

Table 5. 2. TOD layout for pretreated WJF hydrolysis using NCu-Mo catalysts

Runs	ϕ_{NIRRMo} (wt.%)	ϕ_{MoC} (wt.%)	$\phi_{T_{NIRR}}$ (°C)	$\phi_{t_{NIRR}}$ (min)	G_{NIRR}	Std.	S/N ratio
1	L_{-1}	L_{-1}	L_{-1}	L_{-1}	45.30	$\pm$ 0.21	33.12
2	L_{-1}	L_0	L_0	L_0	54.81	$\pm$ 0.11	34.78
3	L_{-1}	L_1	L_1	L_1	59.20	$\pm$ 0.04	35.45
4	L_0	L_{-1}	L_0	L_1	63.17	$\pm$ 0.17	36.01
5	L_0	L_0	L_1	L_{-1}	75.84	$\pm$ 0.08	37.60
6	L_0	L_1	L_{-1}	L_0	60.10	$\pm$ 0.33	35.58
7	L_1	L_{-1}	L_1	L_0	69.57	$\pm$ 0.09	36.85
8	L_1	L_0	L_{-1}	L_1	60.94	$\pm$ 0.22	35.70
9	L_1	L_1	L_0	L_{-1}	67.10	$\pm$ 0.15	36.53

To assess the effect of NIRR on catalytic properties, GFER supported Cu-Mo catalyst was also prepared through conventional hydrothermal treatment (500W) at optimum Mo loading and designated as CCu-$Mo^{1.0}$ and its performance has been evaluated and compared with NCu-$Mo^{1.0}$ in pretreated WJF hydrolysis reaction at otherwise optimized conditions. Additionally, the performance of the optimized catalysts was also compared to that of a commercial solid acid catalyst, namely Amberlyst-15 (A-15), in the WJF hydrolysis process to assess their effectiveness.

5.1.6. Physicochemical characterization of hydrolysate

Hydrolysate concentrations were evaluated by DNS method [3]. The compositional analysis of hydrolysate was performed by HPLC with RI detector (Perkin Elmer 200 Series) along with 300×7.8 mm Bio-Rad HPXP, 9 µm column and 0.005 M sulfuric acid as mobile

phase (flow rate: 0.6 ml min^{-1}). The hydrolysate constituent's concentrations were quantified from the calibration plots of respective standard constituents. The infrared spectra of the liquid hydrolysate were also analysed by FTIR (FTIR-Shimadzu Alpha, from 400 cm^{-1} to 4000 cm^{-1}).

5.2. Activity 2:

KINETICS OF COMBINED NON-CATALYTIC AND CATALYTIC HYDROLYSIS OF JUTE FIBER UNDER ULTRASONIC-FAR INFRARED ENERGY SYNERGY

Pseudo homogeneous kinetic model had been extensively employed to describe the reaction kinetics even in heterogeneous LB hydrolysis process [4,5]. Nevertheless, several research works reported that commercial ion exchanged acidic resin catalysts such as Amberlyst-15 (A-15; Table 5.3 shows physicochemical properties of A-15), Amberlyst-36 suffer from the leaching of their sulfonic acid functional group ($-SO_3H^+$), in aqueous system [6,7]. Clearly, it is improper to categorize such catalytic hydrolysis process either by a true homogeneous or a true heterogeneous kinetic model; as, part of $-SO_3H^+$ of A-15 undergoes leaching (performing pseudo-homogeneous hydrolysis) while the remainder persists on resin surface (performing heterogeneous hydrolysis). As far as we know, no scientific literature is available on combined homogeneous–heterogeneous LB hydrolysis kinetic model in presence of such acidic resin type catalyst. Besides, the effects of A-15 catalyst's activity decay during LB hydrolysis and evaluation of associated deactivation kinetic model have not been investigated to date. Notably, recently a work done by our research group showed that intensification effect of far-infrared wave (FIRW) in A-15 catalysed watermelon peel hydrolysis process could significantly reduce reaction time and temperature [8].

Table 5. 3. Physicochemical properties of A-15

Physical Properties		Chemical Properties	
Quality	Dry	Matrix	styrene-divinylbenzene (macroreticular)
Particle size	<300µm	Functional group	Sulfonic ($-SO_3H$)
Surface area	$45 m^2/g$	Cation-exchange capacity	4.7 meq/g by dry weight
Average pore diameter	250Aº	Swelling (dry to solvent saturated, %):	60-70% in aqueous medium

Maximum operating temperature	393K	

So, in this work, combined effects of FIRW and ultrasound (US) on intensification of pretreated WJF (PWJF) hydrolysis process using commercial A-15 catalyst in aqueous phase for fast reducing sugar (RS) yield has been meticulously investigated. Afterwards, a new kinetic model consisting of non-catalytic PWJF hydrolysis along with parallel pseudo-homogeneous (due to leaching of H^+ ions from A-15) and heterogeneous (on A-15 surface) catalytic PWJF process hydrolysis has been formulated and the model was validated. Moreover, the PWJF hydrolysis process was optimized employing TOD and at optimized hydrolysis conditions, the intensification efficacy of US-FIRW system over that of FIRW, US and conventional thermal system (CTS) in the PWJF hydrolysis process was evaluated in terms of RS yield.

5.2.1. Pretreatment of WJF

The procured WJF was thoroughly washed using deionized water and cut into small pieces (2 ± 0.1 mm). Afterwards, the WJF was grinded by a ball mill and subsequently dried in a hot air-oven at 60 ºC for 4 h. After that, pretreatment of WJF was done by modified Ammonia fiber expansion (AFEX) method according to our previous study [8]. Lignin was separated from the pretreated mix by reported method [9] and the PWJF was subjected to subsequent hydrolysis step. Compositional analyses (Table 5.4) of the WJF and PWJF were done according to the Anthrone method [10] and NREL LAP [11]. Reducing sugar content in pretreated mix was measured using DNS method [3].

Table 5. 4. Compositional analysis of WJF and PWJF

Component (%)	WJF	PWJF mix
Cellulose	62.73	81.46
Hemicellulose	18.41	13.23
Lignin	14.57	3.86
Others	4.29	1.45

5.2.2. Hydrolysis of PWJF

5.2.2.1. Reactor configuration and hydrolysis of PWJF

Hydrolysis of PWJF was performed in a uniquely designed isothermal batch reactor system equipped with ultrasonication bath (100 W; 40 kHz) and far infrared wave (150 W; 15 μm^{-1} mm) (US-FIRW). A diagram of the US-FIRW assisted batch reactor is shown in Figure 5.3. In a representative run, a measured amount of PWJF mix was taken in a three-neck flask, followed by addition of required amount of A-15 catalyst and deionized water at the pre-set controlled temperature to perform hydrolysis of PWJF over a specified time span (Table 5.5). A PID temperature controller was provided to keep a constant temperature throughout the hydrolysis mix. Subsequently, vacuum micro-filtration (0.45 µm) was conducted to separate the PWJF residue and the catalyst from the hydrolysate.

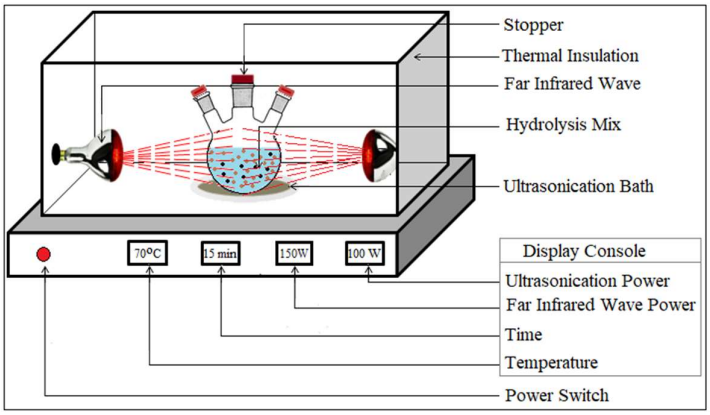

Figure 5. 3. Diagram of the US-FIRW assisted batch reactor

In order to assess the superiority of US-FIRW energized reactor, PWJF was also hydrolysed in the individual FIRW (150 W; 15 μm^{-1} mm) energized reactor, US energized reactor (100 W; 40 kHz) and CTS (500 W electrical heating mantle) at the derived optimum conditions. Notably, reactors with FIRW and CTS comprises of a centrally fitted mechanical stirrer (flat blade turbine comprising of 6 blades (length: 15 mm; width: 2 mm) and a central shaft (length: 310 mm; diameter: 10 mm) instead of ultrasonication.

As A-15 suffers from leaching of its functional group in hot aqueous medium; in the present work, regeneration of A-15 was done by following the work reported by Lee [12] and Rinaldi [13]. After hydrolysis, the used catalyst was washed with H_2SO_4 to regain the $SO_3^-H^+$ active sites on the polymer matrix of A-15 catalyst. Additionally, the PWJF hydrolysis process was also conducted using used catalyst to evaluate the time dependent catalyst activity term.

5.2.2.2. *Experimental design of PWJF hydrolysis process*

Taguchi orthogonal design (TOD) was employed for PWJF hydrolysis using nine (9) experimental runs (Table 5.6) with select process parameters viz., hydrolysis temperature (φ_{HT}), hydrolysis period (φ_{HP}), catalyst concentration (φ_{HC}), water loading (φ_{WB}).

The effects of self-governing process parameters on the response parameter [reducing sugar (RS) yield (ω_{RS})] and the optimal process variables corresponding to maximum ω_{RS} was estimated by TOD through evaluation of S/N ratios (Table 5.6) and ANOVA. The response parameter (ω_{RS}) was optimized employing the 'larger is better' criterion for S/N ratio (Equation 5.2)

$$S/N\ ratio = -10\ log(\frac{1}{n}\sum_{i=1}^{n}\frac{1}{\omega_{RS,i}^2}) \quad (5.2)$$

Where, i symbolizes the number of replications, n represents number of experimental runs performed at a particular set condition, ω_{RS} denotes response parameter, RS yield. The ω_{RS} was calculated by Equation-5.3 [14,15]:

$$\omega_{RS} = [\frac{\text{glucose }(g) + (\text{celloboise }(g)\times 1.053)}{\text{cellulose }(g)\times 1.111} + \frac{\text{xylose }(g)+\text{arabinose }(g)}{\text{hemicellulose }(g)\times 1.136}]\times 100 \quad (5.3)$$

Where, the multiplication factors 1.111, 1.053 and 1.136 represent the mass accumulation during hydrolysis of cellulose to glucose, cellobiose to glucose and hemicellulose to xylose and arabinose respectively.

Table 5. 5. Self-governing process parameters for hydrolysis of PWJF

Process parameters	$\boldsymbol{\varphi_{HT}}$ (°C)	$\boldsymbol{\varphi_{HP}}$ (min)	$\boldsymbol{\varphi_{HC}}$ (wt.%)	$\boldsymbol{\varphi_{WB}}$ (w/w)
L_{-1}	60	10	0.5	10
L_0	70	15	1.5	20
L_1	80	20	2.5	30

L_{-1}: lower level; L_0: middle level; L_1: upper level

Table 5. 6. TOD of PWJF hydrolysis process

Trial no	$\boldsymbol{\varphi_{HT}}$ (°C)	$\boldsymbol{\varphi_{HP}}$ (min)	$\boldsymbol{\varphi_{HC}}$ (wt.%)	$\boldsymbol{\varphi_{WB}}$ (w/w)	$\boldsymbol{\omega_{RS}}$	Std.	S/N ratio
1	L_{-1}	L_{-1}	L_{-1}	L_{-1}	44.60	$\pm$ 0.11	32.98
2	L_{-1}	L_0	L_0	L_0	53.76	$\pm$ 0.04	34.60
3	L_{-1}	L_1	L_1	L_1	57.46	$\pm$ 0.24	35.18

4	L_0	L_{-1}	L_0	L_1	61.20	± 0.06	35.73
5	L_0	L_0	L_1	L_{-1}	74.82	± 0.04	37.48
6	L_0	L_1	L_{-1}	L_0	58.13	± 0.23	35.28
7	L_1	L_{-1}	L_1	L_0	68.10	± 0.10	36.66
8	L_1	L_0	L_{-1}	L_1	59.63	± 0.02	35.50
9	L_1	L_1	L_0	L_{-1}	65.23	± 0.10	36.28

5.2.3. Physicochemical characterization of WJF and hydrolysate

After hydrolysis, RS concentrations were measured by standard DNS method. The hydrolysate compositions were analysed by HPLC with refractive index (RI) detector (Perkin Elmer 200 Series) along with 300×7.8 mm Bio-Rad HPXP, 9 μm column at a flow rate of 0.6 ml. min^{-1} of 0.005 M of sulfuric acid (mobile phase). For precise measurement of HMF concentration, HMF was first extracted from aqueous hydrolysate using n-butanol and analysed in a UV detector at 284 nm [16]. The hydrolysate constituent's concentrations were quantified from the calibration plots of respective standard constituents. The XRD (X-ray diffraction) patterns of WJF, PWJF and hydrolysed PWJF residues at optimal conditions from different reactors were analysed to detect the changes in crystallinity of cellulose using a Cu Kα source equipped with an Intel CPS 120 hemispherical detector (Rigaku Miniflex Co. Japan). Analysis was performed at 2θ ranging from 10° to 90° at a scanning speed of 1° min^{-1}. The chemical characteristics of raw WJF, PWJF and optimally hydrolysed PWJF residues and the hydrolysates were analysed by FTIR (FTIR-Shimadzu Alpha, from 400 cm^{-1} to 4000 cm^{-1}).

5.2.4. Formulation of PWJF hydrolysis reaction kinetics

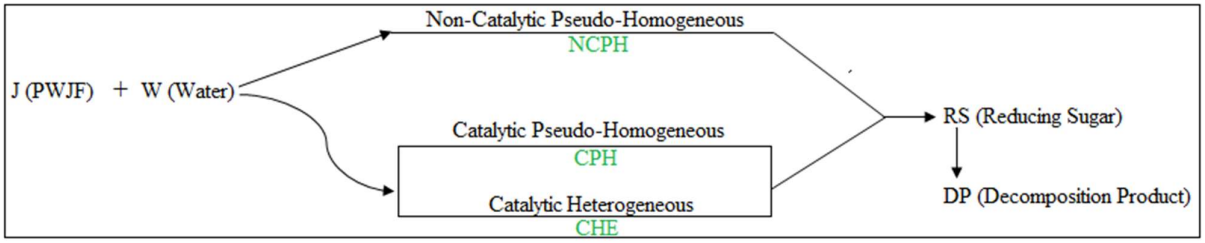

Figure 5. 4. Reaction pathways of PWJF hydrolysis

Figure 5.4 depicts the scheme of a simplified kinetic model for PWJF hydrolysis involving possible reaction pathways. Kinetic model was formulated for PWJF hydrolysis that

includes simultaneous cellulose and hemicellulose decomposition in bulk phase (aqueous phase) as well as on catalyst surface. The model was developed considering following assumptions: First, the hydrolysis of PWJF in bulk phase proceeds through combination of irreversible pseudo-homogeneous reactions which include both non-catalytic and catalytic reactions. Second, hydrolysis of PWJF also occurs on catalyst surface through irreversible heterogeneous mechanism. Thus, the overall reaction rate can be formulated by combining irreversible pseudo-homogeneous and heterogeneous reaction rate expressions:

$$-r_{overall} = -\frac{dC_J}{dt} = (-r_{NC}) + (1-\xi)\eta\,(-r_H) + \xi\eta(-r_{Ht}) \qquad (5.4)$$

Where, $-r_{overall}$ (mol L^{-1} min^{-1}),$-r_{NC}$ (mol L^{-1} min^{-1}),$-r_{Ht}$ (mol $gcat.^{-1}$ min^{-1}),$-r_H$ (mol $gcat.^{-1}$ min^{-1}) are the overall hydrolysis rate, non-catalytic hydrolysis rate, heterogeneous catalytic hydrolysis rate and homogeneous catalytic hydrolysis rate for PWJF hydrolysis respectively. η (gcat. L^{-1}) represents the bulk density of the catalyst (A-15); whereas ξ represents the heterogeneous A-15 catalyst activity.

The non-catalytic and catalytic pseudo-homogeneous rate expressions for PWJF hydrolysis under optimal process conditions in batch reactor have been expressed by Equation-5.5 & 5.6 respectively.

$$-r_{NC} = -\frac{dC_J}{dt} = k_{NC}C_J C_W \qquad (5.5)$$

$$-r_H = -\frac{dC_J}{dt} = k_H C_J C_W \qquad (5.6)$$

Where,C_J,C_W are concentrations of PWJF (mol L^{-1}), water (mol L^{-1}) at time t (min) respectively; k_{NC} (L mol^{-1} min^{-1}),k_H (L^2 mol^{-1} $gcat.^{-1}$ min^{-1}) are the non-catalytic and catalytic pseudo-homogeneous reaction rate constant for decomposition of PWJF respectively. The non-catalytic hydrolysis rate was separately evaluated by conducting hydrolysis reaction of PWJF under US-FIRW, FIRW, US and CTS without using catalyst at TOD derived optimal condition. Concentration of PWJF (C_J) was calculated by Equation-5.7:

$$C_J = C_{Cellulose} + C_{Hemicellulose} \qquad (5.7)$$

Where

$$C_{Cellulose} = \frac{\text{mass of cellulose } (g)}{\text{molecular weight of one anhydrous glucose unit} \times \text{volume of hydrolysis mix } (L)}$$

$$C_{Hemicellulose} = \frac{\text{mass of hemicellulose } (g)}{\text{molecular weight of one anhydrous xylose unit} \times \text{volume of hydrolysis mix } (L)}$$

To evaluate the temperature-time dependent catalyst activity, hydrolysis runs were also conducted at TOD derived optimal condition in all reactors using both fresh and used catalyst of different ages. The catalyst activity and deactivation rate were evaluated using Equation-5.8.

$$\xi = \frac{-r_{overall}(t)}{-r_{overall}(t=0)} \tag{5.8}$$

Where, $-r_{overall}(t)$ represents the hydrolysis rate employingA-15 that has been used for a time t; $-r_{overall}(t=0)$ represents the hydrolysis rate using fresh A-15.

In formulating kinetic model for irreversible heterogeneous surface reaction on A-15 catalyst surface, both Langmuir-Hinshelwood kinetic model (LH) and Eley-Rideal (ER) model have been considered. In developing the single site ER kinetic model, it was considered that on A-15 active sites, the reactant PWJF does not get adsorbed whereas for dual site LH kinetic model, it was considered that both reactants (PWJF and H_2O) get adsorbed on the catalyst sites. Furthermore, for both models, the surface reaction was considered as the rate controlling step. The proposed ER model is represented by:

$$-r_{Ht}^{\oplus} = \frac{k^{\oplus} C_J C_W}{1 + K_W C_W + K_{RS} C_{RS}} \tag{5.9}$$

The details of the Eley-Rideal (ER) kinetic model formulation steps are as follows

$$W + S \underset{k_{-W}}{\overset{k_W}{\rightleftharpoons}} WS \tag{5.9.1}$$

$$J + WS \xrightarrow{k_S} RSS \tag{5.9.2}$$

$$RSS \underset{k_{RS}}{\overset{k_{-RS}}{\rightleftharpoons}} RS + S \tag{5.9.3}$$

The adsorption rate of *W* on catalyst surface:

$$-r_W = k_W (C_W C_V - \frac{C_{WS}}{K_W}) \tag{5.9.4}$$

The surface reaction rate between adsorbed *W* and un-adsorbed *J*:

$$-r_S = k_S C_J C_{WS} \tag{5.9.5}$$

The desorption rate of *G*:

$$-r_{RS} = k_{-RS} (C_{RSS} - \frac{C_{RS} C_V}{K_{RS}}) \tag{5.9.6}$$

Where, k_W, k_{RS} are adsorption rate constant for 'W', 'RS' and k_{-W}, k_{-RS} are desorption rate constant for 'W', 'RS' respectively. k_S refers to surface reaction rate constant while, K_W, K_{RS} are the adsorption equilibrium constant of 'W' and desorption equilibrium constant of product 'G' respectively. Whereas, C_{WS} is the occupied surface concentration of W.

Since, the surface kinetics (Equation 5.9.2) has been taken as the rate-controlling step; both the adsorption and desorption rate constants (k_W, k_{-RS}) are quite high that $\frac{r_W}{k_W}$ and $\frac{r_{RS}}{k_{-RS}}$ tend to zero and one obtains:

$$\frac{r_W}{k_W} \approx \frac{r_{RS}}{k_{-RS}} \approx 0 \tag{5.9.7}$$

So, from Equation 5.9.4 and 5.9.6 we get,

$$C_W = K_W C_W C_V \tag{5.9.8}$$

$$C_{RSS} = K_{RS} C_{RS} C_V \tag{5.9.9}$$

Total active site concentration:

$$C_T = C_V + C_{WS} + C_{RSS} \tag{5.9.10}$$

So that, $C_V = \frac{C_T}{1 + K_W C_W + K_{RS} C_{RS}}$ (5.9.11)

Thus, from Equation 5.9.8 and 5.9.9 it follows that:

$$C_{WS} = \frac{K_W C_W C_T}{1 + K_W C_W + K_{RS} C_{RS}} \tag{5.9.12}$$

Using Equation 5.9.12 in Equation 5.9.2,

$$-r_S = \frac{k_S K_W C_J C_W C_T}{1 + K_W C_W + K_{RS} C_{RS}} \tag{5.9.13}$$

Equation 5.9.13 may be put in a suitable form:

$$r \approx -r_S = \frac{k^{\oplus} C_J C_W}{1 + K_W C_W + K_{RS} C_{RS}} \tag{5.9.14}$$

Where, $k^{\oplus} = k_S K_\omega C_T$ (5.9.15)

= Heterogeneous reaction rate constant for ER model (L mol^{-1} min^{-1}).

Equation 5.9.14 is the working form of proposed ER kinetic model (Equation-5.9).

The proposed LH model is represented by:

$$-r_{Ht}^{*} = \frac{k^{*} C_J C_W}{(1 + K_J C_J + K_W C_W + K_{RS} C_{RS})^2} \tag{5.10}$$

The details of the *Langmuir–Hinshelwood (*LH) kinetic model formulation steps are

$$J + S \underset{k_{-J}}{\overset{k_J}{\rightleftharpoons}} JS \tag{5.10.1}$$

$$W + S \underset{k_{-W}}{\overset{k_W}{\rightleftharpoons}} WS \tag{5.10.2}$$

$$JS + WS \xrightarrow{k_S} RSS \tag{5.10.3}$$

$$RSS \underset{k_G}{\overset{k_G}{\rightleftharpoons}} RS + S \tag{5.10.4}$$

$$-r_J = k_J (C_J C_V - \frac{C_{JS}}{K_J}) \tag{5.10.5}$$

$$-r_W = k_W (C_W C_V - \frac{C_{WS}}{K_W}) \tag{5.10.6}$$

$$-r_S = k_S C_{JS} C_{WS} \tag{5.10.7}$$

$$-r_{RS} = k_{-RS} (C_{RSS} - \frac{C_{RS} C_V}{K_{RS}}) \tag{5.10.8}$$

Where, k_J, k_W, k_{RS} are adsorption rate constant for '*J*', '*W*', '*RS*' and k_{-J}, k_{-W}, k_{-RS} are desorption rate constant for '*J*', '*W*', '*RS*' respectively. k_S refers to surface reaction rate constant while K_J, K_W, K_{RS} are the adsorption equilibrium constant of '*J*' (L mol^{-1}), adsorption equilibrium constant of '*W*' and desorption equilibrium constant of product '*RS*' respectively. Whereas, C_{JS} C_{WS} are the occupied surface concentration of PWJF and W respectively.

Since, the surface kinetics (Equation 5.10.3) has been recognized as the rate controlling step; both the adsorption and desorption rate constants (k_J, k_W, k_{-RS}) are considerably high, hence, $\frac{r_J}{k_J}, \frac{r_W}{k_W}$ and $\frac{r_{RS}}{k_{-RS}}$ become negligible and accordingly:

$$\frac{r_J}{k_J} \approx \frac{r_W}{k_W} \approx \frac{r_{RS}}{k_{-RS}} \approx 0$$

(5.10.9)

So, from Equations 5.10.5- 5.10.6 and Equation 5.10.8 we get,

$$C_{JS} = K_J C_J C_V$$

(5.10.10)

$$C_{RSS} = K_{RS} C_{RS} C_V$$

(5.10.11)

$$C_{RSS} = K_{RS} C_{RS} C_V$$

(5.10.12)

Total concentration in active site,

$$C_T = C_V + C_{JS} + C_{WS} + C_{RSS} \quad (5.10.13)$$

Then, $$C_V = \frac{C_T}{1 + K_J C_J + K_W C_W + K_{RS} C_{RS}} \quad (5.10.14)$$

Now, using Equation 5.10.10 and Equation 5.10.11 in Equation 5.10.7 we develop:

$$-r_S = k_S (K_J C_J)(K_W C_W) C_V^2 \quad (5.10.15)$$

Therefore, $$-r_S = \frac{k_S K_J K_W C_J C_W C_T^2}{(1 + K_J C_J + K_W C_W + K_{RS} C_{RS})^2} \quad (5.10.16)$$

Equation 5.10.16 may be put in a suitable form:

$$r \approx -r_S = \frac{k^* C_J C_W}{(1 + K_J C_J + K_W C_W + K_G C_G)^2} \quad (5.10.17)$$

Where, $$k^* = k_S K_P K_\omega C_T^2 \quad (5.10.18)$$

= Heterogeneous reaction rate constant for LH model (L mol^{-1} min^{-1}).

Equation 5.10.17 is the working form of proposed LH kinetic model (Equation-5.10).

Here $-r_{Ht}^*$ (mol gcat.$^{-1}$ min^{-1}), $-r_{Ht}^{\oplus}$ (mol gcat.$^{-1}$ min^{-1}) are the PWJF hydrolysis reaction rate for heterogeneous kinetic model according to LH and ER respectively. $k_S$refers to surface reaction rate constant while K_J, K_W, K_{RS} are the adsorption equilibrium constants of '*J*' (PWJF), adsorption equilibrium constant of '*W*' and desorption equilibrium constant of product '*RS*'

respectively. C_T is the total surface concentration of A-15. k^* (mol^{-1} min^{-1}), $k^{\oplus}$ (L mol^{-1} min^{-1}) are the heterogeneous reaction rate constants for ER and LH kinetic models respectively. The RS concentration was calculated by Equation-5.11:

$$C_{\mathrm{RS}} = \left[\frac{\text{glucose}\ (g) + (\text{celloboise}\ (g) \times 1.053)}{\text{molecular weight of glucose}} + \frac{\text{xylose}\ (g) + \text{arabinose}\ (g)}{\text{molecular weight of xylose}}\right] \times \frac{100}{\text{volume of hydrolysis mix}(L)} \qquad (5.11)$$

Therefore, the formulated overall reaction rate expressions (Equation-5.4) for PWJF mix hydrolysis considering combined pseudo-homogeneous-heterogeneous reaction is expressed as follows:

$$-r_{overall} = -\frac{dC_J}{dt} = k_{NC}C_JC_W + (1-\xi)\eta k_H C_J C_W + \frac{\xi\eta k^{\oplus} C_J C_W}{1 + K_W C_W + K_{RS} C_{RS}} \qquad (5.12)$$

$$-r_{overall} = -\frac{dC_J}{dt} = k_{NC}C_JC_W + (1-\xi)\eta k_H C_J C_W + \frac{\xi\eta k^{*} C_J C_W}{(1 + K_J C_J + K_W C_W + K_{RS} C_{RS})^2} \qquad (5.13)$$

Equation-5.12 represents the overall rate expressions as per ER heterogeneous kinetic model (PHHER); whereas, Equation-5.13 represents overall rate expressions as per LH heterogeneous kinetic model (PHHLH).

The activation energy of PWJF hydrolysis process was calculated according to Arrhenius equation (Equation-5.14)

$$k_{NC}, k_H, k^{\oplus}, k^{*} = E_{Jo}\, exp\left[-\frac{E_J}{R}\left(\frac{1}{T_2} - \frac{1}{T_1}\right)\right] \qquad (5.14)$$

Where, T_2 and T_1 denote the two different PWJF hydrolysis temperatures at otherwise optimum conditions derived through TOD. E_J is the activation energy (kJ/mol), E_{Jo} is the pre-exponential factor for PWJF hydrolysis process and R is the gas constant (8.31×10^{-3} kJ/mole K).

The kinetic parameters for proposed kinetic models (PHHER& PHHLH) were evaluated through non-linear fitting of experimental data using *fminsearch* algorithm employing MATLAB R2014a software. Furthermore, after identifying the best-suited model for US-FIRW energized reactor, similar analysis had also been conducted for FIRW, US and CTS in order to compare the performance among these reactors.

5.3. Activity 3:

SUSTAINABLE HMF SYNTHESIS FROM WASTE COOKED RICE WATER USING FLY-ASH BASED AL_2SIO_5 SUPPORTED NANO PHOTOCATALYST UNDER HALOGEN-ULTRASOUND SYNERGISTIC-ENERGY: LCA AND DFT BASED SIMULATION

This study predominantly focuses on the preparation of nano Al_2SiO_5 and nano Fe^{3+}/Fe^{2+} (Fe_3O_4) from coal-based fly ash (FA) through alkali-acid treatment and sol gel method under innovatively integrated tungsten-halogen and ultrasound (THUS) energy-sources and subsequent employment of the prepared Al_2SiO_5 and Fe^{3+}/Fe^{2+} in cost-effective nano-$Fe^{3+}/Fe^{2+}/Al_2SiO_5/Ti^{4+}$ photocatalyst (FA_NPC*) preparation process (Figure 5.5). The efficacy of the FA_NPC* has been studied in HMF production process from waste cooked rice water (CRW) using THUS assisted batch reactor. Box-Benhken design involving response surface methodology (RSM) was employed to optimize the HMF production process. Moreover, the efficacy of THUS stimulated optimal FA_NPC* (FA_NPC*^{O}) has also been compared with its conventionally prepared counterpart (FA_NPC^{CO}) in order to investigate the beneficial effects of THUS over conventionally heated system in FA_NPC* preparation step. The CRW conversion mechanism on FA_NPC* catalyst's surface was investigated theoretically to understand the reaction mechanism at the atomic level. Finally, overall process sustainability was investigated using life cycle assessment (LCA) methodology.

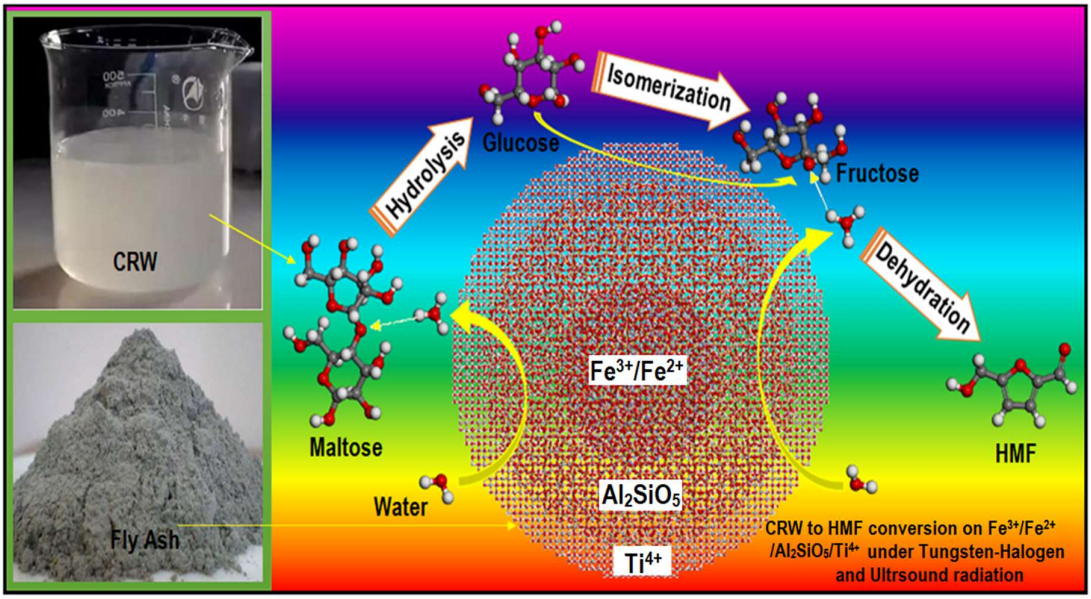

Figure 5. 5. Graphical abstract of the Activity 3

5.3.1. Chemicals and Materials

The Fly Ash (FA) was collected from thermal power plant, West Bengal, India. A kitchen waste, i.e. cooked rice water (CRW) was collected from local restaurant. NaOH, H_2SO_4, Ethanol, Titanium (IV) isopropoxide (TIIP) [$Ti(OCH(CH_3)_2)_4$] were reagent grade and procured from Merck (India).

5.3.2. Extraction of silica-alumina and ferrous material from FA

The FA was heated in a furnace at 900°C for 2 h to remove any carbonaceous impurity (Figure 5.6) and subsequently grinded in ball mill for 1 h to obtain 200 mesh fine FA particles, which was next subjected to magnetic stirring for separation of the ferrous materials. Afterwards, 1 M aqueous solution of NaOH was added to extract the silica and alumina from FA. The FA (50 g) was agitated with 100 mL of the NaOH solution for 0.5 h at 80 °C for the complete separation of silica and alumina. Inductively Coupled Plasma-Optical Emission Spectroscopy (ICP-OES) was employed to find the amount of silicon and aluminium in the extracts. The insoluble impurities were filtered out, whereas the filtrate was diluted 2 times by adding deionized water and deployed for nano silica-alumina preparation.

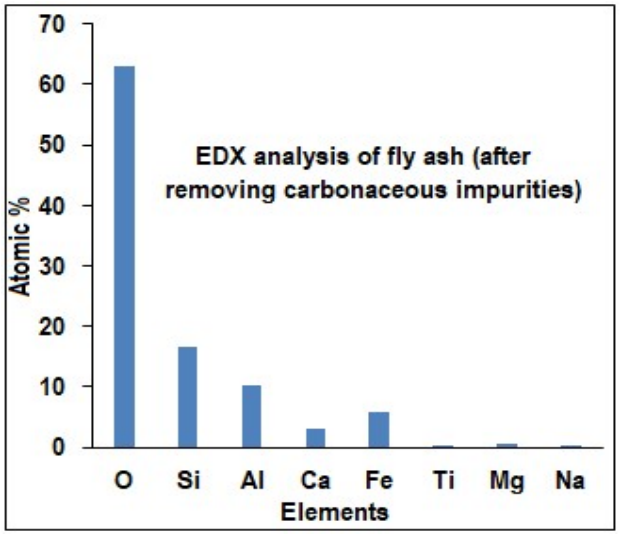

Figure 5. 6. EDX analysis of FA after removing carbonaceous impurities

5.3.3. Preparation of nano-Al_2SiO_5 gel and nano-Fe^{3+}/Fe^{2+} gel

The nano-Al_2SiO_5 gel was prepared from the diluted filtrate by mixing it with 25 wt. % H_2SO_4-ethanol (1:10) solution for 10 min under an innovative assimilated energy-system

comprising tungsten-halogen (TH: 340-850 nm, 150 W) radiation and ultrasound (US: 100 W; 40 kHz) (THUS). Consecutively, the mixture was aged for 1 h and centrifuged to obtain the nano-Al_2SiO_5 particle. Finally, the Al_2SiO_5 was thoroughly cleaned with deionized water and stockpiled in deionized water [17]. On the other hand, the magnetically separated ferrous particles were dissolved in H_2SO_4 [18] and the Fe^{3+}/Fe^{2+} nanoparticle was prepared by slowly adding a 2 M aqueous NH_3 solution under the THUS for 3 min. Subsequently, the precipitate was separated by centrifugation and cleaned with deionized water to obtain nano-Fe^{3+}/Fe^{2+} particles.

5.3.4. Catalyst preparation

The novel bimetallic $Fe^{3+}/Fe^{2+}/Al_2SiO_5/Ti^{4+}$ nano-photocatalysts (FA_NPC*) were prepared by mixing different amount of TIIP (2.5, 5, 7.5 wt. % per g of Al_2SiO_5) with fixed amount of Fe^{3+}/Fe^{2+} (10 wt. % per g of Al_2SiO_5) and Al_2SiO_5 according to Table 2. The mixture was agitated vigorously in isopropanol for 2 h at 60 °C under THUS. Consequently, the mixture was aged for 24 h and ultimately oven-dried (105 °C). Later, the dried mixture was subjected to calcination at 400 °C (according to TGA analysis) for 3 h, and concurrently, the different prepared FA_NPC* were designated as FA_NPC*$^{2.5}$(2.5 wt. % TIIP precursor loading), FA_NPC*^{5} (5 wt. % TIIP precursor loading), and FA_NPC*$^{7.5}$ (7.5 wt. % TIIP precursor loading).

Additionally, to evaluate the effects of THUS on catalytic properties, the optimum FA_NPC* (i.e. FA_NPC*^{O}) was also made by conventional hydrothermal (CH) method (500 W) at optimal loading (5 wt. % TIIP precursor loading) and was designated as FA_NPC^{CO}. The catalytic performance has been evaluated in the conversion of CRW to 5-HMF.

5.3.5. Compositional analysis of CRW

The collected waste CRW (cooked rice water) was purified by extracting the protein using diethyl ether solvent according to Furukawa et al. [19]. Anthrone method was used to determine the total carbohydrate content in CRW using UV-VIS spectrophotometer at 620 nm wavelength (Table 5.7). Furthermore, to analyse the distribution of monosaccharides (glucose), disaccharides (maltose) and polysaccharides in CRW, the suspended solid parts in CRW was separated through centrifugation and the liquid part was analysed through HPLC (Table 5.7).

Table 5. 7. Total carbohydrate content in CRW

Total carbohydrate content	211.734 gm/l
Glucose content (%) in CRW	0.24
Maltose content (%) in CRW	3.4507
polysaccharides content (%) in CRW	96.3

5.3.6. Photocatalytic conversion of CRW to 5-HMF

One-pot photocatalytic conversion of the CRW was performed in the THUS energy-system (TH (340-850 nm, 150 W) and US (100 W; 40 kHz)) assisted batch reactor in presence of the prepared FA_NPC*. The CRW (100 ml) along with a gauged amount of the FA_NPC* was accommodated in a one-necked flask (250 ml) and the reaction mix was heated at a specified temperature. The temperature of the THUS-facilitated batch reactor was monitored by a PID temperature controller. After performing the photocatalytic conversion of CRW for a stipulated time, the reaction mass was chilled down to ambient temperature and the filtrate hydrolysate was collected after separating the FA_NPC* using permanent magnetic bar.

5.3.6.1. Design of Experiment

The photocatalytic CRW hydrolysis using FA_NPC* catalyst for production of platform chemicals viz. 5-(hydroxymethyl) furfural (HMF), glucose was controlled by manipulating four independent process parameters i.e., titanium precursor loading (φ_{Ti}), catalyst concentration (φ_C), reaction temperature (φ_T) and time (φ_t) (with respect to total carbohydrate content in CRW) according to Box-Behnken design (Table 5.8). The HMF yield ($\in_{HMF}$) was measured as the response parameter for each experimental CRW conversion run (Table 5.9) and the optimal parametric values corresponding to maximum $\in_{HMF}$ were determined.

Table 5. 8. Process parameters for HMF production using FA_NPC* photocatalyst

Factors	Units	L_{-1}	L_0	L_1
Reaction temperature (φ_T)	°C	50	60	70
Titanium precursor loading (φ_{Ti})	wt.%	2.5	5	7.5
Catalyst concentration (φ_C)	wt.%	5	7.5	10
Time (φ_t)	Min	30	45	60

Table 5. 9. Design Layout for HMF production using FA_NPC* in THUS assisted batch reactor

Runs	φ_T (°C)	φ_t (min)	φ_{Ti} (wt. %)	φ_C (wt.%)	$\in_{HMF}$ (mol %)
1	60	30	2.5	7.5	14.1
2	50	45	5	10	25.46
3	60	45	2.5	10	18.7
4	60	30	7.5	7.5	21.15
5	70	30	5	7.5	24.89
6	50	60	5	7.5	34.46
7	60	60	2.5	7.5	21.46
8	60	45	7.5	5	25.68
9	60	60	7.5	7.5	31.06
10	70	45	2.5	7.5	21.5
11	70	45	7.5	7.5	28.45
12	50	45	2.5	7.5	18.79
13	50	45	7.5	7.5	21.6
14	50	30	5	7.5	21.15
15	60	45	5	7.5	30.71
16	60	45	7.5	10	27.3
17	70	45	5	10	35.67
18	50	45	5	5	23.8
19	60	30	5	10	29.4
20	70	45	5	5	26.67
21	60	60	5	5	31.24
22	60	30	5	5	20.7
23	70	60	5	7.5	38.37
24	60	60	5	10	38.06
25	60	45	2.5	5	15.3

5.3.7. CRW Conversion analysis

After the photocatalytic conversion, the hydrolysate products were analysed by HPLC with both refractive index (RI) and UV detectors (Waters high performance carbohydrate

column for glucose and C18 column for HMF). Acetonitrile and water mix (75:25 (V/V)) with a flow rate 1.4 ml min^{-1} was utilized as the mobile phase. The samples were purified using syringe filter before the analysis.

The HMF and glucose concentrations in product stream were computed from the calibration charts of standard HMF and glucose solution respectively. Moreover, n-butanol was used to extract HMF from product stream and identified in a UV detector at 284 nm for exact magnitude of HMF concentration [16].

HMF yield and Glucose yield were calculated on the basis of total carbohydrate content in CRW by Equation 5.15 and 5.16 respectively.

$$\in_{HMF} = [\frac{\text{HMF Produced } (g) \times 162.1406}{0.212 \times \text{CRW } (g) \times 126.11}] \times 100 \qquad (5.15)$$

$$\in_{G} = [\frac{\text{Glucose Produced } (g) \times 162.1406}{0.212 \times \text{CRW } (g) \times 180.156}] \times 100 \qquad (5.16)$$

5.3.8. Characterization of nano-Al_2SiO_5, nano-Fe^{3+}/Fe^{2+}, FA_NPC and FA_NPC^{CO}*

Thermo-gravimetric analyses (TGA) of the Al_2SiO_5 and uncalcined FA_NPC* and FA_NPC^{CO} were conducted in a PerkinElmer TGA analyzer (Pyris Diamond TG/DTA) in N_2 from 30 to 800 °C with a 15.0 °C/min temperature increment rate. The infrared-absorption spectra of the calcined Al_2SiO_5, Fe^{3+}/Fe^{2+} and FA_NPC* were identified with FTIR-SHIMADZU (Alpha), from 400 to 4000 cm^{-1}, while the XRD analysis was executed at 2θ ranging from 10° to 90° at 1° min^{-1} scanning speed with a Cu Kα source equipped with an Inel CPS 120 hemispherical detector. The BET and BJH analyses for Al_2SiO_5, Fe^{3+}/Fe^{2+} and FA_NPC* were done using Quantachrome Instruments, Nova 4000e to evaluate specific surface area, pore volume, and pore size distribution. The samples were degassed before BET analysis at 150 °C to separate surface moisture. Acidity of the catalysts and the calcined Al_2SiO_5 were determined using NH_3-TPD analysis deploying Quantachrome Instruments, TPR win v2.1. XPS analysis of the optimal FA_NPC*^{O} was performed to analyse the binding energy of Ti 2p and Fe 2p. HRTEM analysis for Al_2SiO_5, Fe^{3+}/Fe^{2+}, and the FA_NPC*^{O} and FA_NPC^{CO} were conducted in a FEI Titan G2 60 -300 transmission electron microscope by fast-tracking voltage of 300 kV. Moreover, the HRTEM images were analyzed using "GATAN digital micrograph" to identify and calculate the crystallite lattice spacing. The light absorbing capacity of the optimal FA_NPC*^{O} and FA_NPC^{CO} was measured in a PerkinElmer Lamda-365 UV−Visible spectrophotometer over 200−900 nm. Finally, the magnetic properties of FA_NPC*^{O} and FA_NPC^{CO} were analyzed using a Vibrating Sample Magnetometer (VSM).

*5.3.9. Molecular simulation of CRW conversion mechanism on FA_NPC**

To investigate the conversion mechanism of CRW to HMF on FA_NPC*^{O}, first, catalyst's surface was simulated by randomly doping 5 numbers of Al and 5 numbers of Ti atom on unmodified zeolite (as model structure for Al_2SiO_5) structure (lattice parameter: a=20.022, b = 19.899, c= 13.383 (orthorhombic)), which was neutralized with H^+ ion using Material studio "sorption" module. Afterwards, $C_{24}H_{42}O_{21}$ (four glucose unit), $C_{18}H_{32}O_{16}$ (three glucose unit) and $C_{12}H_{22}O_{11}$ (Maltose) were chosen as model molecules for CRW. Geometry of catalysts and reactants were optimized with universal forcefield (UFF) using "forcite" module of BIOVIA Materials Studio®. Notably, during catalyst's surface structure modelling, the effective charges of the atoms (except H^+ ion, where the charge was taken as +1) were taken from cvff forcefield (Al (+1.4), Ti (+2.4), Si (+2.4) and O (-1.2)).

After optimizing the structures of catalyst and reactant molecules, catalyst's active sites were analysed for three consecutive reaction steps in CRW to HMF conversion process viz., CRW hydrolysis, glucose isomerization and fructose dehydration. Initially, adsorption energies of CRW model molecules ($C_{24}H_{42}O_{21}$, $C_{18}H_{32}O_{16}$ and maltose), water, glucose and fructose on 001 plane of catalyst's surface (keeping 50 A˚ vacuum layer between reactant and catalyst's surface) were computed using BIOVIA Materials Studio® software to know the reactant's binding efficacy on catalyst's surface. Subsequently, catalyst's binding sites were analysed using Material Studio's "sorption" module.

After analysing the catalyst's active sites for different transitional conversion stages, finally the reaction mechanism along with the intermediate transition states of glucose formation (CRW hydrolysis), glucose isomerization and fructose dehydration processes on their respective catalyst's active sites were investigated using DFTB (Density Functional Based Tight Binding) module of Amsterdam Modelling Suite. Grimme's extended tight-binding model (GFN1-xTB) in DFTB in conjunction with water solvation model was used to investigate the transition states (TS) and IRC (internal reaction coordinate) paths of three different steps in CRW conversion to HMF.

5.3.10. Environmental impact assessment of CRW conversion process by LCA analysis

OpenLCA 1.9.0 software was used to perform a comparative environmental impact assessment (EIA) analysis between two optimal catalysts, viz. FA_NPC*^{O} and FA_NPC^{CO} for CRW photocatalytic conversion to HMF. Ecoinvent-3.5 database and an LCA methodology

viz., “ReCiPe Midpoint (H)” [20] were used to assess the probable environmental impacts concerning the whole process.

The system boundary (depicted in Figure 5.7) for LCA analysis includes the chemicals transport, nano-Al_2SiO_5 and nano-Fe^{3+}/Fe^{2+} preparation from FA, catalyst preparation and product separation. Moreover, mass allocation was considered for the multi-output processes; wherein the results of EIA were estimated based on 1 kg HMF production at optimized conditions.

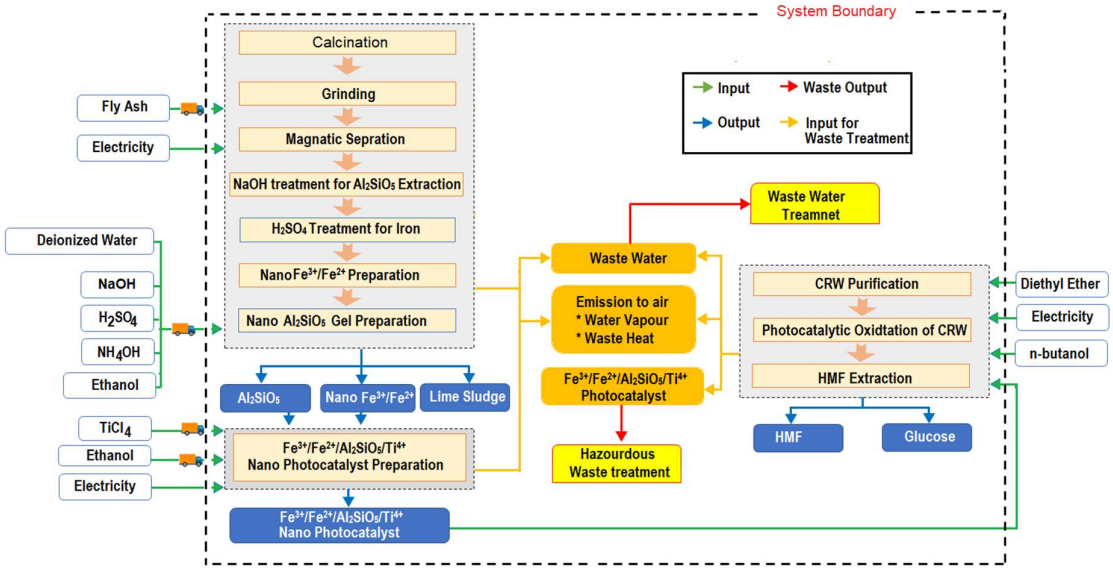

Figure 5. 7. Overall process diagram and system boundaries for photocatalytic CRW conversion process

A life cycle inventory (LCI) database was prepared based on system boundary where the inputs and outputs of the entire process were scaled-up based on functional unit (1 kg HMF). The detailed LCI information has been summarized in Table 5.10. Moreover, information regarding TIIP is not available in the Ecoinvent-3.5 database, hence, it was considered that TIIP is prepared from $TiCl_4$ and the process was modelled as stated by Caramazana-González et al., 2017 [21]. Electric energy utilized in the whole process was presumed to be dissolute to air as waste heat [22]. The process waste viz., waste water and spent photocatalyst was assumed to be treated via waste water treatment process and hazardous waste treatment process (underground deposition) respectively. Notably, the waste lime sludge generated from FA processing was considered as a by-product which can be utilized in concrete preparation process [23].

Table 5. 10. Process input and outputs for CRW conversion process to produce 1 kg of HMF

Category		Value		Unit	Source	Comments
		For FA_NPC*[O]	For FA_NPC[CO]			
Energy Input	Electricity consumed			kWh	Ecoinvent-3.5	
	For calcination	1.00	1.00			
	Grinding	0.250	0.250			
	Magnetic	0.0166	0.0166			
	separation	0.250	0.250			
	NaOH treatment	0.054166	0.054166			
	H_2SO_4 treatment	0.50	1.00			
	Catalyst preparation	0.250	0.250			
	Photocatalytic					
	conversion of CRW	**2.320766**	**2.820766**			
	Total					
Material Input	CRW solution	12.3088	21.79467	Kg	Created	
	Fly Ash (FA)	2.1718	3.845562	Kg	Ecoinvent-3.5	1 kg FA produce 0.12 kg
	Deionized water	1.5	1.5	Kg	Ecoinvent-3.5	of catalyst
	TIIP	0.013031	0.023073	Kg	Created	TIIP assumed to produce
	NaOH	0.0174	0.03076	Kg	Ecoinvent-3.5	from $TiCl_4$ [21]
	H_2SO_4	0.010	0.010	Kg	Ecoinvent-3.5	
	NH_4OH	0.005	0.005	Kg	Ecoinvent-3.5	
	Diethyl ether	0.50	0.50	Kg	Ecoinvent-3.5	
	Ethanol	1.50	1.50	Kg	Ecoinvent-3.5	To extract the HMF
	Butanol	1.50	1.50	Kg	Ecoinvent-3.5	
Emissions to air	Waste heat	8.35475	10.1547	MJ	Ecoinvent-3.5	Assuming all electrical energy dissipated as heat to air (1 kWh =3.6 MJ)
	Water Vapour	0.56013	0.9340	kg	Ecoinvent-3.5	During drying and heating (assuming 5 % of total used water (used in CRW solution as well as in washing))

Transports	CRW solution	0.07693	0.136216	Kg.km	Ecoinvent-3.5	Transport by lorry, capacity: 16 metric ton, EURO IV / BS IV (assuming all materials came from 100 km distance)
	Fly Ash (FA)	0.01357	0.02403	Kg.km	Ecoinvent-3.5	
	Deionized water	0.009375	0.009375	Kg.km	Ecoinvent-3.5	
	TIIP	8.144E-05	0.00014	Kg.km	Ecoinvent-3.5	
	NaOH	0.00010	0.00019	Kg.km	Ecoinvent-3.5	
	H_2SO_4	0.000062	0.000062	Kg.km	Ecoinvent-3.5	
	NH_4OH	0.00003	0.000031	Kg.km	Ecoinvent-3.5	
	Diethyl ether	0.003125	0.003125	Kg.km	Ecoinvent-3.5	
	Ethanol	0.009375	0.009375	Kg.km	Ecoinvent-3.5	
	Butanol	0.009375	0.009375	Kg.km	Ecoinvent-3.5	
	Total	**0.1220376**	**0.191931**	Kg.km	Ecoinvent-3.5	
Waste of materials	Waste Water	1.12026	1.8679	Kg	Ecoinvent-3.5	Considering 10 % of total used water
	Spent catalyst	0.26062	0.405844	Kg	Ecoinvent-3.5	Considering the catalyst deactivation after 1 kg of HMF production
Output	HMF	1	1	Kg	Created	
	Glucose	0.8269	1.137	Kg	Ecoinvent-3.5	Products were allocated on the basis of mass
	Lime Sludge	1.910	2.976	kg	Created	

5.4. Activity 4:

ENERGY-EFFICIENT AND ECO-FRIENDLY CONTINUOUS PRODUCTION OF 5-CMF IN A UV-ULTRASOUND IRRADIATED CATALYTIC PACKED BED REACTOR: HETEROGENEOUS KINETICS, REACTOR SIMULATION AND LCA ANALYSIS

In this work, for the first time a combination of heterogeneous reusable photocatalytic and thermo-catalytic systems was employed, where the TiO_2 photocatalyst was used along with the Brønsted acidic catalyst Smopex-101 to synthesize 5-CMF from starch in a biphasic system employing choline chloride as the chlorine source. The reaction was intensified employing an ultraviolet (UV) and ultrasound (US) irradiation system in both batch reactor (UVUS-BR) and continuous flow rectangular packed bed reactor (UVUS-RPBR). First, the 5-CMF synthesis process was optimized in a batch reactor using the Taguchi orthogonal design (TOD), where selected process factors were optimized to maximize the 5-CMF yield. Afterwards, heterogeneous reaction kinetic models were formulated for the 5-CMF synthesis process under a heterogeneous catalytic system, and kinetic parameters were determined using the experimentally obtained rate data from UVUS-BR under optimized conditions. Finally, the performance of UVUS-RPBR has been assessed for the 5-CMF production process and simulated using the ANSYS FLUENT software. Moreover, an effort was made to identify promising alternative organic solvents based on their extracting efficiency of 5-CMF and associated environmental impacts.

5.4.1. Materials

Soluble starch (SS) (solubility: 20 g/l of water at 25 ºC), glucose, fructose was procured from Merck. Smopex-101 (S-101) fiber (non-porous catalyst with sulfonated acid group; particle diameter: 0.1 mm; length: 4 mm) was collected from Alfa Aesar. Nano TiO_2 (mixture of rutile and anatase phase, particle size < 100 nm), blue Dextran, choline chloride, cyclohexane; dichloroethane (DCE), dichloromethane (DCM), chloroform ($CHCl_3$), Methyl isobutyl ketone (MIBK), Toluene and glass beads (4 mm) were purchased from Sigma-Aldrich. The purity of the solvents was checked through GC-MS analysis before using in the present study. The procured commercial catalysts (TiO_2 and S-101) were oven dried at 80°C for 1 h before utilization in the reaction.

5.4.2. 5-CMF synthesis in isothermal batch reactor configuration

The 5-CMF synthesis process from SS was conducted employing an isothermal batch reactor equipped with UV (8 W; 280-400 nm) and ultrasound (50 W; 20 kHz) (UVUS-BR)

energy system. The power of the UV and US energy was measured using a power meter, and the power density was calculated based on the sample volume where the respective energy was applied. Notably, the sample was placed in close contact with the respective energy source to minimize energy loss. The transparent SS solution was first prepared by mixing 1 g of SS with 5 ml of water and measured amount of choline chloride (Table 5.11) at 80°C for 10 min. Afterwards, a biphasic solution was prepared by mixing the transparent SS aqueous solution with 10 ml of organic solvent (cyclohexane). Finally, the 5-CMF synthesis process was conducted in UVUS-BR by mixing the biphasic solution with a total of 0.1 g of S-101 and TiO_2 solid catalysts at a pre-defined ratio and temperature over a specified time span (Table 5.11). The reactor temperature was controlled using a PID temperature controller. After reaction, the reaction mix was cooled down to room temperature and the organic phase and aqueous phase was separated after collecting the catalyst through filtration. Finally, the product (5-CMF) was collected from cyclohexane (Figure 5.8) using vacuum evaporator and analysed with GC-MS.

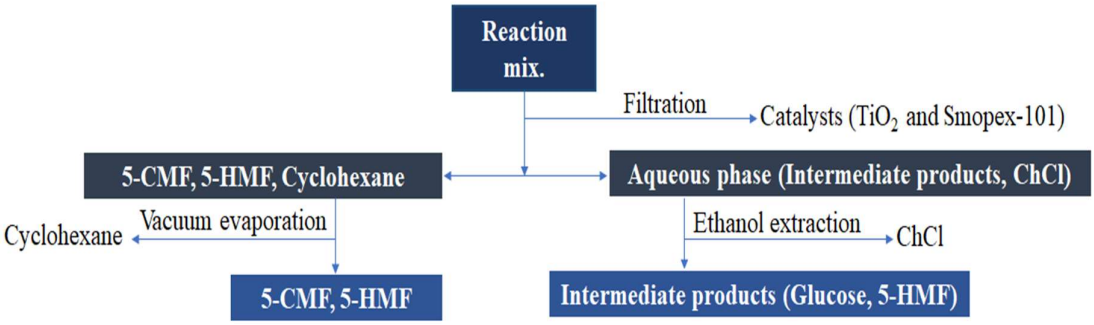

Figure 5. 8. ChCl, cyclohexane, catalysts recycling and product separation

5.4.3. Product Characterization

The organic phase was analysed by GC-MS using HP-5MS column (0.25 × 30 m) where helium (flow rate: 1.0 ml min^{-1}) was used as a carrier gas. Samples were injected with 1 ml with split ratio of 1:10 whereas the inlet and source temperature were kept at 250°C and 280°C respectively. The aqueous phase was analysed by HPLC with both refractive index (RI) and UV detectors (Waters high performance carbohydrate column for glucose, fructose and C18 column for HMF). Acetonitrile and water mix (75:25 (V/V)) with a flow rate 1.4 ml min^{-1} was utilized as the mobile phase. All the samples were purified using syringe filter before the analysis.

5.4.4. 5-CMF synthesis process optimization in UVUS-BR

The 5-CMF synthesis process in UVUS-BR was designed and optimized according to TOD involving four selected process parameters viz., reaction time ($\emptyset_t$), temperature ($\emptyset_T$), S-101: TiO_2 ratio ($\emptyset_{S101/TiO_2}$) and choline chloride to SS ratio ($\emptyset_{ChCl/SS}$) (Table 5.11). The levels of the selected process parameters were chosen based on one factorial experimental analysis. The 5-CMF yields (Y_{CMF}) were measured as the response value for 9 TOD experimental runs (Table 5.12) to evaluate the optimal process conditions for maximization of SS conversion to 5- CMF. Soluble starch (SS) conversion, glucose yield, 5-HMF yield and 5-CMF yield were calculated according to the below equations

$$\text{SS conversion} = [\frac{\text{Initial SS (g)} - \text{Final SS (g)}}{\text{Initial SS (g)}}]\times 100 \quad (5.17)$$

$$\text{Glucose yield } (Y_G) = [\frac{\text{Glucose produced (g)}}{\text{Initial SS (g)}\times 1.111}]\times 100 \quad (5.18)$$

$$5-\text{HMF yield } (Y_{HMF}) = [\frac{\text{5-HMF produced (g)}}{\text{Initial SS (g)}\times 0.7778}]\times 100 \quad (5.19)$$

$$5-\text{CMF yield } (Y_{CMF}) = [\frac{\text{5-CMF produced (g)}}{\text{Initial SS (g)}\times 0.8915}]\times 100 \quad (5.20)$$

The denominating factor 1.111, 0.7778 and 0.8915 accounts for the mass accumulation or mass reduction during conversion of repeating units of starch to glucose, 5-HMF and 5-CMF respectively.

After optimizing the 5-CMF conversion process individual effects of UV, US energy on 5-CMF yield was also investigated at optimized conditions. Moreover, to understand the impact of US and UV energy over conventional heating on 5-CMF yield, a study was also conducted employing only conventional heating at optimized conditions.

Table 5. 11. Independent process parameters and their levels for of 5-CMF synthesis process

Process parameters	Name	Units	L_{-1}	L_0	L_1
$\emptyset_T$	Temperature	°C	60	70	80
$\emptyset_t$	Reaction Time	min	30	60	90
$\emptyset_{S101/TiO_2}$	S-101 to TiO_2 ratio	w/w	0.5	1.5	2.5
$\emptyset_{ChCl/SS}$	ChCl to SS ratio	w/w	1	3	5

L_{-1}: lower level; L_0: middle level; L_1: upper level

Table 5. 12. TOD for 5-CMF synthesis in UVUS-BR

$\emptyset_T$	$\emptyset_t$	$\emptyset_{S101/TiO_2}$	$\emptyset_{ChCl/SS}$	Y_{CMF}	S.D.
L_{-1}	L_{-1}	L_{-1}	L_{-1}	18.10	$\pm$0.50
L_{-1}	L_0	L_0	L_0	30.23	$\pm$0.80
L_{-1}	L_1	L_1	L_1	39.00	$\pm$1.00
L_0	L_{-1}	L_0	L_1	45.4	$\pm$0.30
L_0	L_0	L_1	L_{-1}	33.10	$\pm$0.50
L_0	L_1	L_{-1}	L_0	35.00	$\pm$0.50
L_1	L_{-1}	L_1	L_0	37.82	$\pm$0.25
L_1	L_0	L_{-1}	L_1	58.27	$\pm$0.50
L_1	L_1	L_0	L_{-1}	41.10	$\pm$0.20

After optimization study, the optimized 5-CMF synthesis process was carried out with different solvents, namely dichloroethane (DCE), dichloromethane (DCM), chloroform ($CHCl_3$), methyl isobutyl ketone (MIBK), and toluene to determine the most suitable solvent for the extraction of 5-CMF.

5.4.5. Plausible reaction mechanism and kinetic model formation

The plausible reaction pathway for the synthesis of 5-CMF from SS in a biphasic system under S-101/TiO_2 catalytic system is shown in Figure 5.9. The SS to 5-CMF conversion reaction initiated with hydrolysis step where SS depolymerized to glucose and oligosaccharides with the aid of S-101 surface adsorbed protonated water [16]. Afterwards, glucose was isomerized to fructose on the Lewis acidic sites of TiO_2 surface and subsequently the produced fructose was dehydrated to 5-HMF on the Bronsted acidic sites of S-101 catalyst. Notably, the US energy produces cavitation bubble collapse, high-speed microjets and shockwaves which can enhance the adsorption of reactant molecules on S-101 and TiO_2 surface. The chlorination of 5-HMF to 5-CMF could took place in bulk aqueous phase with the help photo-oxidized Cl^- ion (from ChCl) under UV irradiation [24]. Finally, the produced 5-CMF and 5-HMF transported from aqueous phase to organic (cyclohexane) phase based on their partition coefficient in organic and aqueous phase.

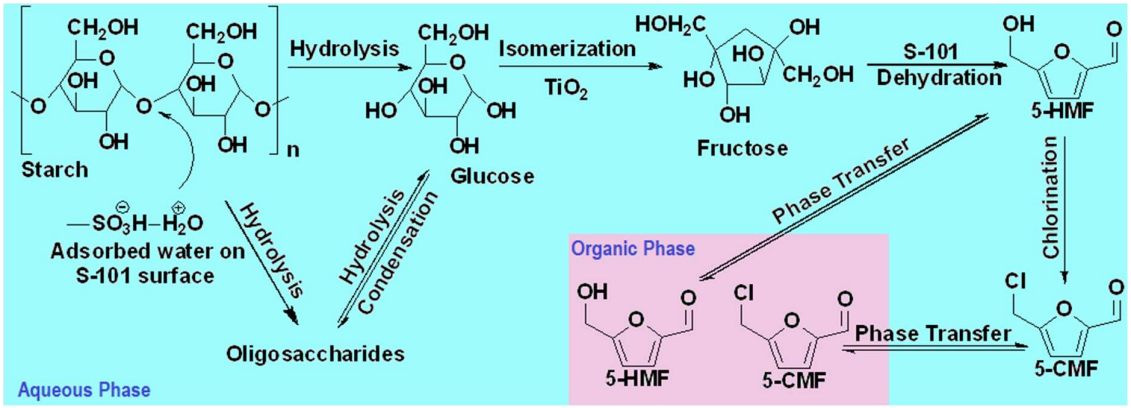

Figure 5. 9. Plausible reaction pathway for 5-CMF synthesis process under S-101 and TiO_2 catalytic system

5.4.6. Kinetic model formulation

Before formulating the reaction kinetic model, first fluid-solid (reactant-catalyst) mass transfer resistance was evaluated to know whether the different reaction steps (SS hydrolysis, glucose dehydration and 5-HMF chlorination step) of 5-CMF synthesis process on catalyst's surface were surface reaction controlled or not. As both the catalysts are non-porous, only external mass transfer resistance between reactants and catalyst's surface was analysed according to Mear's criteria (Ω) [25]. After analysing the external mass transfer resistance (result section 6.4.4) it was observed that all the reaction steps on catalyst's surface are dominated by surface reaction kinetic regime.

The experimental kinetic study of 5-CMF synthesis process was performed in the UVUS-BR at optimized condition. During the experimental kinetic study, glucose, 5-HMF, and 5-CMF were identified as the main products generated within the optimized reaction time (Figure 6.47 (b)). Additionally, oligosaccharides and fructose were detected in trace amount in the product mix. We assumed that the conversion of fructose to 5-HMF through dehydration took place rapidly as it formed [26] and consequently, only a minimal concentration of fructose was detected in the resulting product mixture. Moreover, other degradation products such as levulinic acid, formic acid, and levoglucosan were not generated more than 2.5 mol %; as a result, they are not considered during kinetic model formulation. Therefore, the SS to 5-CMF conversion process under S-101/TiO_2 dual catalytic system was simplified as Figure 5.10.

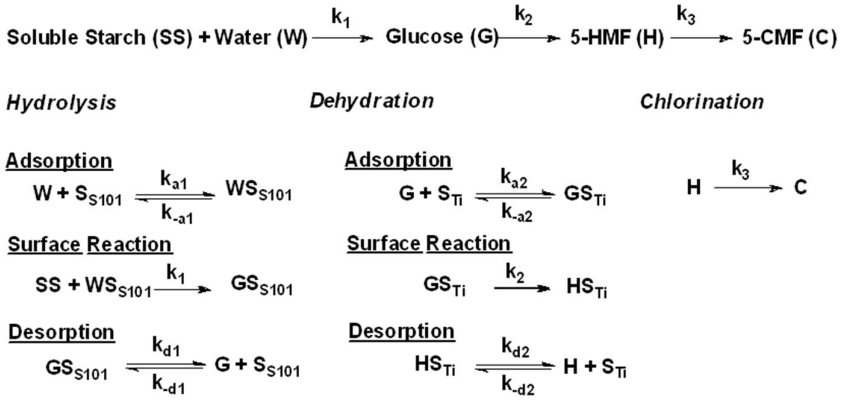

Figure 5. 10. simplified 5-CMF synthesis process

For SS hydrolysis step, it was assumed that the reactant '*SS*' (soluble starch) did not get adsorbed on the S-101 surface and the surface reaction between adsorbed '*W*' (water) and '*SS*' was the rate limiting step and irreversible. Accordingly, the formulated SS hydrolysis rate (mol/g cat. s) equation was obtained as

$$-r_{SS} = \frac{k_1 C_{SS} C_W}{(1 + K_{a1} C_W + K_{d1} C_G)} \tag{5.21}$$

Here k_1 (ml/ mol s) represents apparent reaction rate constant for SS hydrolysis process; K_{a1} and K_{d1} represents equilibrium constants for adsorption and desorption step on S-101 surface; C_{SS}, C_W and C_G stands for concentration (mol / ml) of SS, water and glucose respectively.

For glucose dehydration step, it was assumed that the glucose dehydration reaction on TiO_2 surface was rate limiting step and irreversible. So, the glucose generation rate (mol / g cat. s) formulated as

$$r_G = \frac{k_1 C_{SS} C_W}{(1 + K_{a1} C_W + K_{d1} C_G)} - \frac{k_2 C_G}{(1 + K_{a2} C_G + K_{d2} C_H)} \tag{5.22}$$

Here k_2 (1 / s) represents apparent reaction rate constant for glucose dehydration step; K_{a2} and K_{d2} represents equilibrium constants for adsorption and desorption step on TiO_2 surface. C_H represents the concentration (mol / ml) of 5-HMF.

The 5-HMF and 5-CMF generation rate in aqueous phase was evaluated through experimentally determining partition coefficients of 5-HMF and 5-CMF in aqueous-organic biphasic system. Besides, when formulating 5-HMF chlorination reaction rate equation, it is really difficult to measure the in situ generated photo-oxygenated Cl^- ion present in the reaction mix during the reaction, thus we consider the 5-HMF chlorination reaction is pseudo first-order

reaction with respect to 5-HMF. Accordingly, the 5-HMF (Equation-5.23), 5-CMF (Equation-5.24) generation rates (mol / g cat. s) in aqueous phase was formulated as:

$$r_H = \frac{\frac{k_2 C_G}{(1 + K_{a2} C_G + K_{d2} C_H)} - \frac{k_3 C_H}{\rho_C}}{(1 + \emptyset_H \frac{V_{Org}}{V_{Aqu}})} \quad (5.23)$$

$$r_C = \frac{k_3 C_H}{\rho_C (1 + \emptyset_C \frac{V_{Org}}{V_{Aqu}})} \quad (5.24)$$

Here ρ_C is the bulk density of catalyst (g cat. / ml); $\emptyset_H$ $(or\ \frac{C_{H,Org}}{C_{H,Aqu}})$ and $\emptyset_C$ $(or\ \frac{C_{C,Org}}{C_{C,Aqu}})$ are the partition coefficient of 5-HMF and 5-CMF in aqueous-organic phase respectively. $C_{H,Org}$ and $C_{C,Org}$ are the concentration of 5-HMF and 5-CMF in organic phase and $C_{H,Aqu}$ and $C_{C,Aqu}$ are the concentration of 5-HMF and 5-CMF in aqueous phase. $\frac{V_{Org}}{V_{Aqu}}$ represents the volume ratio of organic and aqueous phase and k_3 (1 / s) represents the apparent reactant rate constant for 5-HMF chlorination step.

The activation energies of different reaction steps were calculated according to Arrhenius equation.

$$k = E_o\, exp\left[-\frac{E}{R}\left(\frac{1}{T_2} - \frac{1}{T_1}\right)\right] \quad (5.25)$$

Where, T_2 and T_1 represent the two different reaction temperatures at otherwise optimum conditions derived through TOD analysis. E (kJ / mol) is the activation energy, E_o is the pre-exponential factor and R is the gas constant (8.31×10^{-3} kJ / mol K).

5.4.7. 5-CMF synthesis in continuous-flow UVUS-RPBR

After optimization and kinetic analysis, the 5-CMF synthesis process was also performed in the continuous-flow catalytic rectangular packed bed reactor i.e., UVUS-RPBR (bed length: 15 cm; width: 5 cm, height: 3 cm) (Figure 5.11(a) & (b)) at the optimized conditions. The decision to select a rectangular packed bed reactor instead of a cylindrical or tube type reactor was motivated by its improved exposure to both the UV source (positioned on the upper surface of the RPBR) and the US source (positioned beneath the lower surface of the RPBR). Additionally, for a given volume, the rectangular shape reactor inherently offers a smaller surface area compared to cylindrical or tube-type reactors, resulting in lower construction costs

for the RPBR in comparison to its counterparts. The reactor bed was filled with the TiO_2 and S-101 catalysts at various bed porosities while maintaining the optimized $\emptyset_{S101/TiO_2}$ level as in UVUS-BR. In order to address the leaching concern, the TiO_2 nanoparticles were initially coated onto glass beads. Subsequently, the TiO_2 coated glass beads were used to fill the reactor bed.

To prepare the TiO_2 coated glass beads, the surface of the glass beads was initially roughened through a chemical etching process by immersing the glass beads in hydrofluoric acid for a duration of 24 hours. Subsequently, the nano TiO_2 powder and HF-treated glass beads were mixed in an acetone medium at a temperature of 70°C. The mixing process was conducted under magnetic stirring conditions at 300 rpm for a period of 3 hours. Following this, the mixture was subjected to oven drying and finally calcined at a temperature of 300°C for a duration of 3 hours to produce TiO_2 coated glass beads (Figure 5.11(b)) with average beads size of 4 mm and average coating thickness of 0.2 mm. According to the BET analysis, the TiO_2 coating applied to the glass beads was found to be non-porous, exhibiting an extremely low amount of average pore volume (0.021 cm^3/g) and an average pore diameter (1.27 nm) that was negligible. The TiO_2 loading weight was determined by measuring the difference between the weight of the glass beads before and after the TiO_2 coating process.

Additionally, the reactor's inlet and outlet were covered with perforated screen [aperture size: 0.1 mm (18 mesh)]. Finally, UV-A (maximum power: 60 W; 280-400 nm) and US (maximum power: 500 W; 20 kHz) energies were employed synergistically to intensify the conversion process and the power of the US and UV system was controlled using regulators. Two syringe pumps having infused flow rate ranging between 1-90 ml/h were used to precisely control the flow rates of the biphasic SS feed solutions. The reaction mix was collected under steady state after carefully monitoring the different energy systems and henceforth controlling the reactor temperature. A check valve was also installed to protect the syringe pump against back flow.

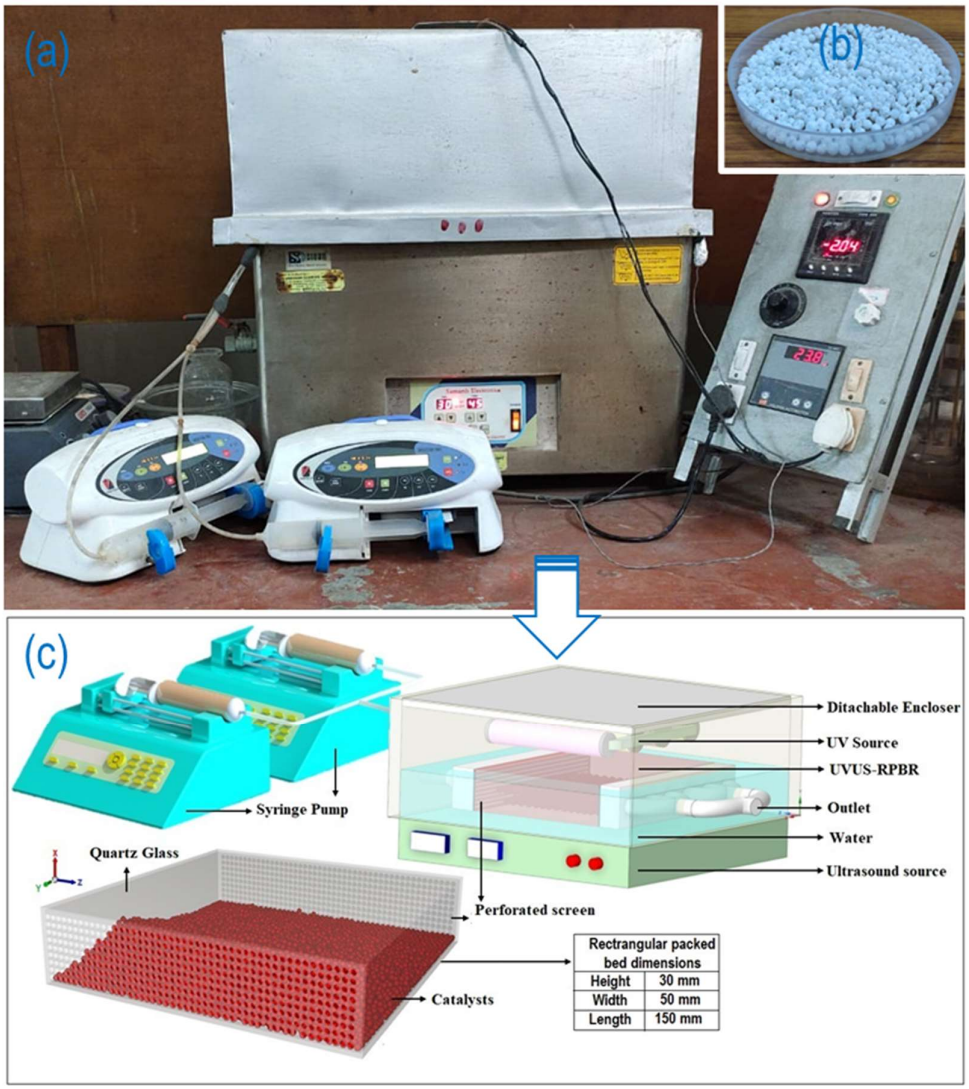

Figure 5. 11. (a) experimental setup of UVUS-RPBR (b) TiO_2 coated glass beads (c) schematic diagram of UVUS-RPBR

To investigate the impact of US energy system on continuous fluid flow behaviour inside the RPBR, a comparative residence time distribution (RTD) study was performed through pulse tracer experiment employing with and without US system. Additionally, to understand the influence of US energy system on RPBR performance, a comparative study was also performed by conducting the reaction without US (UV-RPBR) at the derived optimized conditions. Notably, in UV-RPBR the optimized reaction temperature was attained with the help of conventional heating system (by means of heating coil; power 500 watt). Moreover, the reusability of the catalysts viz., TiO_2 coated glass beads and S-101 were also studied.

5.4.8. RTD analysis for UVUS-RPBR

In pulse tracer experiment, water was used as eluent with the flow rate of 126 ml/h and blue Dextran was used as tracer material which was injected in one shot for the evaluation of the residence time distribution (RTD) parameters of the RPBR with bed porosity of 0.56. The tracer concentrations at outlet stream were measured using a UV-VIS detector at 300 nm and exit-age distribution function (E(t)) with respect to time was evaluated. The Peclet number (*Pe*) was calculated considering 'closed-closed' Danckwerts boundary conditions as per Equation-5.26.

$$\frac{\sigma^2}{\tau_{mean}{}^2} = \frac{2}{Pe} - \frac{2}{Pe^2}(1 - e^{-P}) \qquad (5.26)$$

Where $Pe = \frac{UL}{D}$

Here, L is the reactor length, U is the superficial velocity of water, D is the dispersion number.

5.4.9. Life cycle assessment (LCA) analysis of 5-CMF synthesis process

The potential environmental impacts associated with the optimized 5-CMF synthesis process employing different extracting organic solvents was analysed using OpenLCA 1.9.0 software with Ecoinvent-3.5 database. "ReCiPe Midpoint (H) V1.13" method was used as a life cycle impact assessment (LCIA) methodology to assess the potential environmental impacts [27].

The system boundary (Figure 5.12) for LCA analysis includes the chemicals transport, 5-CMF synthesis process, glass beads supported TiO_2 photocatalyst preparation and product separation, wherein the overall analyses were estimated based on 1 kg 5-CMF production at optimized conditions.

The outcomes of 5-CMF synthesis process were scaled-up according to functional units and used as database for the Life Cycle Inventory (LCI) (Table 5.13 to 5.15). Allocation of reference product (5-CMF) and by-products (glucose, 5-HMF) were done according to their mass. Besides, among total used water it was assumed that 10 % of water lost as water vapor. All electrical energies used in the entire process were considered to be dissipated as waste heat to air [28]. Furthermore, the waste sludge resulting from hydrofluoric acid treatment of glass beads was assumed to be disposed underground via hazardous waste treatment routes.

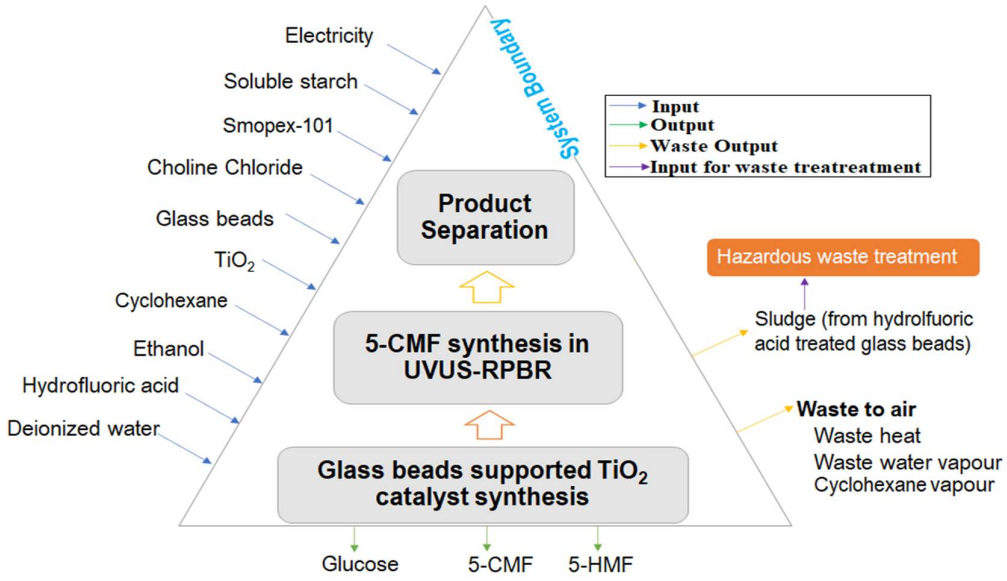

Figure 5. 12. System boundary for LCA analysis of 5-CMF synthesis process

Table 5. 13. LCI data for production of 1 kg of TiO_2 coated glass beads

Category	Flow	Value	Unit	Source	Comments
Energy Input	Electricity consumed	3.3	kWh	Ecoinvent-3.5	
Material Input	Hydrofluoric acid	0.5	Kg	Ecoinvent-3.5	
	TiO_2	0.1	Kg	Ecoinvent-3.5	
	Glass beads	1.0	Kg	Ecoinvent-3.5	
Transports	Hydrofluoric acid	0.0031	Kg.km	Ecoinvent-3.5	Transport by lorry, capacity: 16 metric ton, EURO VI (assuming all materials came from 100 km distance)
	TiO_2	0.000625	Kg.km	Ecoinvent-3.5	
	Glass beads	0.005625	Kg.km	Ecoinvent-3.5	
	Total	**0.00935**	**Kg.km**	Ecoinvent-3.5	
Emissions to air	Waste heat	11.8	MJ	Ecoinvent-3.5	Assuming electrical energy used was dissipated as heat to air (1 kWh =3.6 MJ)
Waste materials	Sludge	0.6	kg	Ecoinvent-3.5	Generated during hydrofluoric acid treatment
Output	TiO_2 coated glass beads	1	Kg	Created	

Table 5. 14. LCI data for production of 1 kg of CMF production in UVUS-RPBR

Category		Flow	Value	Unit	Source	Comments
Energy	Input	Electricity consumed	0.365	kWh	Ecoinvent-3.5	
Material Input		Starch	1.91	Kg	Ecoinvent-3.5	As remaining choline chloride, water recycled back. All cyclohexane was recycled, except for a 5 % volume loss during recycling. Catalysts recycling up to 6 times. For choline chloride separation.
		Choline chloride	0.965	Kg	Ecoinvent-3.5	
		Water	0.0346	Kg	Ecoinvent-3.5	
		Cyclohexane	0	Kg	Ecoinvent-3.5	
		Smopex-101	0.0192	Kg	Created	
		TiO_2 coated glass beads	0.127	Kg	From Table 2S	
		Ethanol	0.10	kg	Ecoinvent-3.5	
Transports		Starch	0.012	Kg.km	Ecoinvent-3.5	Transport by lorry, capacity: 16 metric ton, EURO VI (assuming all materials came from 100 km distance)
		Choline chloride	0.006	Kg.km	Ecoinvent-3.5	
		Water	0.00022	Kg.km	Ecoinvent-3.5	
		Cyclohexane	0.012	Kg.km	Ecoinvent-3.5	
		Smopex-101	0.00012	Kg.km	Ecoinvent-3.5	
		TiO_2 coated glass beads	0.0008	Kg.km	Ecoinvent-3.5	
		Ethanol	0.000625	Kg.km	Ecoinvent-3.5	
		Total	**0.0318**	**Kg.km**	Ecoinvent-3.5	
Emissions	to air	Waste heat	1.314	MJ	Ecoinvent-3.5	Assuming electrical energy used was dissipated as heat to air (1 kWh =3.6 MJ)
		Water vapour	0.084	kg		
Output		5-CMF	1	Kg	Created	
		Glucose	0.345	Kg	Ecoinvent-3.5	
		5-HMF	0.202	Kg	Created	

Table 5. 15. Purification of 1 kg of 5-CMF

Category	Flow	Value	Unit	Source	Comments
Energy Input	Electricity consumed	0.125	kWh	Ecoinvent-3.5	
Material Input	5-CMF	1	Kg	From Table 3S	
Emissions to air	Waste heat	0.45	MJ	Ecoinvent-3.5	Assuming electrical energy used was dissipated as heat to air (1 kWh =3.6 MJ) (5 % of volume loss of total used cyclohexane)
	Cyclohexane	0.95	Kg		

Output	Purified 5-CMF	1	Kg	Created

5.5. Activity 5:

ENVIRONMENTALLY SUSTAINABLE ETHYL LEVULINATE SYNTHESIS FROM DELIGNIFIED SUGARCANE BAGASSE USING TERNARY EUTECTIC SOLVENT UNDER MW-XENON IRRADIATION: ENGINE PERFORMANCE & EMISSION ASSESSMENT

In this study, a Bronsted-Lewis acid-based ternary acidic deep eutectic solvent (TADES) has been prepared using choline chloride-$FeCl_3$-Citric acid and its catalytic properties were investigated in the ethyl levulinate (EL) synthesis process from pretreated sugarcane bagasse (PSCB) under the synergistic effect of MW and xenon (XE) irradiations. The EL production process was optimized and the produced EL was blended with biodiesel-diesel whose fuel properties, engine performance, and exhaust emission profile were also investigated. Overall process sustainability was assessed through life cycle environmental impact analysis.

5.4.1. Materials

Chemicals of analytical reagent grade viz. Ethanol (99.9%), choline chloride (ChCl, 98%), $FeCl_3$ (99.9 %), citric acid (99 %), ethyl levulinate (99 %) were purchased from Merck. Sugarcane bagasse (SCB) was collected from Shree Renuka Sugars Limited, Haldia, India.

5.5.2. Methods

5.5.2.1. Delignification of SCB

The collected SCB first thoroughly rinsed with deionized water and oven dried for 2h at 70° C. Afterwards, the dried SCB was cut into fine particles in a cutting mill (Figure 5.13) and finally grinded into fine powder **(**size range: -240 +300 mesh**)** using ball milling. For the delignification, 50 g of dried SCB powder was then treated with 100 ml of peracetic acid (99% glacial acetic acid: 30% H_2O_2 of 7:3 vol/vol) for 3 h at 70 °C [29]. The resulting mixture was then filtered and the filter cake was washed with hot water to obtain the pretreated-SB (PSCB). Finally, compositional analysis (cellulose, hemicellulose and lignin) and elemental analysis

(CHNS analysis) of the PSCB as well as raw SCB were done, which are tabulated in the Table 5.16.

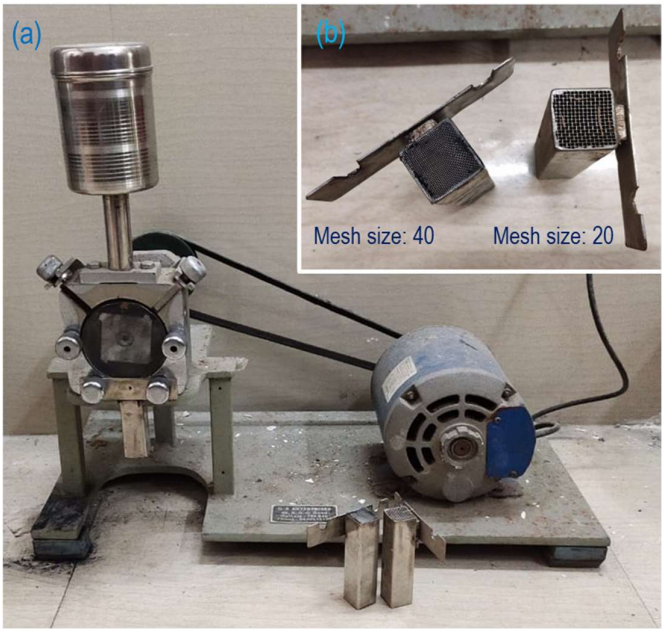

Figure 5. 13. (a) setup of cutting mill with (b) screening mesh

Table 5. 16. Compositional analysis of SCB and PSCB

CHNS analysis	SCB	PSCB	Compositional analysis*	SCB	PSCB
C	40.17	33.42	Cellulose	37.5	49.3
H	5.91	3.95	Hemicellulose	29.3	39.5
N	0.28	0.86	Lignin	23.50	4.3
S	0.008	0.012	Others	9.7	6.9

* Compositional analysis was done based on Anthrone method [10]

5.5.2.2. Preparation of TADES

The TADESs were prepared by mixing 1 mol of choline chloride (ChCl) with a mixture of 1 mol of $FeCl_3$ and citric acid under 80°C heating conditions for 10 minutes. The proportions of $FeCl_3$ and citric acid were adjusted according to Table 5.17. during the synthesis and the prepared TADESs were termed as ChCl-$FeCl_3^{1}$-CA^{2} ($FeCl_3$ to CA mol ratio: 1:2 or 0.5), ChCl-$FeCl_3^{1.5}$-$CA^{1.5}$ ($FeCl_3$ to CA mol ratio: 1.5:1.5 or 1) and ChCl-$FeCl_3^{1.8}$-$CA^{1.2}$ ($FeCl_3$ to CA mol ratio: 1.8:1.2 or 1.5).

5.5.2.3. One pot synthesis of EL from PSCB *using TADES*

One pot synthesis process of EL from PSCB was performed in MW (Frequency: 2.45 GHz) -XE (Wavelength: 190-1100 nm) irradiated stirred batch reactor (MWXER) (Figure 5.14) by reacting 10 ml of aqueous ethanolic solution (ethanol to water vol. ratio: 9:1) with 1g of DSB employing 5ml of TADES at 90°C. to optimize the EL synthesis process parameters, four selected process factors viz., MW power (Ω_P), XE power (Ω_{XE}), $FeCl_3$ to CA mol ratio ($\Omega_{FeCl_3/CA}$) and synthesis time (Ω_t) (Table 5.17) were considered and according to TOD (Table 5.18), 9 experimental runs were conducted in MWXER. The optimum parameter levels were determined for maximising EL yield (mol %) (Ω_{EL}). The levels of the process factors were selected based on single parametric experiments.

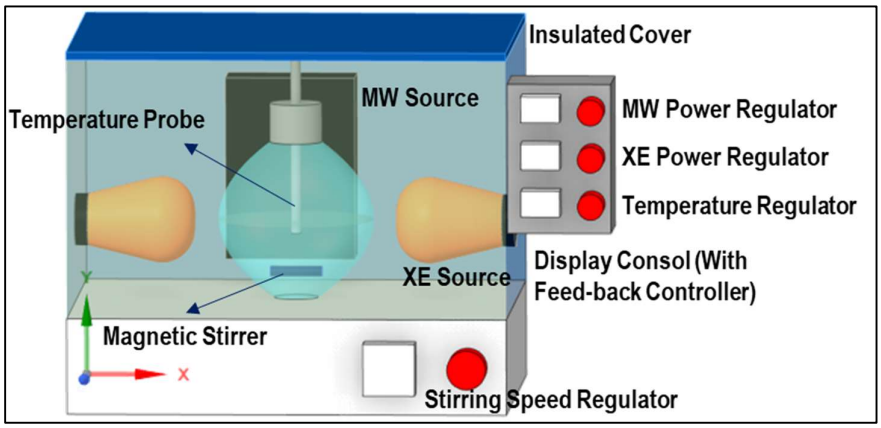

Figure 5. 14. Schematic diagram of MWXER

Table 5. 17. Independent process factors and their levels for Taguchi orthogonal design

Process parameters	Name	Units	L_{-1}	L_0	L_1
Ω_P	MW irradiation power	W	100	200	300
Ω_{XE}	XE irradiation power	W	50	100	150
$\Omega_{FeCl_3/CA}$	$FeCl_3$ to CA mol ratio	(mol/mol)	0.5	1	1.5
Ω_t	Synthesis time	Min	60	90	120

L_{-1}: lower level; L_0: middle level; L_1: upper level

Table 5. 18. TOD for one pot EL synthesis from PSCB

Ω_P (W)	Ω_{XE} (W)	$\Omega_{FeCl_3/CA}$(mol/mol)	Ω_t (min)	Ω_{EL}(mol %)	SD	SN ratio
L_{-1}	L_{-1}	L_{-1}	L_{-1}	23.40	±0.50	27.38
L_{-1}	L_0	L_0	L_0	28.40	±0.15	29.06
L_{-1}	L_1	L_1	L_1	33.50	±0.05	30.50

L_0	L_{-1}	L_0	L_1	42.10	±0.50	32.48
L_0	L_0	L_1	L_{-1}	38.76	±0.30	31.76
L_0	L_1	L_{-1}	L_0	36.40	±0.10	31.22
L_1	L_{-1}	L_1	L_0	53.60	±0.20	34.58
L_1	L_0	L_{-1}	L_1	48.56	±0.30	33.72
L_1	L_1	L_0	L_{-1}	45.90	±0.25	33.23

After optimizing the process factors, the EL synthesis process was also conducted employing individual energy system (MW and XE) at the derived optimum factorial levels to reveal the effect of MW and XE irradiations alone on EL yield. Moreover, experiment was also conducted under conventional heating (500 W) condition at the derived optimum factorial levels to investigate the efficacy of MW-XE energy system over conventional heating on EL yield.

Upon completing each experimental run, the reaction mixture underwent filtration to isolate humin (Figure 5.15). Subsequently, ethanol was separated from the filtrate using a vacuum evaporator. Toluene was then utilized to extract EL from the remaining filtrate. Finally, at 4°C, the separated ethanol was employed to extract TADES, resulting in the precipitation of glucose and oligosaccharides through centrifugation.

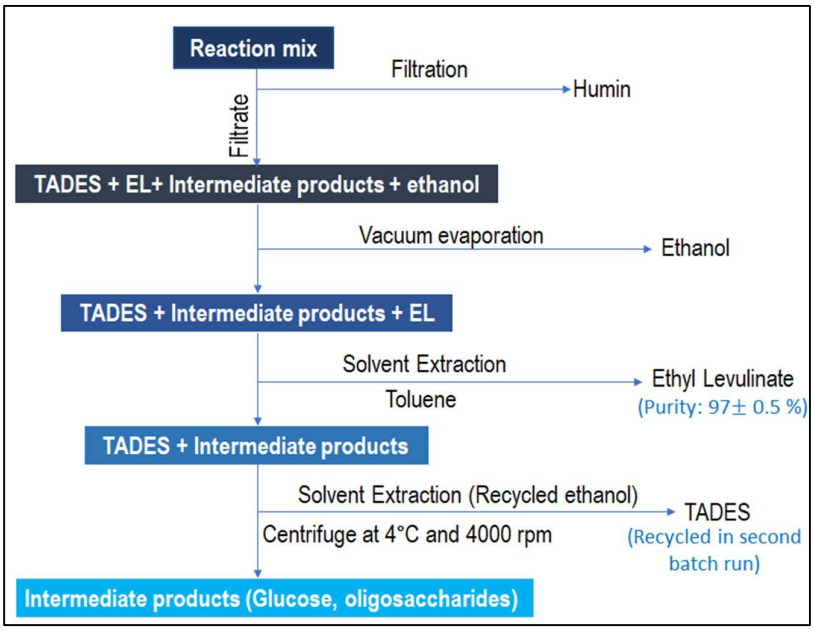

Figure 5. 15. TADES and products separation after PSCB conversion process

5.5.3. Product analysis

After separation, the EL and intermediate products were purified using syringe filter before the analysis. The analysis of the EL was performed using GC-MS with an HP-5MS column (0.25 × 30 m), with helium serving as the carrier gas at a flow rate of 1.0 ml min^{-1}. The samples were injected at a volume of 1 ml with a split ratio of 1:10, while maintaining the inlet and source temperatures at 250°C and 280°C, respectively. EL yield and selectivity were calculated by Equation 5.27 and Equation 5.28 respectively:

$$\Omega_{EL} = \left[\frac{\frac{\text{EL produced } (g)}{144.17}}{[\text{cellulose } (g) \text{ in PSCB } /162.15 + \text{hemicellulose (g) in PSCB}/162.15]}\right] \times 100 \quad (5.27)$$

$$EL\ selectivity = \frac{\text{EL produced } (g)/144.17}{\text{PSCB } conversion} \quad (5.28)$$

The other intermediate products (glucose, oligosaccharides) were analysed using HPLC (Waters high performance carbohydrate column: P/N WAT044355: 4.6 mm * 250 mm column with 4 µm Nova-Pack@ spherical silica bonded with trifunctional amino propyl silane; Waters 410 refractive index (RI) detector). Acetonitrile and water (75:25 (V/V)) with a flow rate 1.4 ml/ min was used as a mobile phase.

5.5.4. Characterization of prepared TADES

After preparing the TADESs, their physical properties such as density, average freezing point and acidity were evaluated. The densities were evaluated using hydrometer and the average freezing points were determined by submerging the TADESs in an ice bath and employing a temperature sensor to measure the temperature of the solvents. The Hemmett acidity (H_0) of the TADESs were determined employing 4-Nitroaniline as basic indicator. First, diluted TADESs (10 mmol/l of water) mixed with 4-Nitroaniline and samples absorbance were measured in UV-VIS spectrophotometer. Finally, H_0 were calculated using the Equation-5.29.

$$H_0 = pK(I)_{aq} + \log\left(\frac{I}{IH^+}\right) \quad (5.29)$$

Here, $pK(I)_{aq}$ represents the thermodynamic ionisation constant (0.99) of the 4-Nitroaniline in water and the $\log\left(\frac{I}{IH^+}\right)$ was measured from the UV-VIS absorbance data at absorbance peak of 380 nm.

Compositional properties were examined through FTIR analysis to gain insights into the structure of TADES. Furthermore, understanding the light absorption capacity and dielectric constant of TADES was crucial in assessing the impact of MW and Xenon irradiation

during the EL synthesis process. Dielectric constant and dissipation factor of TADES was measured using dielectric probe kit. The dissipation factor of TADES determined how much MW energy is going to convert into thermal energy. The dissipation factor ($\tan(\delta)$) of TADES was calculated according to the Equation-5.30.

$$\tan(\delta) = \frac{\varepsilon^{"}}{\varepsilon'} \qquad (5.30)$$

Where, ε' and $\varepsilon^{"}$ represents the real and imaginary part of the complex dielectric constant $[\varepsilon' - i\varepsilon'']$. The refractive index ($n$) was calculated form transmittance (T) data obtained from UV-VIS spectra.

$$n = \frac{1}{T} + \sqrt{\frac{1}{T-1}} \qquad (5.31)$$

5.5.5. EL-Biodiesel-Diesel blending and engine performance of blended fuels

In this work, 5 and 10 vol % of synthesized EL were blended with B10(10 vol % biodiesel and 90 vol % diesel), B20 (20 vol % biodiesel and 80 vol % diesel) and the properties of the synthesized EL and the blended fuels were investigated. The performance of the blended fuels was evaluated in a four-stroke diesel engine (specifications of diesel engine: 553 cc cylinder with 3.7 kW of power) at engine speed of 1000-1500 rpm and exhaust emission was analysed using an exhaust gas analyser (measurement range: CO: 0–15%; HC: 0–20,000 ppm; CO_2: 0–20%; NOx: 0–5000 ppm).

5.5.6. LCA analysis

The overall process sustainability of the EL synthesis process from SCB using TADES was analysed through LCA analysis using OpenLCA software. Moreover, environmental impacts associated with individual irradiation systems were also investigated to understand the overall efficacy of MW and XE irradiation system in EL synthesis process. To explore these impacts, a gate-to-gate LCA approach was utilized, where the 1st system boundary (Figure 5.16) encompasses the transport of chemicals, the pretreatment of waste sugarcane bagasse, the preparation of TADES, and the synthesis process of EL from PSCB using TADES. Finally, to identify the optimum EL blending ratio in B10 and B20, environmental impacts analysis for each blend were also performed employing the engine exhaust emission data though gate to grave approach (2nd boundary system).

A life cycle inventory (LCI) database was prepared based on system boundary where the inputs and outputs of the entire process were scaled-up based on functional unit (1 kg EL) (Detailed LCI database is given in Table 5.19-5.23. "ReCiPe Midpoint (H)" LCA methodology with Ecoinvent-3.5 database [30] was used to evaluate the probable environmental impacts viz. photochemical oxidant formation (kg NMVOC), freshwater ecotoxicity (kg 1,4-DB eq.), natural land transformation (m^2), terrestrial acidification (kg SO_2 eq.), marine eutrophication (kg N eq.), terrestrial ecotoxicity (kg 1,4-DB eq.), human toxicity (kg 1,4-DB eq.), water depletion (m^3), climate change (kg CO_2 eq.), particulate matter formation (kg PM10 eq.), ozone depletion (kg CFC-11 eq.), metal depletion (kg Fe eq.), fossil depletion (kg oil eq.), urban land occupation (m^2*a), ionising radiation (kg U235 eq.), agricultural land occupation (m^2*a), freshwater eutrophication (kg P eq.), marine ecotoxicity (kg 1,4-DB eq.) respectively for the system boundaries shown in Figure 5.16. Notably, it was considered that electric energy used in the MW or XE and vacuum evaporator would be lost to the atmosphere as waste heat.

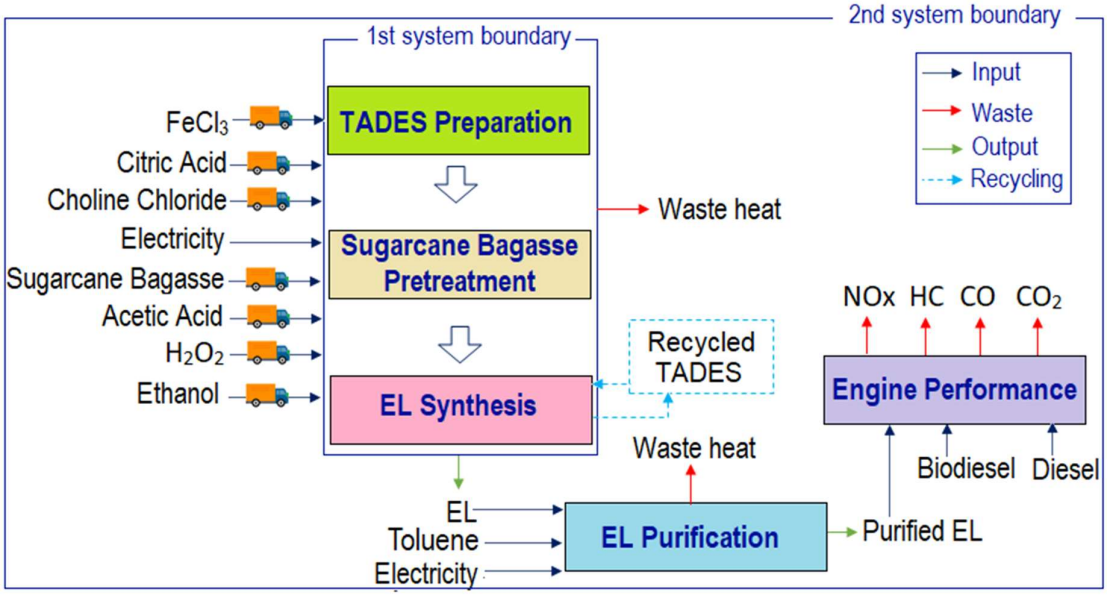

Figure 5. 16. System boundary for LCA analysis

Table 5. 19. LCI database for 1 Kg of optimal TADES (ChCl-$FeCl_3^{1.5}$-$CA^{1.5}$) preparation

Category	Flow	Value	Unit	Source	Comments
Energy Input	Electricity consumed	0.083	kWh	Ecoinvent-3.5	
Material Input	Choline chloride	0.211	Kg	Created	
	$FeCl_3$	0.245	Kg	Ecoinvent-3.5	
	Citric acid	0.291	Kg	Ecoinvent-3.5	

Transports	Choline chloride	0.00132	Kg.km	Ecoinvent-3.5	Transport by lorry, capacity: 16 metric ton, EURO VI (assuming all materials came from 100 km distance)
	$FeCl_3$	0.00153	Kg.km	Ecoinvent-3.5	
	Citric acid	0.00182	Kg.km	Ecoinvent-3.5	
	Total	**0.00467**	**Kg.km**	Ecoinvent-3.5	
Emissions to air	Waste heat	0.2988	MJ	Ecoinvent-3.5	Assuming electrical energy used was dissipated as heat to air (1 kWh =3.6 MJ)
Output	$ChCl\text{-}FeCl_3^{1.5}\text{-}CA^{1.5}$	1	Kg	Created	

Table 5. 20. LCI database for 1 Kg PSCB preparation

Category	Flow	Value	Unit	Source	Comments
Energy Input	Electricity consumed	2	kWh	Ecoinvent-3.5	
Material Input	Sugarcane bagasse	1.45	Kg	Ecoinvent-3.5	
	H_2O_2	0.85	Kg	Ecoinvent-3.5	
	Acetic acid	2.05	Kg	Ecoinvent-3.5	
Transports	Sugarcane bagasse	0.009	Kg.km	Ecoinvent-3.5	Transport by lorry, capacity: 16 metric ton, EURO VI (assuming all materials came from 100 km distance)
	H_2O_2	0.0053	Kg.km	Ecoinvent-3.5	
	Acetic acid	0.0128	Kg.km	Ecoinvent-3.5	
	Total	**0.0271**	**Kg.km**	Ecoinvent-3.5	
Emissions to air	Waste heat	7.2	MJ	Ecoinvent-3.5	Assuming electrical energy used was dissipated as heat to air (1 kWh =3.6 MJ)
Output	DSB	1	Kg	Created	

Table 5. 21. LCI database for 1 Kg EL preparation

Category	Flow	Value	Unit	Source	Comments
Energy Input	Electricity consumed	0.45	kWh	Ecoinvent-3.5	
Material Input	PSCB	1.835	Kg	Ecoinvent-3.5	
	Ethanol	1.267	Kg	Ecoinvent-3.5	(As 90% of ethanol was recovered and all TADES was recycled)
	$ChCl\text{-}FeCl_3^{1.5}\text{-}CA^{1.5}$	0	Kg	Ecoinvent-3.5	
Transports	Ethanol	0.0079	Kg.km	Ecoinvent-3.5	
Emissions to air	Waste heat	1.62	MJ	Ecoinvent-3.5	Assuming electrical energy used was dissipated as heat to air (1 kWh =3.6 MJ)
Output	EL	1	Kg	Created	

Table 5. 22. LCI database for 1 Kg EL purification

Category	Flow	Value	Unit	Source	Comments
Energy Input	Electricity consumed	0.208	kWh	Ecoinvent-3.5	
Material Input	Toluene	0	Kg		All of the toluene was recycled.
Transports	Toluene	0	Kg.km		
Emissions to air	Waste heat	0.7488	MJ	Ecoinvent-3.5	Assuming electrical energy used was dissipated as heat to air (1 kWh =3.6 MJ)
Output	EL	1	Kg	Created	

Table 5. 23. LCI database for exhaust emission of 1 Kg EL-biodiesel-diesel blended fuel

Category	Flow	Value				Unit	Source	Comments
		B10EL5	B10EL10	B20EL5	B20EL10			
Material Input	Diesel	0.855	0.81	0.76	0.72	Kg	Ecoinvent-3.5	
	Biodiesel	0.095	0.09	0.19	0.18		Ecoinvent-3.5	
	EL	0.05	0.1	0.05	0.1		Created	
Emissions to air	HC	81.437	72.6316	77.088	70.9178	mg	Ecoinvent-3.5	From exhaust emission analysis
	NOx	92.838	96.567	94.129	100.119	mg	Ecoinvent-3.5	
	CO	0.0477	0.04257	0.0361	0.02709	g	Ecoinvent-3.5	
	CO_2	4.4118	4.515	4.5795	4.6698	g	Ecoinvent-3.5	
Output	Energy	43018	41762	42591	41357	KJ/Kg	Ecoinvent-3.5	

5.5. Activity 6:

CONTINUOUS ETHYL LEVULINATE PRODUCTION FROM PRETREATED SUGARCANE BAGASSE IN MICROWAVE-VISIBLE IRRADIATED CONTINUOUS STIRRED SLURRY REACTOR: REACTION KINETICS, TECHNO-ECONOMIC & ENVIRONMENTAL SUSTAINABILITY ANALYSES

The primary objective of the current work was to produce EL from sugarcane bagasse (SCB) through a sustainable and energy efficient protocol. To achieve this, various acidic DESs were initially prepared, and their efficacy in EL synthesis was investigated (Figure 5.17) in presence of the NZF photocatalyst under photo-thermal effect of MW and VIS irradiation systems within a batch reactor (MWVIS-BR). Subsequently, the batch EL production process parameters were optimized. Following this, the EL synthesis process was explored within a

continuous stirred slurry reactor system (MWVIS-CSSR), and continuous EL synthesis kinetic analysis was performed. The produced EL was blended with biodiesel-diesel, and its impact on fuel properties, engine performance, and exhaust emissions was analysed, alongside determining the optimal EL blending ratio through environmental impact assessment. Finally, the entire SCB to EL conversion process was upscaled to handle a processing capacity of 2000 kg/h of SCB and simulated using Aspen Plus, followed by a comprehensive sustainability assessment involving economic and environmental impact analyses.

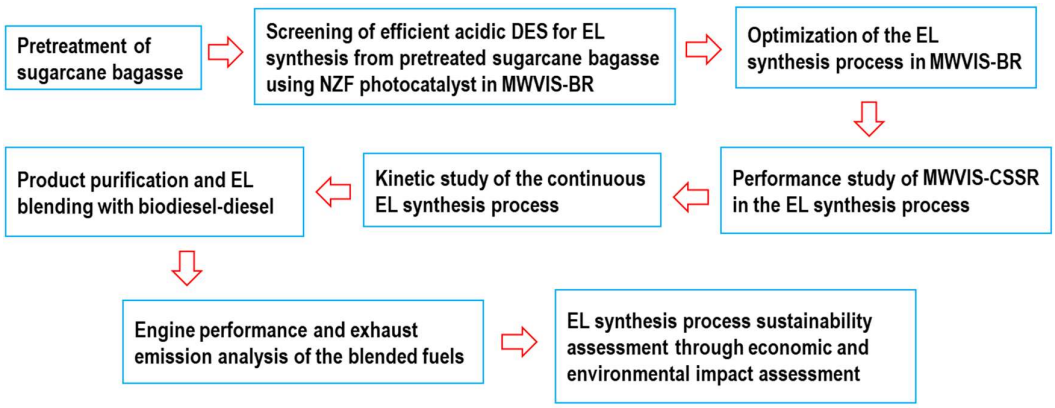

Figure 5. 17. Sequential steps of the present work

5.6.1. Materials

Ethanol (99.9%), choline chloride (ChCl, 98%), p-toluene sulfonic acid ($CH_3C_6H_4SO_3H{\cdot}H_2O$), oxalic acid ($C_2H_2O_4{\cdot}2H_2O$), malonic acid ($CH_2(COOH)_2$), citric acid ($C_6H_8O_7{\cdot}H_2O$), Phenylpropionic acid ($C_9H_{10}O_2$), ethyl levulinate (EL), Levulinic acid, 5-ethoxy methyl furfural (5EMF), Ethyl β-D-glucopyranoside, Ethyl β-D-xylopyranoside, peroxyacetic acid, NaOH were purchased from Merck. Ni-Zn-ferrite (NZF) nanoparticle ($Ni_{0.5}Zn_{0.5}Fe_2O_4$; size < 30 nm) was procured from Nanoshel limited.

5.6.2. Methods

5.6.2.1. Screening of DES for efficient EL synthesis

To assess the efficacy of acidic DES in the efficient synthesis of EL from pretreated sugarcane bagasse (PSCB; composition as mentioned in the activity 5), five acidic DES with a broad pH range were synthesized. The DES were prepared by combining choline chloride (ChCl) with p-toluene sulfonic acid, oxalic acid, malonic acid, citric acid, and Phenylpropionic acid in a 1:1 molar ratio, as specified in Table 5.24 and subsequently employed in the EL synthesis process.

The EL synthesis process was performed in a MW (frequency: 915 MHz; specific power input: 4 watt/ml of reaction volume)-VIS (Wavelength: 400-700 nm; specific power input: 4 watt/ml of reaction volume) irradiated stirred batch reactor (MWVIS-BR) at fixed reaction conditions (temperature: 100°C, time: 45 min; stirring speed: 500 rpm) in presence of NZF photocatalyst. The power of the microwave, visible light energy was measured using a power meter, and the power density was calculated based on the sample volume where the respective energy was applied. Notably, the sample was placed in close contact with the respective energy source to minimize energy loss. In this arrangement, 1 g of PSCB was reacted with 10 ml of ethanol in the presence of fixed amount of the prepared DES and NZF nano-photocatalyst (5 ml of DES and 4 wt. % of NZF, proportional to the PSCB quantity).

Table 5. 24. Components, freezing point, and pH of different prepared acidic DES

Abbreviation	DES	Freezing temperature (°C)	pH (at 298 K)
DES1	choline chloride: p-toluene sulfonic acid	12	-1.45
DES2	choline chloride: oxalic acid	34	-0.97
DES3	choline chloride: malonic acid	10	-0.16
DES4	choline chloride: citric acid	69	0.15
DES5	choline chloride: phenylpropionic acid	20	1.12

5.6.2.2. Characterization of DESs

The physical characteristics of the prepared DESs, including density, viscosity, average freezing point, and acidity were systematically assessed. Hydrometers were employed to determine density, while the average freezing points were determined by submerging the DESs in an ice bath, with a temperature sensor used to measure solvent temperatures. Viscosity measurements were conducted using an Anton Paar Viscometer SVM 3000, and pH values were determined using an Inolab pH meter.

To investigate the thermal stability of the prepared DES, TGA analysis was performed. Additionally, understanding the light absorption capacity of NZF and the complex permittivity of the DES was deemed essential in evaluating the impact of MW and visible irradiation during the EL synthesis process. The light absorption capacity of the NZF photocatalyst in DES-ethanol medium was determined through UV-VIS Spectroscopic analysis. The complex permittivity $[\varepsilon(i\omega) = \varepsilon(\omega)' - i\varepsilon(\omega)'']$ measurement of the DES was carried out using a

dielectric probe kit and penetration depth of MW at 915 MHz frequency was determined employing Equation-5.32.

$$Penetration\ depth = \frac{c}{2\pi f\sqrt{2\varepsilon'[\sqrt{(1+tan^2\delta)}-1]}} \quad (5.32)$$

Where c represents speed of light in free space (3×10^8 m/s), f represents frequency (Hz), $\varepsilon'$is relative permittivity and tan δ is dissipation factor.

5.6.2.3.Optimization of EL synthesis process in MWVIS-BR

After identifying most effective DES, the optimization of other process factors associated with the EL synthesis process viz., viz., Temperature (Ω_T), Stirring speed (Ω_S), NZF to PSCB ratio ($\Omega_{NZF/PSCB}$) and synthesis time (Ω_t) (Table 5.25) were carried out. For this object, Taguchi orthogonal design (TOD) was employed to design experimental runs at different parametric combinations, as outlined in Table 5.26 and a total nine experimental runs were conducted. Notably, the levels of the four process factors were chosen according to the preliminary results obtained from the single factorial experimental studies. After completion of nine experimental runs, the optimum factorial levels for the EL synthesis process in MWVIS-BR were determined through S/N ratios (Equation-5.32) while considering *"larger is better"* option for EL yield (Ω_{EL}) as the response parameter. The Ω_{EL} (mol %) was calculated according to Equation-5.33.

$$S/N\ ratio = -10\log(\frac{1}{n}\sum_{i=1}^{n}\frac{1}{\Omega_{EL}{}^2}) \quad (5.32)$$

$$\Omega_{EL}(mol\ \%) = \frac{g\ of\ EL\ produced}{(g\ of\ Holocellulose\ present\ in\ DSB * 0.8891)} \times 100\% \quad (5.33)$$

Here, i: number of replications, n: number of experimental runs as per TOD. The denominating factor 0.8891 accounts for the mass reduction during conversion of repeating units of holocellulose (hemicellulose + cellulose) present in PSCB to EL.

Table 5. 25. Independent process factors and their levels for EL synthesis in MWVIS-BR

Factors	Name	Units	L_{-1}	L_0	L_1
Ω_T	Reaction temperature	°C	80	90	100
Ω_S	Stirring speed	rpm	400	500	600
$\Omega_{NZF/PSCB}$	NZF to PSCB ratio	(wt. %)	2	4	6

Ω_t	Synthesis time	min	30	45	60

L_{-1}: lower level; L_0: middle level; L_1: upper level

Table 5. 26. Experimental design for one pot EL synthesis from PSCB using TOD

Ω_T (°C)	Ω_t (min)	$\Omega_{NZF/PSCB}$ (wt. %)	Ω_S (rpm)	Ω_{EL} (mol %)	SD	S/N ratio
L_{-1}	L_{-1}	L_{-1}	L_{-1}	20.50	$\pm$0.50	26.23
L_{-1}	L_0	L_0	L_0	29.50	$\pm$0.15	29.39
L_{-1}	L_1	L_1	L_1	27.50	$\pm$0.05	28.78
L_0	L_{-1}	L_0	L_1	31.75	$\pm$0.50	30.03
L_0	L_0	L_1	L_{-1}	44.10	$\pm$0.30	32.88
L_0	L_1	L_{-1}	L_0	36.40	$\pm$0.10	31.22
L_1	L_{-1}	L_1	L_0	47.10	$\pm$0.20	33.46
L_1	L_0	L_{-1}	L_1	39.75	$\pm$0.30	31.98
L_1	L_1	L_0	L_{-1}	50.20	$\pm$0.25	34.01

5.6.3. Product analysis

After completion of EL synthesis process from pretreated sugarcane bagasse, the reaction mix were separated according to the Figure 5.18. After separation, the EL and by-products were purified using syringe filter before the analysis. The analysis of the EL and by products such as ethyl formate (EF), 5-ethoxymethyl furfural (5EMF), 5-hydroxymethyl furfural (5HMF), and ethyl glycopyranosides (EDGP) was performed using GC-MS with an HP-5MS column (0.25 × 30 m), with helium serving as the carrier gas at a flow rate of 1.0 ml min^{-1}. The samples were injected at a volume of 1 ml with a split ratio of 1:10, while maintaining the inlet and source temperatures at 250°C and 280°C, respectively.

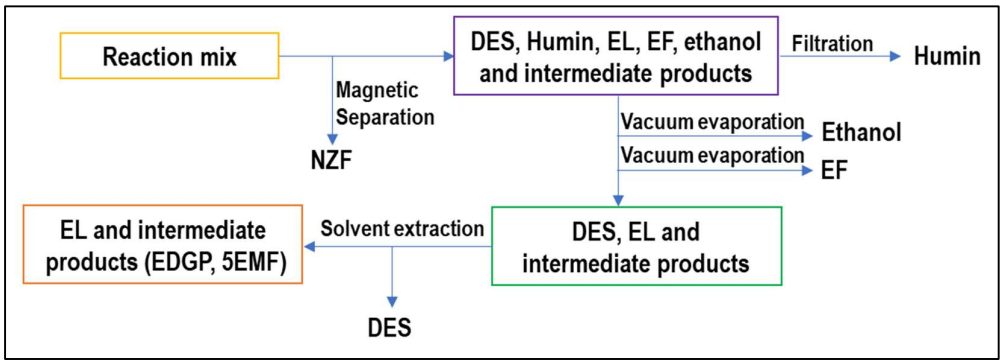

Figure 5. 18. Separation process of EL, DES and NZF photocatalyst

The other intermediate products (glucose, oligosaccharides) were analysed using HPLC (Waters high performance carbohydrate column: P/N WAT044355: 4.6 mm * 250 mm column with 4 µm Nova-Pack@ spherical silica bonded with trifunctional amino propyl silane; Waters 410 refractive index (RI) detector). Acetonitrile and water (75:25 (V/V)) with a flow rate 1.4 ml/ min was used as a mobile phase.

5.6.4. EL synthesis in MWVIS-CSSR

After optimization study in MWVIS-BR, performance of a large MWVIS assisted continuous-stirred slurry reactor i.e., MWVIS-CSSR (reactor diameter: 15 cm; reactors hight: 30 cm; with total working volume of 5 l) (Figure 5.19) in the EL synthesis process was investigated to assess the intensification effects of MW and VIS energy in presence of large reaction volume. The decision to use a CSSR or over a plug flow reactor was driven by the aim to achieve a homogeneous slurry, a characteristic challenging to attain in plug flow systems due to superior reactant mixing and uniform reaction conditions. As shown in the Figure 5.19 and Figure 5.20(a), PSCB and NZF were first fed to a mixing tank through screw feeder, where it was mixed with DES. The resultant mixed slurry was then fed to MWVIS-CSSR (Figure 5.20(b)) through diaphragm pump along with ethanol. The slurry diaphragm pump flow rates were controlled using variable-frequency drive (VFD) controller and to monitor the reactor's temperature, three temperature probes were installed at various radial positions of the reactor. The reaction mix was agitated with a turbine type mechanical impeller at 500 rpm and the product was collected under steady state after carefully monitoring the MW and VIS energy system under controlled reactor temperature (100 °C). The reactor outlet was connected to a magnetic separator, where NZF photocatalyst was separated. Subsequently, the residual slurry was connected to a three-fold vacuum separator unit to separate the humin (Figure 5.20(c)).

Finally, the unreacted ethanol and ethyl formate (EF) were separated through vacuum evaporator and the product EL and DES were isolated through solvent extraction and purification. Lastly, the recovered ethanol and DES were reintroduced into the reactor.

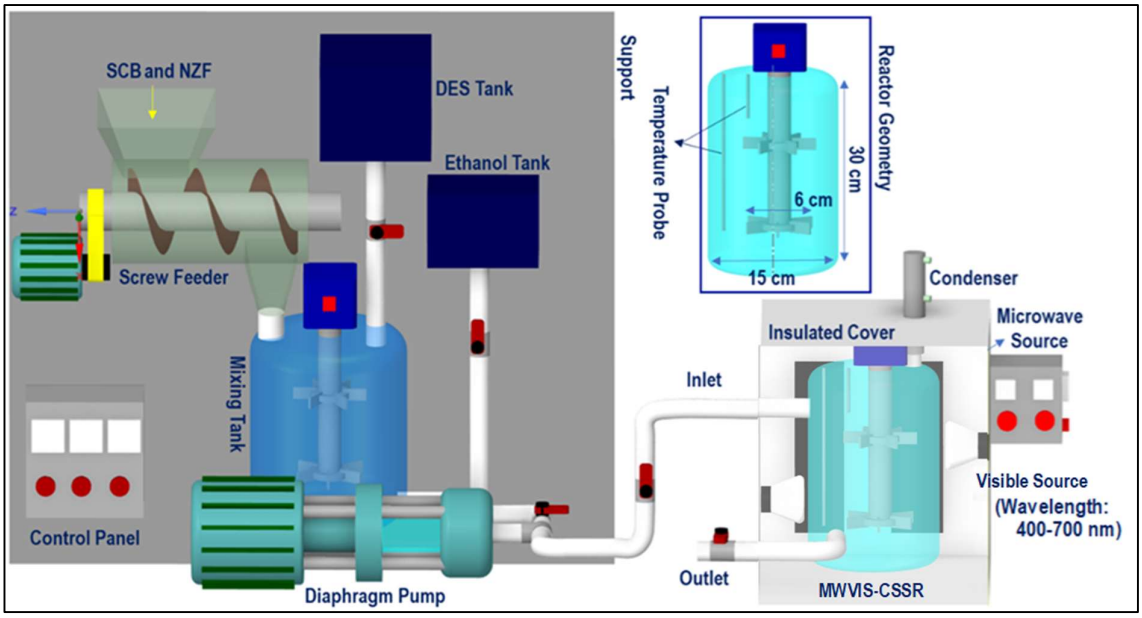

Figure 5. 19. Continuous EL synthesis process in MWVIS-CSSR

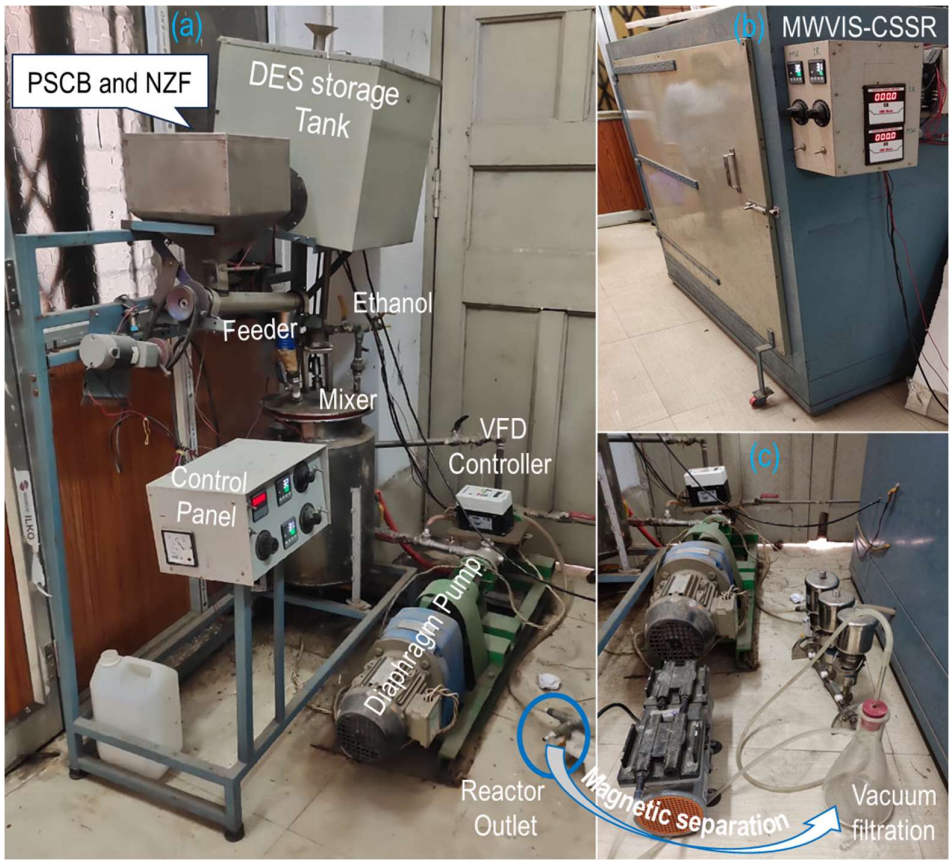

Figure 5. 20. Experimental setup of (a) screw feeder, mixer, diaphragm pump and VFD controller (b) MWVIS-CSSR (c) vacuum filtration unit

5.6.5. Plausible reaction mechanism and kinetic model formation

The plausible reaction pathways for the synthesis of EL from PSCB under optimal reaction conditions are shown in scheme-1. The PSCB to EL conversion reaction initiated with hydrolysis step where PSCB depolymerized to release hexose (glucose and mannose monomers) and pentose (mainly xylose monomer) with the aid of hydrogen bond donor–acceptor complexes of the acidic DES and Lewis acidic sites of NZF photocatalyst. Afterwards, 5EMF was formed from hexose and pentose (not shown in the scheme-1), which may follow two possible routes. In route-1, glucose and mannose were first alcoholised, yielding EDGP, which were then dehydrated to generate 5EMF. In route-2, glucose and mannose were first isomerized to produce fructose, followed by dehydration to produce 5HMF and subsequently, the 5HMF was alcoholised to yield 5EMF. Finally, the produced 5EMF further alcoholised and produced EL and Ethyl formate (EF).

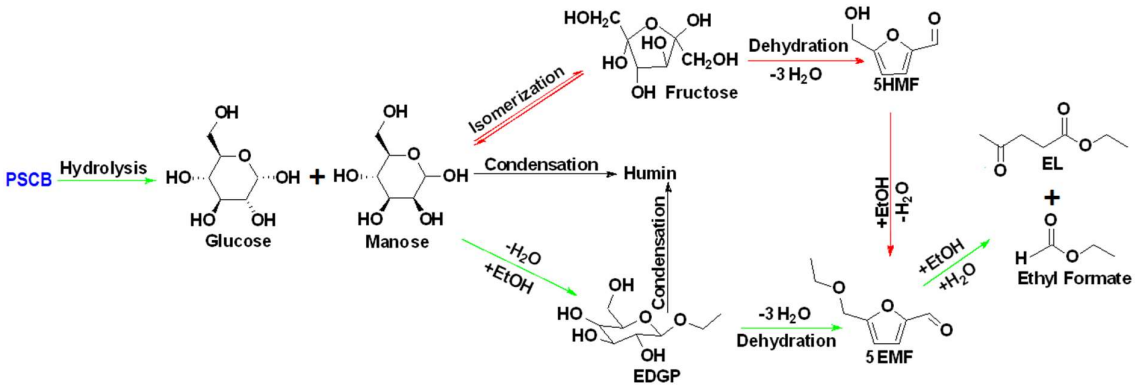

Scheme-1. Possible reaction pathway for EL synthesis from PSCB (green colour represents route-1 and red colour represents route-2)

During experimental kinetic study of the continuous EL synthesis process, EDGP, 5EMF, EL, and EF were identified as the main generated products. Additionally, glucose and 5HMF were detected in trace amount in the product mix. Based on the above results, it was assumed that formation of EDGP form glucose or mannose takes place rapidly and the overall reaction pathway primarily follow route-1 [31]. Moreover, formation of humin was also observed under optimized process conditions. Thus, the continuous PSCB to EL conversion process employing NZF and DES2 was simplified as Figure 5.21.

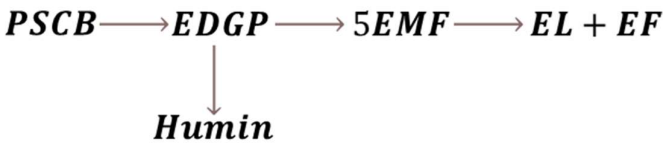

Figure 5. 21. Simplified reaction kinetics of EL synthesis from PSCB

Notably, during experimental investigation, it was observed that under non-catalytic conditions (without NZF and DES), PSCB underwent partial conversion to EDGP in MWVIS-CSSR. Furthermore, in the presence of both homogeneous acidic DES and heterogeneous NZF photocatalyst, PSCB was observed to convert to EL through parallel pathways, including both homogeneous and heterogeneous processes. Consequently, the overall rate of PSCB conversion ($-r_{PSCB}$) process was formulated by combining the non-catalytic ($-r_{NC}$), homogeneous catalytic ($-r_{H1}$) and heterogenous catalytic ($-r_{Ht}$) conversion rate of PSCB. Notably, in formulating the rates for non-catalytic and homogeneous catalytic conversion, a pseudo-homogeneous irreversible first-order kinetic model was assumed, while for heterogeneous catalytic conversion of PSCB, the Eley-Rideal heterogeneous kinetic model was applied. In

formulating Eley-Rideal heterogeneous kinetic model, it was assumed that only ethanol was adsorbed on the NZF photocatalyst's surface (average surface pore size of the NZF: 48 nm, from Brunauer–Emmett–Teller (BET) analysis) and surface reaction was the rate controlling step.

$$-r_{PSCB} = -[r_{NC} + r_{H1} + \rho_{NZF}\, r_{Ht1}] \quad (5.34)$$

$$\text{Or, } -r_{PSCB} = k_{NC}C_{PSCB} + k_{H1}C_{PSCB} + \rho_{NZF}\frac{k_{Ht1}C_E}{1+K_{A1}C_E+K_{D1}C_{EDGP}} \quad (5.35)$$

Accordingly, the formation rate of EDGP (Equation-5.36), 5EMF (Equation-5.37), EL (Equation-5.38) and humin (Equation-39) were also formulated by considering homogeneous pseudo first order kinetic model and heterogeneous Eley-Rideal kinetic model. Notably, the product yields were calculated based on the holocellulose present in the PSCB.

$$r_{EDGP} = k_{NC}C_{PSCB} + k_{H1}C_{PSCB} - k_{H2}C_{EDGP} - k_{H3}C_{EDGP} + \rho_{NZF}[\frac{k_{Ht1}C_E}{1+K_{A1}C_E+K_{D1}C_{EDGP}} - \frac{k_{Ht2}C_{EDGP}}{1+K_{A2}C_{EDGP}+K_{D2}C_{5EM}}] \quad (5.36)$$

$$r_{5EM} = k_{H2}C_{EDGP} - k_{H4}C_{5EMF} + \rho_{NZF}[\frac{k_{Ht2}C_{EDGP}}{1+K_{A2}C_{EDGP}+K_{D2}C_{5EMF}} - \frac{k_{Ht3}C_{5EMF}}{1+K_{A3}C_{5EMF}+K_{D3}C_{EL}}] \quad (5.37)$$

$$r_{EL} = k_{H4}C_{5EMF} + \rho_{NZF}\frac{k_{Ht3}C_{5EM}}{1+K_{A3}C_{5EMF}+K_{D3}C_{EL}} \quad (5.38)$$

$$r_{Humin} = k_{H3}\, C_{EDGP} \quad (5.39)$$

Here C_{DSB} represent the concentration (mol/l) of holocellulose in PSCB whereas, C_E, C_{EDGP}, C_{5EMF}, C_{EF}, C_{Humin} and C_{EL} denote the concentration of ethanol, EDGP, 5EMF, EF, humin and EL, respectively. The NZF photocatalyst bulk density was denoted by ρ_{NZF} (g/l). The non-catalytic rate constant (min^{-1}) was represented by k_{NC} whereas homogeneous catalytic rate constants (min^{-1}) for PSCB, EDGP, 5EMF conversion processes were denoted by k_{H1}, k_{H2}, k_{H4}. The heterogeneous catalytic rate constants (g. of NZF^{-1} min^{-1}) for PSCB, EDGP and 5EMF conversion processes were denoted by k_{Ht} , k_{Ht2}, k_{Ht3}. The adsorption equilibrium constants are represented by K_{A1}, K_{A2}, K_{A3} and the desorption equilibrium constants are denoted by K_{D1}, K_{D2}, K_{D3} respectively.

Finally, the observed rate of conversion or formation of each species were determined employing the CSSR design equation (Equation-5.40) and the kinetic parameters of the

formulated kinetic model equations (Equation-5.35 to 5.39) at different temperatures were evaluated.

$$r_i = \frac{\vartheta_{Slurry}\,(C_i - C_{io})}{V_{CSSR}} \qquad (5.40)$$

Here, V_{CSSR} denotes the volume of CSSR and ϑ_{SLURRY} represents the volumetric slurry flowrate. The C_i and C_{io} represents the final and initial concentration of the i^{th} species, respectively. The activation energies of different reaction steps were calculated according to Arrhenius equation.

$$k_i = A_{oi} e^{\left(-\frac{E_i}{RT}\right)} \qquad (5.41)$$

Here T represents the reaction temperatures while E_i (kJ / mol) and A_{oi} are the activation energy and pre-exponential factor respectively. R is the universal gas constant (8.31×10^{-3} kJ / mol K). The kinetic parameters were estimated by fitting experimental kinetic data using the *fminsearch* algorithm in the MATLAB R2014a software.

5.6.6. EL-Biodiesel-Diesel blending and engine performance of blended fuels

The continuously generated EL was isolated, purified, and then blended with B10 (90 vol % diesel and 10 vol % biodiesel) and B20 (80 vol % diesel and 20 vol % biodiesel) at concentrations of 5% and 10%. Afterwards, the characteristics of the synthesized EL and the resulting blended fuels (EL5B10, EL10B10, EL5B20, EL10B20) were examined (Table 5.27). From Table 5.27, it was observed that the EL blended fuels (EL5B10, EL10B10, EL5B20, EL10B20) showed enhanced characteristics, with a 3-6°C higher flash point and a 1-3°C lower cloud point compared to B10 and B20. After property estimation, a four-stroke diesel engine (553 cc cylinder and 3.7 kW power output) was employed to assess the performance of the blended fuels and the exhaust emissions at engine speed ranged from 1000 to 1500 rpm were examined using an exhaust gas analyser with measurement capabilities for CO (0–15%), HC (0–20,000 ppm), CO_2 (0–20%), and NOx (0–5000 ppm).

Table 5. 27. EL-Biodiesel-Diesel blending fuel properties

Properties	EL	B10	B20	EL5B10	EL10B10	EL5B20	EL10B20
EL blending (vol %)	100	0	0	5	10	5	10
Flash point (°C)	89	71	73	74	76	78	79
Cetane number	5	49.7	51	49.2	48	47.5	46.3

Cloud point (°C)	not determined	-3	-2	-3	-4	-3	-5
Calorific value (J/g)	19146	44275	43825	43018	41762	42591	41357

[B10: 90 vol % diesel-10 vol % biodiesel; B20: 80 vol % diesel-20 vol % biodiesel; EL5B10: 95 vol % B10-5 vol % EL; EL10B10: 90 vol % B10-10 vol % EL; EL5B20: 95 vol % B20-5 vol % EL; EL10B20: 90 vol % B20-10 vol % EL]

5.6.7. EL synthesis process sustainability analysis

To assess the overall sustainability of the EL synthesis process from sugarcane bagasse (SCB) under MWVIS, both techno-economic and environmental impact analyses were conducted and compared with individual irradiation systems. Cañon et al. [32] recently investigated the techno-economic analysis of EL production from Colombian rice straw at a processing capacity of 2000 kg/h. Thus, for techno-economic analysis of the SCB to EL conversion process, as outlined in the current study, was upscaled to a 2000 kg/h processing capacity and simulated in Aspen Plus software. Following the techno-economic assessment, the environmental impacts associated with the upscaled process was examined using OpenLCA software.

5.6.7.1.Process scale-up and economic analysis

For techno-economic analysis, the SCB to EL conversion process was subdivided into four sections and modelled as four hierarchy blocks viz., SCB PRETREATMENT, DES PREPARATION, EL PRODUCTION and PRODUCT PURIFICATION using Aspen Plus software. During simulation of SCB PRETREATMENT hierarchy block, the SCB, containing 10% moisture, was modelled as cellulose, hemicellulose and lignin content. Additionally, information of the missing properties such as solid molar volume, solid heat capacity of cellulose, humin (insoluble solid) and lignin was collected from ASPEN PLUS INHSPCD (NREL Biofuels) databank [33]. Notably, the screw feeder setup utilised in the current study was modelled as pneumatic feeder during aspen plus simulation, where air was used to convey the solid PSCB-NZF mixture. In the simulation of the EL PRODUCTION hierarchy block, the MWVIS-CSSR was modelled as custom CSTR with the help of ASPEN CUSTOM MODELER, where the estimated kinetic parameters of EL synthesis process were used to simulate the PSCB to EL conversion process.

Non-Random Two-Liquid with Redlich-Kwon (NRTL-RK) model was considered as the primary thermodynamic package for phase equilibrium and thermodynamic calculations.

However, in order to successfully simulate the PRODUCT PURIFICATION block in Aspen Plus, we chose to utilize the COSMO-SAC property model for estimating activity coefficients, due to the absence of binary interaction parameters for DES2 with other components in the simulation. The COSMO data (sigma (σ) profile) for individual components (Figure 5.22) were determined through density functional theory (DFT) calculations carried out in the DMOL3 module of the Material Studio software [34].

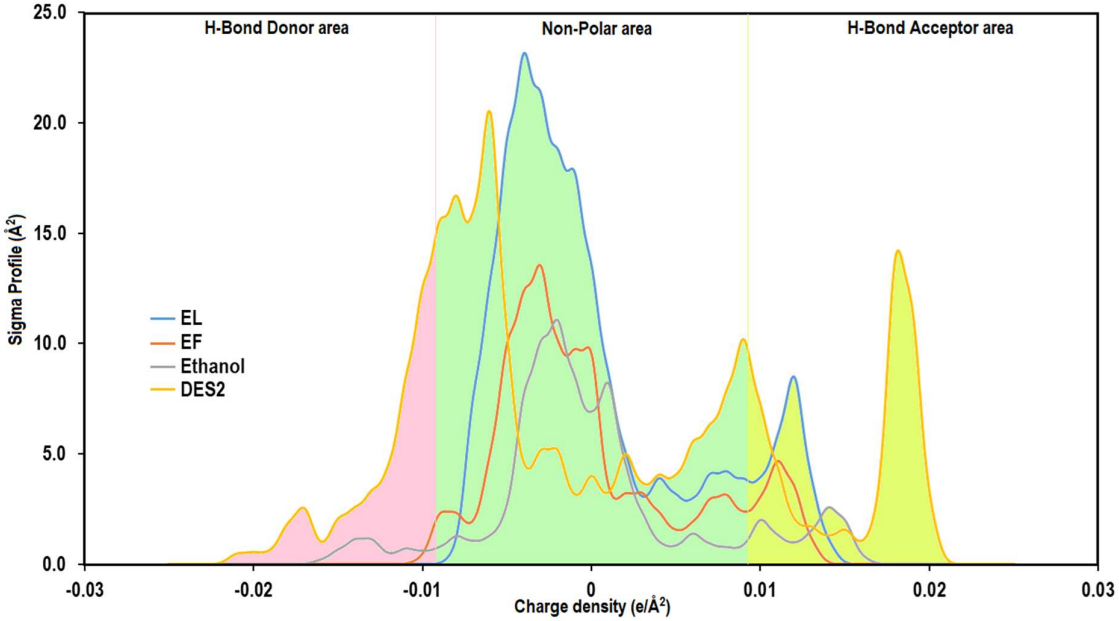

Figure 5. 22. Sigma profile of EL, EF, ethanol and DES2

After successfully simulating the EL conversion process, economic analysis of the plant was conducted using Aspen Plus Economic Analyzer, considering a 20-year plant life and a one-year construction period. Table 5.28. displays the prices of the individual feed stream, utility stream, waste stream, product, and byproduct stream. The price of NaOH (www.echemi.com), peroxy-acetic acid (www.echemi.com), oxalic acid (www.chemanalyst.com), EF (www.indiamart.com) were collected from various sources. Notably, the equipment cost of the MWVIS-CSSR was determined by combining the cost of a closed agitated tank with a similar capacity and an additional cost for MW and VIS generator units. The average reported cost of 100 kW microwave generators typically varies between 75000 and 100000 US$ depending on various design parameters [35]. Therefore, in the MWVIS-CSSR equipment cost calculation, a cost of 1000 US$ per kW for 915 MHz MW generator was considered. Similarly, the equipment cost calculation for the MWVIS-CSSR included a pricing of 1000 US$ per kW for the VIS source [36].

Table 5. 28. Price of the individual feed, utility, product and byproduct streams

Stream	Stream Type	Price (US$/kg)	Reference
SCB	Feed stream	0.024	[31]
Ethanol	Feed stream	0.903	[32]
NaOH	Feed stream	0.212065	
Peroxy-acetic acid	Feed stream	0.344505	
ChCl	Feed stream	0.77	
Oxalic acid	Feed stream	0.56	
Electricity	Utility stream	0.19 (US$/kWh)	[32]
Cooling water	Utility stream	0.001318	[32]
Medium pressure steam	Utility stream	0.008627	[32]
EL	Product stream	3	[32]
EF	Byproduct stream	2.16	
Lignin	Byproduct stream	0.5	[37]
Sodium acetate	Byproduct stream	0.545	[38]
Humin	Waste stream	-0.04	[39]

5.6.7.2.Environmental impact assessment

After economic analysis, the environmental impacts associated with the EL synthesis process was analysed using OpenLCA 1.9 software. Additionally, the environmental impacts related to specific irradiation systems were scrutinized to comprehend the influence of energy consumption in both MW and VIS irradiation systems on the overall environmental footprint. To explore these impacts, a gate-to-gate life cycle assessment (LCA) approach was utilized, where the system boundary (Figure 5.23; 1st system boundary) encompasses the transport of raw materials, the pretreatment of waste SCB, the preparation of DES, and the synthesis and purification process of EL. In the context of transportation, it was assumed that the transportation of all raw materials would cover a distance of 100 kilometres using a 16 metric ton truck equipped with a EURO VI engine. Additionally, the waste humin generated in EL synthesis process was considered to be managed through hazardous waste treatment, specifically underground deposition. It is noteworthy that all electric energy employed in the operation was considered to dissipate into the atmosphere as waste heat [28]. Moreover, to

identify the optimum EL blending ratio in B10 and B20, environmental impacts analysis for each blend were also performed employing the engine exhaust emission data though gate to grave approach (Figure 5.23; 2nd system boundary).

The life cycle inventory (LCI) database was prepared based on the Aspen plus simulated data of the upscaled EL synthesis process. "ReCiPe Midpoint (H)" life cycle analysis methodology [30] with Ecoinvent-3.5 database was used to assess and evaluate the potential environmental impact indicators associated with the EL synthesis process. During LCA analysis, physical allocation was considered for the multioutput processes and LCA results were normalized based on "World ReCiPe H" normalization and weighting factor.

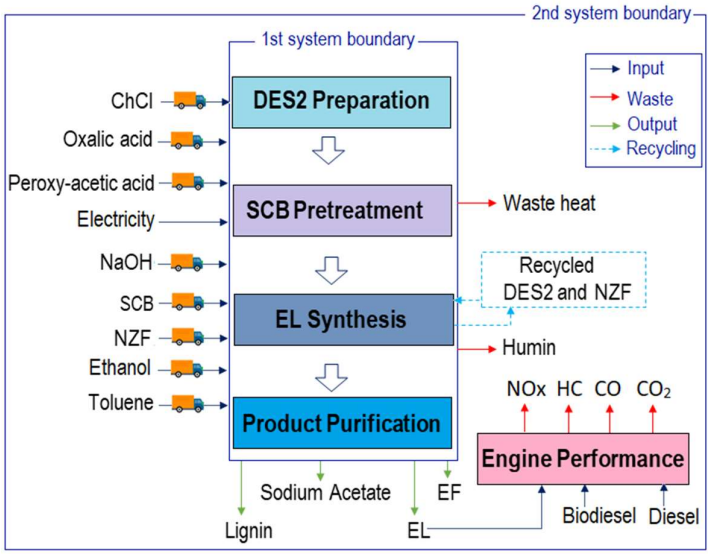

Figure 5. 23. System boundary for LCA analysis of SCB to EL conversion process and EL blended fuels

5.7. Reference

1. Hemmann, F.; Agirrezabal-Telleria, I.; Jaeger, C.; Kemnitz, E.; Quantification of acidic sites of nanoscopic hydroxylated magnesium fluorides by FTIR and 15N MAS NMR spectroscopy. RSC Adv. 2015, 5, 89659
2. Mittal, M.; Sharma, M.; Pandey, O.P. UV–Visible light induced photocatalytic studies of Cu doped ZnO nanoparticles prepared by co-precipitation method. Solar. Energy.2014, 110, 386–397
3. Miller, G.L. Use of Dinitrosalicylic Acid Reagent for Determination of Reducing Sugar. Anal. Chem. 1959, 31, 426–428.
4. Saeman JF. Kinetics of wood saccharifications hydrolysis of cellulose and decomposition of sugars in dilute acid at high temperature. Ind Eng Chem. 1945;37:43-52.
5. Negahdar L, Delidovich I, Palkovits R. Aqueous-phase hydrolysis of cellulose and hemicelluloses over molecular acidic catalysts: insights into the kinetics and reaction mechanism. Appl Catal B Environ. 2016; 184:285-298.
6. Salmi T, Murzin DY, Arvela PC, et al. Kinetic modeling of hemicellu lose hydrolysis in the presence of homogeneous and heterogeneous catalysts. AIChE J. 2014;60:1066-1077.
7. Ali SH. Kinetics of catalytic esterification of propionic acid with different alcohols over Amberlyst 15. Inc. Int J Chem Kinet. 2009;41:432-448.
8. Chatterjee S, Barman S, Chakraborty R. Far infrared radiated energy-proficient rapid one-pot green hydrolysis of waste watermelon peel: optimization and heterogeneous kinetics of glucose synthesis. RSC Adv. 2016; 6: 74278-74287.
9. Arkell A, Olsson J, Wallberg O. Process performance in lignin separation from softwood black liquor by membrane filtration. Chemical Engineering Research and Design. 2014; 92(9):1792-800.
10. Viles Jr FJ, SilvermanL. Determination of Starch and Cellulose with Anthrone. Anal. Chem.1949; 21 (8): 950–953.
11. Sluiter A, Hames B, Ruiz R, Scarlata C, Sluiter J, Templeton D, Crocker D. Determination of structural carbohydrates and lignin in biomass. Laboratory analytical procedure. 2008; 1617:1-6.
12. Lee KM, Ngoh GC, Chua ASM. Ionic liquid-mediated solid acid saccharification of sago waste: kinetic, ionic liquid recovery and solid acid catalyst reusability study. Ind. Crop. Prod. 2015;77: 415–423.
13. Rinaldi R, Meine N, Stein JV, Palkovits R, Schuth F. Which Controls the Depolymerization of Cellulose in Ionic Liquids: The Solid Acid Catalyst or Cellulose? Chem Sus Chem. 2010; 3: 266 – 276.
14. Gao X, Kumar R, Singh S, Simmons BA, Balan V, Dale BE, Wyman CE. Comparison of enzymatic reactivity of corn stover solids prepared by dilute acid, AFEX™, and ionic liquid pretreatments. Biotechnol biofuels. 2014;7(1):71.

15. Suzuki S, Takeoka Y, Rikukawa M, Yoshizawa-Fujita M. Brønsted acidic ionic liquids for cellulose hydrolysis in an aqueous medium: structural effects on acidity and glucose yield. RSC Adv. 2018; 8(26):14623-32.
16. Li J, Xu Y, Zhang M, Wang D. Determination of furfural and 5-hydroxymethylfurfural in biomass hydrolysate by high-performance liquid chromatography. Energ Fuel. 2017; 31(12):13769-74.
17. Cha JH, Choi HH, Jung YG, Choi SC, An GS. Novel synthesis of core–shell structured Fe3O4@ SiO2 nanoparticles via sodium silicate. Ceram Int. 2020.
18. Ghanbari D, Salavati-Niasari M, Ghasemi-Kooch M. A sonochemical method for synthesis of Fe3O4 nanoparticles and thermal stable PVA-based magnetic nanocomposite. J Ind Eng Chem. 2014; 20(6):3970-4.
19. Furukawa H, Kikuchi A, Noriyasu A, Bouteau F, Nishihama S, Yoshizuka K, Li X, Kawano T. Use of liquefied dimethyl ether for the extraction of proteins from vegetable tissues. Solvent Extr Res Dev, Japan. 2016; 23(1):127-35.
20. Bello S, Salim I, Méndez-Trelles P, Rodil E, Feijoo G, Moreira MT. Environmental sustainability assessment of HMF and FDCA production from lignocellulosic biomass through life cycle assessment (LCA). Holzforschung. 2018; 73(1):105-15.
21. Caramazana-Gonzalez P, Dunne PW, Gimeno-Fabra M, Zilka M, Ticha M, Stieberova B, Freiberg F, McKechnie J, Lester EH. Assessing the life cycle environmental impacts of titania nanoparticle production by continuous flow solvo/hydrothermal syntheses. Green Chem. 2017, 19(6) :1536-47.
22. Wu F, Zhou Z, Hicks AL. Life cycle impact of titanium dioxide nanoparticle synthesis through physical, chemical, and biological routes. Environ. Sci. Technol. 2019, 53(8):4078-87.
23. Vashistha P, Singh SK, Dutt D, Kumar V. Synthesis of nanosilica from fly ash and its utilization with lime sludge in concrete: an environmentally friendly and sustainable solution. Clean Technol Envir. 2019; 21(9):1841-53.
24. Cybularczyk-Cecotka M, Szczepanik J, Giedyk M. Photocatalytic strategies for the activation of organic chlorides. Nature Catalysis. 2020 Nov;3(11):872-86.
25. H.S. Fogler, Essentials of Chemical Reaction Engineering, Essenti Chemica Reactio Engi, Pearson Education, 2010.
26. Atanda L, Konarova M, Ma Q, Mukundan S, Shrotri A, Beltramini J. High yield conversion of cellulosic biomass into 5-hydroxymethylfurfural and a study of the reaction kinetics of cellulose to HMF conversion in a biphasic system. Catalysis Science & Technology. 2016;6(16):6257-66.
27. Bose D, Barman S, Chakraborty R. Sustainable development of inexpensive visible-range CuO-TiO2 nano-photocatalysts deploying in situ recovered glass fiber and Cu(CH3COO)2 from waste printed wiring board: Optimal lignin photo-degradation for valuable products, Sustainable Materials and Technologies, 2020, 24, e00162.

28. Wu F, Zhou Z, Hicks AL. Life cycle impact of titanium dioxide nanoparticle synthesis through physical, chemical, and biological routes. Environmental science & technology. 2019 Mar 26;53(8):4078-87.
29. Kumar R, Hu F, Hubbell CA, Ragauskas AJ, & Wyman CE (2013). Comparison of laboratory delignification methods, their selectivity, and impacts on physiochemical characteristics of cellulosic biomass. Bioresour. Technol. 130: 372-381.
30. Pradhan P, Karan P, & Chakraborty R (2021). Life cycle sustainability assessment of optimized biodiesel production from used rice bran oil employing waste derived-hydroxyapatite supported vanadium catalyst. Environ. Sci. Pollut. Res. 1-14.
31. Lilonfe S, Dimitriou I, Davies B, Abdul-Manan AF, McKechnie J. Comparative techno-economic and life cycle analyses of synthetic "drop-in" fuel production from UK wet biomass. Chem. Eng. J. 2024; 479:147516.
32. Cañon C, Sanchez N, Cobo M. Life cycle inventory data for ethyl levulinate production from Colombian rice straw. Data in Brief. 2022; 45:108681.
33. Wooley RJ, Putsche V. Development of an ASPEN PLUS physical property database for biofuels components. National Renewable Energy Lab. (NREL), Golden, CO (United States); 1996.
34. De Riva J, Ferro VR, Moreno D, Diaz I, Palomar J. Aspen Plus supported conceptual design of the aromatic–aliphatic separation from low aromatic content naphtha using 4-methyl-N-butylpyridinium tetrafluoroborate ionic liquid. Fuel. Process. Technol. 2016; 146:29-38.
35. Hasna A. Microwave processing applications in chemical engineering: Cost analysis. J. Appl. Sci. 2011; 11: 3613–3618.
36. Baum H, Geissler T, Westerkamp U. Cost-benefit and break-even analysis of xenon headlights in Germany and in EU-27. Zeitschrift fur Verkehrswissenschaft. 2009; 80(2):118.
37. Ľudmila H, Michal J, Andrea Š, Aleš H. Lignin, potential products and their market value. Wood Res. 2015; 60(6):973-86.
38. Englmair G, Kong W, Berg JB, Furbo S, Fan J. Demonstration of a solar combi-system utilizing stable supercooling of sodium acetate trihydrate for heat storage. Appl. Therm. Eng. 2020; 166:114647.
39. Davis R, Tao L, Tan EC, Biddy MJ, Beckham GT, Scarlata C, Jacobson J, Cafferty K, Ross J, Lukas J, Knorr D. Process design and economics for the conversion of lignocellulosic biomass to hydrocarbons: dilute-acid and enzymatic deconstruction of biomass to sugars and biological conversion of sugars to hydrocarbons. National Renewable Energy Lab. (NREL), Golden, CO (United States); 2013.

CHAPTER VI: RESULTS AND DISCUSSIONS

6.1. Activity 1:

PRINTED CIRCUIT BOARD DERIVED GLASS FIBER-EPOXY RESIN-SUPPORTED MO−CU BIMETALLIC CATALYST FOR GLUCOSE SYNTHESIS

6.1.1. Effects of process parameters on pretreated WJF hydrolysis process

Table 6.1 represents individual ranks of process parameter affecting response parameter (G_{NIRR}) based on Δ-values and S/N ratios; where, the factor corresponding to maximum Δ-value has been ranked one. Furthermore, from analysis of variance (Table 6.2) for pretreated WJF hydrolysis process, it can be observed that the hydrolysis temperature ($\phi_{T_{NIRR}}$) and Mo precursor loading (ϕ_{NIRRMo}) were statistically significant process variables at 95% confidence level (p-value < 0.05). Thus, from Table 6.1 & 6.2 it was concluded that L_0 of ϕ_{NIRRMo} (1.0 wt. %), L_0 of ϕ_{MoC} (5 wt. %), L_1 of $\phi_{T_{NIRR}}$ (80 °C), and L_{-1} of $\phi_{t_{NIRR}}$ (10 min) were the optimum process values rendering maximum glucose yield (75.84 mol %).

Table 6. 1. S/N ratios and Δ of process parameters in pretreated WJF hydrolysis

Level	$\boldsymbol{\phi_{NIRRMo}}$ (wt. %)	$\boldsymbol{\phi_{MoC}}$ (wt. %)	$\boldsymbol{\phi_{T_{NIRR}}}$ (°C)	$\boldsymbol{\phi_{t_{NIRR}}}$ (min)
L_{-1}	34.45	35.33	34.80	35.75*
L_0	36.40*	36.02*	35.77	35.73
L_1	36.36	35.85	36.63*	35.72
Delta (**Δ**)	1.95	0.70	1.83	0.03
Rank	1	3	2	4

Larger is better

Table 6. 2. Analysis of variance (ANOVA) of factors affecting WJF hydrolysis process

Source	DF	Adjusted Sum of square	Adjusted mean Square	F value	P value
$\boldsymbol{\phi_{NIRRMo}}$	1	244.482	244.482	8.53	0.043
$\boldsymbol{\phi_{MoC}}$	1	11.648	11.648	0.41	0.559
$\boldsymbol{\phi_{T_{NIRR}}}$	1	244.099	244.099	8.51	0.043
$\boldsymbol{\phi_{t_{NIRR}}}$	1	4.051	4.051	0.14	0.726
Error	4	114.678	28.670		
Total	8	618.958			

6.1.2. Interactive effects of process parameters on pretreated WJF hydrolysis

Parametric interaction for the pretreated WJF hydrolysis process was depicted in Figure 6.1. Interaction between Mo loading and catalyst concentration (remaining two parameters at optimum level) revealed that an increment in Mo precursor loading resulted in higher glucose yield (G_{NIRR}) [Figure 6.1(a)] at all level of catalyst concentration, which clearly suggested that the prepared Mo-Cu impregnated GFER catalyst immensely favoured pretreated WJF conversion. A similar trend was observed for all values of catalyst concentration. From, Figure 6.1(b) it can be conclude that the hydrolysis process was endothermic in nature as hydrolysis temperature monotonically enhance G_{NIRR}. On the other hand, hydrolysis time has an antagonistic effect on G_{NIRR} due to the degradation of glucose at higher hydrolysis time Figure 6.1(e). Extended hydrolysis times can lead to glucose degradation, negatively impacting yield. This underscores the importance of optimizing reaction duration to balance complete hydrolysis with minimal product degradation. Similar challenges have been noted in other studies [1], where prolonged reaction times resulted in decreased glucose yields due to degradation. The individual parametric effect on G_{NIRR} has been presented in the Figure 6.2.

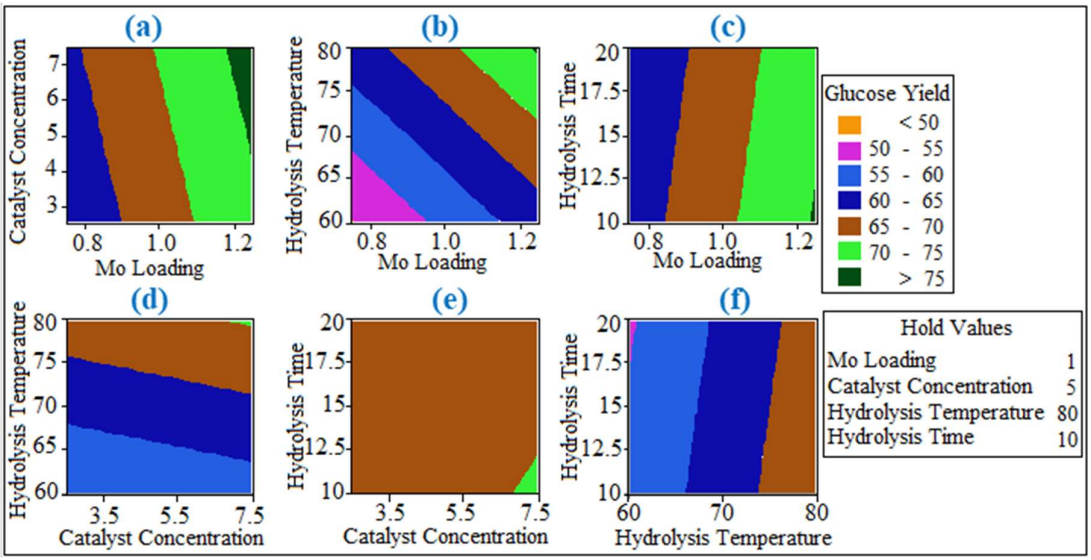

Figure 6. 1. Interaction plots for pretreated WJF hydrolysis process parameters

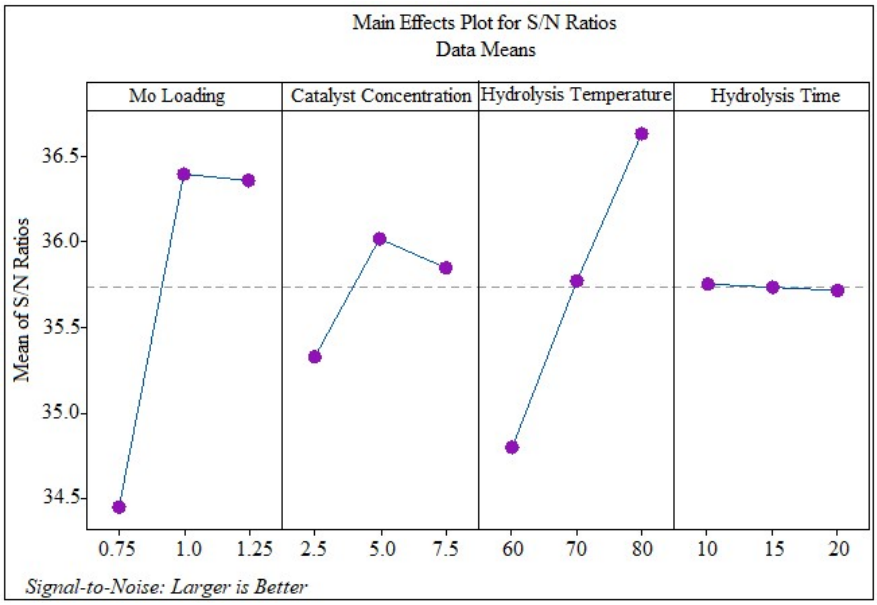

Figure 6. 2. Main effect plots for pretreated WJF hydrolysis process

6.1.3. *Catalyst characterization*

6.1.3.1. Thermogravimetric (TGA) analysis

TGA patterns (Figure 6.3.) of WPCB powder, GFER, CCu-Mo$^{1.0}$ and NCu-Mo$^{1.0}$ manifests the thermal stability and decomposition of samples on heating over a range of temperature from 30 °C to 500 °C. TGA thermogram of WPCB and GFER shows a major weight loss (35 %) over 280–450 °C ascribing to the degradation of epoxy resin. Furthermore, thermal decomposition of GFER was faster compared to WPCB powder due to chemical treatment (showed in FTIR). On the other hand, relatively less weight loss was occurred in NCu-Mo$^{1.0}$ and CCu-Mo$^{1.0}$ due to the ionic polymerization of epoxy resin. Moreover, the TGA plot of the NCu-Mo$^{1.0}$, reveals a weight loss of 2 wt.% over 220–250 °C; which corresponds to the decomposition of the Mo precursor salt i.e., $CH_3COCH=C(O-)CH_3]_2MoO_2$ (decomposition temperature 228-229°C) that lead to liberation of carbon oxides, acetone, methane and isobutene [2]. Notably, NCu-Mo$^{1.0}$ shows better thermal stability compared to the CCu-Mo$^{1.0}$ which reveals better thermal activation of NIRR over conventional hydrothermal treatment in catalyst preparation. Thus, 240 °C was selected as the calcination temperature to prepare GFER supported Cu-Mo catalyst to avoid degradation of epoxy resin. Notably, as the hydrolysis temperature was appreciably low (60 °C–80 °C) than calcination temperature; thermal decomposition of the developed catalysts is unlikely during hydrolysis process.

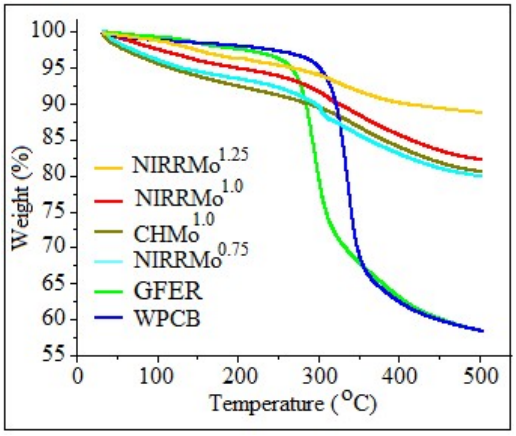

Figure 6. 3. TGA analysis of WPCB, GFER (without Mo loading), NCu-$Mo^{0.75}$, NCu-$Mo^{1.0}$ NCu-$Mo^{1.25}$ and CCu-$Mo^{1.0}$

6.1.3.2. X-Ray diffraction (XRD) analysis

Figure 6.4. depicts XRD patterns for GFER powder and calcined samples [Mo free GFER, NCu-$Mo^{0.75}$, NCu-$Mo^{1.0}$, NCu-$Mo^{1.25}$ and CCu-$Mo^{1.0}$]. Peaks representing the crystalline phase of copper oxide (37.264°, 43.303°,48.799°) (JCPDS 00-048-1548) [3], molybdenum trioxide (MoO_3) (13.76°) (JCPDS 00-005-0503) [4] and molybdenum-di-silicide ($MoSi_2$) (29.94°) were detected for all catalysts. Diffraction patterns evidence the presence of copper (43.28°, 50.39°, 74.12°) [3] in GFER powder which attributes to the existence of the copper oxide in all catalysts and calcined Mo free GFER samples. Notably, with increasing $CH_3COCH{=}C(O\text{-})CH_3]_2MoO_2$ loading (Figure 6.4) the prominence of MoO_3 and $MoSi_2$ peaks were gradually increases in NCu-Mo catalyst which in terns increases the acidity of the catalyst. Furthermore, presence of a more intense peak of MoO_3 was also found in NCu-$Mo^{1.0}$ and NCu-$Mo^{1.25}$ compared to CCu-$Mo^{1.0}$.

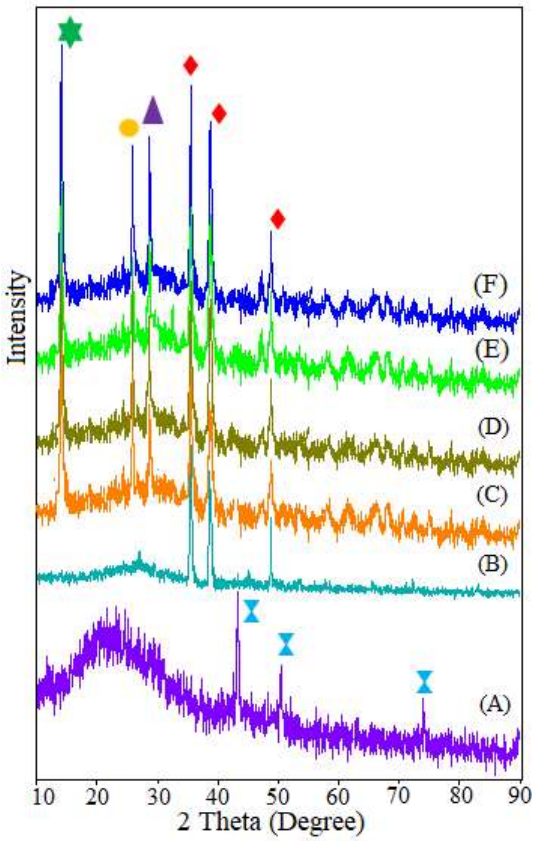

Figure 6. 4. Powder XRD pattern of (a) GFER powder (b) Mo free Calcined GFER powder (c) NCu-Mo0.75 (d) CCu-Mo1.0 (e)NCu-Mo1.0 (f) NCu-Mo1.25 [characteristic peaks due to CuO (♦), MoO_3 (★), $MoSi_2$ (▲),SiO_2 (●), Cu (⧗)]

6.1.3.3. Fourier-Transform infrared spectroscopy (FTIR)

FTIR analysis of GFER and all catalysts sample shows prominent peaks of OH stretching located at 3568.12 cm^{-1} due to the formation of hydroxyl-containing silanol groups which signifies the porous structure of the samples (Figure 6.5) [5]. Vibrations regarding C-H stretch of aromatic and alkane groups are observed at wavelengths 3058.89 cm^{-1} and 2970.13 cm^{-1} respectively. Other adsorption peak at 1454 cm^{-1} and 1510.41 cm^{-1} also assigned to stretching vibration of C-C and C-H bands of alkane and aromatic groups respectively. On other hand, intensity of the strong band located at 2970.13 cm^{-1} in the GFER support has been significantly reduced after calcination at 240°C (Figure 6.5 (a)). Furthermore, reduction of absorption peaks at 1760.23 cm^{-1} and1660.65 cm^{-1} (symmetric stretching of the epoxy ring) for catalyst samples, suggesting the ring-opening cleavage of the epoxy groups by $CH_3COCH{=}C(O\text{-})CH_3]_2MoO_2$ [6]. Furthermore, the vibration at 996.71 cm^{-1} in catalyst samples indicates the presence if Mo which gradually increase with Mo precursor loading [7].

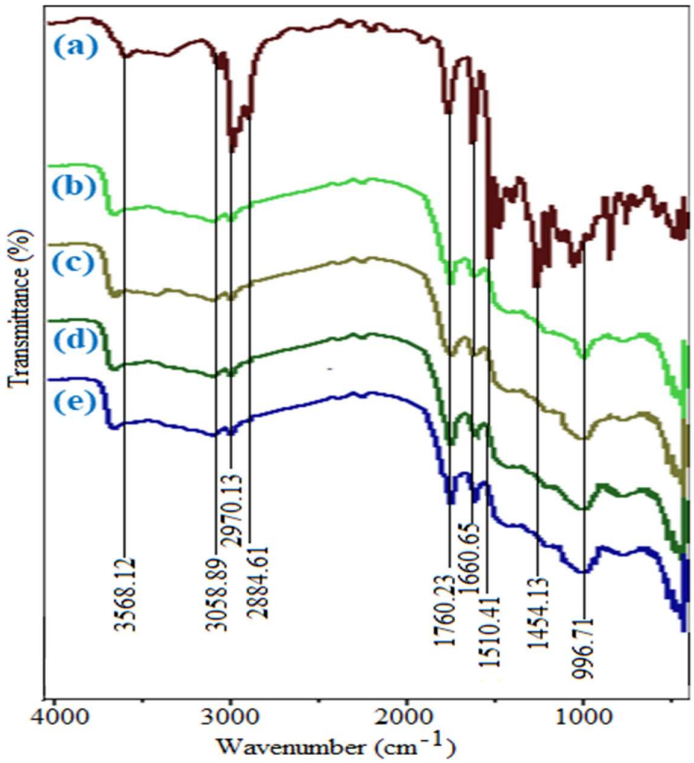

Figure 6. 5. FTIR analysis of (a) GFER (b) NCu-Mo$^{0.75}$ (c) CCu-Mo$^{1.0}$ (d) NCu-Mo$^{1.0}$ (e) NCu-Mo$^{1.25}$

6.1.3.4. NH_3-TPD analyses

Figure 6.6 shows several NH_3-TPD peaks within the temperature range of 150-260°C for catalyst and calcined GFER samples. Presence of weak acidic sites in all samples at 215°C is ascribed to Cu^{2+} ions [8]; whereas, acidic peaks positioned above 235°C have been assigned to Mo^{6+} ions [9]. Moreover, with Mo precursor loading, presence of new acidic-site peaks was observed in all catalyst sample, whose intensity increases with Mo precursor loading up to 1.0 wt. %. Decrease in acidity of NCu-Mo$^{1.25}$ catalyst may be due to substantial loss of Bronsted acidic sites on GFER surface; as Mo^{6+} replaces the Bronsted acidic sites [10]. Notably, at 1.0 wt.% and 1.25 wt.% precursor loading NIRR activated catalysts shows higher acidity compared to CCu-Mo$^{1.0}$ (Table 6.3); which advocates that NIRR has caused better hydrothermal activation during catalyst preparation compared to conventional heating protocol.

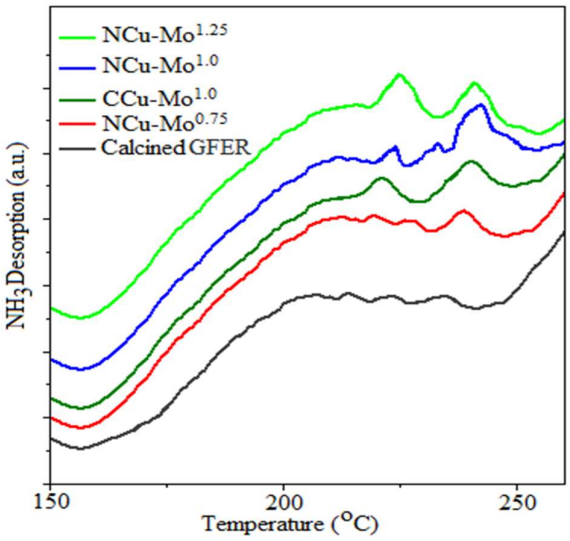

Figure 6. 6. NH_3-TPD analysis of prepared catalysts and calcined GFER

6.1.3.5. FTIR-Pyridine analyses

The nature of the acid sites of NCu-$Mo^{1.0}$, CCu-$Mo^{1.0}$, and calcined GFER have been further studied by FTIR-pyridine analysis (Figure 6.7). Presence of absorption peaks of pyridinium ion at 1538 and 1447 cm^{-1} for calcined GFER are attributed to the Bronsted acid and Lewis acid sites, respectively [11]. Spectrum of NCu-$Mo^{1.0}$, CCu-$Mo^{1.0}$ catalysts, also shows band at 1538 (Bronsted site) and 1447 cm^{-1} (Lewis site) along with a band at 1488 cm^{-1}, which assigned to the intermediate Bronsted and Lewis acid sites [12]. From figure 6, it can be seen that, the Bronsted acid capacity of NCu-$Mo^{1.0}$, CCu-$Mo^{1.0}$ increases compared to calcined GFER which may be due to the development of polymolybdate Keggin structures [13]. Furthermore, under NIRR, relocation & dispersion of active sites (Mo^{+6} and Cu^{+2}) [47] occur that create new pores in GFER framework, which eventually acts as Bronsted acid centres owing to presence of water. Bronsted acidic sites are beneficial to lignocellulosic biomass hydrolysis for conversion to glucose [14]. Notably, NIRR also stimulates inaccessible Cu^{+2} to come out from the internal surface to the exterior of the catalyst [15,16]; thus, rendering more accessibility to Cu^{+2}, which in turn increases Lewis acidity; and thus, overall acidity. Consequently, increment in overall acidity could be achieved in case of NIRR radiated catalyst compared to the conventionally prepared catalyst.

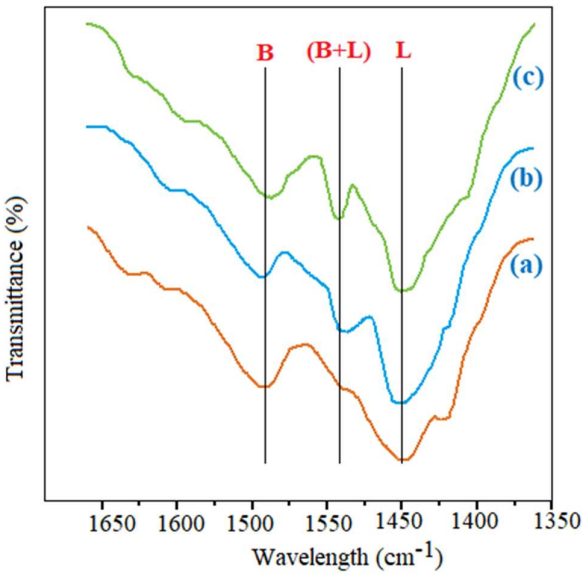

Figure 6. 7. IR spectra of pyridine adsorption of (a) calcined GFER; (b) CCu-Mo$^{1.0}$ and (c) NCu-Mo$^{1.0}$

6.1.3.6. Brunauer–Emmett–Teller (BET) analysis

BET analysis method was employed to determine the specific surface area of the catalysts and GFER support. Table 6.3 demonstrates substantial increases of specific surface area of the optimal NCu-Mo$^{1.0}$ catalyst (45.377 m^2/g) compared to the GFER support (7.049 m^2/g). During calcination step liberation of carbon oxides, acetone, methane and isobutene created new pores in the catalyst matrix; which in turn enhanced surface area of NCu-Mo$^{1.0}$ catalyst; the results of the present study corroborate well with the findings of El-Molla et al. [17] Shape of the adsorption isotherm of the optimal catalyst NCu-Mo$^{1.0}$ catalyst corroborates type I isotherm (IUPAC) (Figure 6.8(a)) implying monolayer adsorption. DFT method was employed to evaluate the NCu-Mo$^{1.0}$ catalyst pore volume (0.04408, 0.02317 cc/g for GFER) and modal pore diameter (1.9334, 0.7482 nm for GFER) (inset of Figure 6.8(a)). Furthermore, from Figure 6.8(b) it can be observed that 51.11 % micropores, 48.89 % mesopores were present in the NCu-Mo$^{1.0}$ catalyst. Notably, as the size of the water molecules were smaller (0.275 nm) than pore diameter of the NCu-Mo$^{1.0}$ catalyst; adsorption of water molecule easily occurred on the surface of the developed catalysts which augmented hydrolysis reaction.

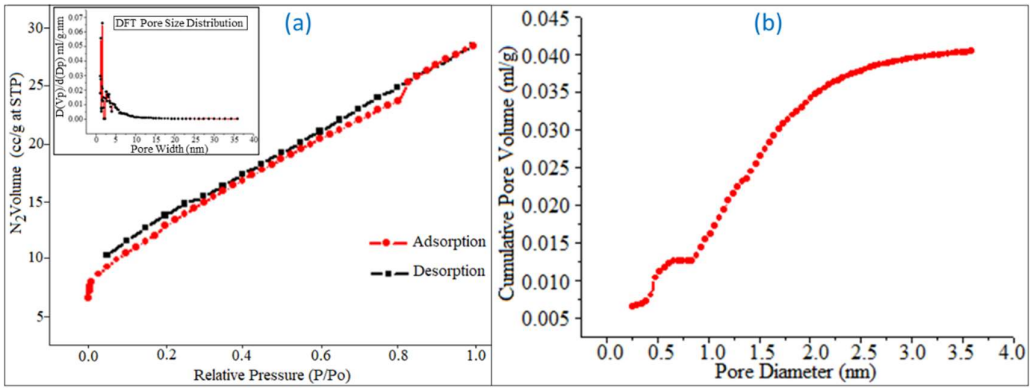

Figure 6. 8. (a) Pore volume vs. relative pressure (P/P_0) [inset: DFT pore size distribution for determination of modal pore diameter]. (b) Cumulative pore volume vs. pore diameter for NCu-$Mo^{1.0}$ catalyst

Table 6. 3. Effects of Mo precursor loading on specific surface area and acidity on prepared catalyst.

Mo Precursor Loading	BET Analysis			NH_3-TPD (mmol NH_3/ g catalyst)	G_{NIRR} Yield (%)
	Surface Area (m^2/g)	Total Pore Volume (cc/g)	Pore Diameter (nm)		
NCu-$Mo^{0.75}$	32.841	0.04082	1.8760	0.37	61.43
NCu-$Mo^{1.0}$	45.377	0.04408	1.9334	0.48	75.84
NCu-$Mo^{1.25}$	39.624	0.04153	1.6725	0.42	69.38
CCu-$Mo^{1.0}$	23.841	0.03328	1.1610	0.40	53.64

6.1.3.7. Scanning electron microscopic (SEM) analysis

SEM images of the optimum NCu-$Mo^{1.0}$ catalyst after calcination at 240°C are depicted in Figure 6.10, which shows irregular rod-shaped fiberglass particles partially surrounded by epoxy resin. Microscopic observation suggests that formation of Lewis acidic sites and Bronsted acidic sites were occurred on partially exposed fiberglass surface.

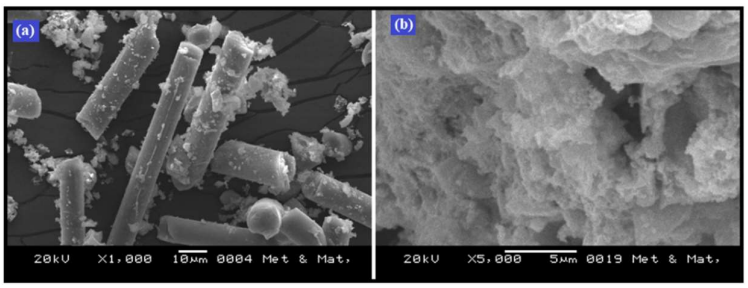

Figure 6. 9. SEM images of NCu-Mo1.0 at different magnification [(a)10 µm; (b) 5 µm]

6.1.3.8. TEM analyses

Morphology of GFER, NCu-Mo$^{1.0}$ and CCu-Mo$^{1.0}$ were further investigated by TEM analysis (Figure 6.10). With Mo precursor doping to GFER, clear contrast enhancement was found in Figure 6.10 (b) and (c) as compare to Figure 6.10 (a). A careful inspection of Figure 6.10 (a), (b) and (c) reveals transformation of surface morphology; whereas NCu-Mo$^{1.0}$ possesses more porous structure in comparison with GFER and CCu-Mo$^{1.0}$. Besides from EDX (Figure 6.11(a)) and HAADF (Figure 6.11(b)) mapping analysis it was observed that all the elements in the NIRR activated NCu-Mo$^{1.0}$ structure uniformly distributed. HRTEM image (Figure 6.12(a)) of NCu-Mo$^{1.0}$ catalyst exhibits presence of MoO_3 and CuO crystallites by white and red rectangles respectively. The lattice spacing of 0.231 nm corresponds to (111) plane of CuO crystallites (JCPDS: no. 48-1548) (indicated by the inclined lines in Figure 6.12 (b)) while the lattice spacing of 0.63 nm represents (020) plane of MoO_3 (indicated by the inclined lines in Figure 6.12 (c)).

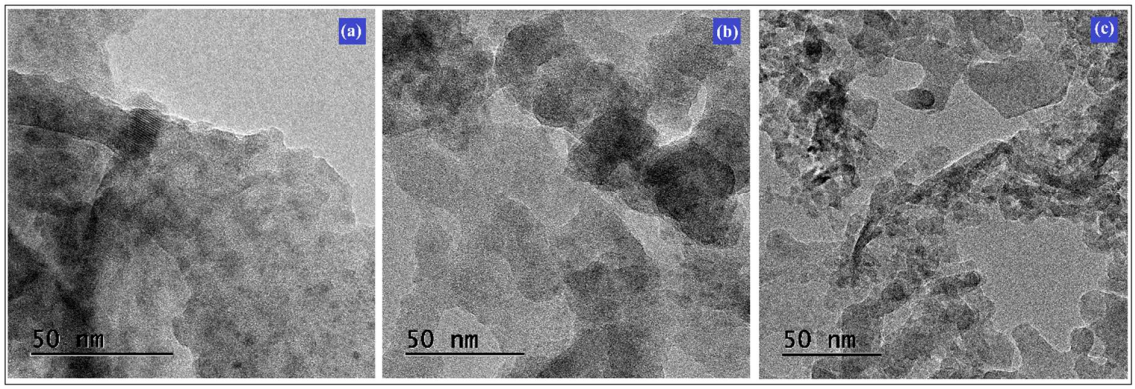

Figure 6. 10. TEM images of (a) GFER; (b) CCu-Mo$^{1.0}$ and (c) NCu-Mo$^{1.0}$

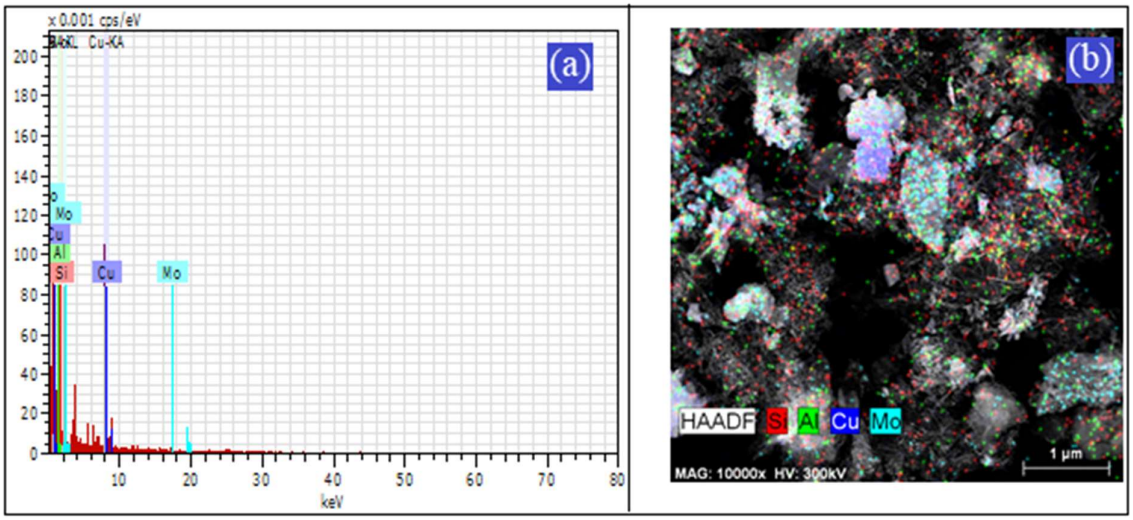

Figure 6. 11. (a) EDX and (b) HAADF-STEM analyses of NCu-Mo$^{1.0}$

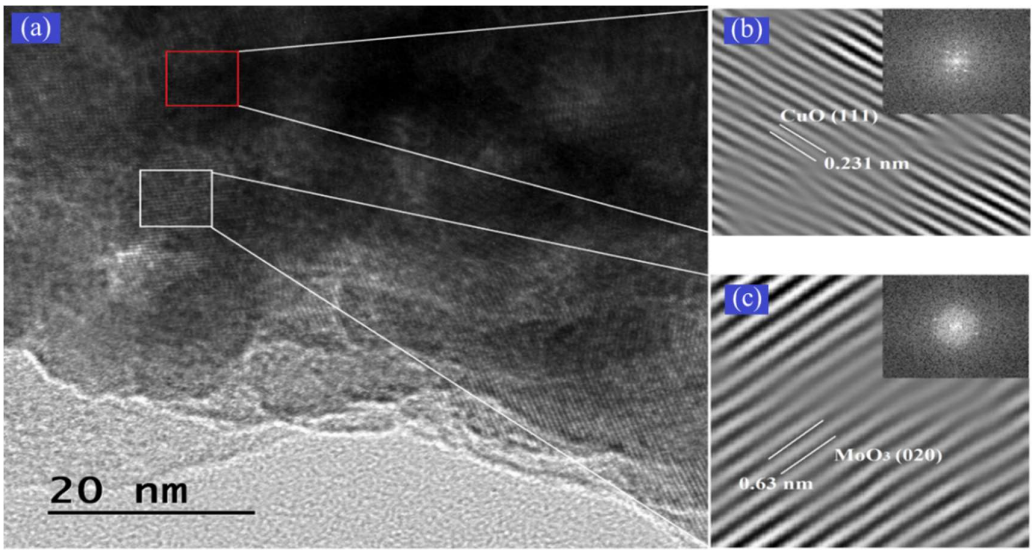

Figure 6. 12. HRTEM image of (a) NCu-Mo$^{1.0}$; (b) magnified view of red rectangle section [Inset shows Fast Fourier transform (FFT) of enclosed region]; (c) magnified view of white rectangle section [Inset shows Fast Fourier transform (FFT) of enclosed region]

6.1.3.9. X-ray Photoelectron Spectroscopic (XPS) analysis

Figure 6.13 displayed the X-ray Photoelectron Spectroscopy (XPS) diagram of the Taguchi derived optimum NCu-Mo$^{1.0}$ catalyst for jute hydrolysis process (A and B). XPS spectra detects two doublets at 234.67 eV and 237.84 corresponding to Mo^{6+} 3d3/2 and Mo^{6+} 3d5/2 respectively [18]. The preceding peaks indicates the higher oxidation state of Mo (MoO_3) in the prepared NCu-Mo$^{1.0}$ catalyst. In Figure 6.13(B), XPS spectra depicts that Cu $2p_{3/2}$ (II) lies at 936.76 eV and with one shake-up satellites at higher binding energy 944.84 eV, which attributed to CuO [19]. Considering these observations, it might be concluded that Cu^{2+} species existing in the prepared NCu-Mo$^{1.0}$ enhanced catalyst acidity (0.48mmol NH_3/ g catalyst) vis-à-vis catalytic activity. From the experimental result of PJF hydrolysis (Table 5.2) it may be inferred that an increase in Mo precursor up to 1.0 wt.% i.e. $CH_3COCH=C(O-)CH_3]_2MoO_2$ loading could improve the catalytic performance which signifies that Mo^{6+} detected in XPS analysis was the major active phase in the pretreated WJF hydrolysis process to yield glucose.

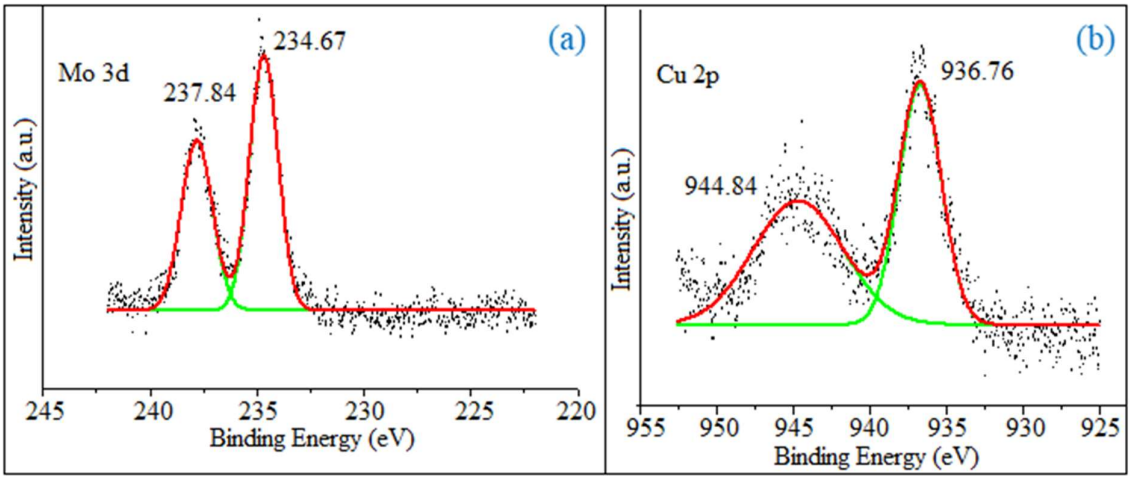

Figure 6. 13. XPS spectra of (A) Mo 3d and (B) Cu 2p of NCu-Mo$^{1.0}$ catalyst.

6.1.4. Possible reaction Mechanism of pretreated WJF hydrolysis using NCu-Mo$^{1.0}$

The Mo^{6+} and Cu^{2+} active phases present in the prepared catalyst (NCu-Mo$^{1.0}$) both behave as Lewis acid whereas Bronsted acidic sites were also present on the prepared catalyst surface [12]. Additionally, Mo free calcined GFER has resulted 44.36 mol % G_{NIRR} yield; whereas, when introduce Mo^{6+} ion in GFER framework, the resultant catalyst renders remarkably higher G_{NIRR} yield (75.84 mol %). The catalytic hydrolysis mechanism of pretreated WJF were depicted in Figure 6.14 which suggest that initially, water molecules (0.275 nm) adsorbed on the catalyst surface (pore dia. 1.9334 nm) and form hydronium ion which in turn resulted formation of H^+ and OH^- ion. Notably, cellulose molecules did not adsorb on catalyst surface which attributed the fact that the H^+ ion attack the cellulosic structure (1,4-β glycosidic linkage) which leading to the formation of glucose molecules.

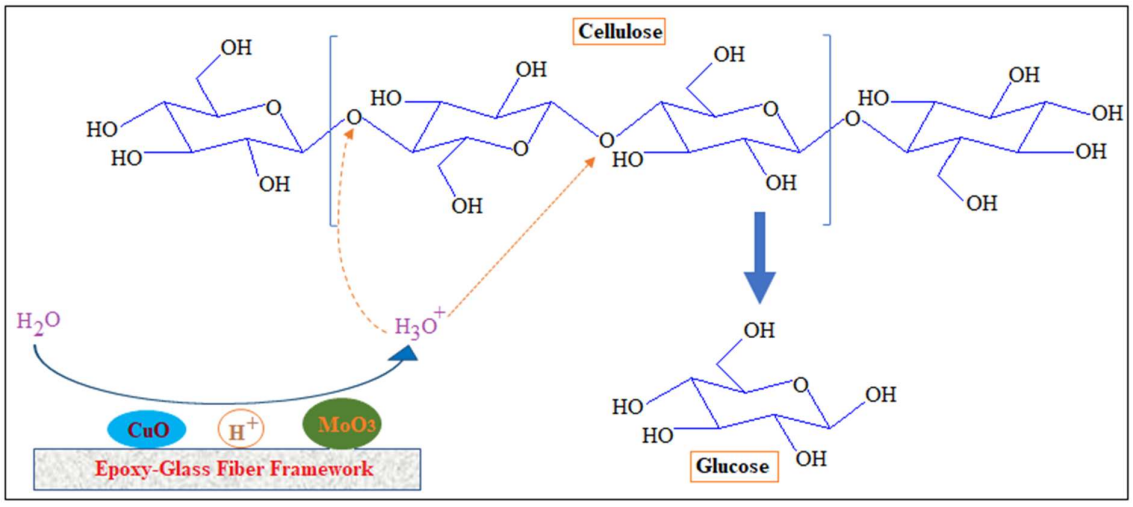

Figure 6. 14. Proposed pretreated WJF hydrolysis mechanism on NCu-Mo1.0 catalyst

6.1.5. Catalytic performance of NCu-Mo$^{1.0}$ catalyst on pretreated WJF hydrolysis process

To understand the efficacy of the optimum NCu-Mo$^{1.0}$ catalyst, hydrolysis of the pretreated WJF also conducted using calcined GFER, CCu-Mo$^{1.0}$ and commercial catalyst A-15 (surface area: 45 m^2/g, pore size: 25 nm, acidity: 4.8 mmol/g catalyst) at TOD derived optimal condition (Figure 6.15). NCu-Mo$^{1.0}$ show shows better activity in terms of glucose yield (75.84 mol %) over A-15 (G_{NIRR}: 61.53 mol %), CCu-Mo$^{1.0}$ (G_{NIRR}: 53.64 mol %), calcined GFER (G_{NIRR}: 38 mol %). The high catalytic activity of NCu-Mo$^{1.0}$ over A-15 can be attributed to the light absorbing ability of the prepared catalyst due to the presence of CuO and $MoSi_2$ [20,21]. UV-Vis spectra of NCu-Mo$^{1.0}$ exhibits UV absorption peak (200-400 nm) in addition to an absorption hump within visible range (between 550 and 700 nm) of electromagnetic spectra. PJF hydrolysis conducted under conventional heating (500 W) using NCu-Mo$^{1.0}$, rendered maximum 63.16 mol % glucose yield in comparison with 75.84 mol % obtained under NIRR at TOD derived optimal condition. Thus, the light absorbing ability of the prepared catalyst was evident. Furthermore, from Figure 6.14, it can be observed that A-15 renders better G_{NIRR} yield compared to CCu-Mo$^{1.0}$ after 5 minutes of hydrolysis reaction, which may be due to the leaching of -SO_3H group from A-15 framework [22] (acts as a homogeneous catalyst). Notably, it should be also mentioned that the optimum glucose yield (75.84 mol %) was much higher compared to reported in the previous work (50 mol %) [23].

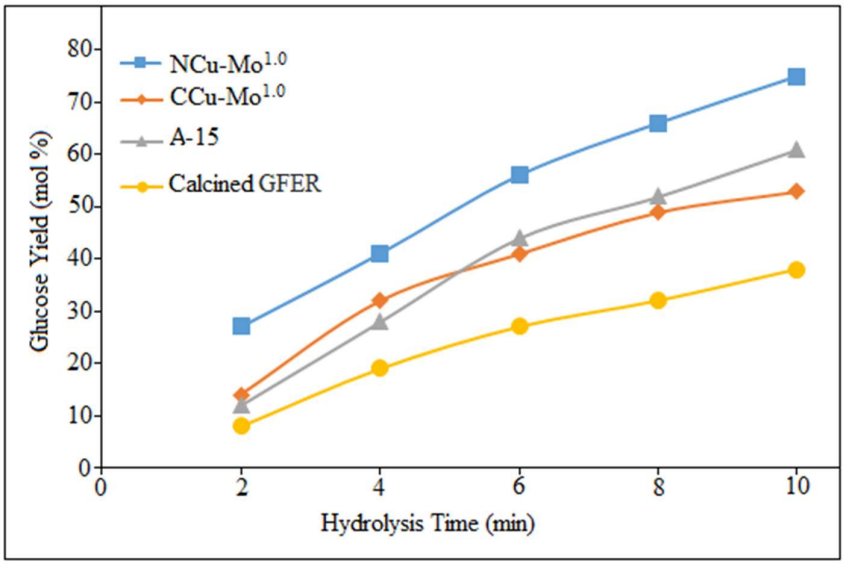

Figure 6. 15. Catalytic performance of NCu-Mo$^{1.0}$, calcined GFER, CCu-Mo$^{1.0}$, and A-15 in pretreated WJF hydrolysis process

6.1.6. Pretreated WJF hydrolysate characterization

6.1.6.1. FTIR analyses of hydrolysate

Hydrolysate obtained from pretreated WJF hydrolysis at optimum condition were analysed through liquid FTIR and compared with characteristic peaks of standard glucose (Figure 6.16). A prominent peak at 3424.18 cm^{-1} attributed to stretching vibrations of O-H group [24] while stretching vibrations at 2965.51 cm^{-1} and 2936.85 cm^{-1} confirms the presence of CH groups [25]. Additionally, presence of H-C-H group was observed at 1422.36 cm^{-1} and 1463.45 cm^{-1}. Peaks at 1618.32 cm^{-1} and 1206.68 cm^{-1} could be ascribed to C=C and C-O-C bonds respectively [26]. Furthermore, peaks at 744.62 cm^{-1} and 610.87 cm-1 indicated the presence of few aromatic functional groups [27]. Thus, Figure 6.16 clearly manifested that these infrared spectra indicate the existence of representative functional groups of glucose in hydrolysate. Moreover, higher intensity of infrared spectra for hydrolysate obtained from NCu-$Mo^{1.0}$ hydrolysed WJF compared to hydrolysate for CCu-$Mo^{1.0}$ indicate the efficacy of NCu-$Mo^{1.0}$ catalyst over CCu-$Mo^{1.0}$.

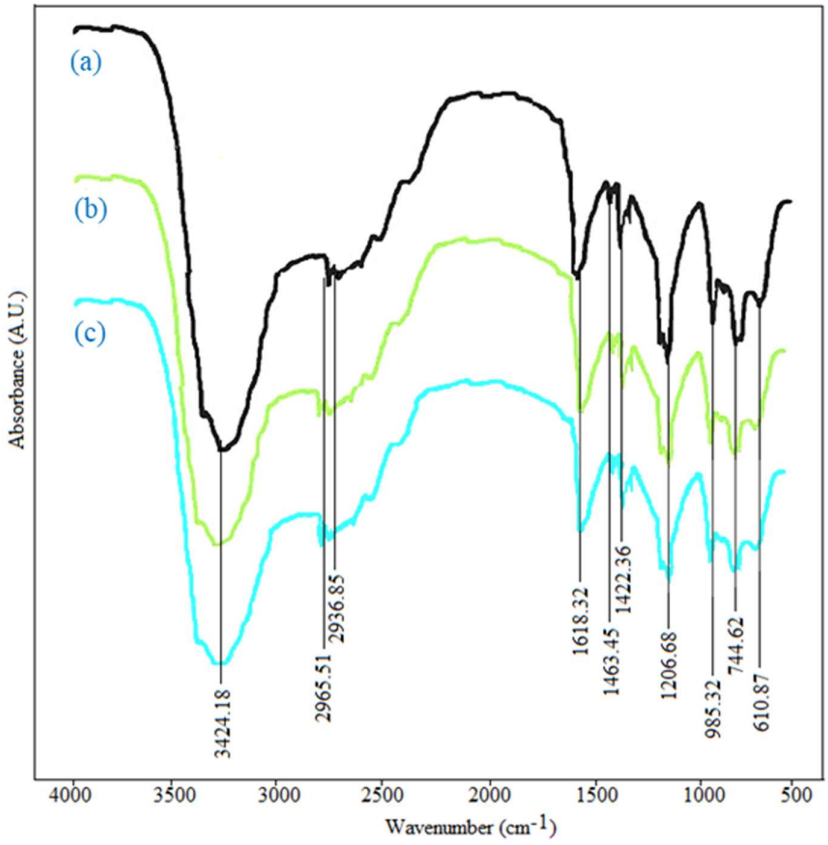

Figure 6. 16. FTIR analyses of (a) standard glucose and hydrolysate obtained from (b) NCu-$Mo^{1.0}$ catalysed hydrolysate and (c) CCu-$Mo^{1.0}$ catalysed hydrolysate

6.1.6.2. High performance liquid chromatography (HPLC) analyses of hydrolysates

Hydrolysate obtained from NCu-Mo$^{1.0}$ and CCu-Mo$^{1.0}$ catalysed pretreated WJF hydrolysis at optimal condition was quantified employing HPLC (Figure 6.16). Hydrolysate constituents such as 5-HMF, xylose and glucose were retaining at 23.83 min 9.84 min and 9.26 min respectively [28,29]. Glucose concentration remarkably higher (68 wt. %) compared to 5-HMF (12 wt. %) and xylose (21 wt. %) for NCu-Mo$^{1.0}$ catalysed pretreated WJF hydrolysis process.

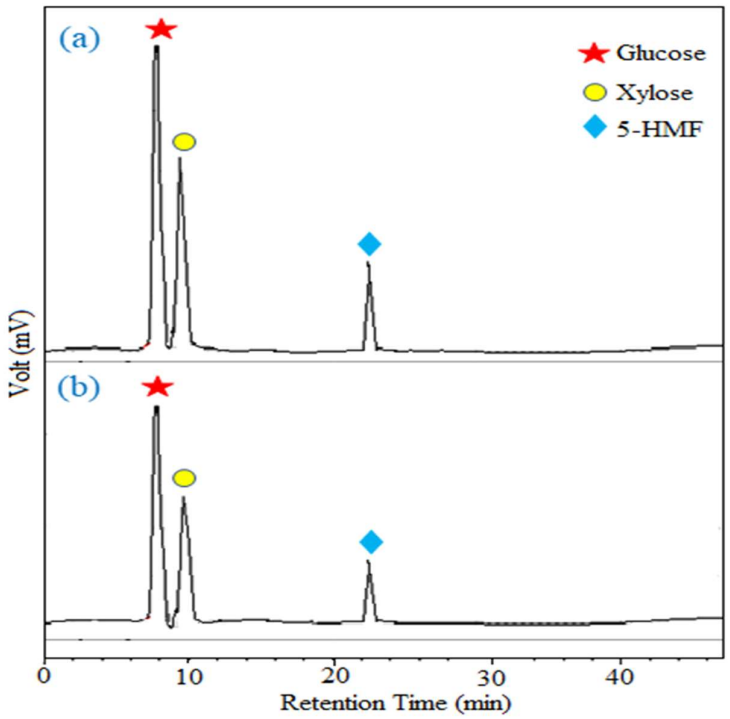

Figure 6. 17. HPLC analysis of hydrolysate obtained from (a) NCu-Mo$^{1.0}$ catalysed and (b) CCu-Mo$^{1.0}$ catalysed WJF hydrolysis process

6.1.7. *Catalyst reusability test*

Reusability of the prepared optimal catalyst NCu-Mo$^{1.0}$ was evaluated by taking seven consecutive experimental runs at optimal PJF hydrolysis condition. After each hydrolysis step, the catalyst was easily recovered by screening (Mesh size: 200 µm) the oven dried (at 105 °C for 1.5 h) the hydrolysis residue. The hydrolysate yield decreased from 75.84 % to 71.39 % after fourth recycle (fifth batch) while, no further decrease in glucose yield was observed in subsequent three more reaction cycles. Inductively coupled plasma optical emission spectroscopy (ICP-OES) of the reused catalyst reveals that insignificant number of active sites leaching (0.11 ppm) has been leached from NCu-Mo$^{1.0}$. while, CCu-Mo$^{1.0}$ suffered leaching up

to 1.76 ppm which corroborates well with Zhao et al. [18]; this further reinforces the superiority of NIRR over CH.

6.2. Activity 2:

KINETICS OF COMBINED NON-CATALYTIC AND CATALYTIC HYDROLYSIS OF JUTE FIBER UNDER ULTRASONIC-FAR INFRARED ENERGY SYNERGY

6.2.1. Effects of process parameters on PWJF hydrolysis process

The effects of the governing process parameters on the PWJF hydrolysis under US-FIRW were assessed through analysis of variance (ANOVA) (Table 6.4). For PWJF hydrolysis process, at 95% confidence level (p-value < 0.05), the hydrolysis reaction temperature (φ_{HT}), catalyst concentration (φ_{HC}) were statistically significant process parameters. Table 6.5 represents ranks of the process parameters based on relative significance (φ_{HT}>φ_{HC}>φ_{HP}>φ_{WB}) on the response (ω_{RS}) using 'higher the better' criterion for SN ratios. Notably, the process parameters corresponding to larger Δ-value exhibited superior effect on the response variable (ω_{RS}) compared to other parameters. Additionally, the maximum S/N ratio values corresponding to a particular level of the process parameters (Table 6.5) which are represented by the asterisk marks, implied that maximum ω_{RS} (74.82 mole %) could be attained at 70°C (φ_{HT}), 2.5 (φ_{HC}), 15 min (φ_{HP}) and 10 (φ_{WB}) for US-FIRW. Notably, at the TOD derived optimal hydrolysis process conditions (Table 6.5) the US-FIRW showed superior effects in terms of RS yield (74.82 mol%) over FIRW (69.63 mol%), US (50.34 mol%) and CTS (48.16mol%), for the hydrolysis of PWJF. Thus, US-FIRW energized reactor was found most efficient in terms of RS yield.

Table 6. 4. Analysis of variance (ANOVA) of factors affecting PWJF hydrolysis process

Source	DF	Adjusted Sum of square	Adjusted mean square	F value	P value
$\boldsymbol{\varphi_{HT}}$ (°C)	1	229.897	229.897	8.09	0.047
$\boldsymbol{\varphi_{HP}}$ (min)	1	7.981	7.981	0.28	0.624
$\boldsymbol{\varphi_{HC}}$ (wt.%)	1	240.920	240.920	8.47	0.044
$\boldsymbol{\varphi_{WB}}$ (w/w)	1	6.742	6.742	0.24	0.652
Error	4	113.725	28.431		

Total	8	599.264

Table 6. 5. S/N ratios and Δ of process variables in hydrolysis of PWJF under US-FIRW

Level	φ_{HT} (°C)	φ_{HP} (min)	φ_{HC} (wt.%)	φ_{WB} (w/w)
L_{-1}	34.26	35.13	34.59	35.59*
L_0	36.17*	35.87*	35.54	35.52
L_1	36.15	35.59	36.44*	35.48
Delta	1.91	0.74	1.85	0.11
Rank	1	3	2	4

6.2.2. Interactive effects of process parameters on PWJF hydrolysis process

Maintaining other process parameters at optimum level, an increment in hydrolysis temperature resulted in higher RS yield (ω_{RS}) (Figure 6.18 (a)), which clearly manifested that the medium was thermally sensitive, and reaction was endothermic in nature. Accordingly, gradual increase in temperature resulted in higher ω_{RS} and vice-versa over the catalyst loading range considered (Figure 6.18 (b)). On the other hand, from Figure 6.18 (c) it could be concluded that water loading had poor impact on ω_{RS} over the temperature range of hydrolysis. A similar trend was followed in Figure 6.18 (e) & 6.18 (f), for all values of hydrolysis period and catalyst concentration respectively.

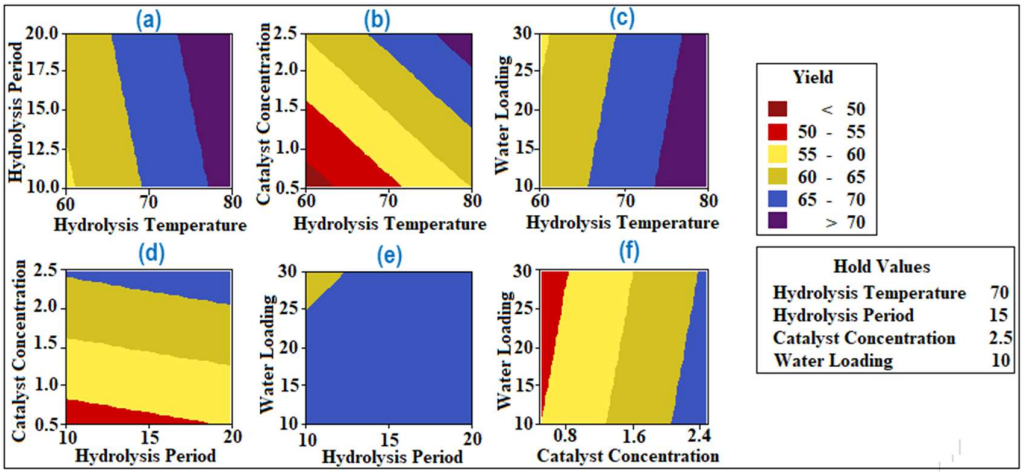

Figure 6. 18. Parametric interactions in hydrolysis of PWJF for reducing sugar yield at optimal conditions.

6.2.3. Performance comparison among US-FIRW, FIRW, US and CTS

One of the prime objectives of this research work was to assess the intensification efficacy among the US-FIRW, FIRW, US and CTS pertaining to the PWJF hydrolysis process for maximum conversion of WJF to RS (Figure 6.19) at optimum hydrolysis conditions. Evidently, a significantly increasing trend of RS concentration in hydrolysate was observed up to optimum time (15 min) under combined US-FIRW compared to that under individual employment of FIRW, US and conventional heating (in CTS). Maximum RS concentration of 0.1232 mol/L (74.82 mol% ω_{RS}), 0.1117 mol/L (69.63 mol% ω_{RS}), 0.0829 mol/L (50.34 mol % ω_{RS}) and 0.0793 mol/L (48.16 mol% ω_{RS}) were achieved under US-FIRW, FIRW, US and CTS in 15 min respectively. Moreover, concentrations of glucose and xylose in hydrolysate were higher for US-FIRW (glucose: 0.0690 mol/L; xylose: 0.0320 mol/L) in comparison with those in FIRW (glucose: 0.0558 mol/L; xylose: 0.0257 mol/L), US (glucose: 0.0447 mol/L; xylose: 0.020 mol/L) and CTS (glucose: 0.0404 mol/L; xylose: 0.0190 mol/L) (Figure 6.20). Notably, to achieve up to 45% RS yield, US-FIRW (105 KJ) consumed 26 % less energy compared to FIRW (143.2 KJ) and 80 % less energy compared to CTS (544.59 KJ). In absence of A-15, all types of reactors set-up viz., US-FIRW, FIRW, US and CTS rendered lower RS yield of 27.09 mol %, 16.51 mol %, 14.42 mol % and 12.62 mol % respectively.

Notably, the US-FIRW reactor (74.82 mol% ω_{RS}) rendered 26.66 mol% higher RS yield compared to the yield (48.16 mol% ω_{RS}) rendered by CTS; whereas, individually FIRW (69.63 mol% ω_{RS}) and US (50.34 mol% ω_{RS}) assisted reactors resulted respectively 21.47 mol % and 2.18 mol % rise in RS yield compared to CTS. Therefore, the synergistic effect of the US and FIRW in the combined US-FIRW reactor, could result [26.66 – (21.47 + 2.18)] 3.01 mol % additional increment in RS yield.

The conversion of PWJF to RS could be enormously augmented and intensified by US-FIRW due to the combined effects of far infrared radiation and ultrasonication. Far infrared wave could penetrate the hydrolysis reaction mix deeper and get absorbed intensely into different cellulosic-layers facilitating breakdown of crystalline structures of jute fiber [30]. Besides, the interactions between the far infrared wave and the reactant molecules generated substantial thermal energy rendering rapid uniform heating and enhanced stretching-bending vibrations resulting in severe molecular collisions, which in turn facilitated intense hydrolysis of PWJF. Additionally, application of ultrasonic energy on hydrolysis mix produces acoustic cavitation, which facilitated liquid circulation and turbulence creation [31] causing further excitation of water molecules that aided in faster and efficient cleaving of linkages in cellulose

and hemicellulose structures. Hence, the conversion of PWJF to RS employing combined application of infrared and ultrasonic wave can be considered as an energy-efficient, time-saving and cost-effective green method for synthesis of RS.

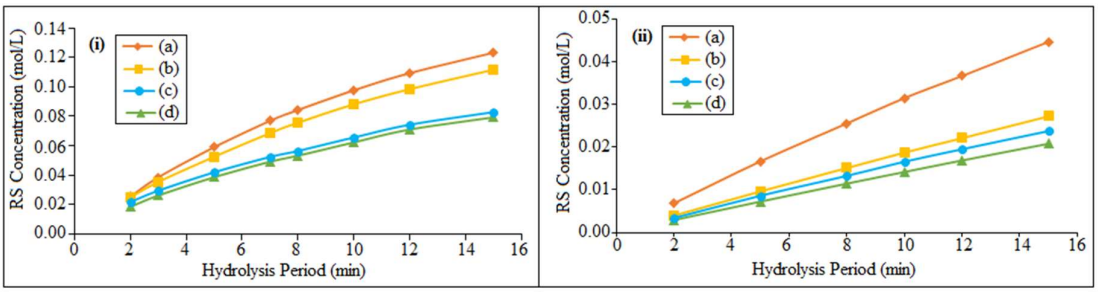

Figure 6. 19. RS concentration profile in (i) catalytic and (ii) non-catalytic hydrolysis of PWJF employing (a) US-FIRW (b) FIRW (c) US and (d) CTS.

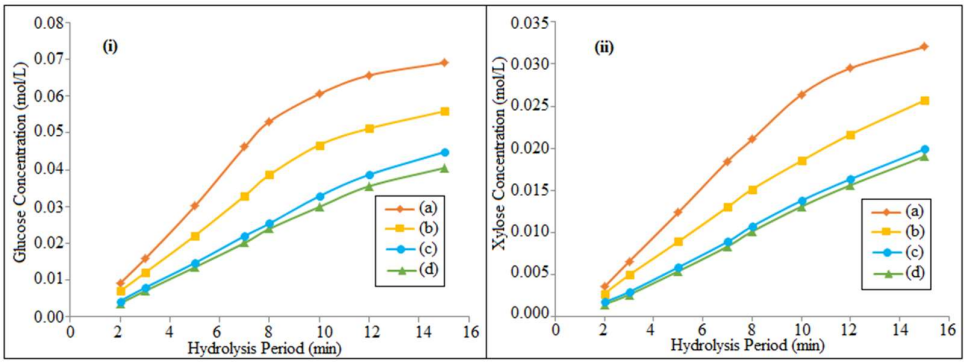

Figure 6. 20. (i) Glucose and (ii) xylose concentration profile in catalytic hydrolysis of PWJF employing (a) US-FIRW (b) FIRW (c) US and (d) CTS.

6.2.4. Hydrolysis Kinetics of PWJF

The non-catalytic hydrolysis kinetic parameters were evaluated for US-FIRW, FIRW, US and CTS employing MATLAB R2014a (Table 6.6). It was evident that under US-FIRW the non-catalytic reaction rate constants are much larger in comparison with FIRW, US and CTS; thus, demonstrating superiority of US-FIRW. The PWJF hydrolysis kinetic data were fitted in the formulated combined pseudo-homogeneous-heterogeneous kinetic models (PHHER & PHHLH) employing MATLAB R2014a at the TOD projected optimal hydrolysis condition. The statistical parameters viz. R^2, R^2adj and RMSE were evaluated for the different reactor systems (US-FIRW, FIRW, US and CTS). Accordingly, the ER model could best describe (highest R^2_{adj} and lowest RMSE) the PWJF hydrolysis kinetics under US-FIRW as well as under FIRW, US and CTS (Table 6.7). Besides, the apparent reaction rate constants and other

kinetic parameters for different models corresponding to all reactor configurations (Table 6.7 and Table 6.8) have been presented.

Table 6. 6. Non-catalytic hydrolysis kinetic parameters

Reactor	Temperature	k_{NC}	R^2	R^2_{adj}
US-FIRW	333	0.0108	0.94	0.94
	343	0.0129	0.97	0.97
	353	0.0153	0.99	0.99
FIRW	333	0.0042	0.99	0.99
	343	0.0073	0.94	0.94
	353	0.0091	0.97	0.97
US	333	0.0036	0.82	0.82
	343	0.0063	0.86	0.86
	353	0.0085	0.99	0.99
CTS	333	0.0031	0.97	0.97
	343	0.0054	0.99	0.99
	353	0.0078	0.97	0.97

Since, A-15 does not completely release H^+ ion from its resin framework due to short period of PWJF hydrolysis process (15 min) [32], it was quite obvious that the hydrolysis process should be considered as a combination of pseudo-homogeneous and heterogeneous mechanism. The best fitted model, PHHER also corroborates with the above fact suggesting that de-polymerization of PWJF could be occurred by means of combined pseudo-homogeneous and heterogeneous pathways.

From Table 6.7 and Table 6.8, it could be inferred that the apparent reaction rate constants under US-FIRW were much greater in comparison with FIRW, US and CTS at all temperatures. Significantly, the values of activation energy (E_J) were much lower in case of US-FIRW in comparison with FIRW, US and CTS (Table 6.8); which indicated appreciably lower energy requirement for US-FIRW while achieving significantly greater and faster RS yield. The numerical values of activation energy pertaining to different reaction pathways in PWJF hydrolysis under optimal condition in US-FIRW was depicted in Figure 6.21.

Table 6. 7. Kinetic parameters as per Equation 5.12 & 5.13 corresponding to US-FIRW, FIRW, US and CTS

Reactor Type	Model type	Temperature	Kinetic parameters						Statistical Criteria		
			k_H	$k^{\oplus}$	k^*	K_J	K_W	K_G	R^2	R^2_{adj}	$RMSE$
US-FIRW	PHHER	333K	0.0641	0.0155			0.00542	0.00009	0.99	0.98	1.97×10^{-4}
		343K	0.0675	0.0231			0.00329	0.0001	0.99	0.98	1.28×10^{-3}
		353K	0.0841	0.0354			0.0032	0.0003	0.99	0.98	4.05×10^{-4}
	PHHLH	333K	0.0640		0.0159	0.0002	0.0082	0.0003	0.99	0.98	1.97×10^{-4}
		343K	0.0674		0.0233	0.0001	0.0036	0.0007	0.99	0.97	2.24×10^{-4}
		353K	0.0842		0.0355	0.0003	0.0032	0.0008	0.99	0.97	4.05×10^{-4}
FIRW	PHHER	333K	0.0315	0.0196			0.0164	0.0018	0.97	0.94	1.67×10^{-4}
		343K	0.0511	0.0286			0.0167	0.0017	0.99	0.94	6.52×10^{-5}
		353K	0.0588	0.0323			0.0183	0.001	0.99	0.99	1.34×10^{-4}
US	PHHER	333K	0.0003	0.0308			0.0004	0.0015	0.98	0.97	1.24×10^{-4}
		343K	0.0006	0.0341			0.0005	0.0014	0.97	0.92	2.35×10^{-4}
		353K	0.00081	0.0425			0.0006	0.0011	0.98	0.95	2.05×10^{-4}
CTS	PHHER	333K	0.0003	0.0306			0.0004	0.0016	0.96	0.94	2.04×10^{-3}
		343K	0.00061	0.0335			0.00049	0.0014	0.95	0.91	2.96×10^{-4}
		353K	0.00084	0.0417			0.00059	0.0011	0.98	0.96	2.42×10^{-4}

Table 6. 8. Activation Energy for non-catalytic and catalytic hydrolysis reaction pertinent to US-FIRW, FIRW, US and CTS

Hydrolysis Reaction Path	US-FIRW		FIRW		US		CTS	
	E_J (KJ mol^{-1})	E_{J0}	E_J (KJ mol^{-1})	E_{J0}	E_J (KJ mol^{-1})	E_{J0}	E_J (KJ mol^{-1})	E_{J0}
NCPH	16.75	4.61	37.66	3.6×10^3	41.51	1.22×10^4	45.80	4.83×10^4
CPH	13.18	7.29	30.65	2.1×10^3	48.71	1.39×10^4	48.11	1.12×10^4
CHE	40.01	2.94×10^4	24.67	1.5×10^2	15.67	8.67	15.06	6.88

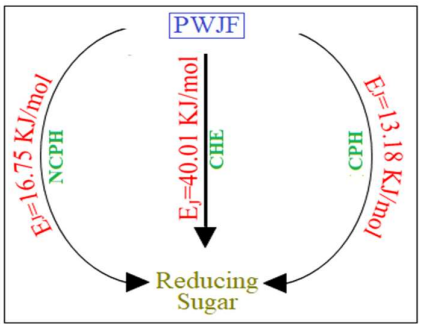

Figure 6. 21. Reaction activation energy pertaining to different reaction pathways in PWJF hydrolysis employing US-FIRW

6.2.5. Analyses of product hydrolysate through FTIR

FTIR spectra of standard glucose and hydrolysate obtained from PWJF hydrolysis process at optimum conditions under US-FIRW, FIRW, US and CTS are depicted in Figure 6.22 (a), Figure 6.22 (b), Figure 6.22 (c), Figure 6.22 (d), Figure 6.22 (e) respectively. Stretching vibrations at 2965.34 cm^{-1} and 2937.85 cm^{-1} depicted the presence of CH groups [33]; while the O-H stretching vibrations of hydrogen bonded hydroxyl (-OH) group was observed at 3425.69 cm^{-1} [34]. The prominent peaks at 1619.45 cm^{-1} and 1207.53 cm^{-1} confirmed the presence of C=C and C-O-C bonds respectively [35]. Moreover, peaks at 1428.56 cm^{-1} and 1462.10 cm^{-1} could be ascribed to the presence of H-C-H group. Additionally, peaks at 744.59 cm^{-1} and 610.85 cm^{-1} could be attributed to the existence of few functional groups in aromatic form [36]. From Figure 6.22, it is clear that these spectra confirm the presence of characteristic functional groups of glucose in hydrolysate. Furthermore, the highest intensity of these spectra in hydrolysate obtained at the optimum condition in US-FIRW compared to FIRW, US and CTS indicate the presence of higher glucose concentration in hydrolysate from US-FIRW than those obtained using FIRW, US and CTS.

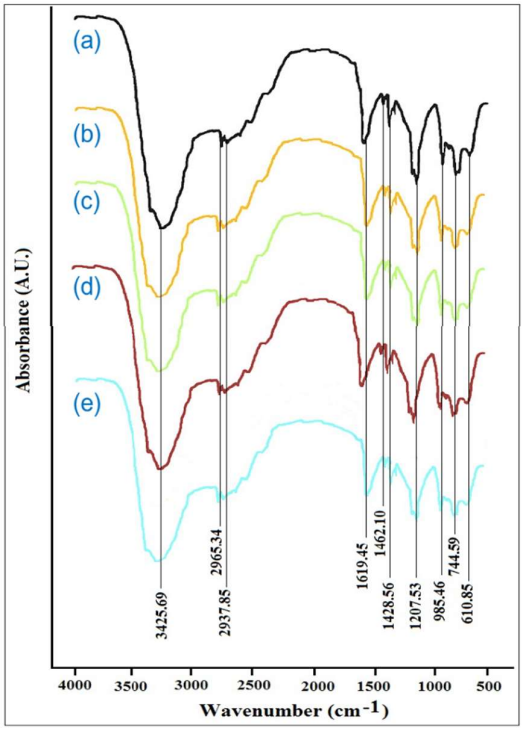

Figure 6. 22. FTIR analyses of (a) standard glucose and hydrolysate obtained under (b) US-FIRW; (c) FIRW; (d) US; (e) CTS at optimal process conditions.

6.2.6. FTIR analyses of WJF, PWJF and optimally hydrolysed PWJF

The FTIR spectra of WJF, PWJF and optimally hydrolysed PWJF residue resulted from US-FIRW, FIRW, US and CTS (Figure 6.23 (a-f)) exhibited peaks at 3424.79 cm^{-1} attributing to the stretching vibration of O-H functional group while peaks at 1664.07 $cm^{-1}$and 1547.43 cm^{-1} corresponded to C=O stretching of lignin [37,38]. Stretching vibrations of CH group of cellulose and hemicelluloses were observed at 2920.46 and 2857.14 cm^{-1} whereas at 934.23 cm^{-1} and 875.36 cm^{-1} (from Figure 23 (a) to Figure 6.23 (f)), gradual decrease of these peaks indicated the stepwise decrease in cellulose and hemicellulose content in waste residue [38]. The peak located at 1050.87 cm^{-1} was ascribed to the presence of C=C vibrations [39]. Additionally, O-H and C-H deformation stretching were detected around 1896.24 cm^{-1} and 2287.26 cm^{-1} [40]. It could be evidenced from Figure 6.23 (a-f) that, gradual rise in peak intensities occurred corresponding to the transformation from raw WJF to PWJF and finally to hydrolysed PWJF residue, since in presence of US-FIRW, the hydrolysis rate of the amorphous cellulose was remarkably greater than that of crystalline cellulose.

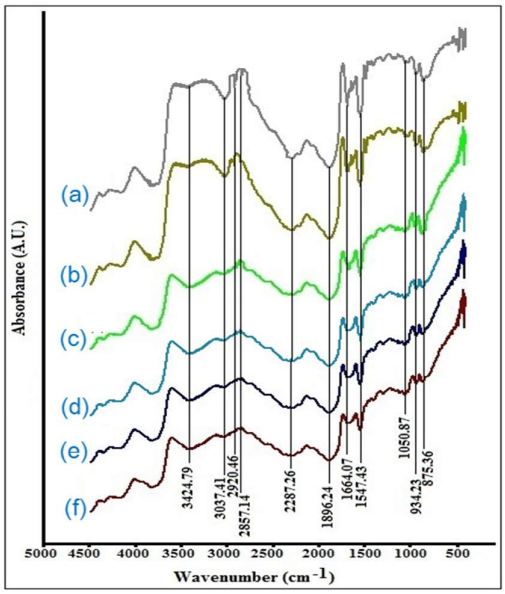

Figure 6. 23. FTIR analyses of (a) raw WJF and WJF residue (b) after pretreatment; (c) after hydrolysis under CTS (d) after hydrolysis under US (e) after hydrolysis under FIRW; (e) after hydrolysis under US-FIRW.

6.2.7. HPLC analyses of hydrolysates

High performance liquid chromatography (HPLC) was deployed to assess the quantitative compositions of hydrolysate obtained at optimal hydrolysis condition in US-FIRW, FIRW, US and CTS. The retention times (Figure 6.24) corresponding to glucose, xylose and 5-HMF were 9.23 min, 9.82 min and 23.81 min respectively which corroborated well with the findings of Duan [41,42]. The glucose concentration (56 mol %) was remarkably higher in comparison with the concentrations of 5-HMF (14 mol %) and xylose (26 mol %) for hydrolysate obtained from US-FIRW.

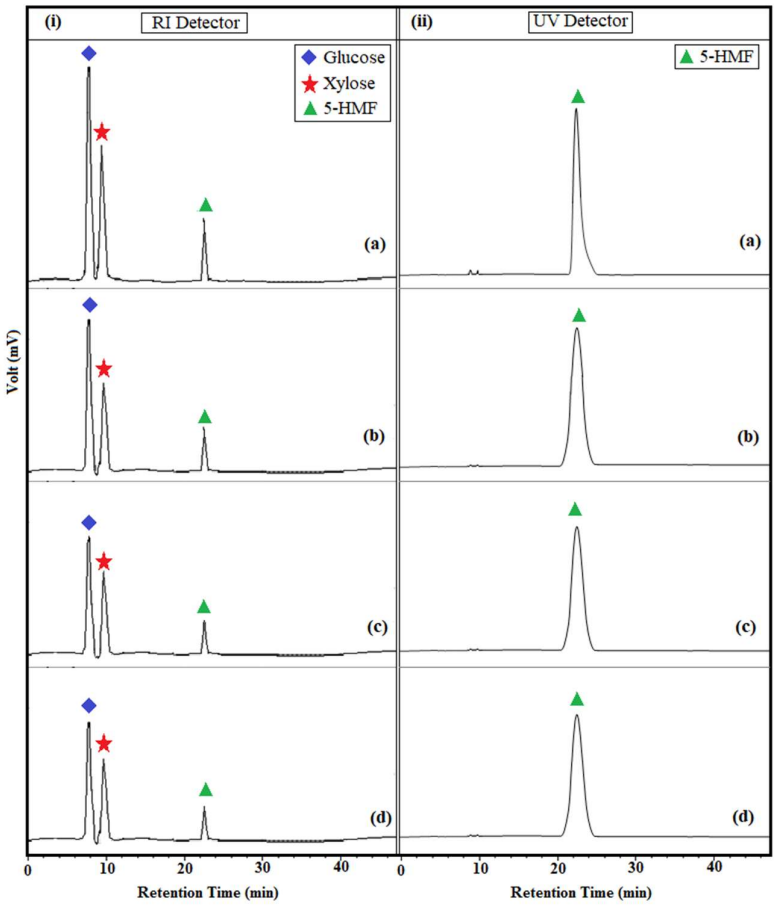

Figure 6. 24. (i) HPLC analysis by RI detector of aqueous hydrolysate produced under (a) US-FIRW (b) FIRW (c) US and (d) CTS at optimal condition; (ii) HPLC analysis by UV detector of extracted HMF.

6.2.8. XRD analysis

The XRD analyses of raw WJF and WJF residue obtained after pretreatment and hydrolysis from US-FIRW, FIRW, US and CTS (Figure 6.25 (a-f) indicated significant peaks at 2θ = 15.67º, 16.62º and 22.16º corresponding to cellulose [43,44]. The result clearly demonstrated a gradual increase in crystallinity index (CrI) from pretreatment to hydrolysis step, owing to the augmented difference between the crystalline and amorphous phases of the cellulose due to depletion of amorphous cellulose near the surface, which was maximum in US-FIRW.

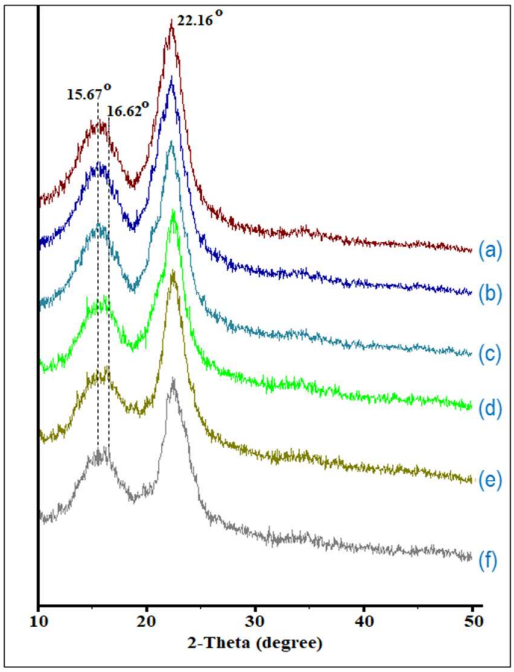

Figure 6. 25. XRD analyses of PWJF residue after optimal hydrolysis under (a) US-FIRW; (b) FIRW; (c) US; (d) CTS and of (e) PWJF (f) WJF.

6.2.9. Mechanism of A-15 catalysed hydrolysis

In the present study, the PHHER model was found best (according to the statistical criteria of Table 6.7) to represent the PWJF hydrolysis kinetics. According to PHHER kinetic model, the partial breakdown of1,4-β glycosidic bond of cellulose and C-O bond of hemicellulose occurred in bulk phase due to leached acidic sites ($-SO_3^-H^+$) of A-15 as well as due to the molecular stretching and formation of cavitation by interaction with FIRW and ultrasonication respectively [45-47]. In accordance with ER model, the diffusion of water molecules (0.96 Å) in to the pores (300 Å) of A-15 catalyst could easily be happened leading further chemisorption. The molecular interactions between water and catalyst facilitating proton (H^+) release from catalyst; thus, leading the generation of hydronium ion which paves the way to the formation of H^+ and OH^- ions [48]. In due course, the emergence of cyclic carbonium ion with half chair configuration comes about by the H^+ ion attacking the 1, 4-β glycosidic linkage of cellulose and C-O bond of hemicellulose. Lastly, formation of reducing sugar (comprising mainly glucose and xylose) molecules occurred due to the OH^- ion transfer to the carbonium ion (Figure 6.26) [49].

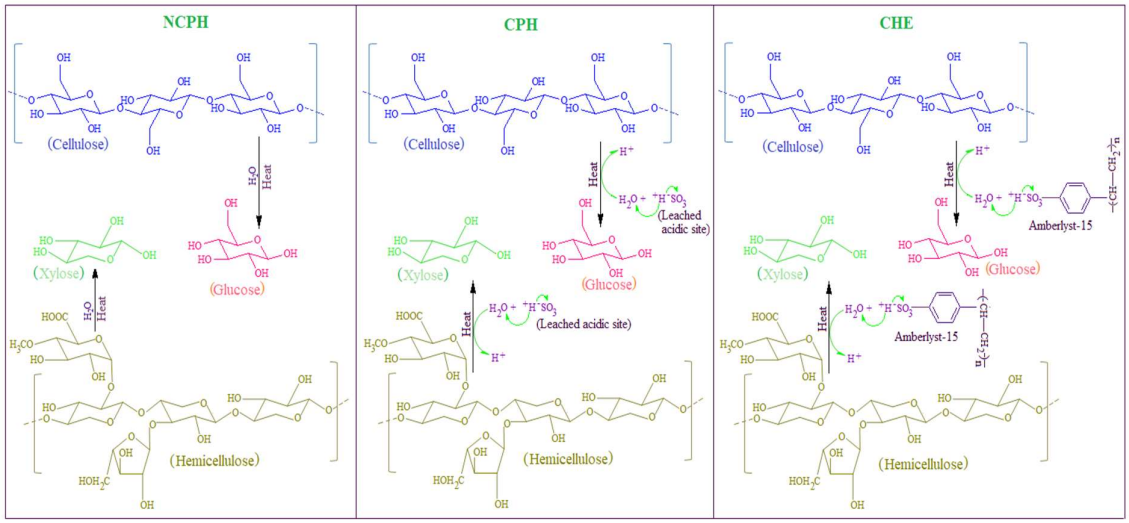

Figure 6. 26. Possible mechanisms of PWJF hydrolysis via different reaction pathways.

6.3. Activity 3:

SUSTAINABLE HMF SYNTHESIS FROM WASTE COOKED RICE WATER USING FLY-ASH BASED AL_2SIO_5 SUPPORTED NANO PHOTOCATALYST UNDER HALOGEN-ULTRASOUND SYNERGISTIC-ENERGY: LCA AND DFT BASED SIMULATION

6.3.1. Influences of process factors and ANOVA

The statistical criteria (viz. standard deviation, R^2, predicted-R^2 and adjusted-R^2) obtained from Model fit summary (Table 6.9) of Box-Bhenken designed photocatalytic conversion process of CRW revealed that the quadratic model could best describe the factorial effects on HMF yield ($\in_{HMF}$) in comparison with the 2FI and linear models. The quadratic model (Equation 6.1) correlates the process factors and the $\in_{HMF}$ (in coded form). Moreover, analysis of variance (ANOVA) depicting F-Value and P-Value (Table 6.10) advocated that the individual parameters (φ_T, φ_t, φ_{Ti} and φ_C) and the quadratic term ($\varphi_{Ti}{}^2$) were statistically significant to affect the $\in_{HMF}$.

Table 6. 9. Model fit summary of quadratic, 2FI and linear models for HMF yield

Source	Standard Deviation	R-Square	Adjusted R-Square
Quadratic	2.20	0.9542	0.8900
2FI	5.19	0.6445	0.3906
Linear	4.46	0.6247	0.5496

Final equation for HMF yield ($\in_{HMF}$) in terms of most significant coded factors:

$$\text{HMF yield} = +30.71 + 2.52 * \varphi_T + 5.27 * \varphi_t + 3.78 * \varphi_{Ti} + 2.60 * \varphi_C - 7.84 * \varphi_{Ti}^2 \quad (6.1)$$

Table 6. 10. ANOVA analysis of process factors for CRW conversion

Source	Sum of Square	DF	Mean Square	F-Value	P-Value	
Model	1012.32	14	72.31	14.87	< 0.0001	significant
φ_T	76.46	1	76.46	15.73	0.0027	
φ_t	333.49	1	333.49	68.59	< 0.0001	
φ_{Ti}	171.69	1	171.69	35.31	0.0001	
φ_C	81.12	1	81.12	16.69	0.0022	
$\varphi_T * \varphi_t$	0.0072	1	0.0072	0.0015	0.9700	
$\varphi_T * \varphi_{Ti}$	4.28	1	4.28	0.8814	0.3700	
$\varphi_T * \varphi_C$	13.47	1	13.47	2.77	0.1270	
$\varphi_t * \varphi_{Ti}$	1.63	1	1.63	0.3344	0.5759	
$\varphi_t * \varphi_C$	0.8836	1	0.8836	0.1817	0.6789	
$\varphi_{Ti} * \varphi_C$	0.7921	1	0.7921	0.1629	0.6950	
$\varphi_T{}^2$	2.17	1	2.17	0.4468	0.5190	
$\varphi_t{}^2$	0.1408	1	0.1408	0.0290	0.8682	
$\varphi_{Ti}{}^2$	173.64	1	173.64	35.72	0.0001	
$\varphi_C{}^2$	4.28	1	4.28	0.8798	0.3703	
Residual	48.62	10	4.86			
Cor Total	1060.93	24				

The interactive effects of TIIP precursor loading (φ_{Ti}) with reaction temperature (φ_T) implied that over the range of precursor loading considered in the present study, at any φ_{Ti}, the $\in_{HMF}$ was observed to rise with φ_T; on the contrary, at any specified φ_T, $\in_{HMF}$ was only found to increase with φ_{Ti} up to 5 wt. % (Figure 6.27). Above 5 wt. % of φ_{Ti}, further increment in φ_{Ti} resulted reduction in surface -OH group on Al_2SiO_5 and led to formation of Ti-O-Si bond (as evinced from FTIR), which in turn reduced the Bronsted acidic sites on the catalyst's surface. Although, Lewis acidic sites increased with enhancement of φ_{Ti}, nonetheless, the reduction in Bronsted acidic sites rendered lower glucose formation, which eventually resulted in lower $\in_{HMF}$. On the other hand, contour plots exhibiting interactions between φ_T with other

process parameters (φ_t, φ_C) revealed that the HMF yield was found to increase with φ_t and φ_C at any specified φ_T. Besides, at a specified φ_t, augmentation in φ_C could enhance $\in_{HMF}$ considerably. Notably, from experimental study it was also revealed that further increment of φ_C and φ_T (outside of level L_1) resulted lower $\in_{HMF}$ due to the degradation of HMF. Thus, φ_T: 70 °C; φ_t: 60 min, φ_{Ti}: 5 wt. % and φ_C: 10 wt. % were considered as the optimized process parameters, which resulted in maximum 38.37 mol % of $\in_{HMF}$.

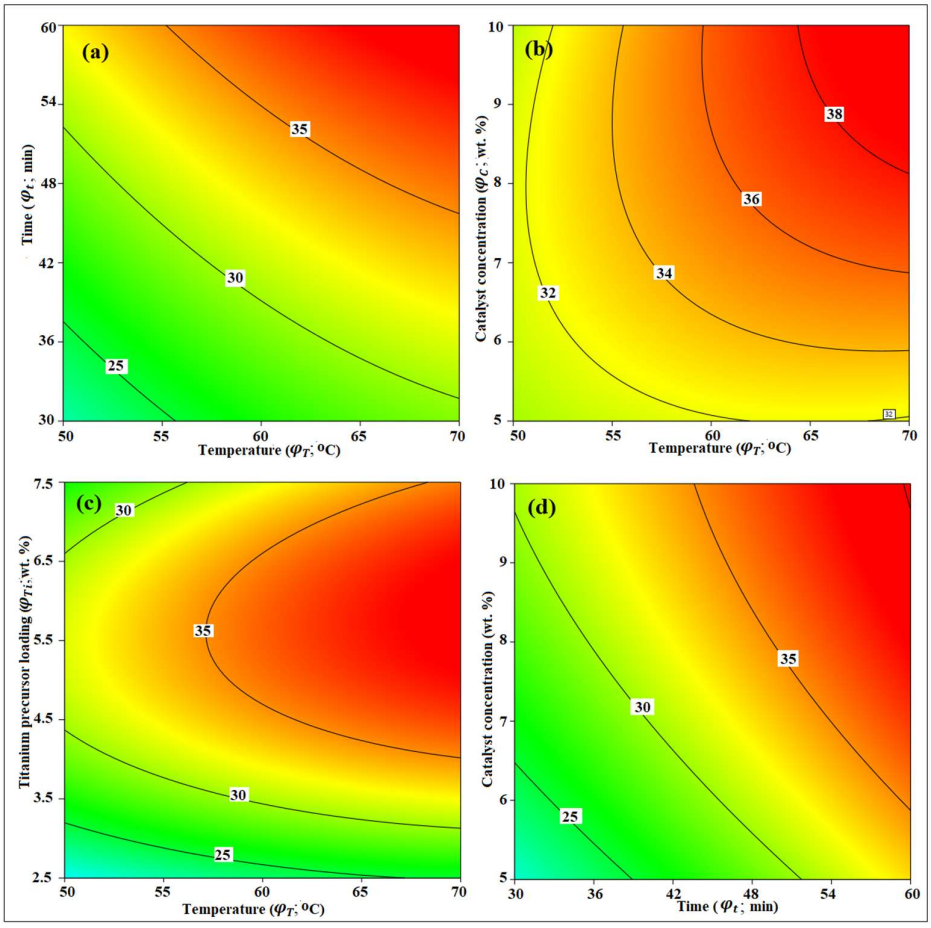

Figure 6. 27. Effects of parametric interaction on HMF yield: (a) reaction time vs temperature; (b) catalyst concentration vs temperature; (c) Titanium precursor loading vs temperature and (d) catalyst concentration vs time.

6.3.2. Catalyst characterization

6.3.2.1. XRD analysis

The XRD diffractograms of the FA_NPC* viz., FA_NPC*$^{2.5}$, FA_NPC*^{5} (FA_NPC*^{O}), FA_NPC*$^{7.5}$ and FA_NPC^{CO} along with nano-Fe^{3+}/Fe^{2+}, Al_2SiO_5 were depicted in Figure 6.28.

XRD analysis of nano-Al_2SiO_5 showed only one peak at 26.602° (JCPDS card no. 22-0018) corresponding to the amorphous phase of Al_2SiO_5, whereas peak at 31.60° representing Al_2SiO_5 appeared for all the catalysts. Furthermore, peaks at 48.15° and 54.55° representing the TiO_2 crystal (JCPDS card no. 21-1276) and those at 35.43°, 62.68° and 72.55° confirmed the presence of Fe_3O_4 (Fe^{3+}/Fe^{2+}) (JCPDS card no. 19-629) crystal in all the catalysts. Besides, the peaks conforming to TiO_2 (Ti^{4+}) intensely increased with increase in TIIP precursor loading in FA_NPC*.

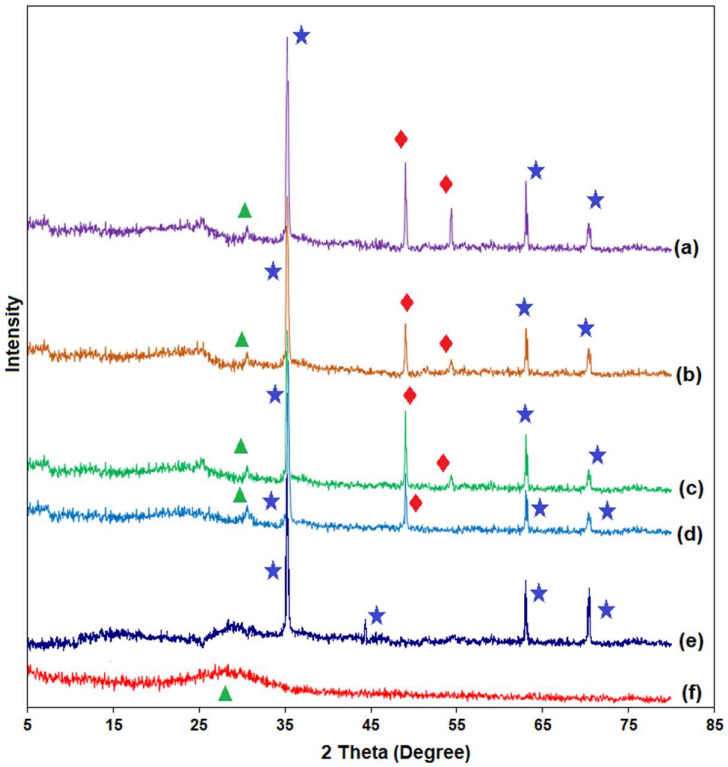

Figure 6. 28. XRD patterns of (a) FA_NPC*$^{2.5}$, (b) FA_NPC*^{5} (FA_NPC*^{O}), (c) FA_NPC*$^{7.5}$, (d) FA_NPCCO (e) Fe_3O_4 (Fe^{3+}/Fe^{2+}) and (f) Al_2SiO_5 [characteristic peaks due to TiO_2 (Ti^{4+}) (♦), Al_2SiO_5 (▲), Fe_3O_4 (★)]

6.3.2.2.FTIR Spectra

The FTIR spectra (Figure 6.29) of nano-Al_2SiO_5 exhibited a weak peak at 3740 cm^{-1} due to the terminal Si-OH group. Furthermore, FTIR spectra of the FA_NPC*, FA_NPC^{CO} and Al_2SiO_5 showed broad peaks at 3430 cm^{-1},1631.96 cm^{-1} and 1099 cm^{-1} due to the presence of surface absorbed water [50] whereas peak at 477 cm^{-1} ascribed to the bending vibrations of Si-O and Al-O [51]. Notably, the intensity of vibrational peak corresponding to 3740 cm^{-1} and 1631.96 cm^{-1} wave numbers for catalysts decreases with increment in Ti^{4+} precursor loading

which indicates ionic substitution of surface -OH group by TIIP through hydrolysis. FTIR spectra of all FA_NPC* and FA_NPC^{CO} also showed a peak at 957.55 cm^{-1}; which corresponded to vibration of Ti-O-Si [52-53]. Moreover, a peak was observed at 693.45 cm^{-1} for all the photocatalyst, which ascribed the existence of Ti-O-Ti stretching modes [54]. FTIR peak at 580 cm^{-1} established the occurrence of Fe^{3+}/Fe^{2+} nanoparticles in all FA_NPC* and FA_NPC^{CO} [55].

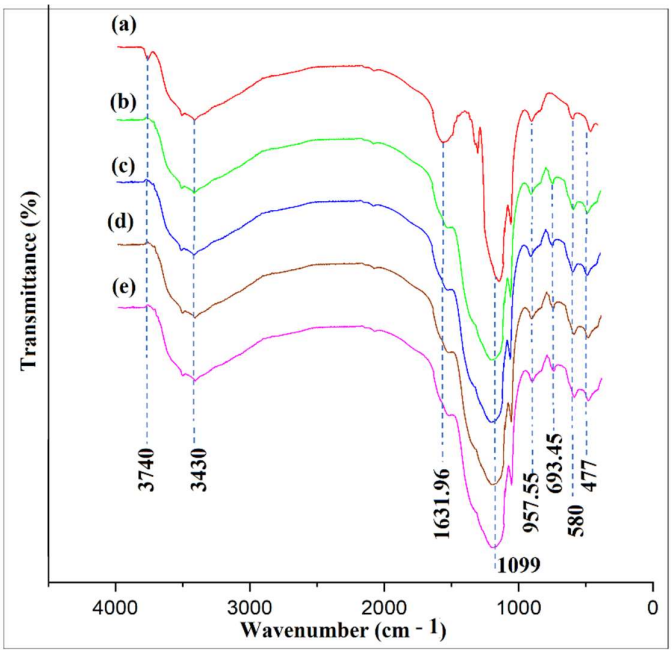

Figure 6. 29. FTIR analyses of (a) Al_2SiO_5 (b) FA_NPC*$^{2.5}$, (c) FA_NPC*^{5} (FA_NPC*^{O}) (d) FA_NPC*$^{7.5}$, (e) FA_NPC^{CO}

6.3.2.3. BET-BJH analyses

The results of BET (Brunauer-Emmett-Teller) analyses of the prepared novel FA_NPC*, FA_NPC^{CO}, nano-Fe^{3+}/Fe^{2+} and nano-Al_2SiO_5 are enumerated in Table 6.10. The specific surface areas of the FA_NPC* viz., FA_NPC*$^{2.5}$ (147.3 m^2. g^{-1}), FA_NPC*^{5} (FA_NPC*^{O}) (142.11 m^2. g^{-1}), FA_NPC*$^{7.5}$ (132.34 m^2. g^{-1}) were lower compared to the FA derived nano Al_2SiO_5 (164.426 m^2. g^{-1}); since, with increase in TIIP precursor loading, the pore (Table 6.11) of the Al_2SiO_5 got partially blocked; which rendered lower specific surface area of the catalysts compared to Al_2SiO_5. Noticeably, the specific surface area of the optimum FA_NPC^{CO} was substantially lower (89.72 m^{2}g^{-1}) compared to its THUS counterpart (142.11 m^2. g^{-1}) due to formation of larger TiO_2 particles on Al_2SiO_5 surface [as confirmed through XRD and HRTEM analyses]. From Figure 6.30, it could be evident that adsorption isotherm of

FA_NPC*^{O} corroborated with type II isotherm (IUPAC) which implied multilayer adsorption. Moreover, the optimum FA_NPC*^{O} modal pore diameter (4.1058 nm) (BJH analysis inset of Figure 6.30) indicated that the prepared catalyst under THUS was a predominantly mesoporous catalyst that exhibited only around 10.27 % micropores and 89.73 % mesopores (Figure 6.31).

Table 6. 11. Morphology and acidity of the nano-Al_2SiO_5, nano-Fe^{3+}/Fe^{2+}, FA_NPC* and FA_NPC^{CO}

Catalyst	BET analysis			NH_3-TPD (mmol NH_3· g catalyst)$^{-1}$)	XRD and HRTEM Average crystallite size (nm)
	Surface area ($m^2.g^{-1}$)	Total pore volume ($cc.g^{-1}$)	Pore diameter (nm)		
FA_NPC*$^{2.5}$	147.3	0.3460	4.5082	2.135	43.72
FA_NPC*^{O}	142.11	0.3033	4.1058	2.327	47.50
FA_NPC*$^{7.5}$	132.34	0.2738	3.7831	2.362	57.08
FA_NPC^{CO}	89.72	0.2490	3.0691	1.905	62.43
Fe^{3+}/Fe^{2+}	82.641	0.3721	5.3500		17.82
Al_2SiO_5	164.426	0.5067	6.2018		23.31

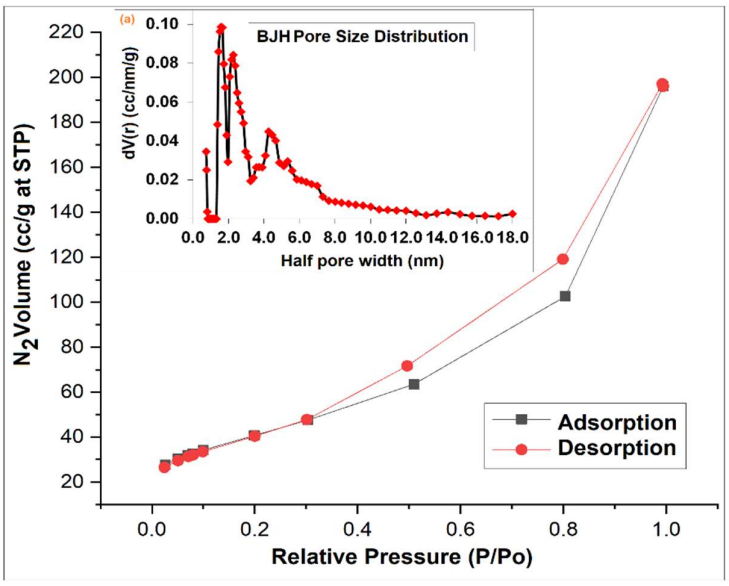

Figure 6. 30. *Pore volume vs relative pressure (P/P_0) of the optimal catalyst FA_NPC*^{O} [inset: BJH pore size distribution for the computation of modal pore diameter]*

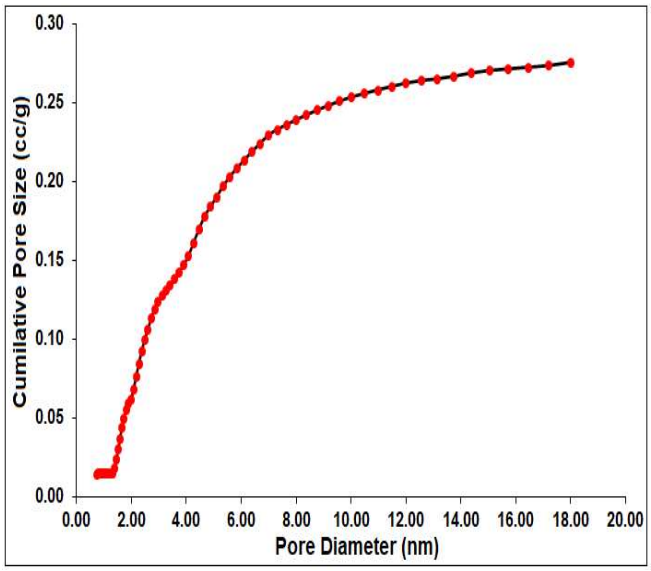

Figure 6. 31. Cumulative pore volume vs. pore diameter for the FA_NPC*^{O} catalyst.

6.2.3.4. HR-TEM analysis

Figure 6.32 displays the high-resolution transmission electron microscopic (HR-TEM) probes of the nano- Fe^{3+}/Fe^{2+}, nano-Al_2SiO_5, FA_NPC*^{O} and FA_NPC^{CO}. From Figure 6.32 (a), it could be clearly interpreted that the FA derived nano-Fe_3O_4 showed cubical structural pattern [56]. Moreover, Figure 6.32 (c), (d) and (e) demonstrated formation of core-shell like structure through incorporation of Ti^{4+} coating on nano- $Fe^{3+}/Fe^{2+}/Al_2SiO_5$ structure as a result of TIIP hydrolysis. Notably, presence of uneven distribution of nano- Fe^{3+}/Fe^{2+} within the Al_2SiO_5 matrix (Figure 6.32 (d)) as well as larger particle growth (Figure 6.32 (f)) were observed for FA_NPC^{CO} (average particle size: 62.43 nm) compared to FA_NPC*^{O} (Figure 6.32 (c)) (average particle size: 47.5 nm), which could certainly advocate for the efficacy of THUS system over CH system. Moreover, the calculated d-spacing using GATAN digital micrograph for nano Ti^{4+} (0.19 nm), Fe^{3+}/Fe^{2+} (0.253 nm), Al_2SiO_5 (0.28 nm) (Figure 6.32 (e)) well corroborated with the XRD results.

Form Figure 6.32 (c), (d) & (e), it has been clearly observed that the Fe^{3+}/Fe^{2+} nanoparticles were fully coated with Al_2SiO_5. The Al_2SiO_5 served as a barrier, preventing photo-generated electrons and holes moving from Fe^{3+}/Fe^{2+} to $Ti^{4+}$and vice versa [37,38]. As a result, Al_2SiO_5 blocked Fe^{3+}/Fe^{2+} nanoparticles from participating in the reaction, while also

preventing photo dissolution of Fe^{3+}/Fe^{2+} in the aqueous reaction media and preserving the catalyst's magnetic property (Figure 6.38).

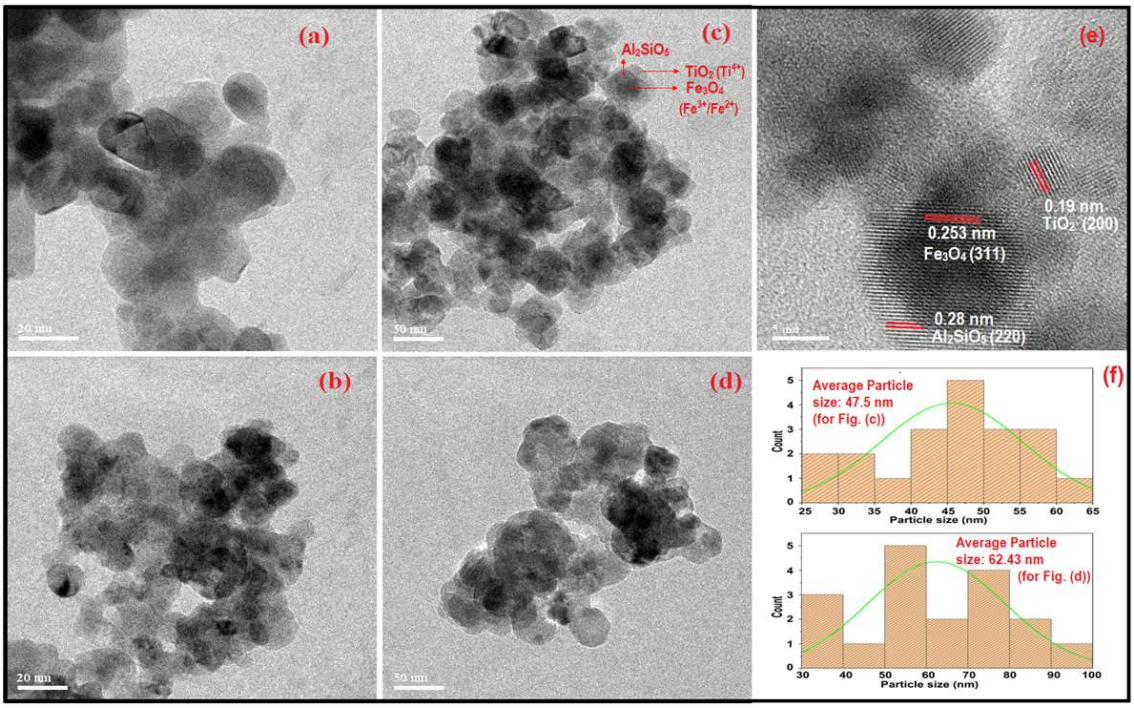

Figure 6. 32. HR-TEM images of (a) nano-Fe^{3+}/Fe^{2+} (Fe_3O_4) (b) Al_2SiO_5 (c) FA_NPC*^{O} and (d) FA_NPC^{CO} (e) FA_NPC*^{O} with lattice spacing of nano-Fe^{3+}/Fe^{2+} (Fe_3O_4), Ti^{4+} (TiO_2), Al_2SiO_5 (f) average particle size analysis for Figure 6.30. (c) and (d).

6.3.2.5. Acidity of FA_NPC and FA_NPC^{CO}*

NH_3-TPD analyses over the range 100-800°C confirmed the existences of several weak (around 150-300°C), medium (around 350-400°C) and strong (around 650-780°C) acidic sites in all FA_NPC* and FA_NPC^{CO}. Notably, Figure 6.33 (a, b & c) revealed that with increase in TIIP loading (φ_{Ti}), the NH_3 desorption peak intensity increased in lower temperature region and reduced in higher temperature zone; which evidently specified that the weak acidic sites concentration can be increased with increment in φ_{Ti} [57]. With reference to the above observations, it could also be inferred that the ionic substitution of surface -OH group by Ti and the formation of Si-O-Ti bond increased at higher φ_{Ti}. Notably, strong acidic sites could be beneficial for starch hydrolysis and fructose dehydration process whereas weak acidic sites could promote the fructose isomerization process [58].

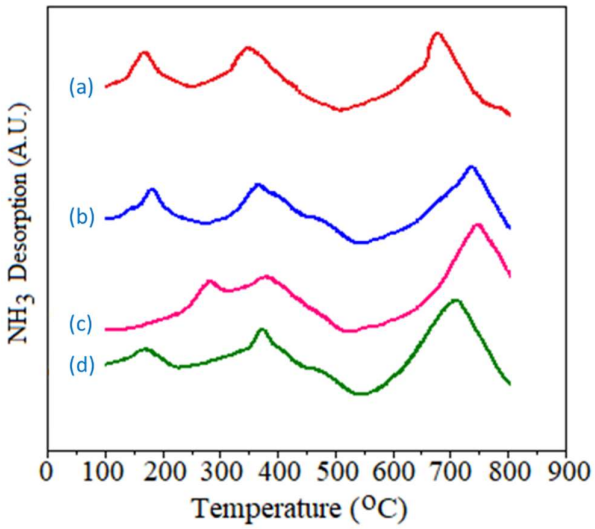

Figure 6. 33. NH_3-TPD analyses of (a) FA_NPC*$^{7.5}$ (b) FA_NPC*^{O} (c) FA_NPC*$^{2.5}$ and (d) FA_NPC^{CO}

6.3.2.6. TGA analysis

Thermal stability of the prepared uncalcined Al_2SiO_5, FA_NPC*^{O} and FA_NPC^{CO} (Figure 6.34) samples were investigated through Thermo-gravimetric analyses (TGA) in a broad range of temperature from 30 to 800 °C. A weight loss of 2.7 % and 2.4 % occurred for Al_2SiO_5 due to evaporation of moisture and interlayer water removal between 30-200°C and between 200-400°C respectively. Besides, further 8.2 % weight loss of Al_2SiO_5 (from 400°C to 600°C) could be attributed to the desorption of water from germinal silanol and vicinal silanol [59]. Noticeably, the TGA plot for both FA_NPC*^{O} and FA_NPC^{CO} exhibited around 3 % of weight loss between 200-400°C due to the breakdown of titanium precursor salt (TIIP decomposition temperature 400 °C) [60]. Moreover, both FA_NPC*^{O} and FA_NPC^{CO} also showed large amount of weight loss (11.3 %) between 400-600°C due to dehydroxylation of Al_2SiO_5, whereas no further weight loss was observed with increasing temperature. Thus, 600°C temperature was considered as calcination temperature for both the FA_NPC*^{O} and FA_NPC^{CO}. Understandably, as the CRW photo-conversion temperature (70 °C) was considerably low, the thermal decomposition of the prepared photocatalyst was unlikely to occur during the HMF production process; thus, implying high thermal stability of the prepared catalysts.

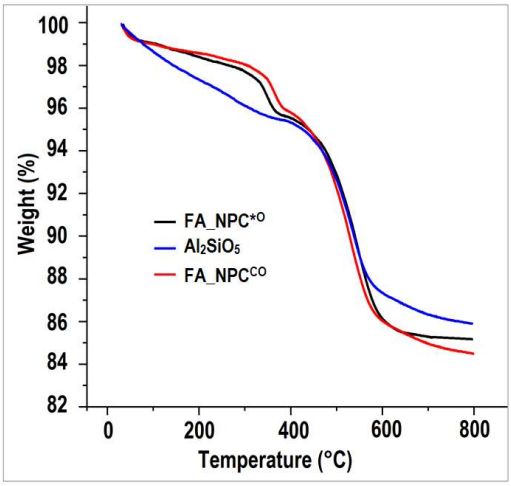

Figure 6. 34. TGA analysis of Al_2SiO_5, FA_NPC*^{O} and FA_NPC^{CO}

6.3.2.8. UV-Vis DRS analysis of FA_NPC^{O} and FA_NPC^{CO}*

The UV-Vis DRS analysis of optimal FA_NPC*^{O} and FA_NPC^{CO} were depicted in Figure 6.35 which exhibited that the THUS activated FA_NPC*^{O} possessed strong adsorption in visible region (up to 600 nm) compared to CH activated FA_NPC^{CO} (up to 535 nm). The band gap energy (Eg) for FA_NPC*^{O} (Eg = 2.78 eV) and FA_NPC^{CO} (Eg = 2.97 eV) were calculated from the reflectance spectra using Kubelka–Munk equation and Tauc plot (Figure 6.35 (a); only shows for FA_NPC*^{O}) which was much lower compared to pure TiO_2. From the above result, it could be inferred that the formation of smaller Ti^{4+} (TiO_2) nanoparticles on $Fe^{3+}/Fe^{2+}/SiO_2$ surface could form a better composite semiconductor in FA_NPC*^{O} compared to FA_NPC^{CO}, which in turn enhanced the light absorbing ability of the FA_NPC*^{O}. The computed Eg corroborated with the result obtained by Fu et al., 2019 [64].

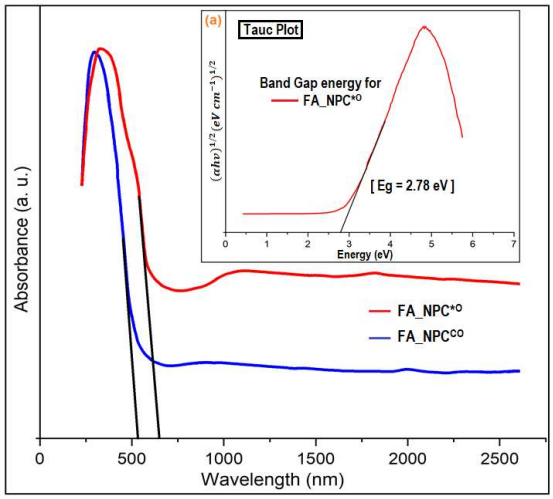

Figure 6. 35. UV-Vis DRS analysis of optimal FA_NPC*^{O} and FA_NPC^{CO}

6.3.2.7. XPS analysis

The XPS analysis of the optimal FA_NPC*^{O} (Figure 6.36) revealed the oxidation sates of its metal constituents. Firstly, peaks at 74.123 eV and 102.34 eV confirmed the presence of Al 2p and Si 2p respectively (Figure 6.36 (a) & (b)). Considering these observations, it could be ascertained that FA_NPC*^{O} contained Al_2SiO_5 [61]. XPS spectra detected two doublets at 459.76 and 465.64 eV matching with Ti $2p_{1/2}$ and Ti $2p_{3/2}$ respectively, which could be ascribed to tetragonal structure of Ti^{4+} [Figure 6.36 (c)] [62]. The binding energies located at 711eV, 724.6 eV (characterized the peaks of Fe^{3+}) and at 710.2 eV, 722.7 eV (characterized the peaks of Fe^{2+}) evidenced the presence of Fe_3O_4 (Figure 6.36 (d)) [63].

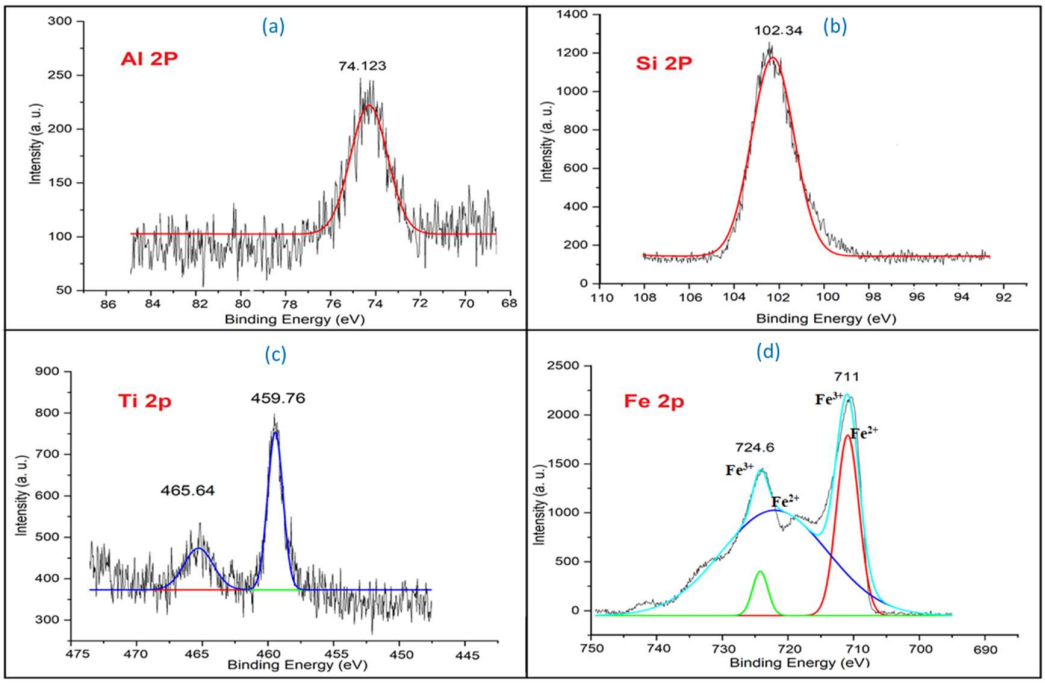

Figure 6. 36. XPS analysis of FA_NPC*^{O}

6.3.3. Performance assessment of prepared photo-catalysts in CRW conversion

Photocatalytic efficacy of the optimum catalyst FA_NPC*^{O} in comparison with its conventionally prepared counterpart, i.e., FA_NPC^{CO}, was investigated in CRW conversion process in terms of HMF yield ($\in_{HMF}$) at the Box-Behnken design derived optimal condition. From Figure 6.37, it could be clearly observed that FA_NPC*^{O} rendered appreciably higher $\in_{HMF}$ (38.37 %) over FA_NPC^{CO} ($\in_{HMF}$: 21.67 %) within optimal time of 60 min. Notably, higher glucose yield ($\in_{G}$: 31.73 mol %) was also achieved using FA_NPC*^{O} in comparison with that obtained employing the FA_NPC^{CO} ($\in_{G}$: 24.64 mol %). The superior catalytic activity

of FA_NPC*^{O} could be ascribed to the enhanced surface area, better light absorbing ability and presence of optimal coupling of Bronsted and Lewis acidic sites in FA_NPC*^{O}. Notably, the novel FA_NPC*^{O} catalyst could augment $\in_{HMF}$ considerably at relatively milder process conditions compared to the reported previous (Table 6.12).

Moreover, the CRW conversion process under different radiation systems viz., TH, US as well as conventional heating (CH) were also invested using FA_NPC*^{O} at optimized conditions (Figure 6.37 (II)). Interestingly, the combined THUS energy system showed synergistic effects as it rendered higher $\in_{HMF}$ (38.37 mol %) compared to TH (24.35 mol %) and US (9.78 mol %) alone. On the other hand, catalytic effect of Fe^{3+}/Fe^{2+} nanoparticles on $\in_{HMF}$ was also studied (Figure 6.37 (II) (d)) and the experimental study revealed that nano-Fe^{3+}/Fe^{2+} alone showed negligible effect under both THUS (1.42 mol %) and CH (not found any HMF; not shown in figure).

Table 6. 12. Comparative performance assessments of the novel catalyst with previous works in one-pot HMF production

Reference	Feedstock	Catalyst	Process conditions	$\in_{HMF}$ (mol%)
[65]	Rice waste	$SnCl_4$	140ºC and 40 minutes DMSO/water media	22.7
[66]	Bread waste	sulfonated biochar	180 °C in 20 min DMSO/water media	30.4
[67]	Starch	$CrCl_2$	120°C and 60 min	27±1
[68]	Cellulose in [EMIM]Cl	nano silica functionalized -SO_3H and -NH_2	120°C and 3h	20±1
Present Work	CRW	FA_NPC*^{O}	70°C and 60 min	38.37

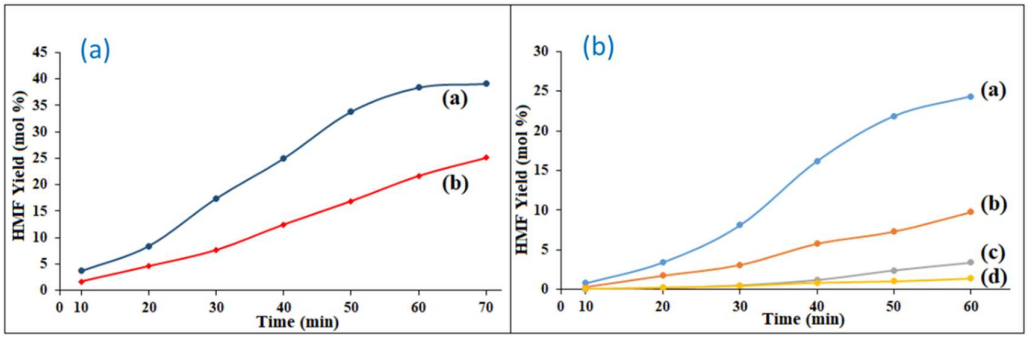

Figure 6. 37. (I) Comparative catalytic efficacy of: (a) FA_NPC*^{O} and (b) FA_NPC^{CO} under THUS; (II) CRW conversion under (a) TH (b) US (c) CH using FA_NPC*^{O} and (d) CRW conversion under THUS using nano-Fe^{3+}/Fe^{2+}

6.3.5. Reusability of the optimal FA_NPC^{O}*

The reusability test of the FA_NPC*^{O} was analysed by performing 10th consecutive batch experiments of CRW conversion process at the Box-Behnken design derived optimal condition. After each reaction cycles, the catalyst (saturation magnetizations (Figure 6.38) of FA_NPC*^{O}: 27.43 emu/g and FA_NPC^{CO}: 18.76 emu/g) could be easily recovered by a permanent magnetic bar and was subsequently washed with distilled water and oven-dried at 105 °C for 10 mins. The HMF yield ($\in_{HMF}$) decreased from 38.37 to 35.18 % after 6th recycle while no more reduction in $\in_{HMF}$ was detected in subsequent four more reaction rounds. Moreover, ICP analysis of the recycled FA_NPC*^{O} revealed that a trivial amount of Ti active sites (0.18 ppm) leached after 10th cycle. Hence, the high-performance FA_NPC*^{O} demonstrated commendable reusability attributes in CRW conversion while achieving high $\in_{HMF}$.

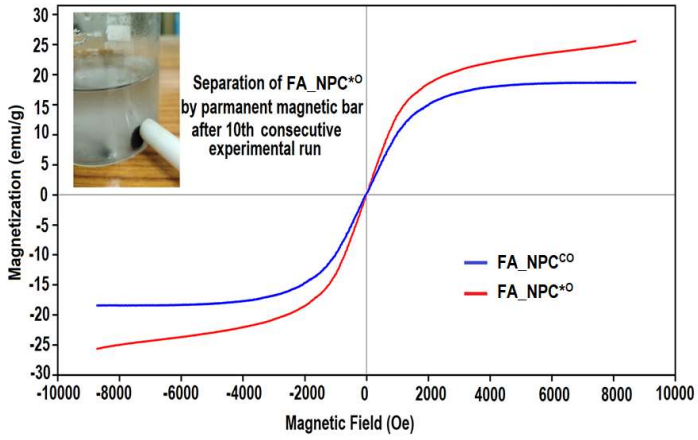

Figure 6. 38. Vibrating-sample magnetometer curve (VSM) of FA_NPC*^{O} and FA_NPC^{CO}

6.3.6. *Plausible reaction mechanism of HMF formation on FA_NPC*^{O}*

Unmodified zeolite structure (as model structure for Al_2SiO_5) and simulated catalyst's (FA_NPC*^{O}) surface structure is depicted in Figure 6.39 (a). & (b). The H^+ neutralization study using sorption module revealed that H^+ ion was bonded with the O atom of Si-Al bridge (Figure 6.39 (b)) within the catalyst's porous framework.

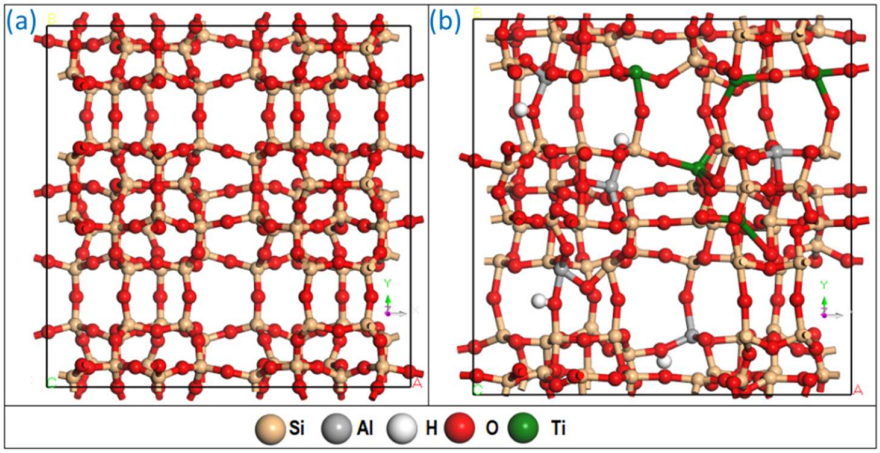

Figure 6. 39. (a) Zeolite structure (b) simulated FA_NPC*^{O} surface structure

The calculated adsorption energy of water molecule on catalysts surface was much lower (-9.074 kcal/mol) compared to those of CRW model molecules, which implied that the catalyst's surface possessed higher adsorption affinity towards H_2O than CRW model molecules. Notably, Material Studio "sorption" module analysis suggested that H_2O molecule preferred to bind with the -OH bond of the Si-Al bridge (highlighted with white colour circle in Figure 6.40 (a)). The aforementioned observations inferred that the CRW hydrolysis step could be initiated with the water adsorption on catalyst's surface, afterwards CRW hydrolysis occurred in bulk phase. Accordingly, reaction mechanism search (DFTB module of Amsterdam Modelling Suite) of this step (Figure 6.41) affirmed that water was adsorbed on -OH bond of the Si-Al bridge (which acted as a Brønsted acid site) render in H_3O^+ ion generation. Afterwards, H_3O^+ attacked 1,4-α glycosidic linkage of CRW molecule (only shown for maltose molecule) resulting in glucose formation. Vibrational analyses confirmed the intermediate transition structures (TS1 & TS2) in CRW hydrolysis step, which corroborated well with the previous study [69].

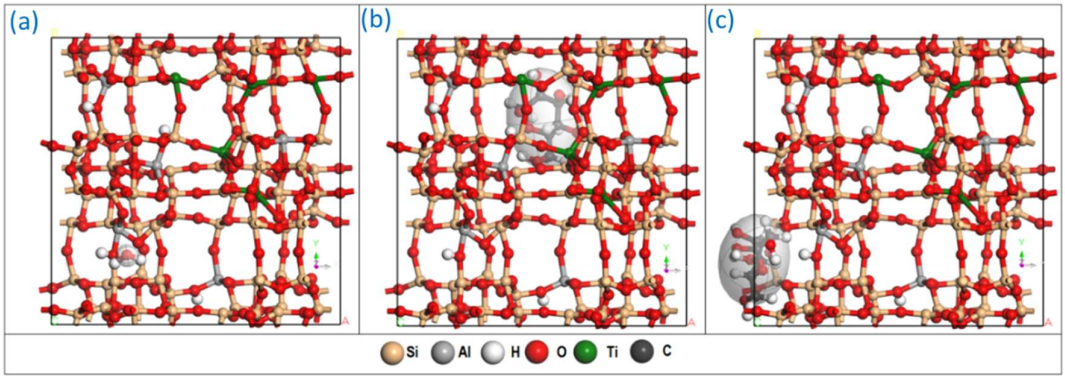

Figure 6. 40. Sorption sites for (a) water, (b) glucose, (c) fructose in FA_NPC*^{O} framework

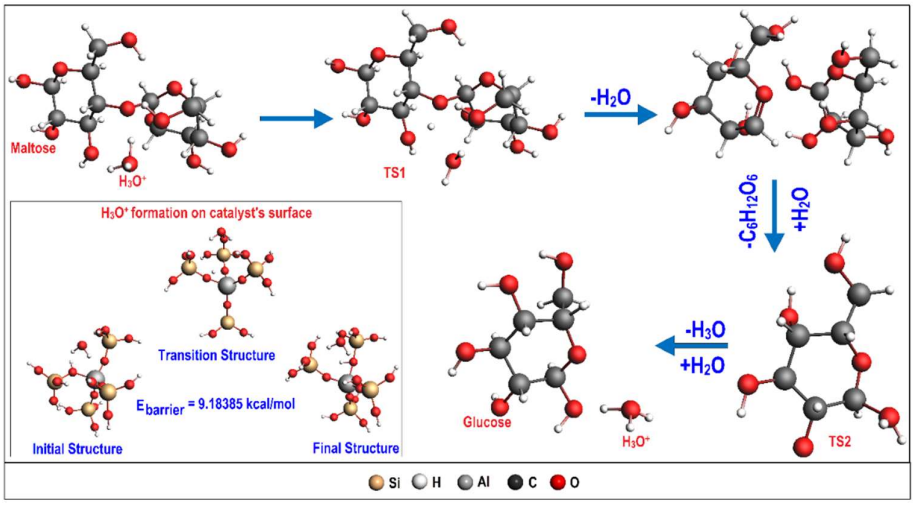

Figure 6. 41. Proposed reaction mechanism for CRW hydrolysis on FA_NPC*^{O}

"Sorption" analysis for glucose on catalyst's framework revealed that glucose molecules preferred to interact with Ti cations (Lewis acid sites) instead of -OH sites (Bronsted acid sites) of Si-Al bridge (Figure 6.40 (b)). Moreover, adsorption energy calculation inferred that catalyst's framework showed high adsorption affinity towards glucose (adsorption energy: -6.66 kcal/mol). Thus, glucose isomerisation reaction mechanism was investigated considering Ti as active site (Figure 6.42). IRC and TS search analyses revealed that glucose isomerisation reaction started with ring opening of glucose molecule on Ti-site. Then, two stages of ketone-enol isomerisation took place on the straight chain glucose molecule; followed by fructose formation through the ring closing reaction.

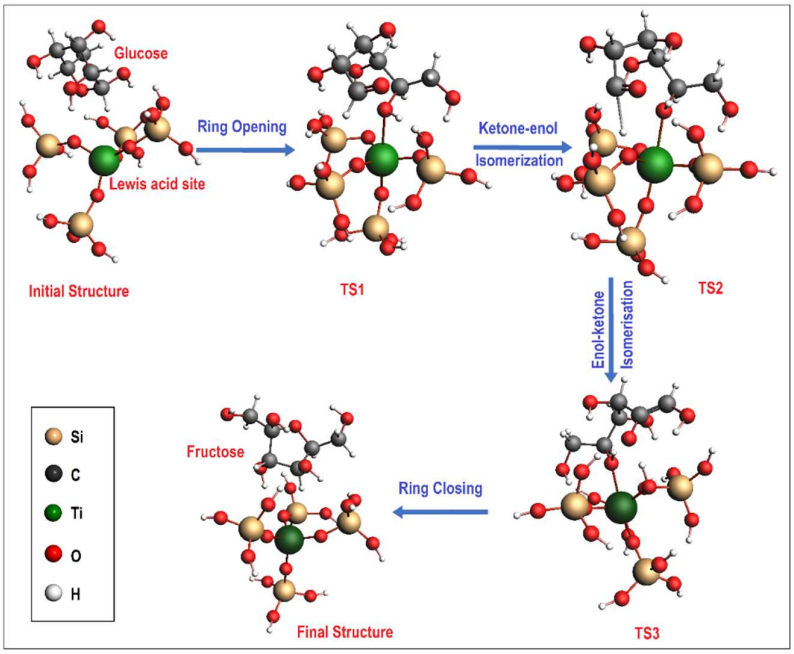

Figure 6. 42. Glucose isomerisation mechanism on FA_NPC*^{O}

In contrast, 'sorption' analysis for fructose in catalyst's framework demonstrated that fructose tended to attach near -OH site (Brønsted acid site) of Si-Al bridge (Figure 6.40 (c)), which advocated that the Brønsted acid site played a crucial role in fructose dehydration step. Interestingly, surface adsorption energy calculation suggested lower adsorption affinity of fructose (adsorption energy: -7.70 kcal/mol) compared to water. Moreover, the computed energy barrier (51.059 kcal/mol) for fructose dehydration by catalyst's surface Brønsted acidic sites (-OH site) was much higher compared to H_3O^+ formation (9.18 kcal/mol); hence, the possibility of occurrence of the fructose dehydration process by H_3O^+ was more in the bulk phase of the reaction medium compared to that on catalyst surface by -OH site of Si-Al bridge. Accordingly, the fructose dehydration mechanism (Figure 6.43) was investigated considering interaction of fructose with H_3O^+ ion in bulk phase of reaction medium. The analyses further exhibited that fructose dehydration process occurred through three stages of water eliminations along with one isomerisation step which well corroborated with the previous findings.

Although the influence of THUS energy on the current reaction mechanism has not been demonstrated through molecular dynamics, it can be inferred that US energy induces cavitation bubble collapse, high-speed microjets, and shockwaves, facilitating the penetration of reactant molecules into the micropores and mesopores of the porous FA_NPC*^{O} catalyst. On the other hand, TH energy activated the FA_NPC*O photocatalyst by promoting electron mobility from valence band to conduction band which lowers the activation energy for the

chemisorption of reactant molecules on the catalyst surface, thereby enhancing the 5-HMF yield, as confirmed by experimental observations.

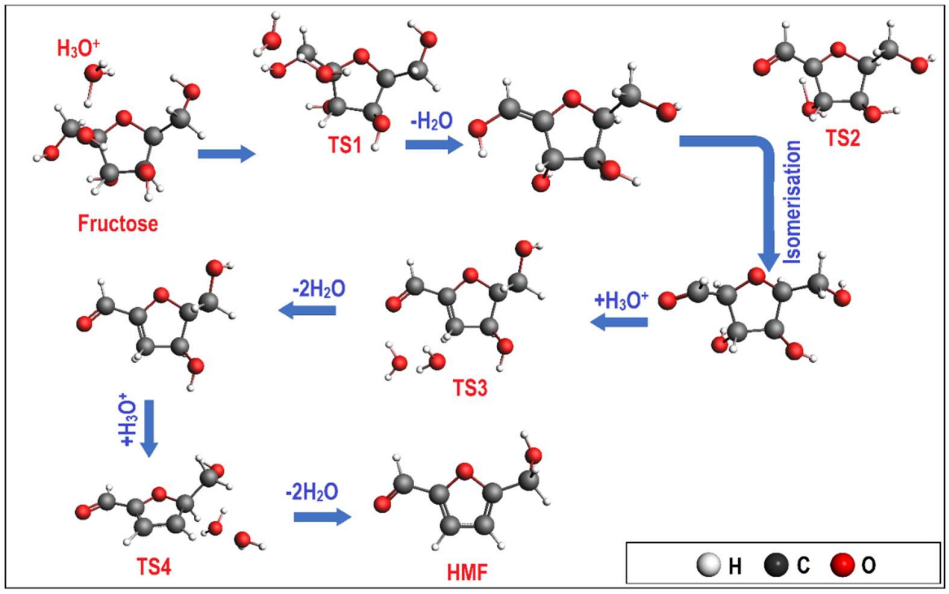

Figure 6. 43. Fructose dehydration mechanism on FA_NPC*^{O}

6.37. *LCA of photocatalytic conversion of CRW*

According to the EIA results computed through LCA methodology viz., ReCiPe Midpoint (H), the prominent impact indicators were observed to be marine ecotoxicity (METPinf), freshwater ecotoxicity (FETPinf), freshwater eutrophication (FEP), human toxicity (HTPinf), fossil depletion (FDP), marine eutrophication (MEP), particulate matter formation (PMFP), climate change (GWP100), terrestrial acidification (TAP100), metal depletion (MDP), photochemical oxidant formation (POFP) (Figure 6.44) (after normalization; unit: per person per year). The comparative environmental impact assessment results of CRW conversion process employing the FA_NPC*^{O} and FA_NPC^{CO} are depicted in Figure 6.43 (a). From Figure 6.45 (a), it could be clearly observed that the FA_NPC*^{O} catalysed CRW conversion process ensued lower environmental impacts for all indicators compared to FA_NPC^{CO}. Notably, CRW conversion process using FA_NPC*^{O} with recycling up to 10th cycle, shows much less impacts than CRW conversion without catalyst recycling process. Furthermore, from Figure 6.45 (b), it was observed that catalyst preparation (contribution rages: 32.60-47.65 %, where ethanol contributed 80 %), CRW processing with di-ethyl ether (contribution rages: 22.86-33.44 %), HMF purification (contribution rages: 16.68-24.51%, where butanol contributed 75 %), waste water treatment (contribution rages: 1.44-13.21 %) are the foremost contributors to the total environmental impacts in the FA_NPC*^{O} catalysed CRW conversion process. Thus, recycling

of organic solvents viz., ethanol, di-ethyl ether and butanol or usages of more eco-friendly solvent could reduce the overall environmental impacts and make the process more sustainable.

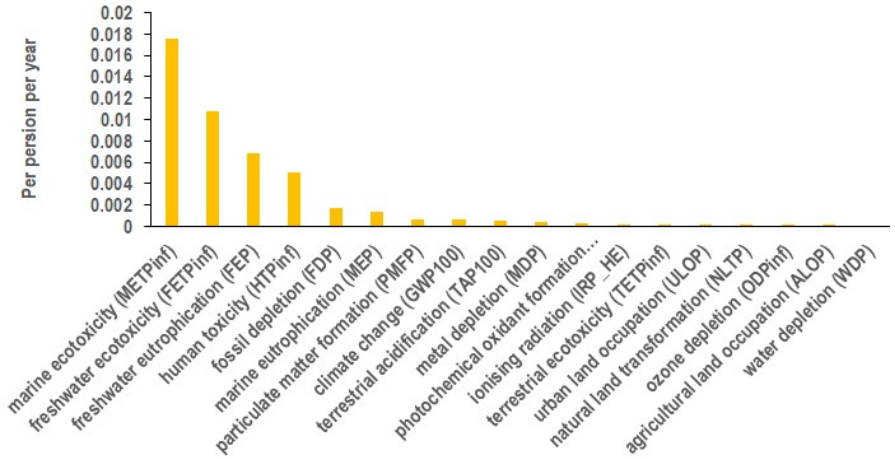

Figure 6. 44. EIA results of photocatalytic CRW conversion using FA_NPC*^{O}

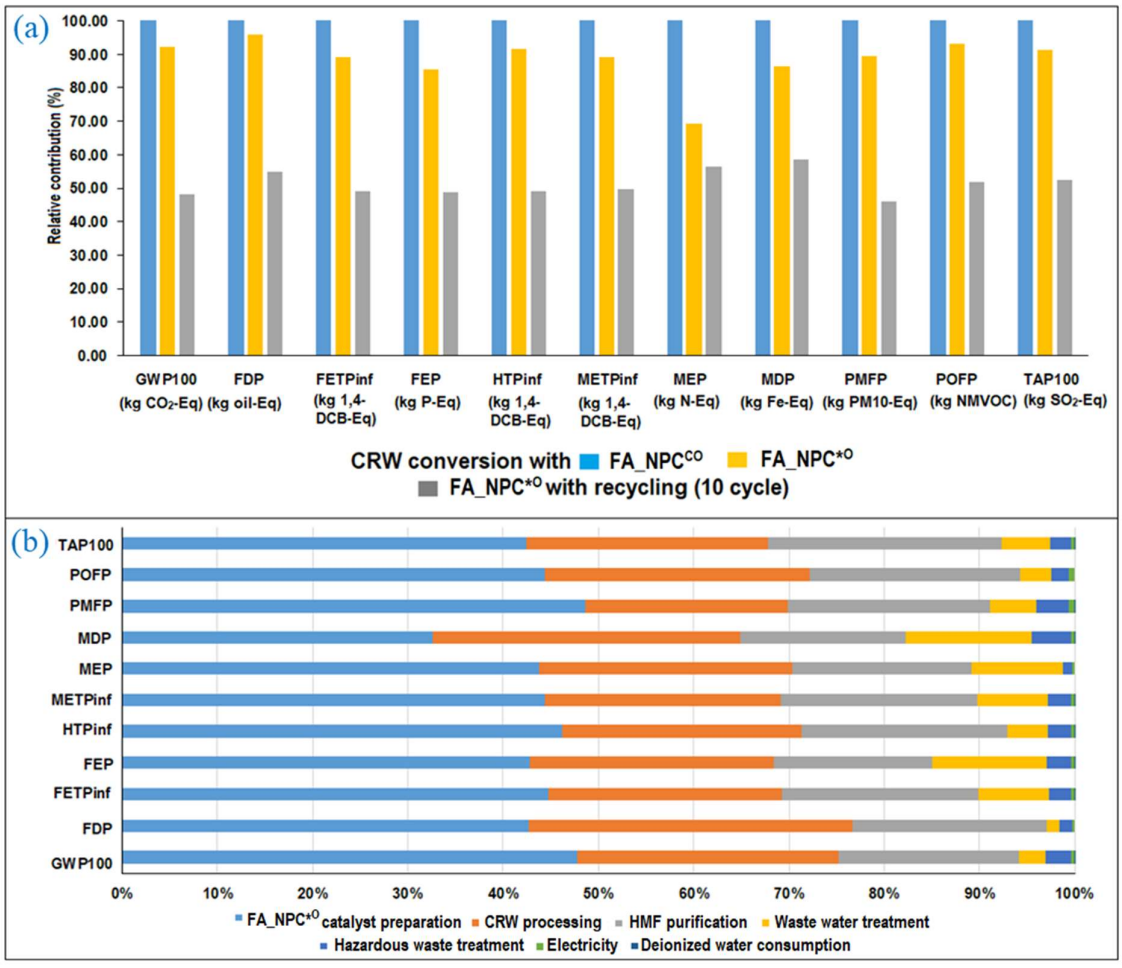

Figure 6. 45. (a) Comparative environmental impact analyses for CRW conversion process using FA_NPC*^{O}, FA_NPC^{CO} and FA_NPC*^{O} with recycling (up to 10 cycle) [the maximum result of each indicator was set to 100 %] (b) Relative percentage contributions of different process inputs in CRW conversion process employing optimal FA_NPC*^{O}.

6.4. Activity 4:

ENERGY-EFFICIENT AND ECO-FRIENDLY CONTINUOUS PRODUCTION OF 5-CMF IN A UV-ULTRASOUND IRRADIATED CATALYTIC PACKED BED REACTOR: HETEROGENEOUS KINETICS, REACTOR SIMULATION AND LCA ANALYSIS

6.4.1. Optimization of 5-CMF synthesis process parameters in UVUS-BR

Analysis of variance analysis (ANOVA) of 5-CMF synthesis process factors in UVUS-BR indicated that the $\emptyset_T$ and $\emptyset_{ChCl/SS}$ were statistically significant factors (p-value< 0.05) (Table 6.13). Notably, Table 6.14 revealed that the process factors with higher Δ values showed stronger influence on the response factor (Y_{CMF}). Accordingly, the order in which the relative significance of the process factors on the response (Y_{CMF}) could be arranged as: $\emptyset_{ChCl/SS} > \Omega_T > \Omega_t > \emptyset_{S101/TiO_2}$. Moreover, the highest S/N ratio value for each process factor was denoted by an asterisk (Table 6.13), which showed that the optimized process condition for the 5-CMF synthesis process in UVUS-BR was 5 ($\emptyset_{ChCl/SS}$), 80 °C (Ω_T), 60 min (Ω_t) and 1.5 ($\emptyset_{S101/TiO_2}$), which results the highest possible Y_{CMF} of 60.54 mol %.

Table 6. 13. ANOVA of 5-CMF synthesis process

Source	DF	Adj. SS	Adj. MS	F-Value	P-Value
Regression	4	855.000	213.750	8.64	0.030
$\emptyset_T$	1	400.167	400.167	16.17	0.016
$\emptyset_t$	1	37.500	37.500	1.52	0.286
$\emptyset_{S101/TiO_2}$	1	0.667	0.667	0.03	0.878
$\emptyset_{ChCl/SS}$	1	416.667	416.667	16.84	0.015
Error	4	99.000	24.750		
Total	8	954.000			

Table 6. 14. Response Table for Signal to Noise Ratios (larger is better)

Level	$\emptyset_T$	$\emptyset_t$	$\emptyset_{S101/TiO_2}$	$\emptyset_{ChCl/SS}$

L_{-1}	28.82	29.84	30.42	29.24
L_0	31.44	31.73*	31.62*	30.60
L_1	32.96*	31.65	31.19	33.38*
Δ	4.14	1.88	1.20	4.14
Rank	2	3	4	1

Effects of individual ultrasonic (US) and ultraviolet (UV) energy on 5-CMF yield study revealed that using US energy, a 5-CMF yield of 7.8 mol% was achieved, accompanied by a 39 mol% yield of 5-HMF. In contrast, UV energy, applied without US (with heating provided through conventional means), produced a 5-CMF yield of 41.50 mol%, with no detectable 5-HMF. When UV energy was employed without conventional heating or US energy, the yield of 5-CMF was negligible, at less than 2 mol% whereas only conventional heating produced 5.6 mol % 5-CMF yield with 17 mol% of 5-HMF.

6.4.2. Effect of process parameters on Y_{CMF}

In Figure 6.46 (a), the effect of $\emptyset_{S101/TiO_2}$ on Y_{CMF} was illustrated which indicated that initially, as $\emptyset_{S10\ /TiO_2}$ increased up to 1.5 wt. %, Y_{CMF} exhibited an upward trend. However, beyond this point, Y_{CMF} started to decrease monotonically as $\emptyset_{S101/TiO_2}$ continued to increase. Interestingly, no 5-HMF was found when only TiO_2 photocatalyst was used and consequently no 5-CMF was formed. On the other hand, when only S-101 used, 33.46 mol % of Y_{HMF} was produced and negligible amount of 5-CMF yield (< 5 mol %) was observed. So, from the above observation it could be concluded that chlorination of 5-CMF mostly happened in presence of TiO_2 photocatalyst. Additionally, Figure 6.46 (b) demonstrated that with increasing $\emptyset_{ChCl/SS}$, the Y_{CMF} monotonically increased. Notably, it was found that without ChCl no 5-CMF was produced, which suggested that Cl^- ion of ChCl acts as a chlorine source in the 5-HMF chlorination process, which could be activated through photo-oxidation by the photogenerated hole on the TiO_2 surface under UV radiation [70].

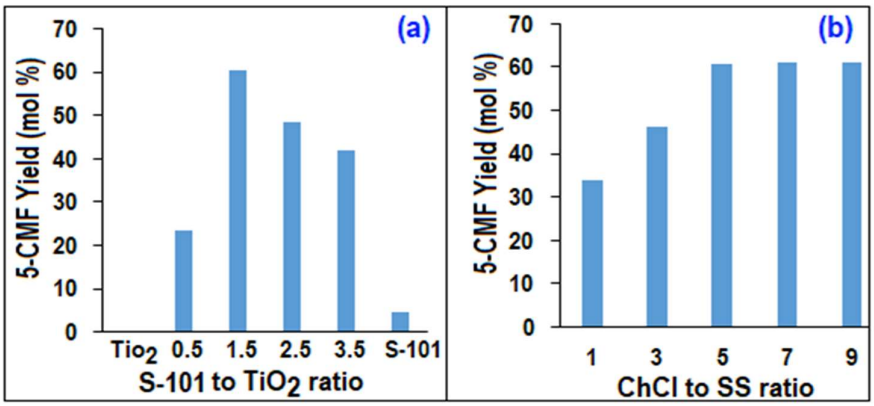

Figure 6. 46. (a) S-101 to TiO_2 ratio and (b) ChCl to SS ratio effect on 5-CMF yield

Figure 6.47 (a) demonstrated that Y_{CMF} increased with increasing temperature ($\emptyset_T$) up to 80°C; after that the Y_{CMF} decreased due to degradation of 5-CMF or 5-HMF to Levulinic acid which could be easily observed from Figure 6.47 (b). Notably, the maximum achievable temperature in UVUS-BR was limited to 85 °C. As a result, the 5-CMF synthesis process was investigated up to this temperature constraint. On the other hand, the 5-CMF yield monotonically increased with increasing reaction time up to 60 min (Figure 6.47 (b)); afterwards Y_{CMF} started to decrease and increase in Levulinic acid yield was observed.

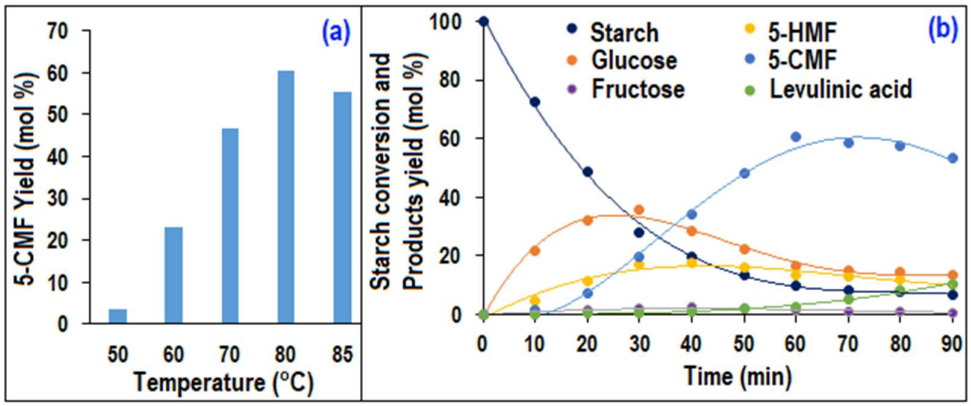

Figure 6. 47. Effect of (a) temperature and (b) time on 5-CMF yield

6.4.3. Effect of extracting solvents on 5-CMF yield

In order to investigate the impact of various extracting solvents on the isolation of 5-CMF, a selection of common halogenated solvents (DCE, DCM, Chloroform) and non-halogenated solvents (Toluene, cyclohexane, MIBK) was utilized. The findings, presented in Figure 6.48 (a), indicate that DCE, among the halogenated organic solvents, demonstrated the highest efficiency in isolating 5-CMF (yield: 65.4; purity: 97± 0.5 %). Conversely, among the non-

halogenated solvents, cyclohexane exhibited a promising effect in the isolation of 5-CMF (Y_{CMF}: 60.54; purity: 96 %).

Based on extracting organic solvents efficacy in terms of isolated 5-CMF yield from SS and energy requirement for 1 kg of solvent recycling through vacuum evaporation (Table 6.15), a comparative life cycle analysis was performed. During LCA analysis it was assumed that 5% of solvent was loss during recycling. The results indicated that DCM and chloroform exhibited significantly higher environmental impacts concerning climate change and human toxicity indicators (Figure 6.48 (b)) when compared to other solvents. Notably, in terms of 5-CMF yield isolation during the synthesis process, DCE and cyclohexane demonstrated higher efficacy. Consequently, their environmental impact contributions were further compared (Figure 6.48 (c)). The analysis showed that cyclohexane contributed less environmental impacts in terms of climate change compared to DCE. However, both solvents had similar environmental impacts in terms of human toxicity. As a result, cyclohexane was identified as a promising extracting solvent for the 5-CMF synthesis process in future studies. Notably, the price of the solvents is an important factor in selecting a suitable solvent for 5-CMF extraction process, but proper recycling of the solvent can render the price factor insignificant, despite its initial importance in solvent selection.

After selecting the cyclohexane as suitable extracting solvent, 5-CMF yields form different starting monosaccharides such as fructose, glucose were also evaluated at optimized conditions; where it was observed that maximum 81.15 and 68.5 mol % of 5-CMF yield can be achieved form fructose and glucose respectively.

Table 6. 15. Solvents properties, price [71] and energy requirement for recycling 1 kg of solvent

Solvents	Boiling point (K) at 1.01325 bar	Price ($/ton)	Heat capacity (KJ/Kg. K)	Energy required to recycle 1 kg solvent (KJ)
DCM	312.75	355.45	1.28	50.74
DCE	357.15	369.90	1.06	89.04
Chloroform	233.15	289.80	1.02	61.27
Toluene	383.75	988.83	1.89	209.19
Cyclohexane	353.90	921.78	1.69	136.59
MIBK	389.15	1722.53	2.17	252.25

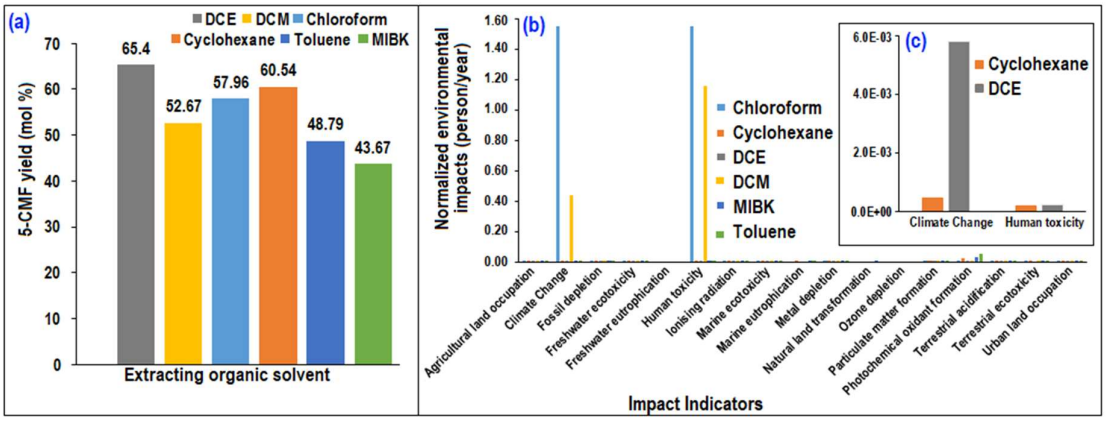

Figure 6. 48. (a) extracting solvent efficacy in terms of 5-CMF yield (b) significant impact indicators associated with solvent recycling process (c) environmental impacts of cyclohexane and DCE in climate change and human toxicity

6.4.4. Kinetics parameters evaluation for 5-CMF synthesis process

The calculated **Ω** values for all reaction steps in the synthesis process of 5-CMF (0.084 for SS hydrolysis, 0.042 for glucose dehydration, and 0.11 for the 5-HMF chlorination step) consistently remain below 0.15. These results indicate that, as per the Mears criterion, the impact of external mass transfer resistance between reactants and catalyst particles is negligible throughout the various reaction steps involved in producing 5-CMF. Moreover, at optimized organic-aqueous volume ration (1.953), the partition coefficient values of 5-HMF and 5-CMF were determined, and the obtained partition coefficients for 5-HMF ($\emptyset_H$) and 5-CMF ($\emptyset_C$) were 0.061 and 485, respectively.

The SS to 5-CMF conversion kinetic data obtained from UVUS-BR at the optimal reaction conditions were fitted in the formulated kinetic models employing MATLAB R2014a (Table 6.16) at different temperatures. From Table 6.16, it can be observed that the formulated kinetic models demonstrated close proximity to experimental data with high R^2 adj. ($\geq$ 0.93) and low RMSE values ($\leq$ 6.15E-07). Accordingly, the kinetic rate constants and equilibrium constants for different reactions steps involved in 5-CMF synthesis process were evaluated and tabulated in Table 6.15. Finally, the rate constants of involved reaction steps at different temperatures were used to determine the activation energies (E) and pre-exponential factors (E_0), which are align well with the previous studies [72,73], providing further validation for the accuracy of the findings. The evaluated activation energies for SS hydrolysis, Glucose dehydration and 5-HMF chlorination step were 79.04 kJ/mol, 61.55 kJ/mol and 52.2 kJ/mol, respectively.

Table 6. 16. Estimated kinetic parameters for ER model of SS hydrolysis in UVUS-BR

Temperature	k_1 [ml/ mol. s]	k_2 [1 / s]	k_3 [1 / s]	K_{a1}	K_{d1}	K_{a2}	K_{d2}	R^2	R^2_{adj}	RMSE
333	6.4E-3	5.4E-4	1.1E-2	5.62E-3	2.73E-3	5.87E-3	2.95E-3	0.98	0.95	6.15E-07
343	2.25E-2	1.12E-3	1.95E-2	5.57E-3	2.78E-3	5.81E-3	3.1E-3	0.99	0.93	5.77E-07
353	3.2E-2	1.9E-3	3.2E-2	5.5E-3	2.83E-3	5.74E-3	3.23E-3	0.99	0.99	5.64E-07

6.4.5. 5-CMF synthesis in UVUS-RPBR system

The 5-CMF synthesis process in UVUS-RPBR was initially explored using various reactor bed porosities (Figure 6.49) while maintaining the feed space time in UVUS-RPBR at the same level as the batch optimized time (60 min), under otherwise optimized batch process conditions viz. 5 ($\emptyset_{ChCl/SS}$), 80 °C (Ω_T), and 1.5 ($\emptyset_{S101/TiO_2}$). Moreover, the UV and US specific power inputs for UV (0.40 watt/ml) and US (2.5 watt/ml) energy system were also kept at the same level as in the batch process using regulators. According to Figure 6.49 (a), it can be observed that at constant space time of 60 min, the UVUS-RPBR with reactor bed porosity of 0.56 could render almost identical 5-CMF yield (58.75 mol %) compared to the UVUS-BR (60.54 mol %). On the other hand, when the bed porosity remained constant at 0.56, any liquid hourly space velocity (LHSV) exceeding 9.95 ml/g cat. h (total syringe pump infused rate of 126 ml/h) leads to an observable reduction in the yield of 5-CMF (according to Figure 6.49 (b)), as anticipated. Besides, a decrease in the yield of 5-CMF was also observed at LHSV below 9.95 ml/g cat. h (Figure 6.49 (b)), which could potentially be attributed to the degradation of 5-CMF into levulinic acid due to uneven mixing of organic phase with aqueous phase. The reduced axial mixing in the biphasic fluid occurred due to a lower Peclet number when the advective transport rate decreased at lower LHSV, which in turn, led to a lesser extraction of CMF from the aqueous phase into the organic phase, ultimately resulting in an increased levulinic acid yield.

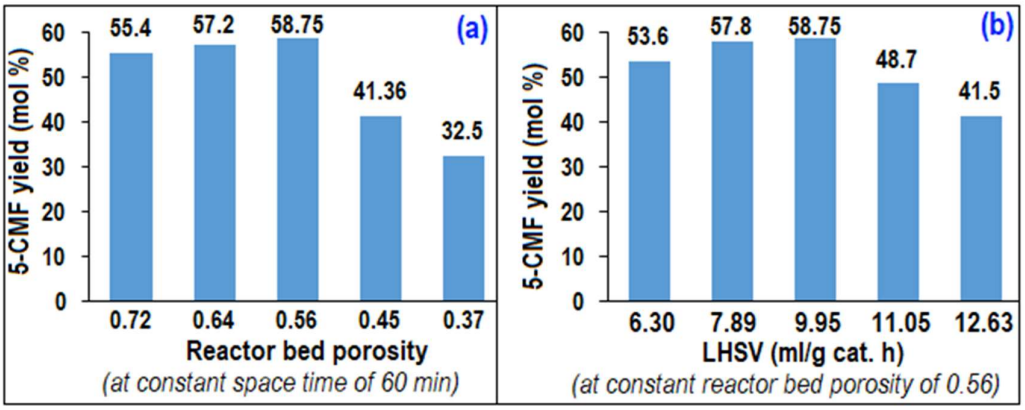

Figure 6. 49. Effect of (a) bed porosity and (b) LHSV on 5-CMF yield in UVUS-RPBR

The reusability of the catalysts also studied in UVUS-RPBR, which revealed that the glass beads supported TiO_2 photocatalyst and S-101 showed no decrease in activity (in terms of 5-CMF yield) up to 6 h, with a constant space time yield of 0.0191 mol/L. h (same as 58.75 mol % of 5-CMF yield). Afterwards, a decline in the catalyst's activity was observed (< 6 % in terms of 5-CMF yield at 7^{th} h), despite the absence of any detectable leaching of TiO_2 from the glass beads. This decrease in activity could potentially be attributed to the surface poisoning of TiO_2 caused by chloride ions. Notably, the used glass beads supported TiO_2 photocatalyst can be easily recycled by simply heating it at 120 °C in an oven furnace for one hour.

6.4.6. Effect of US and UV on RPBR performance

The UV-RPBR (without US; heating was done with the help of conventional heating) rendered only 41.50 mol % 5-CMF yield which is 29 % less compared to that achieved in UVUS-RPBR at otherwise optimized condition. From this result, it could be interpreted that the nonideality in RPBR could be greatly reduced using ultrasound generated acoustic cavitation by enhancing the mass transfer rate and reducing the liquid reactant channelling [74,75]. On the other hand, significantly low amount (< 8 mol %) of 5-CMF yield (and 5-HMF yield > 39 mol %) was achieved in US-RPBR (without UV) which clearly advocate the fact that the chlorination 5-HMF was primarily occurred under UV energy. These above results indicated that synergistic effect of US and UV irradiation system in RPBR significantly enhanced the 5-CMF yield (58.75 mol %) compared to the individual US (< 8 mol %) and UV (41.50 mol %) irradiation system. Notably, UVUS-RPBR consumed less energy (0.274 kWh) compared to UV-RPBR (0.55 kWh) to achieve the 41.50 mol % 5-CMF yield, which advocates the energy efficiency of UVUS system over UV-conventionally heated system.

Based on the results obtained from UV-RPBR, we were motivated to delve deeper into the influence of ultrasound (US) on the flow pattern in RPBR. To achieve this, pulse tracer experiments were carried out in the RPBR with and without the US system. The exit-age distribution function (E(t)) of the tracer in the UVUS-RPBR and UV-RPBR (without US) were calculated as a function of time and the obtained results are demonstrated in Figure 6.50. The results revealed that at RPBR bed porosity of 0.56 and tracer flow rate of 126 ml/h (superficial velocity: 0.0023 cm/s), the obtained mean space time was 58.6 min for UVUS-RPBR and 50.9 min for UV-RPBR and the corresponding Peclet number (*Pe*) and dispersion number (*D*) for UVUS-RPBR and UV-RPBR were 119.83, 45.34 and 0.00028, 0.00076, respectively. Comparison of dispersion numbers inferred that the nonideality in the RPBR reactor could be substantially reduced (more than 60 %) by incorporating the US system which eventually increased the efficacy of UVUS-RPBR in terms of 5-CMF yield.

Notably, for comparison, a tracer test was also conducted in a cylindrical packed-bed reactor to examine the impact of ultrasound (US) under conditions of equal bed porosity and inlet flowrate as the RPBR. The results showed a mean space time of 55.21 min, with a Peclet number (Pe) of 72.08 and a dispersion number (D) of 0.00047. These findings clearly demonstrate that ultrasound energy exhibited superior performance in reducing the nonuniformity of velocity distribution in the RPBR when compared to the cylindrical packed bed reactor.

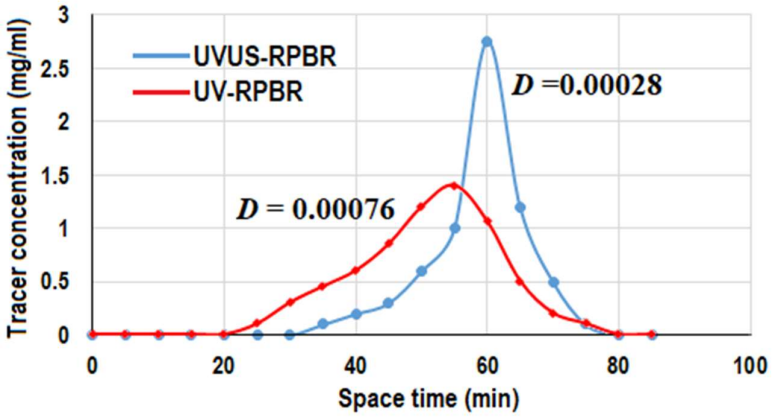

Figure 6. 50. Tracer concentration vs time data for UVUS-RPBR and UV-RPBR

6.4.7. Simulation study of UVUS-RPBR using ANSYS Fluent software

The local distribution of the flow variables viz., pressure and velocity in UVUS-RPBR is not possible to evaluate through standard experimental techniques. However, this data can be readily obtained through CFD simulations. ANSYS Fluent software was utilized to conduct

simulations on both the UVUS-RPBR and UV-RPBR systems, aiming to investigate the influence of ultrasound (US) on the distribution of local velocity and pressure.

In the simulation study, the deformation of the rectangular (150 mm × 50 mm × 30 mm) bed reactor (RBR) without packing was first studied during ultrasonication using ANSYS Workbench. In ANSYS Workbench, the Transient Structural module was integrated with the Fluent module, as depicted in Figure 6.51. To apply voltage to the piezoelectric material, APDL commands were employed, and the material properties were provided in Figure 6.52. The results indicated that when the RBR was exposed to US energy at a feed flow rate of 126 ml/h, it exhibited a maximum vibration amplitude of 0.237 mm, as illustrated in Figure 6.53.

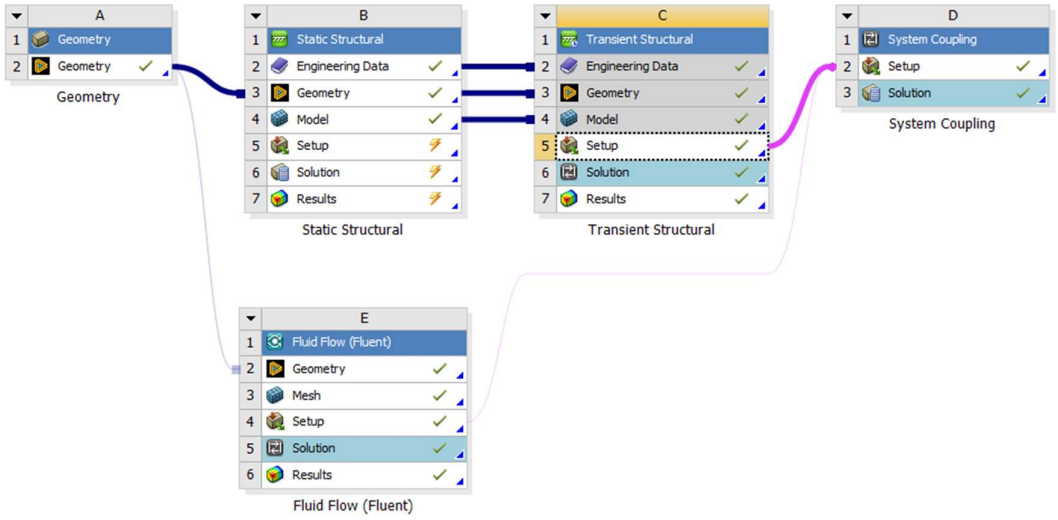

Figure 6. 51. ANSYS Transient Structural and ANSYS Fluent coupling for the simulation of UVUS-RPBR

	A	B	C	D	E
1	Property	Value	Unit		
2	Material Field Variables	Table			
3	Density	4500	k...		
4	Isotropic Secant Coefficient of Thermal Expansion				
6	~~Isotropic Elasticity~~				
7	Derive from	Young's Modulus ...			
8	Young's Modulus	2E+11	Pa		
9	Poisson's Ratio	0.3			
10	Bulk Modulus	1.6667E+11	Pa		
11	Shear Modulus	7.6923E+10	Pa		
12	Orthotropic Elasticity				
13	Young's Modulus X direction	7.856E+10	Pa		
14	Young's Modulus Y direction	7.856E+10	Pa		
15	Young's Modulus Z direction	6.2498E+10	Pa		
16	Poisson's Ratio XY	0.28798			
17	Poisson's Ratio YZ	0.45204			
18	Poisson's Ratio XZ	0.45204			
19	Shear Modulus XY	3E+10	Pa		
20	Shear Modulus YZ	2.6E+10	Pa		
21	Shear Modulus XZ	2.6E+10	Pa		
22	Strain-Life Parameters				
30	S-N Curve	Tabular			
34	Tensile Yield Strength	2.5E+08	Pa		
35	Compressive Yield Strength	2.5E+08	Pa		
36	Tensile Ultimate Strength	4.6E+08	Pa		
37	Compressive Ultimate Strength	0	Pa		

Figure 6. 52. Piezoelectric material properties

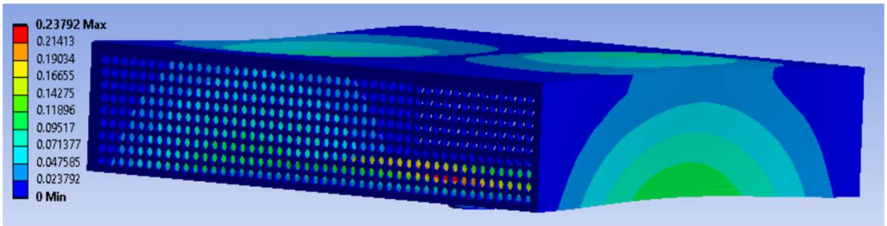

Figure 6. 53. Simulated vibration of RPBR under US energy

Once the vibrational amplitude of the rectangular bed reactor (RBR) was assessed, the transient simulation study (Figure 6.54 and Table 6.17) focusing on the local velocity and pressure distribution within the RPBR (RBR with catalyst packing) was investigated. To simplify the computational complexity, a 2D computational domain of 150 mm in length and 30 mm in height was considered.

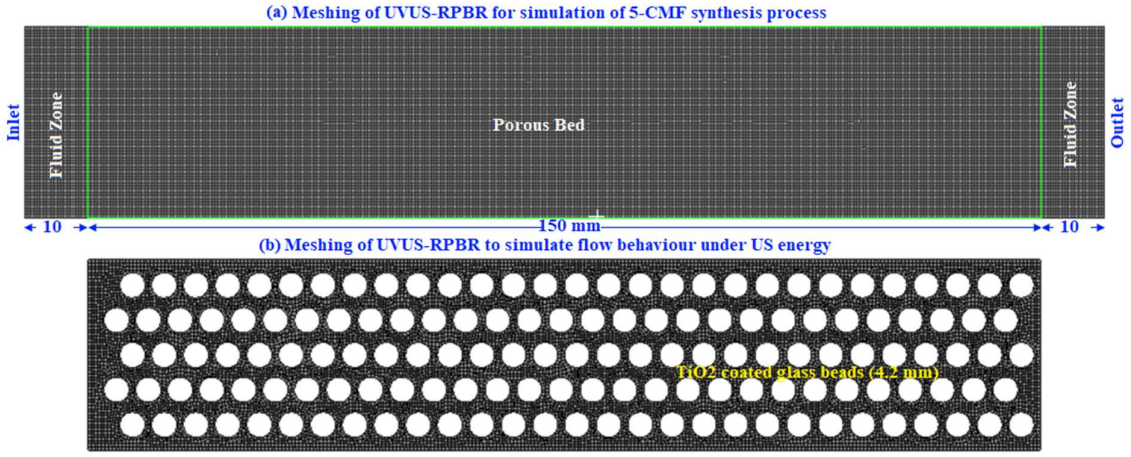

Figure 6. 54. Meshing of UVUS-RPBR for the simulation study

Table 6. 17. Operational parameter for transient simulation

Parameters	Values
Temperature (K)	353
Pressure (Pa)	101325
Superficial aqueous liquid feed velocity (m/s)	4.1E-5
Reactor width (m)	0.05
Reactor height (m)	0.03
Reactor length (m)	0.15
Bed porosity	0.56
TiO_2 coated glass beads diameter (m)	0.0042
Mesh size (m)	0.0005
Step size	0.1
Time steps	36000

In the RPBR, the flow pattern was significantly influenced by the presence of large glass bead coated TiO_2 particles (with a diameter of 4.2 mm) compared to the S-101 fine particles (with a diameter of 0.1 mm). Therefore, to model the RPBR with bed porosity of 0.56, the 2D domain was filled with equally spaced 145 circles with diameter of 4.2 mm. Finally, to simulate the vibrational motion of each circle and the reactor wall with amplitude of 0.237 mm and frequency of 20 kHz during ultrasonication, a user defined function (UDF) was used and the flow variables in UVUS-RPBR were simulated.

The simulation results demonstrated that under US energy, the RPBR exhibited uniform local pressure (Figure 6.55) and velocity (Figure 6.56) distributions, aligning well with the findings from the experimental residence time distribution (RTD) study (low dispersion number: 0.00028). On the other hand, in the UV-RPBR case, Figure 6.55 & 6.56 revealed non-uniform pressure distribution and nearly zero velocity between the circles, indicating that the introduction of US energy substantially enhanced the non-ideal behaviour of the RPBR.

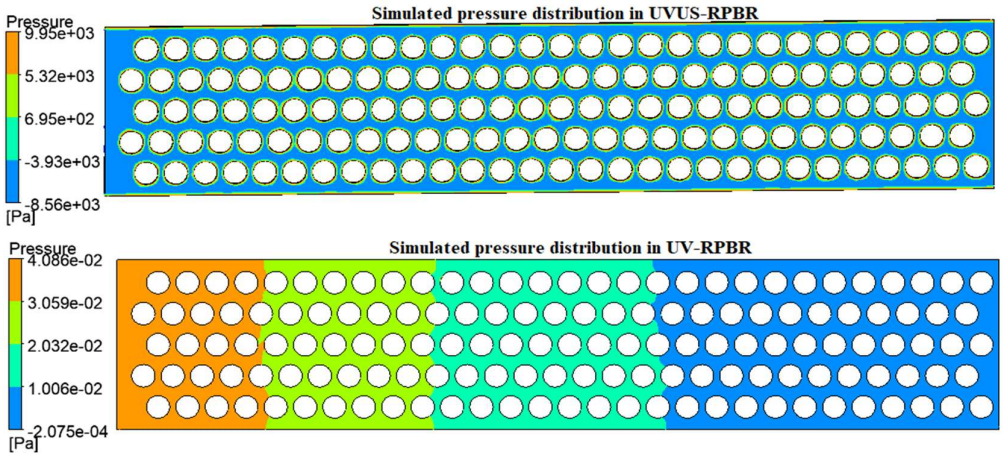

Figure 6. 55. Pressure distribution in UVUS-RPBR and UV-RPBR

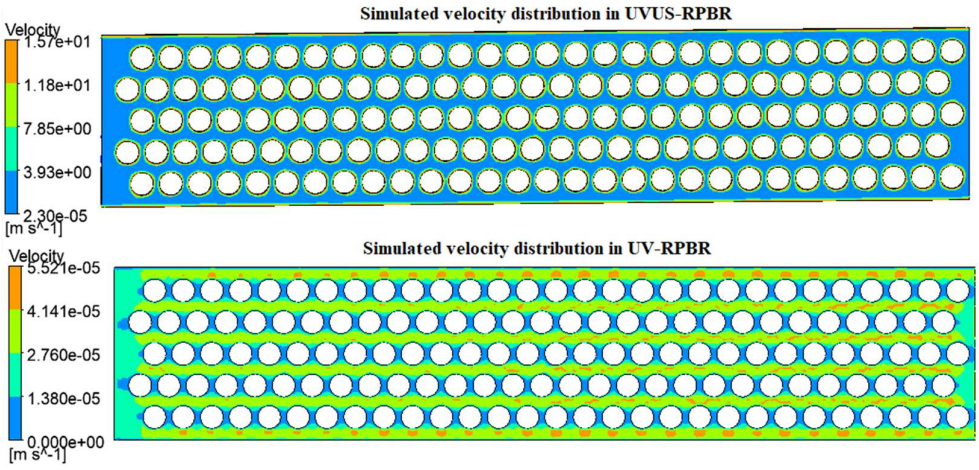

Figure 6. 56. Velocity distribution in UVUS-RPBR and UV-RPBR

After analysing the effect of US energy on RPBR in the simulation study, the batch reaction kinetic parameters were employed to simulate the 5-CMF reaction in UVUS-RPBR. Here, the RPBR was considered as porous bed with porosity of 0.56 and internal resistance of 0.1. Moreover, it was also considered that the SS to 5-CMF synthesis reaction steps only

occurred in the porous bed (on catalyst's surface). Finally, a user defined function with DEFINE_VR_RATE macro was used to simulate the 5-CMF synthesis process at optimized condition. Figure 6.57 showed the simulated molar concentration of SS (C6h11o5), glucose (C6h12o6), 5-HMF(C6h6o3) and 5-CMF (C6h5o2cl) across the reactor length of the UVUS-RPBR which are similar to experimentally obtained glucose, 5-HMF and 5-CMF yield of 13.2 mol %, 14.60 mol % and 60.54 mol % at the reactor outlet.

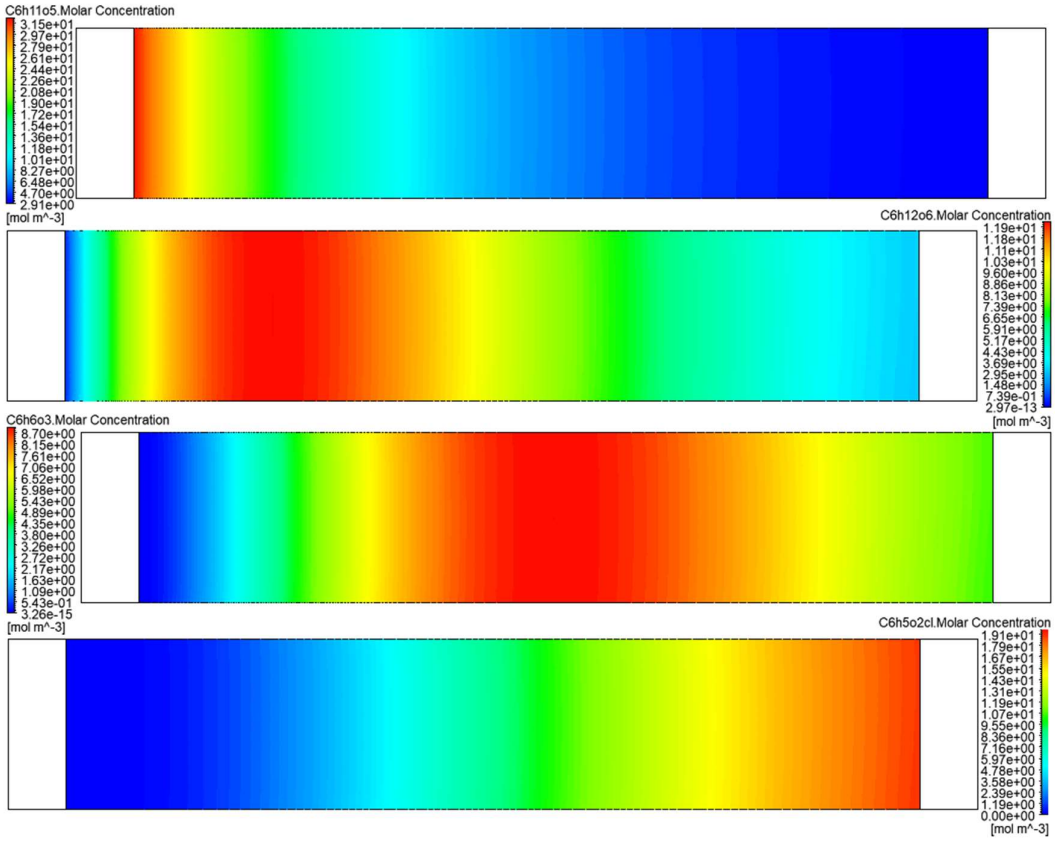

Figure 6. 57. Simulated SS, glucose, 5-HMF and 5-CMF mole fraction across reactor length

6.4.8. Environmental impacts of SS to 5-CMF synthesis process

The LCA analysis of overall 5-CMF synthesis process revealed that the most prominent normalized (person / year) "ReCiPe Midpoint (H) V1.13" indicators (Figure 6.58 (a)) were marine ecotoxicity, freshwater ecotoxicity, human toxicity, freshwater eutrophication, marine eutrophication and photochemical oxidant formation. Moreover, Figure 6.58 (b) demonstrates the individual contributions of each process to the overall environmental impacts. It reveals that, among all the process, the 5-CMF synthesis process in UVUS-RPBR had the highest environmental impacts in all the impact indicators, except for the photochemical oxidant formation indicator. The utilization of soluble starch was identified as the main cause of the

highest environmental impacts observed in the 5-CMF synthesis process. To mitigate these impacts, exploring alternatives to this particular starch source, such as lignocellulosic biomass, could be beneficial. Notably, the product separation process is found to have the most significant impact on the photochemical oxidant formation indicator, primarily attributed to the presence of cyclohexane. Figure 6.59 illustrated comparative environmental impacts of optimized 5-CMF synthesis process associated with UVUS-RPBR and UV-RPBR systems, which clearly revealed that the UVUS-RPBR resulted lowest impacts in all prominent indicators in comparison with UV-RPBR.

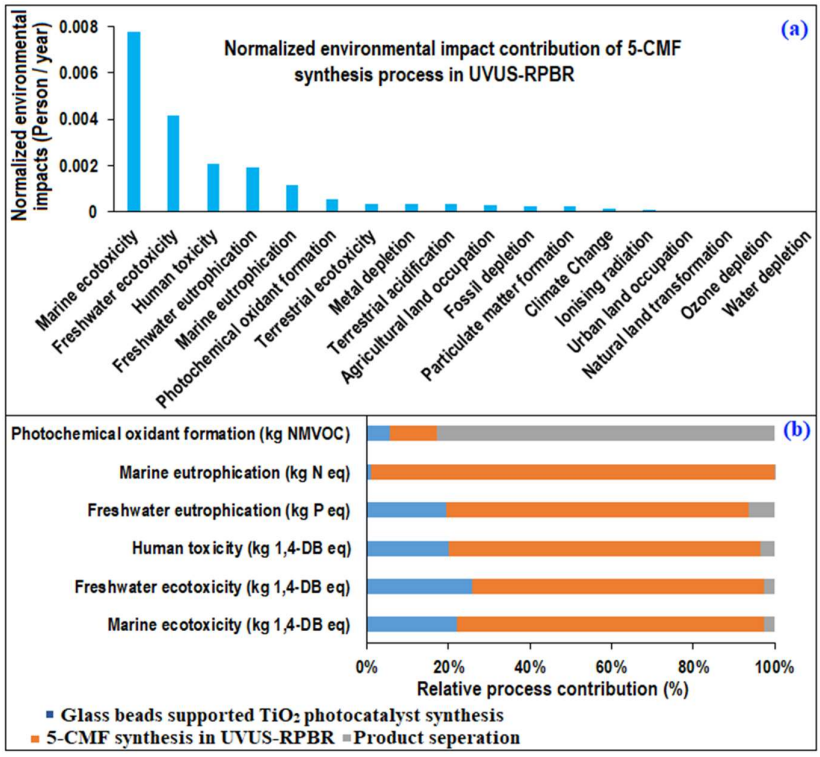

Figure 6. 58. (a) normalized environmental impacts of 5-CMF synthesis process (b) relative process contributions in total environmental impacts of 5-CMF synthesis process.

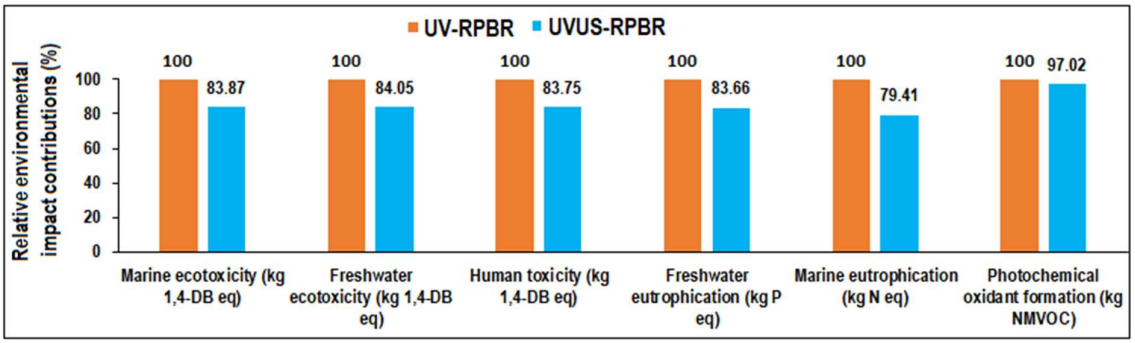

Figure 6. 59. Environmental impacts of 5-CMF synthesis process associated with UVUS-RPBR and UV-RPBR. [the maximum result of each indicator was set to 100 %]

6.4.9. Comparative study with previously reported relevant works on 5-CMF synthesis process

The present work's results are compared with previous studies, which are tabulated in Table 6.18. Although, no work was reported on 5-CMF synthesis in packed bed reactor involving reusable heterogeneous TiO_2 and S-101 dual catalysts. Although, Brasholz et al. [76] and Kohl et al. [77] achieved high 5-CMF yields (>80 mol %) from fructose using concentrated HCl (32%) in a small high pressure (10 bar) plug flow reactor (reaction volume: 10 ml; inner diameter: 1 mm) with short residence times (< 2 min); however, the authors noted that at reaction temperatures exceeding 80°C, pressure fluctuations within the reactor temperatures exceeding 80°C, pressure fluctuations within the reactor became significant due to the formation of humics. Moreover, in present study, we obtained higher 5-CMF yields at much lower pressure (atmospheric pressure) from glucose compared to the work by Brasholz. Besides, when synthesizing 5-CMF from fructose, we achieved the same yield as reported by Chen et al. [78] at a lower temperature using the reusable heterogenous catalyst (S-101 and TiO_2) under the synergistic effects of UV-US irradiation; which could mitigate harmful environmental impacts. Significantly, this study achieved greater space-time yields (mol/L. h) of 5-CMF from all the utilized feedstocks (fructose, glucose, and SS) compared to those reported Chen et al. [78]

Table 6. 18. Comparative assessment with the previous works on 5-CMF synthesis process

Reaction condition	Catalyst	Heating system	Extracting solvent	Feedstock	5-CMF yield (mol %)	Space time yield of 5-CMF (mol/L. h)	Ref.
120°C; 30 min; Batch reactor	ChCl-$AlCl_3 \cdot 6H_2O$-oxalic acid	Conventional	DCE	Fructose	86	0.023	78
				Sucrose	80	0.021	
				Glucose	70	0.019	
				Cellulose	30	0.008	
				Bamboo	29	0.0077	
100°C; 1.67 min; PFR	HCl	Conventional	DCM	Fructose	81	0.132	76
				Glucose	58	0.184	
90°C;1.5 min; PFR	HCl	Conventional	DCE	Fructose	85	0.215	77
80°C; 60 min Batch reactor	S-101 and TiO_2; ChCl	UVUS Specific power input: 2.9 watt/ml	Cyclohexane	Fructose	86.0	0.028	This work
				Glucose	72.5	0.0235	
				SS	60.54	0.020	

80°C; 60 min Packed bed reactor	S-101 and TiO_2; ChCl (Bed porosity: 0.56)	UVUS Specific power input: 2.9 watt/ml	Cyclohexane	Fructose Glucose SS	86.0 72.0 58.75	0.028 0.0235 0.0191	This work

6.5. Activity 5:

ENVIRONMENTALLY SUSTAINABLE ETHYL LEVULINATE SYNTHESIS FROM DELIGNIFIED SUGARCANE BAGASSE USING TERNARY EUTECTIC SOLVENT UNDER MW-XENON IRRADIATION: ENGINE PERFORMANCE & EMISSION ASSESSMENT

6.5.1. Optimization of EL synthesis process

Analysis of variance (ANOVA) of one pot EL synthesis in MWXER indicated that the Ω_P, $\Omega_{FeCl_3/CA}$ and $\Omega_t$were statistically significant factors (p-value< 0.05) (Table 6.19). Notably, Table 6.20 revealed that the process factors with higher Δ values showed stronger influence on the response factor (Ω_{EL}). Accordingly, the order in which the relative significance of the process factors on the response (Ω_{EL}) could be arranged was: Ω_P>$\Omega_{FeCl_3/CA}$>Ω_t>Ω_{XE}. Moreover, the highest S/N ratio value for each process factor was denoted by an asterisk (Table 6.20), which showed that the optimized process factors were 300 W (Ω_P), 1 mol/mol ($\Omega_{FeCl_3/CA}$), 90 min(Ω_t), 150 W (Ω_{XE}); which provided a maximum experimental 61.3 mol % EL yield with selectivity of 87.70±0.5 % (other byproducts were glucose (yield: 5.6 mol %), 5-HMF (yield: 1.6±0.5 mol %), Levulinic acid (yield: 1.4 mol %))in MWXER.

Table 6. 19. *Analysis of variance analysis (ANOVA)*

Source	DF	Adj. SS	Adj. MS	F-Value	P-Value
Regression	4	752.5	188.1	373.05	0.0001
Ω_P	1	656.4	656.4	1301.7	0.0001
Ω_{XE}	1	1.8	1.8	3.60	0.131
$\Omega_{FeCl_3/CA}$	1	51.0	51.0	101.21	0.001
Ω_t	1	43.2	43.2	85.67	0.001
Error	4	2.0	0.504		
Total	8	754.5			

Table 6. 20. S/N ratio of EL synthesis process

Level	Ω_P	Ω_{XE}	$\Omega_{FeCl_3/CA}$	Ω_t
L_{-1}	28.9	31.4	30.78	30.80
L_0	31.8	31.5	32.28*	31.6*
L_1	33.8*	31.6*	31.68	31.24
Delta	4.86	0.17	1.51	1.44
Rank	1	4	2	3

6.5.2. Individual parametric effects on EL synthesis process

After optimization, individual impact of MW and XE on EL synthesis process at optimized condition were investigated. Figure 6.60 (a) demonstrates that in the MW-irradiated system, the yield of EL showed a continuous increase as the MW power was raised up to the optimal level of 300 Watts. With higher MW power, there is a more pronounced modification in the internal energy of the reacting molecules, resulting in a greater reduction in activation energy [79], which in turn, facilitates easier chemical reactions. However, beyond this point, the EL yield began to decline with higher MW power, possibly attributed to the formation of humin as a result of excessive MW input. On the other hand, the EL yield monotonically increased with increasing XE power (Figure 6.60 (b)), but beyond the optimum XE power, the increase in EL yield was negligible. Notably, from Figure 6.60 (c), it could be observed that synergistic effect of MW and XE irradiation system significantly enhanced the EL yield (61.3 mol %) compared to the individual MW (34.52 mol %) and XE (22.67 mol %) irradiation system. Moreover, without MW and XE, the conventional reaction system only yields 12.8 mol % of EL. The enhanced EL synthesis in the MWXE system results from the synergistic effect of accelerated microwave-induced heating with TADES, utilizing dipolar rotation and ionic conduction [80], and activation energy reduction in reacting molecules through internal energy modification via MW and XE energy absorption by TADES.

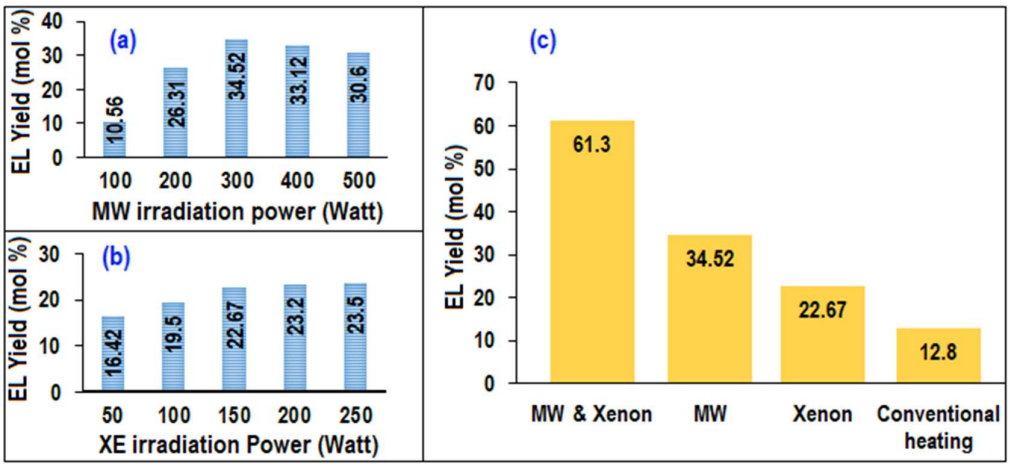

Figure 6. 60. Effect of (a) MW power (b) XE power on EL yield (c) EL yield (Reaction conditions:1 mol/mol ($\Omega_{FeCl_3/CA}$), 90 min (Ω_t), TADES to PSCB ratio: 5 wt./wt.) under individual irradiation system

The impact of the $FeCl_3$ to CA mol ratio ($\Omega_{FeCl_3/CA}$) on EL yield was depicted in Figure 6.61 (a), revealing that the maximum EL yield was achieved at $\Omega_{FeCl_3/CA}$ of 1. This observation can be rationalized by referring to Table 6.21, where it was noted that the TADES at $\Omega_{FeCl_3/CA}$ of 1 (ChCl-$FeCl_3^{1.5}$-$CA^{1.5}$) exhibited the highest Hemmett acidity, thereby enhancing the EL yield. Interestingly, when the EL synthesis process was performed using a commercial ionic liquid (BMIMCl) under identical reaction conditions, only a 43.2 mol % EL yield was obtained. This finding implies that the utilization of the optimal TADES could be advantageous compared to conventional ionic liquids for EL synthesis in the MWXER system. Furthermore, there was only a marginal increase in the EL yield when the reaction time was extended beyond the optimal level. The analysis of the effect of reaction temperature on EL yield, as depicted in Figure 6.61 (b), indicated that beyond a reaction temperature of 90 °C, the EL yield began to decrease, possibly due to the formation of humin at higher temperatures.

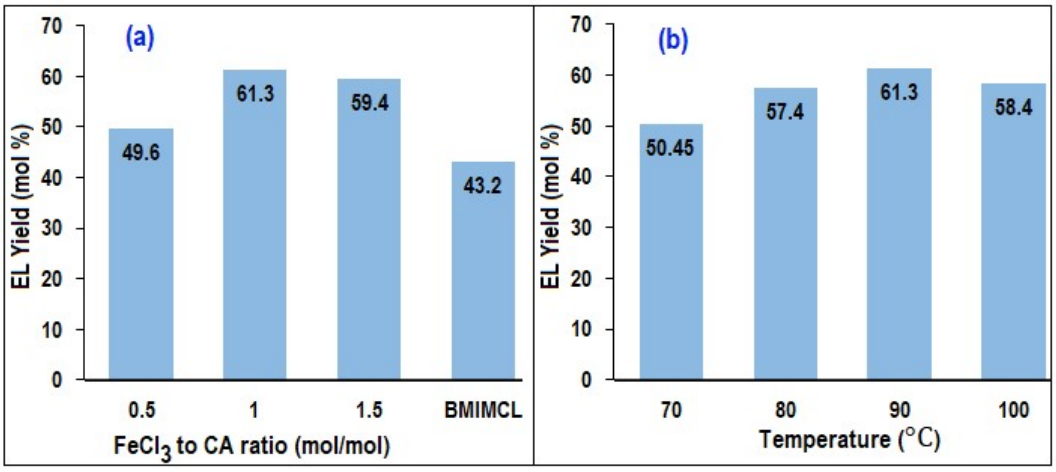

Figure 6. 61. Effect of (a) $FeCl_3$ to CA ration and (b) Temperature on EL yield (Reaction conditions: 300 W (Ω_P), 90 min (Ω_t), 150 W (Ω_{XE}), TADES to PSCB ratio: 5 wt./wt., BMIMCl to PSCB ratio: 5 wt./wt.)

6.5.3. Property of synthesized TADES

Physicochemical properties such as density, freezing point, Hemmett acidity, refractive index and dissipation factor of TADESs were shown in Table 6.21. The optimal TADES (ChCl-$FeCl_3^{1.5}$-$CA^{1.5}$) showed highest Hemmett acidity compared to other TADES. Interestingly the dissipation factor for MW energy (2.45GHz) of optimum TADES was also higher than that of the other TADESs, indicating its ability to convert a maximum amount of MW energy into heat. The combination of higher Hemmett acidity and dissipation factor in the optimal TADES contributes to achieving the maximum EL yield. Furthermore, it was observed that all the prepared TADES efficiently absorbed a broad range of UV-Visible light up to a wavelength of 550 nm with intense peak at 360 nm which suggested the presence of photoactive complex of $FeCl_4^-$ in the prepared TADES [81]. This characteristic indicates that the TADES effectively absorbs XE radiation during the EL synthesis process, thereby enhancing the EL yield.

Table 6. 21. Physicochemical properties of TADES

Properties	Density ($g.cm^{-3}$)	Freezing Point (°C)	Hemmett Acidity (H_0)	Refractive index (η)	Dissipation Factor (tan(δ))
ChCl-$FeCl_3^1$-CA^2	1.58	14 ± 1	0.84	1.33	0.427
ChCl-$FeCl_3^{1.5}$-$CA^{1.5}$	1.60	14 ± 1	0.92	1.35	0.546
ChCl-$FeCl_3^{1.8}$-$CA^{1.2}$	1.64	14 ± 1.5	0.88	1.36	0.538

Following the analysis of the physicochemical properties of TADESs, the thermal stability and photostability of the optimal TADES were examined. For the investigation of photostability, the optimal TADES was kept under XE irradiation at otherwise identical reaction conditions without reactants for several hours. Subsequently, the FTIR analysis of the optimal TADES before and after the photo-treatment was conducted. The FTIR spectrum (Figure 6.62 (a)) shows the characteristic peak of the C–N^+ groups associated to ChCl at 920 cm^{-1} [82]. Additionally, the FTIR spectrum showed the usual broad band of stretching vibrations of the OH bond between 3100 and 3500 cm^{-1}, while absorption bands at 1090 and 870 cm^{-1} belong to Fe–Cl bond [83]. The FTIR spectrum of the before and after photo-treated TADES revealed that no substantial alteration in the bond structure was observed, indicating that the optimal TADES possesses a high level of photostability. The TGA analysis of the optimal TADES (shown in Figure 6.62 (b)) demonstrated that the TADES exhibited stability up to approximately 280±10 °C, beyond which it began to degrade. It is worth noting that the current reaction temperature was 90°C, indicating that the optimal TADES did not undergo thermal degradation during the EL synthesis process. To assess the recyclability of the TADES, the EL synthesis process was conducted using recycled TADES. Remarkably, the recycled TADES yielded identical EL results compared to the freshly prepared TADES, indicating its successful reusability.

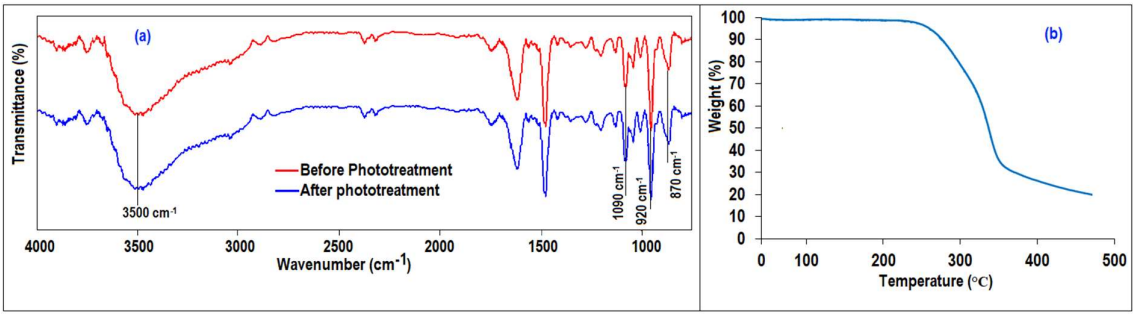

Figure 6. 62. (a) FTIR analysis and (b) TGA analysis of the Optimal TADES

6.5.4. Comparative study with previous work on one pot EL synthesis process

In order to gain insights into the feasibility and potential advancements offered by the current research, a comparative analysis was conducted, evaluating the present work alongside previously reported studies on one-pot EL synthesis processes from cellulosic biomass. From Table 6.22, it can be seen that only one work was demonstrated on EL synthesis process from sugarcane bagasse (Gomes et al. 2022), reporting a maximum 59 mol % EL yield could be achieved from raw sugarcane bagasse using (TauIm)(HSO_4) ionic liquid under MW irradiation

at 190°C and 60 min. Notably, in the present work, EL synthesis process from raw or untreated sugarcane bagasse employing TADES over 60 min could render a maximum 48.5 mol % EL yield at a much lower temperature of 90°C saving significant energy requirement. As shown in Table 6.22, a significant higher EL yield of 61.3% could be obtained employing delignified sugarcane bagasse at the optimal process condition. Therefore, it is attractive to convert delignified sugarcane bagasse more efficiently into EL, besides, mitigating the issues related to product separation. In summary, the utilization of TADES in the EL synthesis process from PSCB, under the combined influence of microwave and xenon irradiation, holds great promise as an effective and environmentally-friendly approach.

Table 6. 22. Comparative study with previous work on one pot EL synthesis process

Feedstock	Reaction conditions	Heating system	EL yield (mol %)	Reference
Dried conifer wood	200°C; 4 h; Catalyst: 2-naphthalenesulfonic acid	Conventional	48.5	[84]
Pretreated corn stover	160°C; 30 min; Catalyst: H_2SO_4	Microwave (600 W)	31.23	[85]
Pretreated corn stover	160°C; 2 h; catalyst: (Bmim-SO_3H) (HSO_4) and Al_2SO_4	Microwave (power not reported)	55.58	[86]
Sugarcane bagasse	190°C; 60 min; catalyst: (TauIm)(HSO_4)	Microwave (power not reported)	59	[87]
Pretreated Sugarcane bagasse	**90°C; 90 min; Catalyst: TADES**	**Microwave (300 W); Xenon (150 W)**	**61.3**	**Our work**

6.5.5. EL-Biodiesel-Diesel blending fuel properties

The properties of the optimally synthesized EL and its various blends with B10/B20 [biodiesel (10/20 vol%)-diesel (90/80%)] i.e. (EL5B10, EL10B10, EL5B20, EL10B20) such as flash point (°C), cetane number, cloud point (°C) and pour point (°C) have been estimated (Table 6.23). The properties of different blends such as flash point (3-6°C increased) and cloud point (1-3°C reduced) could be improved compared to B10 and B20.

Table 6. 23. Properties of EL-Biodiesel-Diesel blended fuels

Properties	EL	B10	B20	EL5B10	EL10B10	EL5B20	EL10B20
EL blending (vol %)	100	0	0	5	10	5	10
Flash point (°C)	89	71	73	74	76	78	79

Cetane number	5	49.7	51	49.2	48	47.5	46.3
Cloud point (°C)	not determined	-3	-2	-3	-4	-3	-5
Calorific value (J/g)	19146	44275	43825	43018	41762	42591	41357

[B10: 10 vol % biodiesel-90 vol % diesel; B20: 10 vol % biodiesel-90 vol % diesel; EL5B10: 5 vol % EL-95 vol % B10; EL10B10: 10 vol % EL- 90 vol % B10; EL5B20: 5 vol % EL-95 vol % B20; EL10B20: 10 vol % EL- 90 vol % B20]

6.5.6. Engine performance and exhaust analysis

Engine performance analysis for different EL-biodiesel-diesel blended fuels (EL5B10, EL10B10, EL5B20, EL10B20) revealed that with increment in EL vol % in B10 and B20, the brake-specific fuel consumption (BSFC) slightly increased (1-2.7 %) at 1500 rpm engine speed (Figure 6.61 (a)). However, break thermal efficiency was found to increase monotonically for B10 with augmented blending proportion of EL (Figure 6.61 (b)).

The exhaust analysis (HC, NOx, CO_2, CO emission) was depicted in Figure 6.61 (c (I -IV)) which indicated that with increasing EL content in B10 and B20, HC emission was significantly reduced up to 31-21 % compared to the reference blended fuels viz. B10 and B20. This decrease in HC emissions is attributed to improved combustion of the fuel blends within the combustion chamber, facilitated by the presence of oxygen in EL [88]. Advantageously, the NOx emission (Figure 6.61 (c(II))) values for B10EL5, B10EL10, B20EL5 were lesser compared to B10 and B20, however, NOx emissions were found to increase with increasing EL. The potential explanation for the increase in NOx emissions is that the rising EL content enhances combustion efficiency, leading to higher maximum temperatures during the combustion of the blended fuels, which in turn, creates more favourable conditions for NOx formation [89]. Remarkably, with increasing EL volume in EL-biodiesel-diesel blend, the CO emission (Figure 6.61 (c(III))) gradually decreased (7.3-36 %) and CO_2 emission (Figure 6.61 (c(IV))) gradually increased (2.8-5.7 %) compared to the reference blended fuels viz. B10 and B20 at 1500 rpm diesel engine speed.

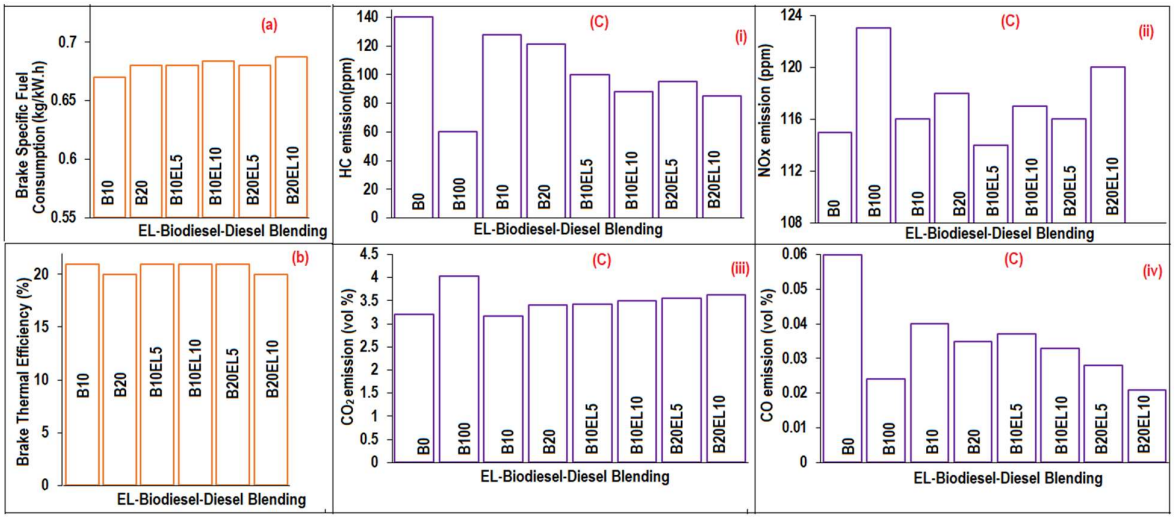

Figure 6. 63. (a) BSFC (b) Break thermal efficiency (c) exhaust emission analyses: (i) HC, (ii) NOx, (iii) CO_2, (iv) CO of different blends

6.5.7. Life cycle environmental impact analysis

Figure 6.62 (a) illustrated normalized environmental impacts (per person per year) associated optimized EL synthesis process in MWXER which clearly revealed that the most prominent ReCiPe Midpoint (H) impact indicators were marine ecotoxicity (0.07722), freshwater eutrophication (0.04986), freshwater ecotoxicity (0.02347), human toxicity (0.01972), fossil depletion (0.0052), climate change (0.00229), particulate matter formation (0.00278), terrestrial ecotoxicity (0.00603). The utilization of fossil fuel for transportation of chemicals and waste sugarcane bagasse lead to the substantial emissions of nitrates and NOx, significantly contributing to marine ecotoxicity, freshwater eutrophication, and freshwater ecotoxicity, making them the highest contributors to the overall environmental impacts [90]. Moreover, individual process contribution in the prominent impact indicators were shown in Figure 6.62 (b), which suggested that the sugarcane bagasse pretreatment process contributes almost 50 % of overall process environmental impacts in all indicators except terrestrial ecotoxicity. Application of benign solvents instead of acetic acid or other green pretreatment strategy could mitigate the environmental impacts associated with pretreatment process.

Comparative LCA study for various reactor systems performance in EL synthesis process was also investigated and shown in Figure 6.63. Clearly, MWXER contributes less environmental impacts in all indicators compared to other reactor systems. The EL synthesis process in MWXER contributes less environmental impacts in marine ecotoxicity, human

toxicity, fossil depletion, climate change by 77.9 %, 77.4 %, 78.4 % and 77.5 %, respectively in comparison with CTR. Notably, optimized EL synthesis process in MWXER also contributes higher environmental impacts when employed standard BMIMCl ionic liquid instead of TADES, which advocates the superior efficacy of optimized TADES over BMIMCl ionic liquid in EL synthesis process.

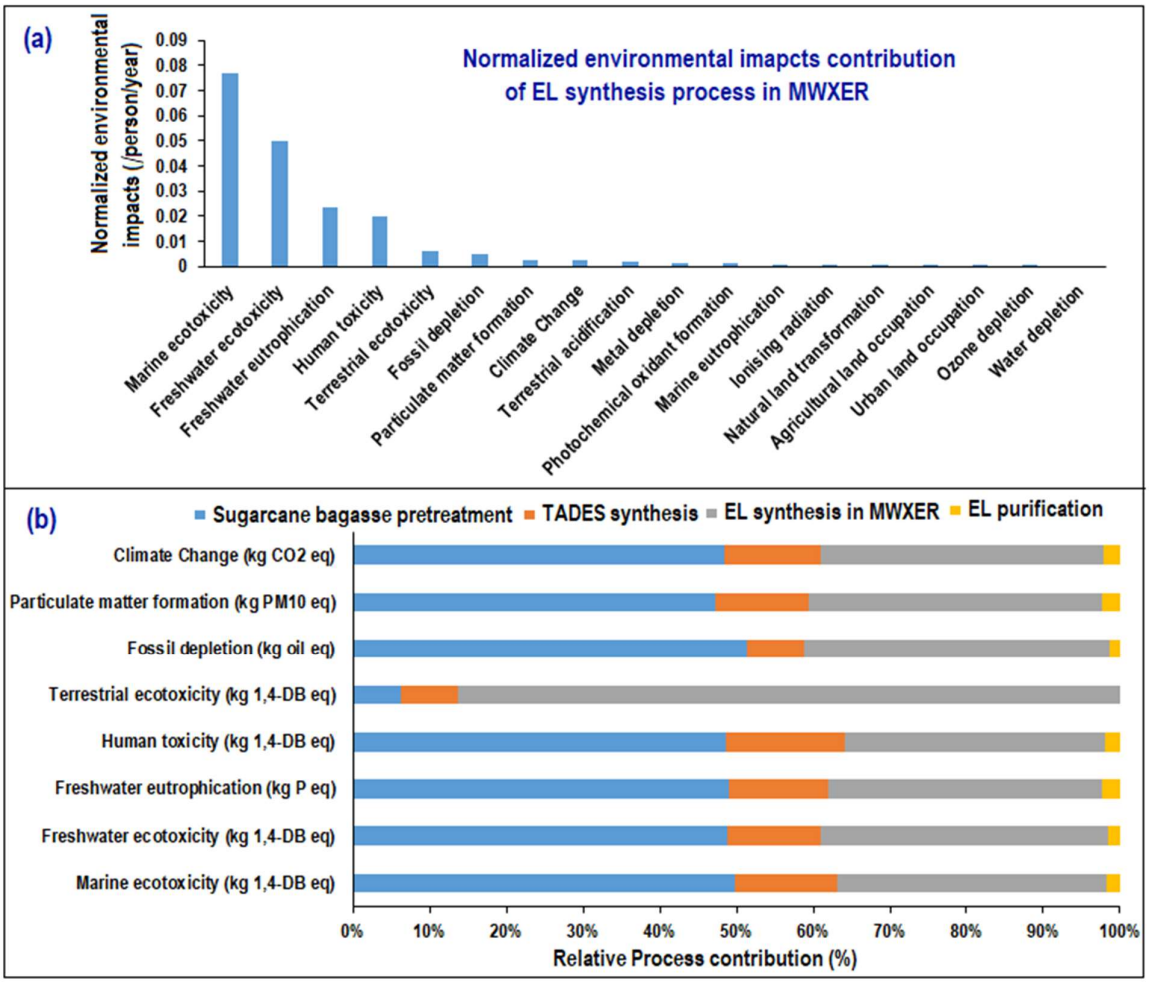

Figure 6. 64. (a) Normalized environmental impact contribution of EL synthesis process under MWXER (b) Individual process contributions in potential environmental impact factors

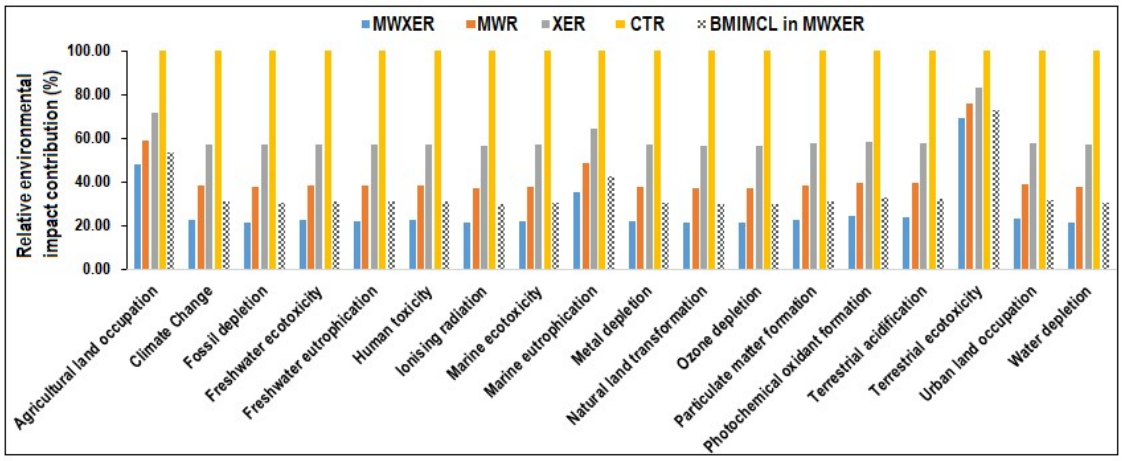

Figure 6. 65. Comparative study among various reactor systems performance in EL synthesis process

Comparative LCA study based on exhaust emission data and energy output of the blended fuels revealed that 5 vol % EL blends with B10 contributed lowest environmental impacts in climate change (kg CO_2eq) among all other fuel blends (Figure 6.64). Thus, 5 vol % EL blending in B10 [biodiesel-diesel: 10:90 vol %] could substantially reduce overall environmental impacts, although B10EL5 fuel blend showed higher HC and CO emission among other EL-biodiesel-diesel blends. Notably, the B10EL5 blended fuel exhibited lower NOx emissions compared to other blends, establishing it as a lesser contributor to climate change (1.72E-02 Kg CO_2 eq.) [91].

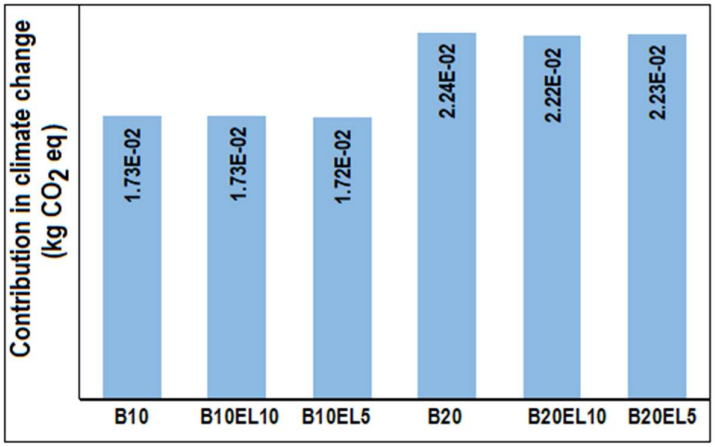

Figure 6. 66. Global warming contribution of different blends

6.6. Activity 6:

CONTINUOUS ETHYL LEVULINATE PRODUCTION FROM PRETREATED SUGARCANE BAGASSE IN MICROWAVE-VISIBLE IRRADIATED CONTINUOUS STIRRED SLURRY REACTOR: REACTION KINETICS, TECHNO-ECONOMIC & ENVIRONMENTAL SUSTAINABILITY ANALYSES

6.6.1. Screening of DES

In Figure 6.65 (a), it is evident that oxalic acid-based DES (DES2) exhibited the highest EL yield from PSCB in presence of NZF photo-catalyst, despite its higher pH value compared to DES1. Interestingly, in the absence of the NZF photo-catalyst, DES1, with the lowest pH value, achieved the highest EL yield (31.0 mol %) compared to the other prepared DESs under same reaction conditions. This discrepancy was attributed to the partial solubility of the NZF catalyst in DES1 at 100°C, leading to its ineffective performance under VIS irradiation. Additionally, TGA analysis (Figure 6.65 (b)) revealed that DES2 was thermally stable at reaction temperature and it also has low viscosity (Figure 6.65 (c)) and density (Figure 6.65 (d)) at reaction temperature, which facilitates the reaction. Thus, considering the experimental findings and the physical properties of the DESs, it could be concluded that DES2 is the most efficient medium for synthesizing EL from PSCB in the presence of the NZF photo-catalyst. As a result, for subsequent investigations, the EL synthesis process was conducted using DES2 as the chosen medium.

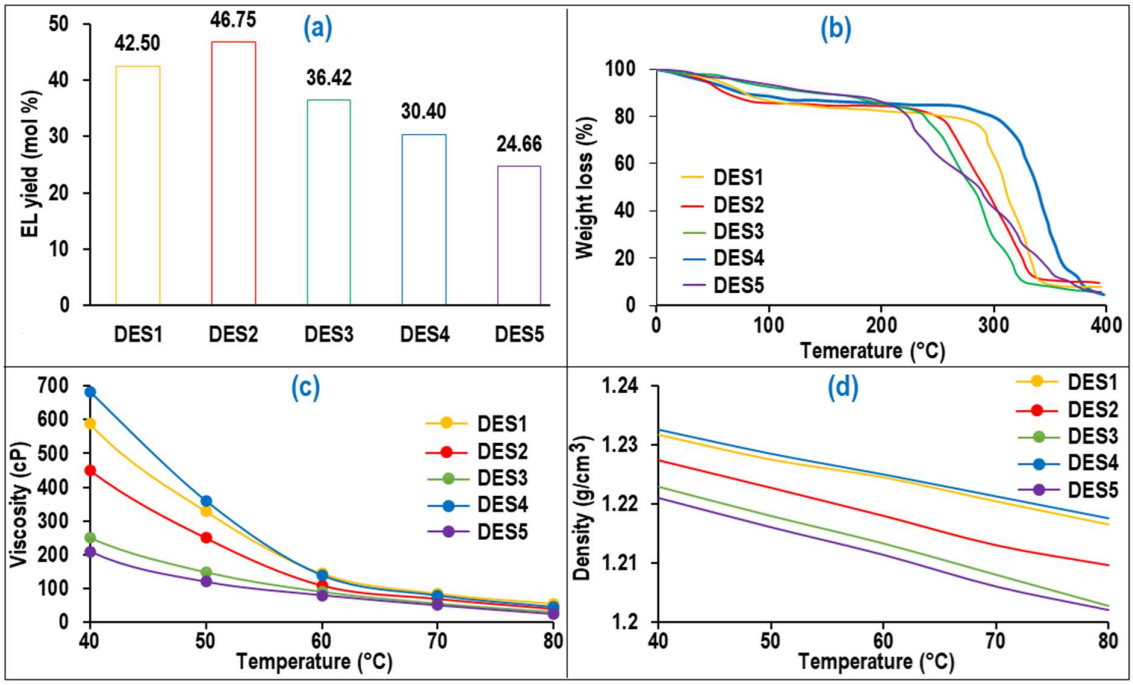

Figure 6. 67. (a) EL yield in prepared DES (reaction conditions: Ω_T: 100°C; $\Omega_{NZF/PSCB}$: 4 wt. %; Ω_t: 45 min; Ω_S: 500 rpm) (b) TGA analyses of DES (c) density and (d) viscosity of DES

6.6.2. Optimization of EL synthesis process

ANOVA analysis for the EL synthesis process in MWVIS-BR indicated that the Ω_T and $\Omega_{NZF/PSCB}$ were the most statistically significant factors (p-value< 0.05) (Table 6.24). The normal probability plot of residuals and the Model fit summary along with correlation between process factors and Ω_{EL} was shown in Figure 6.66. Notably, Table 6.25 revealed that the process factors with higher Δ values showed stronger influence on the response factor (Ω_{EL}). Accordingly, the order in which the relative significance of the process factors on the response (Ω_{EL}) could be arranged was: $\Omega_T > \Omega_{NZF/PSCB} > \Omega_t > \Omega_S$. Moreover, the highest S/N ratio value for each process factor was denoted by an asterisk (Table 6.25), which showed that the optimized process factors were 100°C (Ω_T), 6 wt. % ($\Omega_{NZF/PSCB}$), 45 min (Ω_t), and 500 rpm (Ω_S); which provided a maximum experimental 54.50 mol % of EL yield (selectivity: 97.85 %) in MWVIS-BR in presence of DES2 medium.

Table 6. 24. Analysis of variance analysis (ANOVA) of EL synthesis in MWVIS-BR

Source	DF	Adj. SS	Adj. MS	F-Value	P-Value
Regression	4	749.93	187.484	28.10	0.003

Ω_T	1	591.03	591.034	88.58	0.001
Ω_t	1	36.26	36.260	5.43	0.080
$\Omega_{NZF/PSCB}$	1	81.03	81.034	12.14	0.025
Ω_S	1	41.61	41.607	6.24	0.067
Error	4	26.69	6.672		
Total	8	776.62			

Table 6. 25. S/N ratio of EL synthesis process in MWVIS-BR

Level	Ω_T	Ω_t	$\Omega_{NZF/PSCB}$	Ω_S
L-1	28.14	29.91	29.81	31.05
L_0	31.38	31.42*	31.15	31.36*
L_1	33.15*	31.34	31.71*	30.27
Delta	5.01	1.51	1.90	1.09
Rank	1	3	2	4

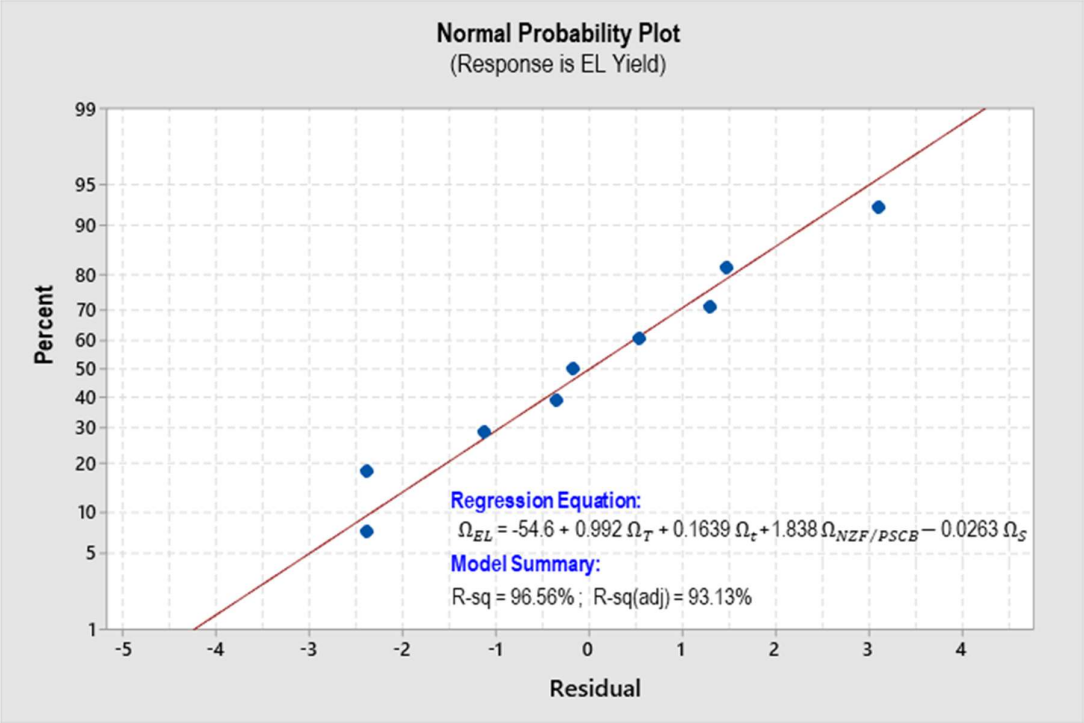

Figure 6. 68. Normal probability plot of residuals

6.6.3. Individual parametric effects on EL synthesis process

After optimization, individual impact of process factors on EL synthesis process at optimized condition were investigated. The analysis of the effect of reaction temperature on

EL yield, as depicted in Figure 6.67 (a), indicated that beyond a reaction temperature of 100 °C, the EL yield began to decrease, possibly due to the formation of humin from EDGP at higher temperatures. Furthermore, the EL yield monotonically increased with increasing stirring speed up to 500 rpm (Figure 6.67 (b)) where mass transfer resistance was negligible. However, the EL yield started to decrease due to the vortex formation when the stirring speed was extended beyond the optimal level.

The impact of the NZF to PSCB ratio ($\Omega_{NZF/PSCB}$) on EL yield was depicted in Figure 6.67 (c), revealed that there was a marginal increase in EL yield beyond optimal $\Omega_{NZF/PSCB}$ value of 6 wt. %. A similar trend was also observed when the DES2 to PSCB ratio was increased beyond 5 wt./wt. On the other hand, the optimum ethanol loading per gram of PSCB was found to be 10 ml; beyond that point, the EL yield started to decrease (as depicted in Figure 6.67 (d)). This decrease in yield can be attributed to the higher ethanol loading, which results in a reduction of acid concentration within the reaction medium and a decrease in the absorption capacity of MW.

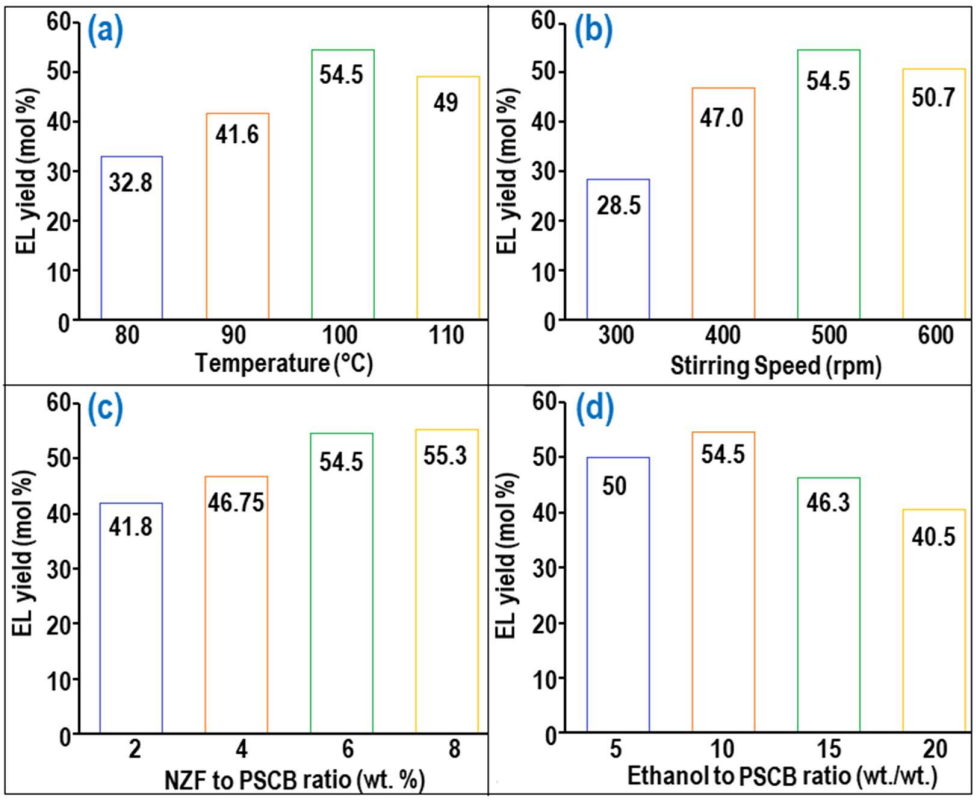

Figure 6. 69. Effect of (a) temperature and (b) stirring speed on EL yield (c) NZF to PSCB ratio and (b) ethanol to PSCB ratio on EL yield

6.6.4. MWVIS-CSSR performance study in EL synthesis process

Performance of the 5 l MWVIS-CSSR was examined in the EL synthesis process at various feed flow rate while maintaining the otherwise optimized batch process conditions viz. 100°C (Ω_T), 6 wt. % ($\Omega_{NZF/PSCB}$), and 500 rpm (Ω_S). Figure 6.68 (a), illustrated that under steady state conditions, similar EL yield as in MWVIS-BR (54.50 mol %) could be achieved in MWVIS-CSSR at a slurry feed flowrate of 35 ml/min (space time: 142 min). Notably, further decreasing the feed flow rate, didn't increase the EL yield much (2.7 % EL yield increment). The reusability study of the DES2 medium was conducted using a fresh NZF photocatalyst in the MWVIS-CSSR which revealed that the oxalic acid-choline chloride-based DES medium could be easily reused up to 5 times without compromising the EL yield (Figure 6.68 (b)). Importantly, no decrease in the efficacy of the NZF photocatalyst, as measured by EL yield, was observed throughout the NZF reusability study.

Interestingly, to facilitate comparison, experimental runs for EL production from SCB and cellulose were conducted at a feed flow rate of 35 ml/min. Notably, EL yield from cellulose was 43 mol %, while EL from SCB reached 58.60 mol %. However, despite the higher EL yield from SCB compared to PSCB, separating EL and recycling the DES2 from the product mixture after the reaction proved to be challenging.

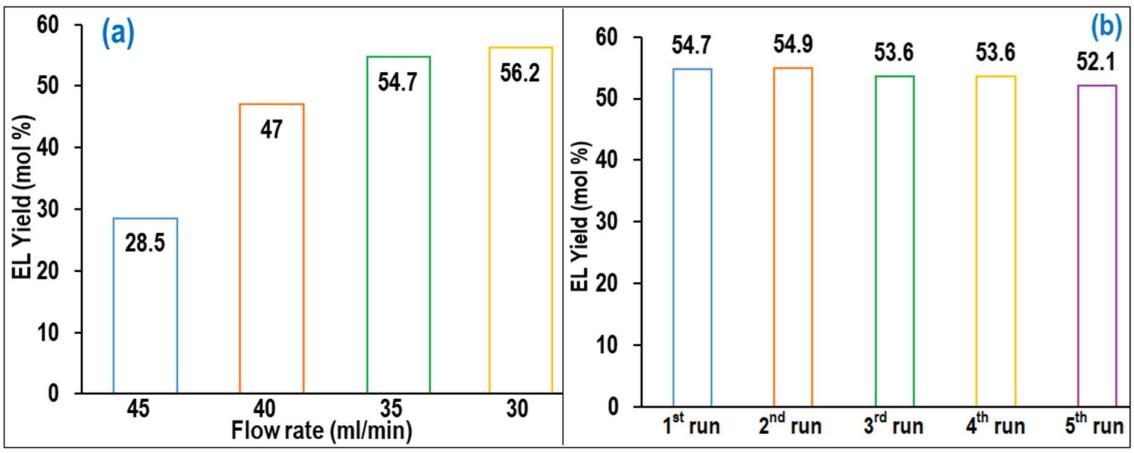

Figure 6. 70.(a) effect of feed flow rate (b) DES2 reusability study on EL yield in MWVIS-CSSR

The impact of individual and combined MW and VIS energy systems on EL yield in the large MWVIS-CSSR was also explored and illustrated in Figure 6.69 (a). This inquiry revealed a synergistic effect in the combined MW and VIS irradiation system, significantly

enhancing EL yield (54.7 mol %) compared to individual MW (29.45 mol %) and VIS (20.1 mol %) irradiation systems. The synergistic effect of MW-induced heating, driven by dipolar rotation and ionic conduction mechansim in presence of DES2 [92], coupled with the absorption of VIS energy by the NZF photocatalyst, modifies the internal energy of the reacting molecules and decrease the activation energy [93], enabling the higher EL yield in presence of MWVIS system.

To further compare the MW-VIS system with conventional heating, the EL synthesis process employing DES2 and NZF photocatalyst was also performed in a conventionally heated CSSR. In this setup, a heated oil bath (constant power input: 500 W) served as the heat source, submerging 80% of the reactor while maintaining all other optimized reaction parameters as in the MWVIS-CSSR. As shown in Fig. 6.71(a), the conventionally heated CSSR achieved an EL yield of only 17.4 mol% at optimized reaction conditions, highlighting the superior intensification effects of MW and VIS energy in the EL synthesis process.

Notably, the specific energy consumption for achieving 54.7 mol % EL yield with combined MW (0.05 kW. h/l) and VIS (0.02 kW. h/l) energy (Figure 6.69 (b)) in the large 5 l CSSR (total specific energy consumption: 0.07 kW. h/l) was substantially lower than in the smaller 15 ml batch reactor system (6 kW. h/l). This observation is in line with Bermúdez et al [94] findings, showing that raising sample weight from 5 to 100 g leads to a significant 90-95% reduction in the MW specific energy consumption for sample heating, while beyond 200 g, the specific energy consumption of MW energy remains relatively constant.

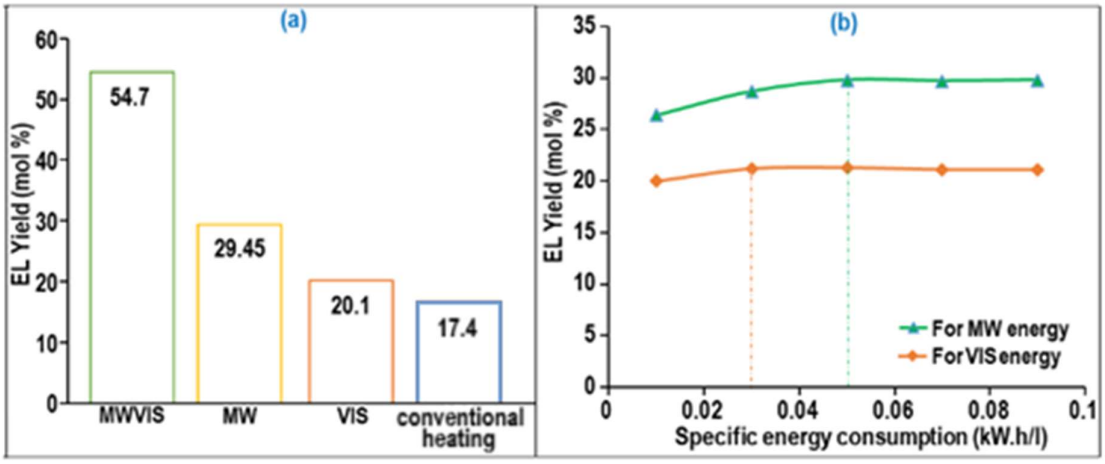

Figure 6. 71. (a) EL production by MW, VIS and Conventional heating (b) specific energy consumption by MW and VIS system in 5 l CSSR

6.6.5. Kinetics parameters evaluation for EL synthesis process in MWVIS-CSSR

The PSCB to EL continuous conversion kinetic data (Figure 6.70) obtained from MWVIS-CSSR at different reaction temperatures at otherwise optimal reaction conditions were fitted in the formulated kinetic models employing MATLAB R2014a. Notably, the formulated kinetic models exhibit remarkable agreement with experimental data, showcasing high R^2 adj. (≥ 0.95) and low RMSE values (≤ 5.15E-07) (Table 6.26). Accordingly, the kinetic rate constants for the different reactions steps involved in PSCB to EL synthesis process viz., PSCB conversion (Equation 5.35), EDGP formation (Equation 5.36), 5EMF formation (equation 5.37), EL formation (Equation 5.38) and humin formation (Equation 5.39) were evaluated and tabulated in Table 6.26.

$$-r_{PSCB} = k_{NC}C_{PSCB} + k_{H1}C_{PSCB} + \rho_{NZF}\frac{k_{Ht}\ C_E}{1+K_{A1}C_E+K_{D1}C_{EDGP}} \quad (5.35)$$

$$r_{EDGP} = k_{NC}C_{PSCB} + k_{H1}C_{PSCB} - k_{H2}C_{EDGP} - k_{H3}C_{EDGP} + \rho_{NZF}[\frac{k_{Ht}\ C_E}{1+K_{A1}C_E+K_{D1}C_{EDGP}} - \frac{k_{Ht2}C_{EDGP}}{1+K_{A2}C_{EDGP}+K_{D2}C_{5EMF}}] \quad (5.36)$$

$$r_{5EMF} = k_{H2}C_{EDGP} - k_{H4}C_{5EMF} + \rho_{NZF}[\frac{k_{Ht2}C_{EDGP}}{1+K_{A2}C_{EDGP}+K_{D2}C_{5EMF}} - \frac{k_{Ht3}C_{5EM}}{1+K_{A3}C_{5EMF}+K_{D3}C_{EL}}] \quad (5.37)$$

$$r_{EL} = k_{H4}C_{5EMF} + \rho_{NZF}\frac{k_{Ht3}C_{5EMF}}{1+K_{A3}C_{5EMF}+K_{D3}C_{EL}} \quad (5.38)$$

$$r_{Humin} = k_{H3}\ C_{EDGP} \quad (5.39)$$

Analysis of Table 6.26 revealed that the rate of the conversion reaction from PSCB to EDGP was significantly slower in the heterogeneous catalytic route (2.0E-04 g. of NZF^{-1} min^{-1}) compared to the homogeneous counterpart (0.0428 min^{-1}). However, the heterogeneous catalyst, NZF, demonstrated significant advancements in enhancing the rate of the EDGP to 5EMF and 5EMF to EL conversion steps (Table 6.26), aligning closely with the performance of the homogeneous counterpart i.e., DES2. Besides, the evaluated activation energies (E) and pre-exponential factors (A_o) (Table 6.27) suggested that the conversion reaction from EDGP to Humin exhibits the highest activation energy (96.467 kJ/mol) among all the reaction steps involved in the PSCB to EL synthesis process, suggesting NZF photocatalyst and DES2 could effectively inhibit humin generation.

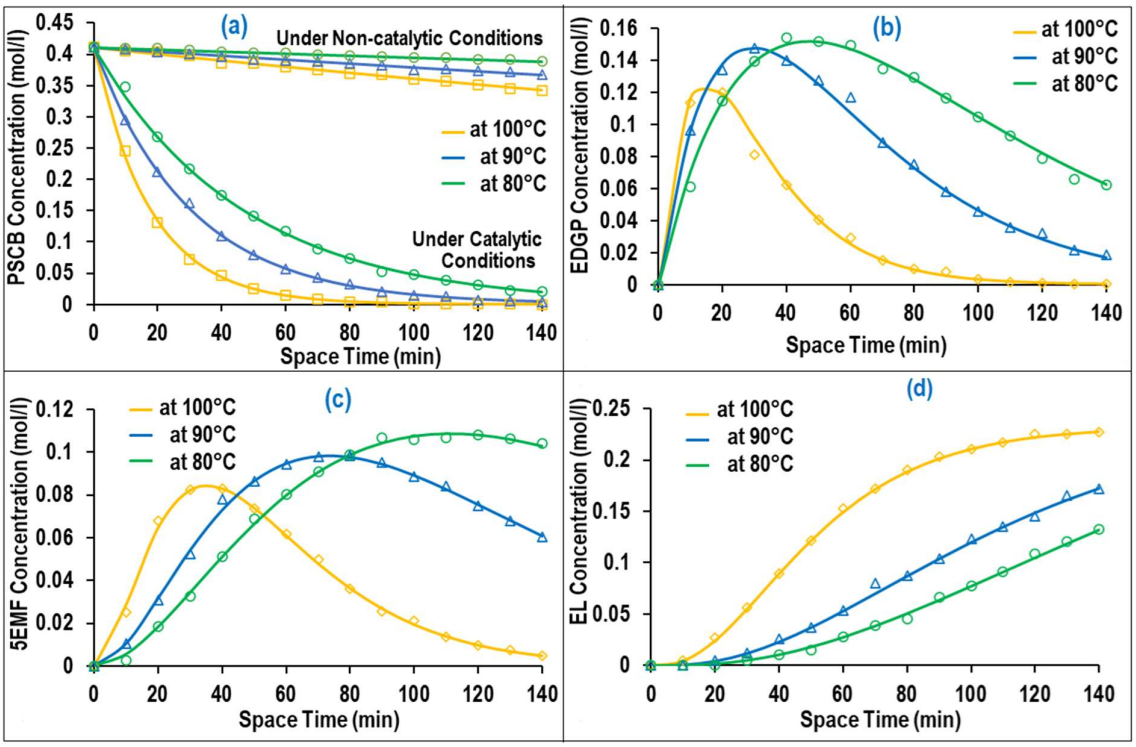

Figure 6. 72. (a) PSCB (under catalytic and non-catalytic conditions) (b) EDGP and (c) 5EMF and (d) EL concentration at different reaction temperatures [line: predicted yield; marker: actual yield]

Table 6. 26. Estimated kinetic parameters of PSCB to EL conversion reaction steps

Temperature	Rate constants								R^2	R^2_{adj}	RMSE
	k_{NC}	k_{H1}	k_{H2}	k_{H3}	k_{H4}	K_{Ht1}	K_{Ht2}	K_{Ht3}			
373	0.0013	0.0428	0.0128	0.0152	0.035	2.0E-04	0.0037	0.0028	0.96	0.95	5.15E-07
363	0.0008	0.0306	0.0116	0.0122	0.014	1.0E-04	0.0025	0.0023	0.99	0.99	5.77E-07
353	0.0004	0.0205	0.0075	0.007	0.006	4.44E-05	0.0020	0.0017	0.98	0.97	5.64E-07

Table 6. 27. Estimated activation energy and pre-exponential factors of PSCB to EL conversion reaction steps

Reaction Step	Non-catalytic reaction pathway		Homogeneous catalytic reaction pathway		Heterogeneous catalytic reaction pathway	
	E (kJ / mol)	A_o	E (kJ / mol)	A_o	E (kJ / mol)	A_o
PSCB to EDGP conversion	64.601	1.49E+6	40.167	18196.78	91.520	1.53E+9
EDGP to 5EMF conversion			29.161	160.20	33.185	161.41
5EMF to EL conversion			42.440	14071.40	26.590	15.26

EDGP to Humin conversion	96.467	1.11E+12

6.6.6. *Techno-economic analysis of the SCB to EL conversion process*

Figure 6.71 depicted a successful simulation of the SCB to EL conversion process, showcasing four hierarchical blocks (DES PREPARATION, SCB PRETREATMENT, EL PRODUCTION, and PRODUCT PURIFICATION) along with corresponding feed and product flow rates. The SCB PRETREATMENT hierarchical block was simulated with a processing capacity of 2000 kg/h of SCB, resulting in the production of 378 kg/h of lignin, 4314 kg/h of sodium acetate, and 1423 kg/h of PSCB. Notably, RSTOIC model was used to simulate the pretreatment and neutralization reactor. Detailed process flow-diagram of the simulated SCB PRETREATMENT was given in the Figure 6.72.

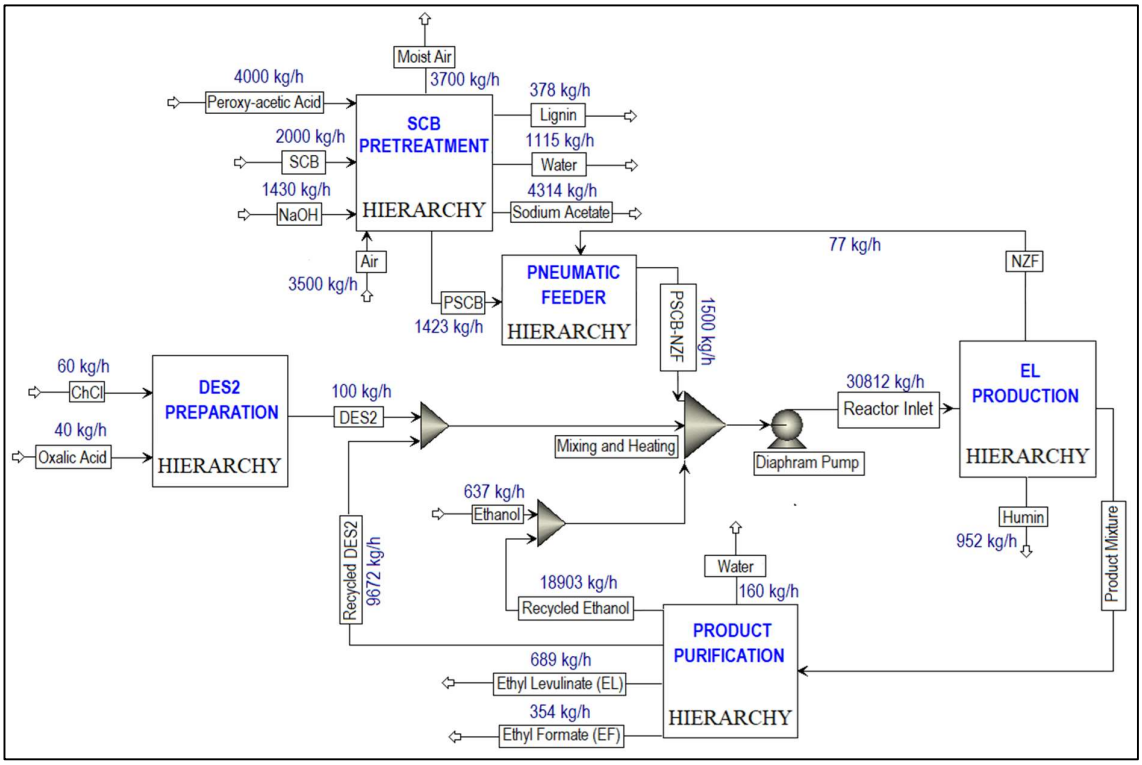

Figure 6. 73. Simulated process flow diagram of the SCB to EL conversion process

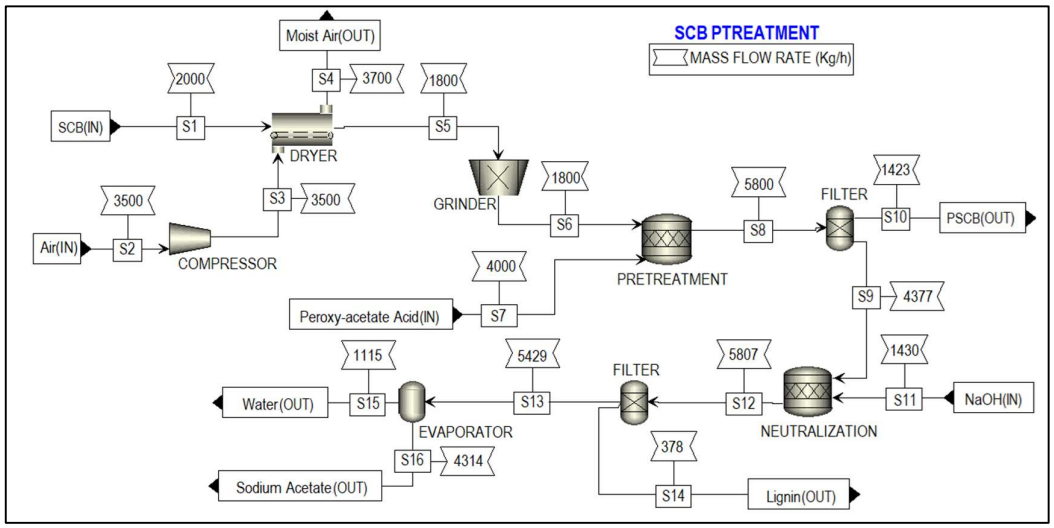

Figure 6. 74. Simulated process flow diagram of the SCB PRETREATMENT hierarchy block

Within the EL PRODUCTION hierarchy block (Figure 6.73), the MWVIS-CSSR was simulated as a single CSTR (reactor volume: 72 m^3, space time: 142 min), enabling the processing of 30812 kg/h of the reaction mixture. Following the completion of the reaction, the NZF magnetic photocatalyst was separated using a magnetic separator. Subsequently, humin was isolated through filtration, and the remaining liquid product mixture was directed to the PRODUCT PURIFICATION hierarchy block. Notably, during the humin separation process, it was assumed that 1% of the total utilized DES2 was lost.

Although, MWVIS-CSSR was simulated as a single reactor (72 m^3 volume), upscaling to such large volume poses challenges. One of the key challenges associated with large MW or photo-reactors is uneven distribution of electromagnetic energy due to their short penetration depth in the reactor medium. In this context, a well-executed reactor design typically involved the consideration of the penetration depth of MW within the reaction medium, in conjunction with other conventional design factors. Goyal et al [95] reported the significance of considering microwave penetration depth when the reactor's maximum diameter exceeds four times that depth, in order to achieve consistent and uniform microwave heating. Based on complex permittivity [$\varepsilon(i\omega) = \varepsilon(\omega)' - i\varepsilon(\omega)''$] (Figure 6.74 (a)) and calculated penetration depth from Equation-5.32 (0.246 m) of DES2-ethanol medium at 915 MHz MW frequency, it can be observed that the 5-liter MWVIS-CSSR can easily scaled up to 1 m^3 volume (by increasing the reactor height and diameter by 6 times, while maintaining the same height-to-diameter ratio as in the MWVIS-CSSR). Conversely, in terms of scaling up the CSSR with respect to VIS

penetration depth poses no challenges, as the size of the $Ni_{0.5}Zn_{0.5}Fe_2O_4$ photocatalyst is smaller (< 30 nm) than VIS penetration depth (Figure 6.74 (b)) and the reaction medium exhibits transparency to VIS irradiation. Notably, various companies have already designed and implemented industrial-scale MW intensified CSSR (www.nanomagtech.com) and photo-CSSR (www.ekato.com) systems for different reaction applications, however, no previous literature company that reported or designed a combined MW and VIS irradiated large-scale CSSR system. Thus, based on the MW and VIS energy penetration depths in our reaction medium and insights drawn from analogous large-scale industrial reactor designs, it would be practical to employ 72 CSSR with a 1 m^3 reactor volume each, connected in parallel instead of using a single 72 m^3 single CSSR. This approach will not only guarantee consistent MW heating and VIS absorption by the reaction medium but also reduce the issue of uneven residence time distribution, which is a concern when using a large single CSSR.

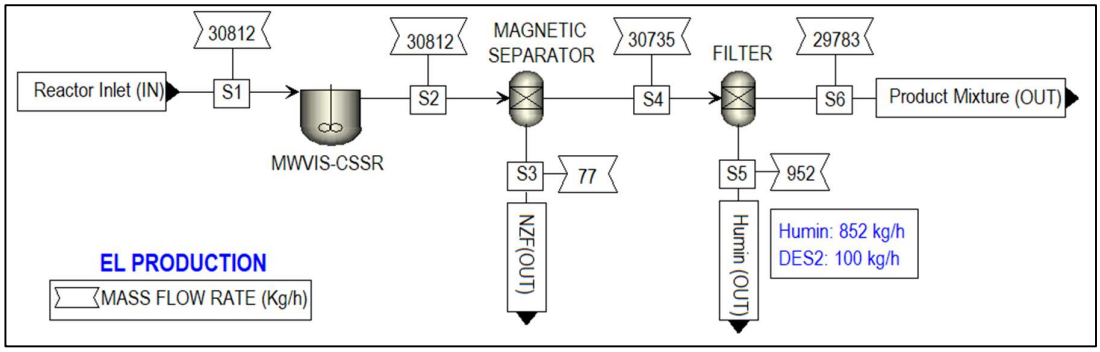

Figure 6. 75. Simulated process flow diagram of the EL PRODUCTION hierarchy block

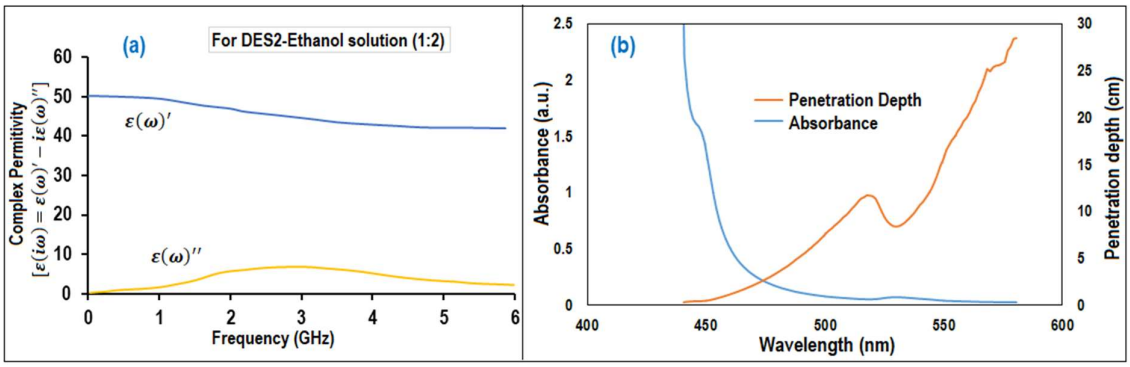

Figure 6. 76. (a) complex permittivity of DES2 (b) UV-VIS absorption spectroscopic analysis of NZF photocatalyst in DES2 medium

Figure 6.75 illustrated the simulated PRODUCT PURIFICATION hierarchical block, involving crucial unit operations such as distillation, extractions, and evaporation for the

efficient separation of EL, DES2, ethanol, and EF. The hierarchical block commenced with distillation column 1, accomplishing complete separation of EF and a partial separation of ethanol from the product mixture. Subsequently, the remaining product mixture was sent to distillation column 2, where complete separation of ethanol was achieved. An extractor was then used to separate DES2 from the bottom product of distillate 2, employing toluene as the extracting solvent. Finally, EL (purity > 99 %) was separated from the extract solvent by evaporating and recycling the toluene. Notably, in the purification process, DES2 served as an entrainer [96] in distillation column 3, facilitating the separation of ethanol from the EF-ethanol mixture that was initially obtained as a distillate from distillation column 1. Subsequently, EF was completely isolated from DES2 through evaporation, resulting in the collection of 99% pure EF, while DES2 was recycled back into the distillation column 3.

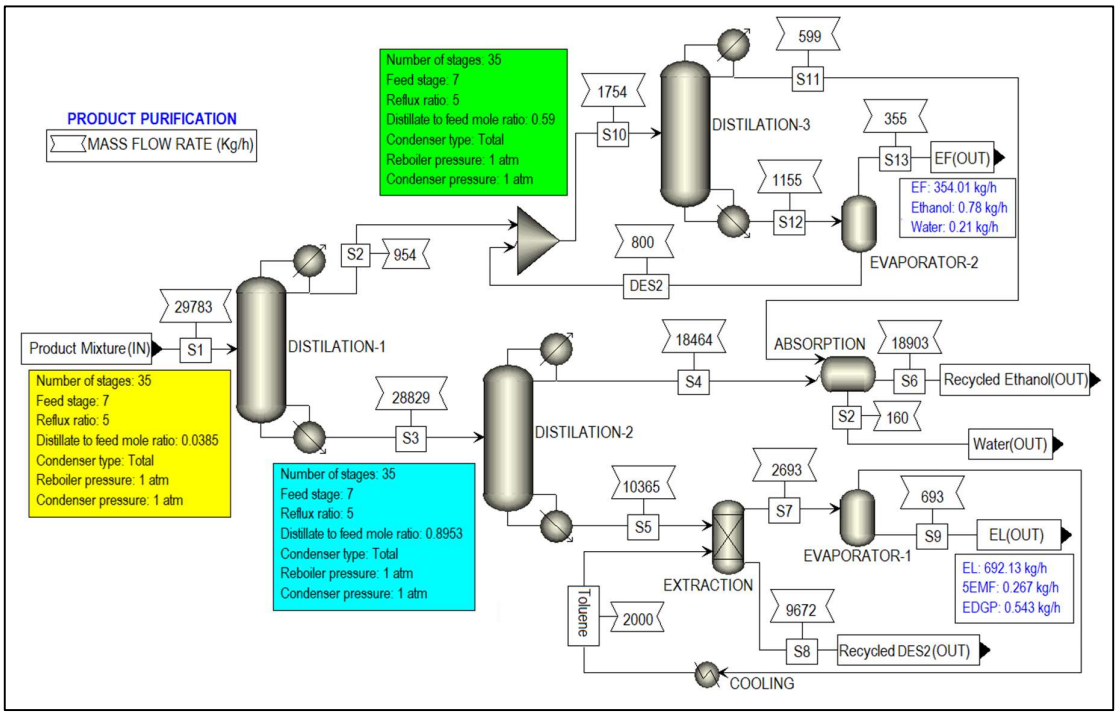

Figure 6. 77. Simulated process flow diagram of the PRODUCT PURIFICATION hierarchy block

In Figure 6.76 (a), the depicted data illustrated the overall capital expenses (CAPEX) and annual operating expenses (OPEX) associated with the simulated conversion process from SCB to EL, conducted at a processing capacity of 2000 SCB per hour. Analysis of Figure 6.76 (a) revealed that raw material costs constituted the predominant share of the total annual OPEX, comprising 45%, with utility costs following closely at 34%. On the other hand, Figure 6.76

(b) highlighted that the major equipment contributing to the total equipment costs are the reactors (50%), followed by the distillation column (26%) and heat exchanger (16%). Notably, within the total reactors cost (cost of pretreatment reactor, neutralizer and MWVIS-CSSR), the MWVIS-CSSR alone accounted for a total cost of 2.89E+06 US$, representing 67% of the total reactors cost. Despite the higher cost of the MWVIS-CSSR, the annual electricity consumption cost of the MWVIS system represents only 11% of the total annual utility cost, amounting to a total of 4.92E+05 US$.

Upon commencement of operations, the simulated process reveals an annual product sale of 3.96E+07 US$, with 1.74E+07 US$ from annual EL sales and an additional 6.42E+06 US$ stemming from annual EF sales. The sales revenue data provides insightful financial metrics for the simulated process, including a robust internal rate of return (IRR) of 54.25% with a net present value (NPV) of 8.22E+05 US$, signifying the project's profitability. Additionally, the payback period is estimated at 4.91 years (including 1 year of construction period), demonstrating the time required for the initial investment to be recouped through generated profits. Zhuo et al [97] conducted an economic analysis on large scale EL production from corn straw, with an annual processing capacity of 70,000 ton of corn straw and reported that the calculated IRR of the large-scale production system was 35.08 % and the payback period was 5.32 years. Notably, economic analyses were also carried out for the SCB to EL conversion process utilizing MW-CSSR and VIS-CSSR, which revealed that the process involving MW-assisted CSSR yielded an IRR of 24.5% with a payback period of 13.45 years whereas the process involving VIS-assisted CSSR showed no economic profit within the plant's lifetime of 20 years. Therefore, from the economic analysis, it is evident that the utilization of MWVIS-CSSR significantly enhances the financial feasibility and attractiveness of the continuous SCB to EL conversion process.

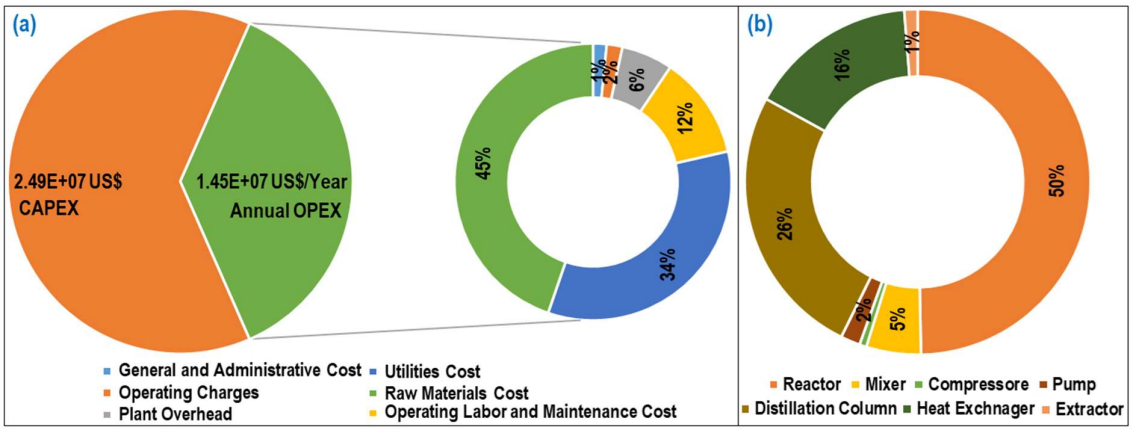

Figure 6. 78. (a) total CAPEX and annual OPEX of the SCB to EL synthesis process (b) Share of major equipment in the total equipment costs.

6.6.7. Environmental sustainability analysis of SCB to EL conversion process

Figure 6.77 (a) illustrated the normalized environmental impacts (per person per year) of the most significant ReCiPe Midpoint (H) impact indicators associated with the simulated continuous EL synthesis process under MWVIS irradiation. The use of fossil fuels for transporting chemicals and waste SCB [98], along with the utilization of coal-based electricity [99], results in significant emissions of nitrates and nitrogen oxides (NOx). These emissions play a substantial role in contributing to marine ecotoxicity (0.08142), freshwater ecotoxicity (0.05277), freshwater eutrophication (0.02586), human toxicity (0.02143) and terrestrial ecotoxicity (0.00805). Furthermore, the breakdown of percentage contributions by sub-processes in the significant indicators (Figure 7.77 (b)) revealed that product purification and EL production sub-processes were the primary contributors, followed by SCB pretreatment and DES2 preparation. The observed pattern is attributed to the utilization of coal-based steam and electricity to meet the high energy demand during product purification and EL production. Notably, Cañon et al [100] conducted a LCA analysis of the ethyl levulinate production process from Colombian rice straw derived levulinic acid and reported a comparable freshwater eutrophication value (1.624E-3 kg P eq.), slightly higher than the result obtained in the present study, indicating the environmental sustainability of the current process. The other minor environmental impact indicators associate to the simulated EL conversion process and their normalized contributions were presented in the Figure 6.78.

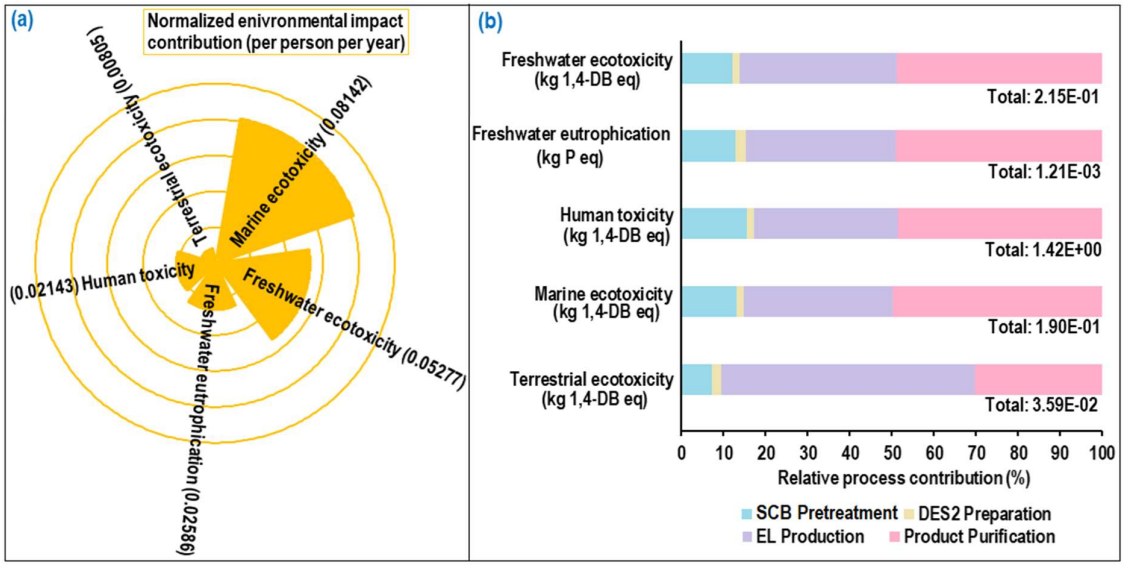

Figure 6. 79. (a) Normalized environmental impact contribution (b) relative percentage contribution of sub-processes in most prominent environmental impact indicators associated with simulated continuous EL conversion process under MWVIS

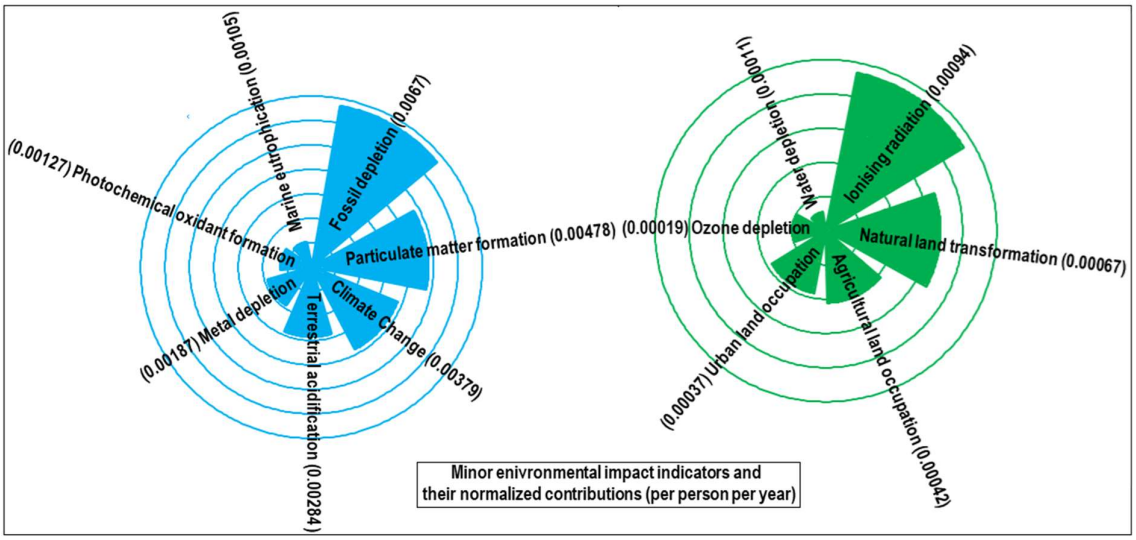

Figure 6. 80. minor environmental impact indicators and their normalized environmental impact contributions in SCB to EL conversion process within MWVIS-CSSR

Comparative environmental impact assessment study (Figure 6.79 (a)) for reactor systems indicated that MWVIS-CSSR contributes less environmental impacts in all indicators compared to MW-CSSR and VIS-CSSR systems. Thus, the synergistic MWVIS irradiation system not only enhanced the EL yield, but also contributes less environmental impacts in marine ecotoxicity, freshwater ecotoxicity, freshwater eutrophication, human toxicity and

terrestrial ecotoxicity by 40-60 %, 41-62 %, 40-60%, 39-61 % and 9-17 %, respectively in comparison with MW and VIS system.

Interestingly a comparative environmental impact analysis based on the blended fuels exhaust emission and energy output data, showed that 5 vol % EL blending with B10 exhibited the least environmental impacts in terms of climate change (kg CO_2 eq.) among all other fuel blends (Figure 6.79 (b)). Consequently, the integration of 5 vol % EL into B10 (biodiesel-diesel: 10:90 vol %) could significantly diminish overall environmental impacts, despite the B10EL5 blend showing elevated HC and CO emissions compared to other EL-biodiesel-diesel blends. A plausible explanation for this phenomenon could be the reduced NOx emissions by B10EL5 compared to other blends, thereby establishing itself as a less significant contributor to climate change (1.72E-02 kg CO_2 eq.) [101].

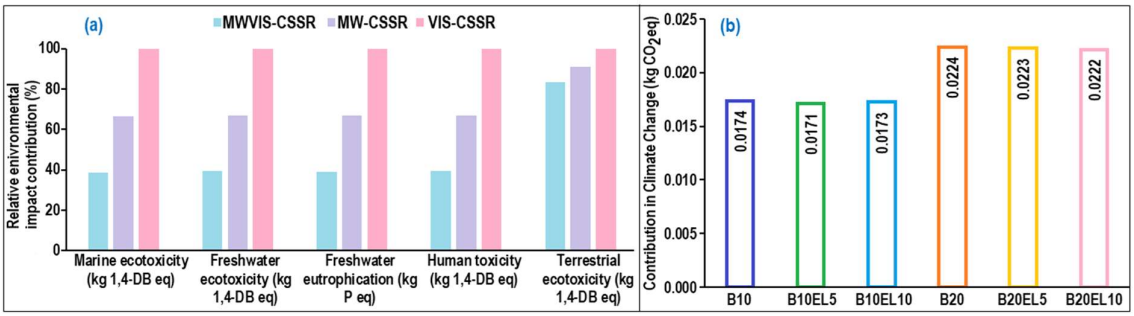

Figure 6. 81. (a) relative environmental impact contribution of different reactor systems in EL synthesis process [maximum result of each indicator was set to 100%] (b) global warming contribution of different EL blended fuels

The comprehensive evaluation of both techno-economic and environmental impact analyses revealed that the continuous EL conversion process utilizing the integrated MWVIS irradiation system in a CSSR demonstrated enhanced overall process sustainability. This was evident in terms of both economic feasibility and environmental sustainability when compared to employing individual irradiation systems. The synergistic effect of MW and VIS irradiation in presence of NZF photocatalyst and DES2 medium contributed to improved efficiency, cost-effectiveness, and reduced environmental impacts, making it a promising approach for continuous ethyl levulinate production.

6.7. Reference

1. Jeong TaeSu JT, Choi ChangHo CC, Lee JiYe LJ, Oh KyeongKeun OK. Behaviors of glucose decomposition during acid-catalyzed hydrothermal hydrolysis of pretreated Gelidium amansii.
2. Ismail, H.M. Characterization of the decomposition products of zirconium acetylacetonate: nitrogen adsorption and spectrothermal investigation. Powder Technology. 1995; 1;85(3):253-9.
3. Sahai, A.; Goswami, N.; Kaushik, S.D.; Tripathi, S. Cu/Cu 2 O/CuO nanoparticles: novel synthesis by exploding wire technique and extensive characterization. Appl. Surf. Sci.2016, 390, 974-83.
4. Khojastehnezhad, A.; Moeinpou, F.; Vafaei, M. Molybdenum Oxide Supported on Silica (MoO3/SiO2): An Efficient and Reusable Catalyst for the Synthesis of 1, 8-dioxodecahydroacridines Under Solvent-free Conditions. J. Mex. Chem. Soc.2015, 59, 29-35.
5. Hadi, P.; Gao, P.; Barford, J.P.; McKay, G. Novel application of the nonmetallic fraction of the recycled printed circuit boards as a toxic heavy metal adsorbent. J. Hazard. Mater.2013, 252, 166–170
6. Arnold, U.; Habicht, W.; Döring, M. Metal Doped Epoxy Resins–New Catalysts for the Epoxidation of Alkenes with High Long-Term Activities. Adv. Synth. Catal.2006, 348, 142-50.
7. Khojastehnezhad, A.; Moeinpou, F.; Vafaei, M. Molybdenum Oxide Supported on Silica (MoO3/SiO2): An Efficient and Reusable Catalyst for the Synthesis of 1, 8-dioxodecahydroacridines Under Solvent-free Conditions. J. Mex. Chem. Soc. 2015, 59, 29-35.
8. Wang, C.H.; Lee, C.N.; Weng, H.S. Effect of Acid Treatment on the Performance of the CuO− MoO3/Al2O3 Catalyst for the Destructive Oxidation of (CH3) 2S2. Ind. Eng. Chem. Res.1998, 37, 1774-80.
9. Umbarkar, S.B.; Biradar, A.V.; Mathew, S.M.; Shelke, S.B.; Malshe, K.M.; Patil, P.T.; Dagde, S.P.; Niphadkar, S.P.; Dongare, M.K. Vapor phase nitration of benzene using mesoporousMoO 3/SiO 2 solid acid catalyst. Green. Chem. 2006, 8, 488-93.
10. Liu, B.; France, L.; Wu, C.; Jiang, Z.; Kuznetsov, V.L.; AlMegren, H.; AlKinany, M.; Aldrees, S.A.; Xiao, T.; Edwards, P.P. Methanol-to-hydrocarbons conversion over MoO3/H-ZSM-5 catalysts prepared via lower temperature calcination: A route to tailor the distribution and evolution of promoter Mo species, and their corresponding catalytic properties. Chem. Sci. 2015,6, 5152-5163
11. Mohamed, M.M. Fourier-transform infrared/photoacoustic study of pyridine adsorbed on silica supported copper-molybdenum catalysts. Spectrochim. Acta. A. Mol. Biomol. Spectrosc. 1995, 51, 1-9.
12. Kataoka, T.; Dumesic, J.A. Acidity of unsupported and silica-supported vanadia, molybdena, and titania as studied by pyridine adsorption. J. Catal. 1988, 112, 66-79.
13. Skupiński, W.; Malesa, M. An infrared study on the MoO3/SiO2 catalytic system employed in toluene nitration. Applied Catalysis A: General. 2002;236; 223-34.

14. El-Shobaky, G.A.; Fagal, G.A.; Petro, N.; Dessouki, A.M. Effects of gamma irradiation on surface and catalytic properties of Co3O4 supported on Al2O3. Int. J. Radiat. Appl. Instrum. C. Radiat. Phys. Chem. 1987, 29, 39-43.
15. Zhao, Y.; Wang, S.; Lin, H.; Chen, J.; Xu, H. Influence of a Lewis acid and a Brønsted acid on the conversion of microcrystalline cellulose into 5-hydroxymethylfurfural in a single-phase reaction system of water and 1, 2-dimethoxyethane. RSC Advances. 2018;8(13); 7235-42.
16. de Oliveira, A.D.; da Silva Costa, L.R.; de Oliveira Pires, L.H.; do Nascimento, L.A.; Angélica, R.S.; da Costa, C.E.; Zamian, J.R.; da Rocha Filho, G.N. Microwave-assisted preparation of a new esterification catalyst from wasted flint kaolin. Fuel. 2013,103,626-31.
17. El-Molla, S.A.; Hammed, M.N.; El-Shobaky, G.A. Catalytic conversion of isopropanol over NiO/MgO system doped with Li2O. Materials Letters. 2004;58(6);1003-11.
18. Zhao, J.; Jayakumar, A.; Lee, J.M. Bifunctional Sulfonated MoO3–ZrO2 Binary Oxide Catalysts for the One-Step Synthesis of 2, 5-Diformylfuran from Fructose. ACS Sustain. Chem. Eng.2018, 6, 2976-82.
19. Liu, Y.; Bailey, P.; Noakes, T.C.; Thompson, G.E.; Skeldon, P.; Alexander, M.R. Chemical environment of copper at the surface of a CuAl2 model alloy: XPS, MEIS and TEM analyses. Surface and Interface Analysis: An International Journal devoted to the development and application of techniques for the analysis of surfaces, interfaces and thin films. 2004, 36, 339-46.
20. Choudhury, B.; Dey, M.; Choudhury, A. Shallow and deep trap emission and luminescence quenching of TiO2 nanoparticles on Cu doping. Appl. Nanosci. 2014, 1, 4(4):499-506.
21. Filonov AB, Tralle IE, Dorozhkin NN, Migas DB, Shaposhnikov VL, Petrov GV, Anishchik VM, Borisenko VE. Semiconducting properties of hexagonal chromium, molybdenum, and tungsten disilicides. Physica. Status. Solidi. (b). 1994;186(1); 209-15.
22. Rinaldi, R.; Meine, N.; Stein, J.V.; Palkovits, R.; Schuth, F. Which Controls the Depolymerization of Cellulose in Ionic Liquids: The Solid Acid Catalyst or Cellulose? Chem. Sus. Chem.2010, 3, 266 – 276.
23. Guo, F.; Fang, Z.; Xu, C.C.; Smith, Jr. R.L. Solid acid mediated hydrolysis of biomass for producing biofuels. Prog. Energ. Combust. 2012, 38, 672-90.
24. Bauer, B.; Floyd, T.A. Monitoring of glucose in biological fluids by Fourier–transform infrared spectrometry with a cylindrical internal reflectance cell. Anal. Chim. Acta.1987, 197, 295–301.
25. Gremlich, H.U. Weinheim, Switzerland: VCH, 1994, Vol. B5, 429–69
26. Ward, K.J.; Haaland, D.M.; Robinson, M.R.; Eaton, R.P. Post-Prandial Blood Glucose Determination by Quantitative Mid-Infrared Spectroscopy. Appl. Spectrosc.1992, 46, 959–65.
27. Petibois, C.; Rigalleau, V.; Melin, A.; Perromat, A.; Cazorla, G.; Gin, H.; Deleris. G. Determination of glucose in dried serum samples by Fourier-transform infrared spectroscopy. Clin. Chem.1999, 45, 1530–1535.

28. Llano, T.; Quijorna, N.; Andrés, A.; Coz, A. Sugar, acid and furfural quantification in a sulphite pulp mill: Feedstock, product and hydrolysate analysis by HPLC/RID. Biotechnol. Rep.2017, 15, 75–83.
29. Duan, S.; Feng, X.; Cheng, L.; Peng, Y.; Zheng, K.; Liu, Z. Bio degumming technology of jute bast by Pectobacterium sp. AMB Expr.2016, 6-86.
30. Karan P, Mukhopadhyay P, Chakraborty R. Intensification of monostearin (phase change material) synthesis in infrared radiated rotating reactor: Optimization and heterogeneous kinetics. Energ Convers Manage. 2017; 138:577-86.
31. Holkar CR, Jadhav AJ, Bhavsar PS, Kannan S, Pinjari DV, Pandit AB. Acoustic cavitation assisted alkaline hydrolysis of wool based keratins to produce organic amendment fertilizers. ACS Sustain Chem Eng. 2016;4(5):2789-96.
32. Rinaldi R, Meine N, Stein JV, Palkovits R, Schuth F. Which Controls the Depolymerization of Cellulose in Ionic Liquids: The Solid Acid Catalyst or Cellulose? Chem Sus Chem. 2010; 3: 266 – 276.
33. Bauer B, Floyd T A. Monitoring of glucose in biological fluids by Fourier–transform infrared spectrometry with a cylindrical internal reflectance cell. Anal. Chim. Acta. 1987; 197: 295–301.
34. Gremlich HU. Vol. B5. Weinheim, Switzerland: VCH, 1994; 429–69
35. Ward KJ, Haaland DM, Robinson MR, Eaton RP: Post-Prandial Blood Glucose Determination by Quantitative Mid-Infrared Spectroscopy. Appl. Spectrosc. 1992; 46: 959–65.
36. Petibois C, Rigalleau V, Melin A, Perromat A, Cazorla G, Gin H, Deleris G. Determination of glucose in dried serum samples by Fourier-transform infrared spectroscopy. Clin. Chem. 1999; 45:9, 1530–1535.
37. Kubo S, Kadla JF. Hydrogen bonding in lignin: a Fourier transform infrared model compound study. Bio macromolecules.2005; 6: 2815–21.
38. Schwanninger M, Rodrigues J, Pereira H, Hinterstoisser B. Effects of shorttime vibratory ball milling on the shape of FT-IR spectra of wood and cellulose. Vib Spectrosc. 2004; 36:23–40.
39. Sills DL, Gossett JM. Using FTIR to predict saccharification from enzymatic hydrolysis of alkali pretreated biomasses. Biotechnol Bioeng. 2012; 109: 353–62.
40. Baillères H, Davrieux F, Ham-Pichavant F. Near infrared analysis as a tool forrapid screening of some major wood characteristics in a eucalyptus breedingprogram. Annal Forest Sci.2002; 59: 479–90.
41. Llano T, Quijorna N, Andrés A, Coz A. Sugar, acid and furfural quantification in a sulphite pulp mill: Feedstock, product and hydrolysate analysis by HPLC/RID. Biotechnology Reports. 2017; 15: 75–83.
42. Duan S, Feng X, Cheng L, Peng Y, Zheng K, Liu Z. Biodegumming technology of jute bast by Pectobacterium sp. AMB Expr. 2016; 6-86.

43. Jahan MS, Saeed A, He S, Ni Y, Jute as raw material for the preparation of microcrystalline cellulose. Cellulose. 2011; 18:451–459.
44. Trache D, Donnot A, Khimeche K, Benelmir R, Brosse N. Physico-chemical properties and thermal stability of microcrystalline cellulose isolated from Alfa fibres. Carbohyd Polym. 2014; 104:223-30.
45. Yu Y, Wu H.Significant Differences in the Hydrolysis Behavior of Amorphous and Crystalline Portions within Microcrystalline Cellulose in Hot-Compressed Water. Ind. Eng. Chem. Res. 2010; 49: 3902–3909.
46. Shaveta, Bansal N, Singh P. F/Cl mediated microwave assisted breakdown of cellulose to glucose. Tetrahedron Letters.2014; 55: 2467–2470.
47. Santos D, Silva UF, Duarte FA, Bizzi CA, Flores EMM, Mello PA. Ultrasound-assisted Acid Hydrolysis of Cellulose to Chemical Building Blocks: Application to Furfural Synthesis. Ultrason Sonochem.2018; 40: 81-88.
48. Bhaumik P, Dhepe PL. Biomass Sugars for NonFuel Applications. 2015; 1:153.
49. Zhou CH, Xia X, Lin CX, Tong DS, Beltramini J. Catalytic conversion of lignocellulosic biomass to fine chemicals and fuels. Chem. Soc. Rev. 2011; 40: 5588–56.
50. Erjavec B, Hudoklin P, Perc K, Tišler T, DolencM S, Pintar A. Glass fiber-supported TiO2 photocatalyst: Efficient mineralization and removal of toxicity/estrogenicity of bisphenol A and its analogs. Appl Catal B-Environ, 2016, 183: 149-158.
51. Hartati H, Purwaningsih A, Tjahjandarie TS, Saputri NH, Puspitasari IS, Lamanele CN, Sa'adah AA, Haque AS, Mardho DZ. Synthesis of amorphous aluminosilicate from impure Indonesian kaolin. Open Chemistry. 2020;18(1): 295-302.
52. He C., Tian B., Zhang J., Thermally stable SiO2-doped mesoporous anatase TiO2 with large surface area and excellent photocatalytic activity, J. Colloid Interface Sci. 344 (2010) 382-389.
53. Huang C.-H., Bai H., Liu S.-L., Huang Y.-L., Tseng Y.-H., Synthesis of neutral SiO2/TiO2 hydrosol and its photocatalytic degradation of nitric oxide gas, Micro & Nano Lett. 6 (2011) 646-649
54. Fan Y, Ma C, Li W, Yin Y. Synthesis and properties of Fe3O4/SiO2/TiO2 nanocomposites by hydrothermal synthetic method. Materials science in semiconductor processing. 2012;15(5):582-5.
55. K. Woo, H. J. Lee, J. P. Ahn and Y. S. Park, Adv. Mater., 2003, 15, 1761.
56. Khurshid H, Li W, Chandra S, Phan MH, Hadjipanayis GC, Mukherjee P, Srikanth H. Mechanism and controlled growth of shape and size variant core/shell FeO/Fe 3 O 4 nanoparticles. Nanoscale. 2013; 5(17):7942-52.
57. Zhang L, Zhang Y, Chen S. Effect of promoter SiO2, TiO2 or SiO2-TiO2 on the performance of CuO-ZnO-Al2O3 catalyst for methanol synthesis from CO2 hydrogenation. Appl Catal A-Gen, 2012, 415: 118-123.

58. Hita I, Deuss P J, Bonura G, Frusteri F, Heeres H J. Biobased chemicals from the catalytic depolymerization of Kraft lignin using supported noble metal-based catalysts. Fuel Process Technol, 2018, 179: 143-153.
59. Yan F, Jiang J, Li K, Liu N, Chen X, Gao Y, Tian S. Green synthesis of nanosilica from coal fly ash and its stabilizing effect on CaO sorbents for CO2 capture. Environ Sci Technol. 2017; 51(13):7606-15.
60. Qourzal S, Assabbane A, Ait-IchouY.Synthesis of TiO2 via hydrolysis of titanium tetraisopropoxide and its photocatalytic activity on a suspended mixture with activated carbon in the degradation of 2-naphthol. J. Photochem. Photobiol. A, 2004, 163(3): 317-321.
61. Ohuchi FS, Ghose S, Engelhard MH, Baer DR. Chemical bonding and electronic structures of the Al2SiO5 polymorphs, andalusite, sillimanite, and kyanite: X-ray photoelectron-and electron energy loss spectroscopy studies. American Mineralogist. 2006; 91(5-6):740-6.
62. Zhu L, Hong M, HoGW.Fabrication of wheat grain textured TiO2/CuO composite nanofibers for enhanced solar H2 generation and degradation performance. Nano Energy, 2015, 11: 28-37.
63. Wang F, Li M, Yu L, Sun F, Wang Z, Zhang L, Zeng H, Xu X. Corn-like, recoverable γ-Fe 2 O 3@ SiO 2@ TiO 2 photocatalyst induced by magnetic dipole interactions. Sci Rep-Uk. 2017; 7(1):1-0.
64. Fu C, Liu X, Wang Y, Li L, Zhang Z. Preparation and characterization of Fe 3 O 4@ SiO 2@ TiO 2–Co/rGO magnetic visible light photocatalyst for water treatment. RSC advances. 2019;9(35):20256-65.
65. Lam CM, Iris KM, Hsu SC, Tsang DC. Life-cycle assessment on food waste valorisation to value-added products. Journal of Cleaner Production. 2018; 199:840-8.
66. Cao L, Iris KM, Chen SS, Tsang DC, Wang L, Xiong X, Zhang S, Ok YS, Kwon EE, Song H, Poon CS. Production of 5-hydroxymethylfurfural from starch-rich food waste catalyzed by sulfonated biochar. Bioresource technology. 2018; 252:76-82.
67. Chun JA, Lee JW, Yi YB, Hong SS, Chung CH. Direct conversion of starch to hydroxymethyl furfural in the presence of an ionic liquid with metal chloride. Starch-Starke. 2010; 62(6):326-30.
68. Silahua-Pavón AA, Espinosa-González CG, Ortiz-Chi F, Pacheco-Sosa JG, Pérez-Vidal H, Arévalo-Pérez JC, Godavarthi S, Torres-Torres JG. Production of 5-HMF from glucose using TiO2-ZrO2 catalysts: effect of the sol-gel synthesis additive. Catal Commun. 2019; 129:105723.
69. Guo W, Zuo M, Zhao J, Li C, Xu Q, Xu C, Wu H, Sun Z, Chu W. Novel Brønsted–Lewis acidic di-cationic ionic liquid for efficient conversion carbohydrate to platform compound. Cellulose. 2020:1-2.
70. M. Cybularczyk-Cecotka, J. Szczepanik and M. Giedyk, Nature Catalysis, 2020, 3, 872-886.
71. Echemi. (n. d). retrieved January 16, 2021, from https://www.echemi.com/weekly-price-list.html
72. C. A. Antonyraj, A. J. Chennattussery and A. Haridas, International Journal of Chemical Kinetics, 2021, 53, 825-833.

73. P. Rojahn, K. D. Nigam and F. Schael, Chemical Engineering Journal, 2022, 450, 138243.
74. Y. Luo, J. Z. Luo, X. J. Yue, Y. J. Song, G. W. Chu, Y. Liu, Y. Le and J. F. Chen, Chemical Engineering Journal, 2018, 331, 510-516.
75. F. J. Navarro-Brull, A. R. Teixeira, J. Zhang, R. Gómez and K. F. Jensen, Industrial & Engineering Chemistry Research, 2018, 57, 122-128.
76. M. Brasholz, K. Von Kaenel, C. H. Hornung, S. Saubern and J. Tsanaktsidis, Green Chemistry, 2011, 13, 1114-1117.
77. T. M. Kohl, B. Bizet, P. Kevan, C. Sellwood, J. Tsanaktsidis and C. H. Hornun, Reaction Chemistry & Engineering, 2017, 2, 541-549.
78. B. Chen, Z. Li, Y. Feng, W. Hao, Y. Sun, X. Tang, ... and L. Lin, ChemSusChem, 2021, 14, 847-851.
79. Zhou, J, Xu W, You Z, Wang Z, Luo Y, Gao L, Yin C, Peng R, and Lan L. (2016). A new type of power energy for accelerating chemical reactions: the nature of a microwave-driving force for accelerating chemical reactions. Sci Rep. 6(1): 25149.
80. Mannhold R, Kubinyi H, & Folkers G, 2006. Molecular interaction fields: applications in drug discovery and ADME prediction. John Wiley & Sons.
81. Dai ZY, Zhang SQ, Hong X, Wang PS, & Gong LZ (2022). A practical FeCl3/HCl photocatalyst for versatile aliphatic C–H functionalization. Chem Catalysis. 2(5): 1211-1222.
82. Delgado-Mellado N, Larriba M, Navarro P, Rigual V, Ayuso M, García J, Rodríguez F (2018) Thermal stability of choline chloride deep eutectic solvents by TGA/FTIR-ATR analysis. J Mol Liq 260:3743.
83. Li Y, Tian X, He X, Liu Y, Ye J, Wei Y (2020) Comprehensive reutilization of iron in iron ore tailings: preparation and char acterization of magnetic flocculants. Environ Sci Pollut Res 27:37011–21.
84. Mascal M, & Nikitin EB (2010). Comment on processes for the direct conversion of cellulose or cellulosic biomass into levulinate esters. ChemSusChem. 3(12): 1349-1351.
85. Liu H, Zhang Y, Hou T, Chen X, Gao C, Han L, & Xiao W (2018). Mechanical deconstruction of corn stover as an entry process to facilitate the microwave-assisted production of ethyl levulinate. Fuel Process. Technol.174: 53-60.
86. Liu H, Meng H, Cong H, Shen X, Chen X, Xing H, & Dai J (2022). Alcoholysis kinetics and mechanism studies of ethyl levulinate production from ball milled corn stover. RSC Adv. 12(53): 34145-34153.
87. Gomes GR, Scopel E, Rocha NL, Breitkreitz MC, Cormanich RA, Rezende CA, & Pastre JC (2022). Direct Ethyl Levulinate Production from Raw Lignocellulosic Biomass Mediated by a Novel Taurine-Based Imidazolium Ionic Liquid. ACS Sustainable Chem. Eng.10(48): 15876-15888.

88. Prasad L, Pradhan S, Das LM, & Naik SN. (2012). Experimental assessment of toxic phorbol ester in oil, biodiesel and seed cake of Jatropha curcas and use of biodiesel in diesel engine. Appl. Energy. 93: 245-250.
89. Lei T, Wang Z, Chang X, Lin L, Yan X, Sun Y, Shi X, He X, and Zhu J. (2016). Performance and emission characteristics of a diesel engine running on optimized ethyl levulinate–biodiesel–diesel blends. Energy. 95:9-40.
90. Sun C, Chen L, Zhai L, Liu H, Wang K, Jiao C, Shen Z. (2020). National assessment of nitrogen fertilizers fate and related environmental impacts of multiple pathways in China. J. Clean. Prod. 277: 123519
91. Lu Y, Shao M, Zheng C, Ji H, Gao X, Wang Q. (2020). Air pollutant emissions from fossil fuel consumption in China: current status and future predictions. Atmos. Environ. 231: 117536
92. Mannhold R, Kubinyi H, Folkers G. Molecular interaction fields: applications in drug discovery and ADME prediction. John Wiley & Sons; 2006.
93. Zhou J, Xu W, You Z, Wang Z, Luo Y, Gao L, Yin C, Peng R, Lan L. A new type of power energy for accelerating chemical reactions: the nature of a microwave-driving force for accelerating chemical reactions. Sci. Rep-UK. 2016; 6(1):25149.
94. Bermúdez JM, Beneroso D, Rey-Raap N, Arenillas A, Menéndez JA. Energy consumption estimation in the scaling-up of microwave heating processes. Chem. Eng. Process.: Process Intensification. 2015; 95:1-8.
95. Goyal H, Mehdad A, Lobo RF, Stefanidis GD, Vlachos DG. Scaleup of a single-mode microwave reactor. Ind. Eng. Chem. Res. 2019;59(6):2516-23.
96. Neubauer M, Wallek T, Lux S. Deep eutectic solvents as entrainers in extractive distillation–A review. Chem. Eng. Res. Des. 2022; 184:402-18.
97. Zhuo C, Xueqin L, Zhiwei W, Yantao Y, Tanglei S, Taoli H, Peng L, Yanling L, Youqing W, Tingzhou L, Jingshen Q. Techno-economic and whole life cycle assessment of ester fuels production from agricultural waste via hydrothermal liquefaction. Ind. Crop. Prod. 2023; 192:116096.
98. Sun C, Chen L, Zhai L, Liu H, Wang K, Jiao C, Shen Z. National assessment of nitrogen fertilizers fate and related environmental impacts of multiple pathways in China. J. Clean. Prod. 2020; 277:123519.
99. Felix M, Gheewala SH. Environmental toxicity potential from electricity generation in Tanzania. The Int. J. Life. Cycle. Ass. 2014; 19:1424-32.
100. Lu, Y., Shao, M., Zheng, C., Ji, H., Gao, X., Wang, Q., 2020. Air pollutant emissions from fossil fuel consumption in China: current status and future predictions. Atmos. Environ. 231, 117536.
101. Cañon C, Sanchez N, Cobo M. Life cycle inventory data for ethyl levulinate production from Colombian rice straw. Data in Brief. 2022; 45:108681.

CHAPTER VII: CONCLUSION

Activity 1: ***PRINTED CIRCUIT BOARD DERIVED GLASS FIBRE-EPOXY RESIN SUPPORTED MO-CU BIMETALLIC CATALYST FOR GLUCOSE SYNTHESIS***

Waste printed circuit board (PCB) derived epoxy-glass fiber (GFER) supported Mo-Cu Bronsted-Lewis acid catalysts can be developed employing both near infrared radiation (NIRR) and conventional hydrothermal treatment. NIRR promoted catalyst shows superiority over conventional hydrothermal treated catalyst in terms of catalytic properties, glucose yield in jute fiber hydrolysis process. The waste PCB was effectively exploited in developing reusable, highly efficient supported acid catalyst, hence creating another effective avenue of e-waste valorisation for the generation of value-added chemicals from lignocellulosic biomass.

Activity 2: ***KINETICS OF COMBINED NON-CATALYTIC AND CATALYTIC HYDROLYSIS OF JUTE FIBER UNDER ULTRASONIC-FAR INFRARED ENERGY SYNERGY***

The work describes a significantly efficient, energy-proficient reactor amalgamated with far infrared wave and ultrasonic wave for hydrolysis of waste jute fiber rendering augmented and accelerated reducing sugar yield in comparison with individual far infrared wave energized reactor, ultrasonication energized reactor and conventional thermal reactor. The proposed combined pseudo-homogeneous-heterogeneous kinetic models provide an accurate interpretation of the experimental data. The evaluated hydrolysis rate laws, as well as the kinetic parameters, are expected to be useful to future researchers and practicing technologists for design and scale-up of such reactor systems. Thus, a promising, combined application of ultrasound and far-infrared waves for energy-efficient hydrolysis of waste jute fiber for improved synthesis of reducing sugar could be developed through a sustainable green technology.

Activity 3: ***SUSTAINABLE HMF SYNTHESIS FROM WASTE COOKED RICE WATER USING FLY-ASH BASED AL_2SIO_5 SUPPORTED NANO-PHOTOCATALYST UNDER HALOGEN-ULTRASOUND SYNERGISTIC-ENERGY: LCA AND DFT BASED SIMULATION***

An innovative $Fe^{3+}/Fe^{2+}/Al_2SiO_5/Ti^{4+}$ nano-photocatalyst (FA_NPC*) possessing both Brønsted and Lewis acid sites could be successfully developed using fly ash-based nano-

Al_2SiO_5 and nano-Fe^{3+}/Fe^{2+} employing a proficient assimilated energy-system comprising tungsten-halogen radiation and ultrasound (THUS). Advantageously, remarkable increments in BET surface area (58.39 %) and surface acidity (22.15 %) while appreciable reductions in particle size (23.91 %) and band gap energy (6.39 %) in THUS activated optimal FA_NPC* (FA_NPC*^{O}) compared to its conventional analog (FA_NPC^{CO}) could be achieved. The FA_NPC*^{O} rendered 77.06 % higher HMF yield through photo-hydrolytic conversion of waste cooked rice water (CRW) as compared to the FA_NPC^{CO}; thus, evinced the advantage of using the integrated THUS energy-system. Thus, utilization of waste fly ash for development of inexpensive, high-efficacy and recyclable nano-photocatalyst that exhibited boosted performance under THUS, could procreate new-fangled environment-friendly avenues for energy-efficient sustainable synthesis of HMF and similar platform chemicals.

Activity 4: ***ENERGY-EFFICIENT AND ECO-FRIENDLY CONTINUOUS PRODUCTION OF 5-CMF IN A UV-ULTRASOUND IRRADIATED CATALYTIC PACKED BED REACTOR: HETEROGENEOUS KINETICS, REACTOR SIMULATION AND LCA ANALYSIS***

5-CMF from soluble starch (SS) was energy-efficiently synthesized through an environment-friendly synthesis protocol in both batch (UVUS-BR) and continuous-flow rectangular packed bed reactor (UVUS-RPBR) employing heterogenous Smopex-101 and TiO_2 dual catalytic system in presence of cyclohexane as the extracting solvent under UV-ultrasound (US) irradiations. At mild optimal operating conditions (80 °C, 60 min), synergistic effect of US-UV irradiation system in UVUS-RPBR significantly enhanced the 5-CMF yield (58.75 mol %) compared to the individual US (< 8 mol %) and UV (41.50 mol %) irradiation system. Moreover, RTD analysis and ANSYS simulation study revealed that the nonideality of RPBR could be greatly reduced under ultrasound energy (63 % less compared to without US system). Additionally, the efficacy of UVUS-RPBR was successfully simulated using ANSYS fluent software for 5-CMF synthesis by incorporating experimentally evaluated heterogeneous surface reaction kinetic model parameters; which can be useful for scale-up of such reactor. Notably, based on comparative LCA analysis, cyclohexane was identified as the most environmentally advantageous solvent for extracting 5-CMF. The development of the UVUS-RPBR have the potential to pave the way for proficient continuous synthesis of 5-CMF utilizing such dual heterogenous catalytic system; thus, opening a new avenue towards process scale-up for industrial application.

Activity 5: ***ENVIRONMENTALLY SUSTAINABLE ETHYL LEVULINATE SYNTHESIS FROM DELIGNIFIED SUGARCANE BAGASSE USING TERNARY EUTECTIC SOLVENT UNDER MW-XENON IRRADIATION: ENGINE PERFORMANCE & EMISSION ASSESSMENT***

Sustainable one pot synthesis of EL from delignified sugarcane bagasse mediated by photoactive ternary acidic deep eutectic solvents (TADES) under microwave-xenon irradiations could achieve maximum 61.3 mol % of EL yield at mild reaction conditions (90°C, 90 min). Moreover, the work also highlights sustainable extraction of ethyl levulinate (purity 97$\pm$0.5 %) and reuse of TADES in the process. Exhaust analysis of EL-biodiesel-diesel blends and life cycle environmental impact assessment showed that the 5 vol % EL blending in B10 could substantially reduce overall environmental impacts. The efficient EL synthesis process, using the photoactive TADES from delignified sugarcane bagasse under the combined influence of microwave-xenon irradiation, and its subsequent application in assessment of engine performance & emission profile, imply great promise in terms of the energy-proficient and environment-friendly approach.

Activity 6: ***CONTINUOUS ETHYL LEVULINATE PRODUCTION FROM PRETREATED SUGARCANE BAGASSE IN MICROWAVE-VISIBLE IRRADIATED CONTINUOUS STIRRED SLURRY REACTOR: REACTION KINETICS, TECHNO-ECONOMIC & ENVIRONMENTAL SUSTAINABILITY ANALYSES***

Sustainable continuous valorisation of pretreated sugarcane bagasse (PSCB) into ethyl levulinate (EL) was achieved employing an innovative microwave-visible irradiated continuous stirred slurry reactor (MWVIS-CSSR). Under mild reaction conditions (142 min residence time and 100°C reaction temperature), the MWVIS-CSSR could render 54.7 mol % EL yield in presence of a magnetic $Ni_{0.5}Zn_{0.5}Fe_2O_4$ (NZF) photocatalyst and oxalic acid-choline chloride based acidic deep eutectic solvent (DES2). Remarkably, the synergistic impacts of MW and VIS irradiations substantially augmented the EL yield (54.7 mol %), considerably exceeding the yields achieved with individual application of MW (29.45 mol %) and VIS (20.1 mol %) irradiations. Moreover, the developed novel reaction kinetic model for the PSCB to EL conversion process, formulated by considering parallel non-catalytic and homogeneous-heterogeneous catalytic routes, have proven to accurately interpret the experimental data. The techno-economic study and comparative environmental impact assessment revealed that the continuous conversion of sugarcane bagasse to EL employing MWVIS-CSSR exhibited

superior economic feasibility (internal rate of return: 54.25 %) and contributed less environmental impacts (marine ecotoxicity: 1.90E-01 kg 1,4-DB eq., freshwater ecotoxicity: 2.15E-01 kg 1,4-DB eq. and human toxicity: 1.42E+00 kg 1,4-DB eq.) compared to the EL conversion process in individual MW-CSSR and VIS-CSSR. Thus, the current continuous EL synthesis process, along with its subsequent application in assessing engine performance and engine emission profile, not only underscores the potential for sustainable EL production through leveraging sugarcane bagasse but also signifies a significant step toward addressing energy efficiency and environmental concerns in the realm of drop-in-biofuel synthesis and its sustainable applications towards improvement in diesel engine performance and mitigation of adverse climate changes.

CHAPTER VIII: FUTURE SCOPE OF WORK

Previous chapters illustrate elaborate descriptions of the work conducted while focusing on the preparation and application of green cost-effective catalysts for the synthesis of platform chemicals and drop-in-biofuel through hydrolytic transformation of lignocellulosic biomass in energy-efficient reactors. However, this final chapter suggests a few future recommendations in which further investigations could be carried out.

- Application of waste printed circuit board and fly ash derived supported catalysts in continuous flow packed bed reactor configuration to investigate the on-stream stability of the developed catalyst in lignocellulosic biomass conversion process.
- Exploration of the combined effect of microwave and UV radiation on the progress of the chemical reaction/reaction kinetics.
- Development of a novel cost-effective deep eutectic solvent that has the capability to dissolve LB, thereby enabling efficient conversion of LB in both batch and continuous mode.
- Studies on continuous production of other valuable levulinate esters viz., methyl levulinate, butyl levulinate using the prepared catalyst.

Sourav Barman
27.05.2024.

27.05.2024.

ACS OMEGA

Article

Cite This: ACS Omega 2018, 3, 18499−18509

http://pubs.acs.org/journal/acsodf

Printed Circuit Board-Derived Glass Fiber-Epoxy Resin-Supported Mo−Cu Bimetallic Catalyst for Glucose Synthesis

Sourav Barman and Rajat Chakraborty*

Department of Chemical Engineering, Jadavpur University, Kolkata 700032, India

Supporting Information

ABSTRACT: A glass fiber-epoxy resin (GFER) framework derived from mixed waste printed circuit boards (MWPCBs) was utilized to prepare a cost-effective, reusable Mo−Cu bimetallic Bronsted−Lewis solid acid catalyst through wet-impregnation under near-infrared radiation (NIRR) activation. The efficacy of the novel Mo−Cu catalyst was assessed in the synthesis of glucose through hydrolysis of jute (*Corchorus olitorius*) fiber, and the process parameters were optimized (Mo precursor loading: 1.0 wt %, catalyst concentration: 5 wt %, hydrolysis temperature: 80 °C, and hydrolysis time: 10 min) through Taguchi orthogonal design. The GFER support and the prepared catalysts were characterized through thermogravimetric, X-ray diffraction (XRD), Fourier-transform infrared (FTIR), Brunauer−Emmett−Teller (BET)−density functional theory, and TPD analyses. The optimal Mo−Cu catalyst and the GFER support possessed 45.377 and 7.049 m^2/g BET area, 0.04408 and 0.02317 cc/g pore volume, 1.9334 and 0.7482 nm modal pore size, and surface acidity of 0.48 and 0.40 mmol NH_3/g catalyst, respectively. X-ray photoelectron spectroscopy bands confirmed the coexistence of Mo^{6+} and Cu^{2+} species; XRD and FTIR analyses indicated the presence of MoO_3 and CuO crystalline phases in all prepared catalysts. The optimal catalyst prepared through NIRR (wavelength 0.75−1.4 μm)-activated hydrothermal treatment resulted in a significantly greater glucose yield (75.84 mol %) than that achieved (53.64 mol %) using a conventionally prepared catalyst. Thus, an energy-efficient application of NIRR (100 W) could significantly improve catalytic properties over conventional hydrothermal treatment (500 W). The present investigation provides an innovative application of MWPCB-derived GFER as a promising cost-effective support for the preparation of highly efficient inexpensive solid catalysts for sustainable synthesis of glucose from low-cost waste jute fiber.

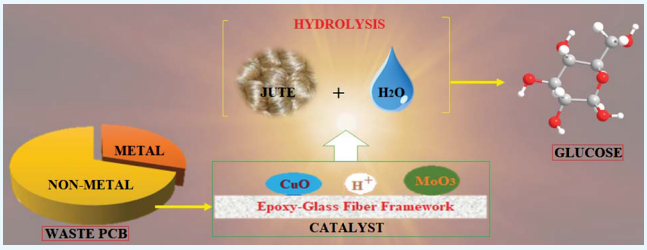

1. INTRODUCTION

Printed Circuit Board (PCB) is an integral component of any electronic equipment as it electrically connects and mechanically supports other electronic components. According to Global E-waste Monitor 2017, globally 44.7 million metric tonnes of e-waste was generated,[1] fueling concerns about the growing threats to the environment and public health. Waste PCBs are still being chiefly disposed in open air or in landfills that pose grave threat to the environment. Accumulation of waste PCBs is not only a crisis of quantity but also an alarming environmental concern because of the presence of toxic ingredients that results in occupational, environmental, and human health threats.

Recovery and recycling of the metallic part from mixed waste PCBs (MWPCBs) drew the attention of many researchers because of the potential profitability through metal recovery; however, glass fiber-epoxy resin (GFER) which makes up around 65−70% of waste PCBs[2] has been overlooked because of lesser economic value. Various separation processes of metal and nonmetallic ingredients of MWPCBs viz. physical recycling processes (e.g., shredding, hammer milling, ball milling, corona discharge separation, magnetic separation, eddy current separation, air classification, flotation, gravity separation, and density-based separation),[3−6] thermal processing (pyrolysis, gasification, and plasma treatment),[7−9] hydrometallurgical processing,[10,11] and solvent extraction (dimethyl sulfoxide, dimethyl formamide, *N*-dimethyl pyrrolidone, and ionic liquids)[12−14] had been reported in last few decades. In recent years, hydrometallurgical processes attracted particular attention for the treatment of WPCBs. Several researchers reported the effectiveness of strong acids as a leachant for leaching of metals from waste PCBs; nevertheless, the generation of toxic gases (viz. Cl_2, SO_3, and NO_x) and the acidic waste streams during the leaching process are detrimental to the environment. Jadhav et al.[11] deployed a less hazardous organic acid viz. citric acid (0.5 M) along with hydrogen peroxide (1.76 M) as an effective leachant that rendered complete metal leaching to obtain GFER from a 4 × 4 cm^2 WPCB in 4 h.

Several scientific reports have been published on direct reutilization of GFER for the production of fuels (pyrolytic oil) and chemicals by thermal and catalytic pyrolysis; however, focus has been shifted toward the recovery of the GFER for alternative uses because of the low energy efficiency of the

Received: October 11, 2018
Accepted: December 6, 2018
Published: December 27, 2018

DOI: 10.1021/acsomega.8b02754
ACS Omega 2018, 3, 18499−18509

Received: 23 September 2018 | Revised: 12 April 2019 | Accepted: 24 May 2019

DOI: 10.1002/aic.16677

REACTION ENGINEERING, KINETICS AND CATALYSIS

AIChE JOURNAL

Kinetics of combined noncatalytic and catalytic hydrolysis of jute fiber under ultrasonic–far infrared energy synergy

Sourav Barman | Rajat Chakraborty

Chemical Engineering Department, Jadavpur University, Kolkata, India

Correspondence
Rajat Chakraborty, Chemical Engineering Department, Jadavpur University, Kolkata 700032, India.
Email: rajat_chakraborty25@yahoo.com; rajat.chakraborty@jadavpuruniversity.in

Funding information
University Grants Commission

Abstract

Hydrolysis of pretreated waste jute fiber was intensified for maximizing reducing sugar (RS) yield deploying a novel reactor equipped with ultrasonic–far-infrared-waves (US–FIRW). At optimal 70°C temperature, 2.5 wt% Amberlyst-15 catalyst concentration, 15 min hydrolysis time and 10 (wt/wt) water loading; US–FIRW rendered significantly greater RS yield (74.82 mol%) compared to other reactors provided with far-infrared-wave (69.63 mol%), ultrasonication (50.34 mol%), and conventional thermal system (48.16 mol%). Kinetic models were developed considering noncatalytic-pseudo-homogenous (NCPH) in addition to the combined catalytic-pseudo-homogeneous (CPH) and catalytic heterogeneous (CHE) hydrolysis pathways. The results revealed that pseudo-homogenous–heterogeneous Eley–Rideal (PHHER) model could represent the hydrolysis kinetics most accurately. Remarkably, the lowest activation energy [16.75 kJ mol^{-1} (NCPH), 13.82 kJ mol^{-1} (CPH), 40.01 kJ mol^{-1} (CHE)] required in US–FIRW evidently established its greater energy-efficiency among investigated reactors. The novel reactor and the simulated kinetic models can be applicable to other lignocellulosic biomass conversion for sustainable biorefinery.

KEYWORDS
combined pseudo-homogeneous–heterogeneous kinetic, far infrared-ultrasonic-wave, hydrolysis, reducing sugar, waste jute fiber

1 | INTRODUCTION

Efficient hydrolysis of lignocellulosic biomass (LB) is one of the most investigated fields for biomass valorization globally. Disintegration of LB and maximization of monosaccharides yield through economically viable way are the major concerns to the researchers. Jute fiber, being an abundantly available biomass resource of cellulose (60–70 wt% cellulose, 25–30 wt% hemicellulose, and 10–12 wt% lignin)[1,2] could be utilized as a feedstock for hydrolytic conversion into valuable products. Jute fiber could also be utilized for production of microcrystalline cellulose, nanocellulose, and cellulose nanofibrils.[2,3] Nevertheless, only scanty works were reported on jute hydrolysis for reducing sugar (RS) production.[4,5] Roy[5] reported that 50% (wt/vol) RS could be produced from pretreated jute powder through enzymatic hydrolysis pathway using immobilized enzymes from *Macrophomina phaseolina*. More recently, Matsagar[6] produced furfural with a maximum yield of 86% from jute using 1-methyl-3(3-sulfopropyl)-imidazolium hydrogen sulfate ($[C_3SO_3HMIM][HSO_4]$) brønsted acidic ionic liquid catalyst at 160°C and 1 hr. Evidently, the scientific reports indicate insufficient works have been conducted on the jute fiber hydrolysis process for production of RS irrespective of its high cellulose content.

Studies on hydrolysis of LB using homogeneous acid catalysts revealed that several demerits viz. difficulty in product recovery and catalyst recyclability, equipment corrosion, waste stream generation were associated with this hydrolysis process.[7-9] Conversely, from recent studies it revealed that, reusable heterogeneous acid catalyst could be the possible option to overcome the above-mentioned bottlenecks. Nevertheless, sustainable heterogeneous acid catalyzed hydrolysis

Journal of Environmental Chemical Engineering 9 (2021) 106736

Contents lists available at ScienceDirect

Journal of Environmental Chemical Engineering

journal homepage: www.elsevier.com/locate/jece

Sustainable HMF synthesis from waste cooked rice water using fly-ash based Al_2SiO_5 supported nano-photocatalyst under halogen-ultrasound synergistic-energy: LCA and DFT based simulation

Sourav Barman, Rajat Chakraborty *

Chemical Engineering Department, Jadavpur University, Kolkata 700032, India

ARTICLE INFO

Editor: Despo Kassinos

Keywords:
Tungsten halogen-ultrasound stimulated nano-photocatalyst
Fly ash based nano-Al_2SiO_5
Waste cooked rice water
HMF synthesis
Density Functional Based Tight Binding
Environmental impact assessment

ABSTRACT

Innovative $Fe^{3+}/Fe^{2+}/Al_2SiO_5/Ti^{4+}$ nano-photocatalyst (FA_NPC*) was successfully prepared employing fly ash (FA)-based unique nano-Al_2SiO_5 and nano-Fe^{3+}/Fe^{2+} in an innovative assimilated energy-system comprising tungsten-halogen radiation and ultrasound (THUS). The energy-efficient THUS activated optimal FA_NPC* (FA_NPC*°) possessed favourably higher specific surface area (142.11 m^2/g), finer nanoparticles (47.50 nm) and lower band gap energy (2.78 eV) compared (89.72 m^2/g, 62.43 nm, 2.97 eV respectively) to its conventionally prepared analog (FA_NPC^{CO}). The FA_NPC*° rendered a significantly higher HMF yield (38.37 mol%) from a kitchen waste viz., cooked rice water (CRW) under THUS at 70 °C in only 60 min compared to 21.67 mol% HMF yield provided by FA_NPC^{CO}. The DFT based study revealed that the CRW conversion process to HMF occurred through water adsorption on FA_NPC* surface for H_3O^+ formation, followed by H_3O^+ induced CRW hydrolysis, subsequent glucose isomerization on -Ti active sites and finally fructose dehydration by H_3O^+. The LCA of the overall process confirmed that the FA_NPC*° catalysed CRW conversion process could appreciably alleviate harmful environmental parameters, viz. global warming, fossil depletion, human toxicity and metal depletion by 7.65%, 4.15%, 8.56% and 13.57% respectively in comparison with FA_NPC^{CO}. Thus, the THUS stimulated system could favourably demonstrate the efficient and eco-friendly utilisations of two abundant waste resources, viz. fly ash and cooked rice water for a sustainable production of HMF.

1. Introduction

India, being the third-largest coal-based power generator, co-produces large quantities of fly ash (FA) throughout the year. According to central electricity authority of India (2018–19), 217.04 million tons FA was generated that possessed high concentrations of amorphous aluminosilicate and iron oxide [1,2] which could be utilized in development of value-added products. In last few decades, extraction of silica alumina [3] and iron oxide nanoparticle [4] from FA had been intensively studied and previous reports revealed that alkali-acid dissolution method along with sol-gel technique were the promising options to develop silica and iron oxide nanoparticle. Vashistha et al., 2019 [5] extracted silica from FA through NaOH treatment and produced nano-silica using H_2SO_4 as a precipitating agent. Recently, several researchers [6,7] reported that application of electromagnetic radiation for nano particle preparation exhibited significant beneficial effects viz. reduction in crystallization time, high nucleation rate and homogeneous crystal growth. Ghanbari et al., 2014 [8] reported that Fe_3O_4 nano particle could be prepared without inert atmosphere using 2 M NH_4OH solution within a very short period of time (3 min) under ultrasound (US) treatment as an intensification technique. More recently, the work [9] reported by our group revealed that tungsten-halogen (TH) radiation-activated glass fiber supported CuO-TiO_2 nano-photocatalyst showed higher photo-catalytic activity compared to conventionally prepared catalyst owing to impregnation of finer crystallites of nano--TiO_2 and CuO (7.31 nm) on glass fiber support. Notably, no work so far has been available on silica-alumina and iron nanoparticle extraction from FA using combined US and TH radiated energy-systems for possible advantages.

Although bulk TiO_2 is considered as an effective photo-catalyst due to its high stability, and inhibition to photo-corrosion, it suffers from a serious drawback particularly with respect to its inability to absorb light in the visible zone and difficulty in removal from reaction mix. Previous work [10] inferred that doping of Fe_3O_4 on TiO_2 could be a promising

* Corresponding author.
E-mail addresses: rajat_chakraborty25@yahoo.com, rajat.chakraborty@jadavpuruniversity.in (R. Chakraborty).

https://doi.org/10.1016/j.jece.2021.106736
Received 29 August 2021; Received in revised form 12 October 2021; Accepted 2 November 2021
Available online 12 November 2021

Reaction Chemistry & Engineering

ROYAL SOCIETY OF CHEMISTRY

PAPER

View Article Online
View Journal | View Issue

Cite this: *React. Chem. Eng.*, 2024, **9**, 160

Energy-efficient and eco-friendly continuous production of 5-CMF in a UV-ultrasound irradiated catalytic packed bed reactor: heterogeneous kinetics, reactor simulation and LCA analysis†

Sourav Barman and Rajat Chakraborty *

Received 29th July 2023,
Accepted 27th September 2023

DOI: 10.1039/d3re00406f

rsc.li/reaction-engineering

For the first time, a reusable heterogeneous Smopex-101 and TiO_2 dual catalytic system was employed successfully for the energy-efficient and eco-friendly synthesis of 5-(chloromethyl) furfural (5-CMF) from soluble starch (SS) under the synergistic photo-thermal effect of UV-ultrasound (US) irradiation. Under mild optimal operating conditions (80 °C, 60 min), the batch (UVUS-BR) and continuous-flow rectangular packed bed reactors (UVUS-RPBR) both resulted in maximum 5-CMF yields of 60.54 mol% and 58.75 mol%, respectively. Significantly, the first-ever heterogeneous surface reaction kinetic model was formulated for the 5-CMF synthesis process, which revealed that the activation energies needed for the different reaction steps involved in the consecutive reaction pathway were 79.04 kJ mol^{-1} (SS hydrolysis), 61.55 kJ mol^{-1} (glucose dehydration), and 52.2 kJ mol^{-1} (5-hydroxymethylfurfural chlorination). RTD analysis and ANSYS fluent simulation study revealed that the utilization of the US energy significantly reduced the non-ideal behavior of UVUS-RPBR (63% reduction in dispersion number). Moreover, the efficacy of UVUS-RPBR in the 5-CMF synthesis process was evaluated, employing the experimentally validated heterogeneous kinetic model parameters. Furthermore, based on comparative LCA analysis, cyclohexane was identified as the most favorable solvent for *in situ* 5-CMF (purity: 96%) extraction due to its potential environmental advantages over other solvents. The outcomes of the present study can be useful for the scale-up of such reactors for industrial application.

1. Introduction

5-(Chloromethyl) furfural (5-CMF) has recently gained significant attention as a substitute for 5-HMF, primarily because of its higher stability and outstanding hydrophobic properties.[1] These unique properties of 5-CMF not only simplify the isolation and purification processes, but also enhance the overall yield of 5-CMF from challenging substrates, such as starch, cellulose, and untreated cellulosic biomass. Furthermore, 5-CMF can be efficiently transformed into various valuable chemicals, such as 2,5-furandicarboxylate, alkoxymethyl furfurals, δ-amino levulinic acid and drop-in biofuels.[2,3]

Several 5-CMF synthesis processes from carbohydrates and cellulosic biomasses in biphasic systems have been developed in the last decades. Mascal *et al.*[4] efficiently prepared 5-CMF (yield >80 mol%) from glucose and cellulose using the HCl/dichloroethane (DCE) biphasic system at 100 °C for 3 h. Onkarappa *et al.*[5] used the aqueous HCl (35%)/DCE biphasic reactor system in the presence of benzyl tributylammonium chloride (BTBAC) as a phase transfer catalyst (PTC), and produced 73 mol% of 5-CMF from sucrose at 90 °C and 3 h. Despite achieving a high yield of 5-CMF, some reported processes suffered from the involvement of corrosive concentrated acids (such as HCl) and toxic chlorinated solvents (DCE), whereas some reported processes suffered from severe process conditions (high temperature (>100 °C); long reaction time); which in turn hindered the overall process sustainability. Recently, a few attempts were made to replace the direct utilization of the corrosive HCl catalyst for the synthesis of 5-CMF in biphasic media.[6] For instance, Chen *et al.*[7] reported that the *in situ* generated HCl from choline chloride and oxalic acid can be used to produce 5-CMF (70 mol%) from glucose using three constituent deep eutectic solvents (choline chloride, $AlCl_3 \cdot 6H_2O$, and oxalic acid) and DCE biphasic medium at 120 °C within 30 min. However, no work has been reported on the 5-CMF production employing a heterogeneous solid catalyst alone to

Chemical Engineering Department, Jadavpur University, Kolkata-700032, India. E-mail: rajat_chakraborty25@yahoo.com, rajat.chakraborty@jadavpuruniversity.in; Fax: +91 3324146378; Tel: +91 3324572689

† Electronic supplementary information (ESI) available. See DOI: https://doi.org/10.1039/d3re00406f

Environmental Science and Pollution Research
https://doi.org/10.1007/s11356-024-32231-2

Environmentally sustainable ethyl levulinate synthesis from delignified sugarcane bagasse using ternary eutectic solvent under MW-xenon irradiation: engine performance and emission assessment

Sourav Barman[1] · Sohini Roy Choudhury[1] · Rajat Chakraborty[1]

Received: 20 July 2023 / Accepted: 24 January 2024

Abstract

For the first time, a synergistic energy-efficient combination of microwave-xenon (MW-XE) irradiations in presence of photoactive ternary acidic deep eutectic solvents (TADES) has been applied for intensification of ethyl levulinate synthesis from delignified sugarcane bagasse (DSB) under *mild* (90 min, 90 °C) and environmentally benign process conditions. The Taguchi orthogonal designed optimized conditions (20 W/cm^3 of MW specific irradiation power input, 1 mol/mol of $FeCl_3$ to citric acid ratio, 90 min of reaction time, 150 W of XE specific power input) rendered maximum *61.3* mol% of EL yield (selectivity: 87.70 ± 0.5%). Remarkably, synergistic effect of MW and XE irradiation significantly enhanced the EL yield (61.3 mol%) compared to the individual MW (34.52 mol%) and XE (22.67 mol%) irradiation at otherwise optimized reaction conditions. Moreover, the MWXE irradiated reactor (MWXER) exhibited a significant 79.10% increase in EL yield compared to the conventional thermal reactor (CTR), at the expense of 10% less energy consumption. The ethyl levulinate could be recovered efficiently through *green protocol* from reaction mix resulting in *high purity* (97 ± 0.5%) and TADES was sustainably reused in the process. The optimally generated product EL when blended (5 and 10 vol.%) with B10 and B20 (10% and 20% biodiesel-diesel blend) could provide 21–31% reduction *in HC* and 7.3–36% reduction in CO in comparison with petro-diesel. It was also explored that, at similar optimal parametric combinations, the TADES produced *29.5% greater EL yield* in comparison with the standard ionic liquid BMIMCl. The *life cycle environmental impact analysis (LCEIA)* of the overall process revealed that the 5 vol.% EL blending with B10 contributed lowest environmental impacts mitigating marine ecotoxicity, human toxicity, fossil depletion, and climate change by 77.9%, 77.4%, 78.4% and 77.5%, respectively.

Keywords Ethyl levulinate · Sustainability · Microwave-xenon irradiation · Engine performance · LCA

Abbreviations

LB	Lignocellulosic biomass
EL	Ethyl levulinate
SB	Sugarcane bagasse
DSB	Delignified sugarcane bagasse
ILs	Ionic liquids
DES	Deep eutectic solvent
TADES	Ternary acidic DES
MW	Microwave irradiations
XE	Xenon irradiations
MWXER	MW-XE irradiated stirred batch reactor
CTR	Conventional thermal reactor
TOD-L9	Taguchi orthogonal L-9 design
LCEIA	Life cycle environmental impact analysis
H_0	Hemmett acidity
BSFC	Brake-specific fuel consumption

Greek letters

Ω_P	MW irradiation power (W)
Ω_{XE}	XE irradiation power (W)
$\Omega_{FeCl_3/CA}$	$FeCl_3$ to CA mol ratio (mol/mol)
Ω_t	Synthesis time (min)
Ω_{EL}	EL yield (mol %)

Responsible Editor: Philippe Garrigues

✉ Rajat Chakraborty
rajat_chakraborty25@yahoo.com;
rajat.chakraborty@jadavpuruniversity.in

[1] Chemical Engineering Department, Jadavpur University, Kolkata 700032, India

Published online: 02 February 2024

Certificate of Participation

This is to certify that

Ms. Sourav Burman

has presented a poster entitled "Energy efficient far infrared radiated ammonia fiber expansion pretreatment process for sustainable extraction of cellulose from lignocellulosic biomass" and has participated in the National Seminar on

Innovative Process Technology for Sustainable Development

jointly organized by Calcutta Regional Centre,

Indian Institute of Chemical Engineers, and

CSIR-Central Glass and Ceramic Research Institute, Kolkata

held on 23-24 Feb 2018

at IIChE Auditorium & K.P. Bose Auditorium, JU Campus

Mr. Uttam Kumar Basu	Prof. Priyabrata Sarkar	Prof. Amalesh Sirkar
Joint Convener	Joint Convener	Chairman, CRC

International Seminar on Sustainable 2-G Biorefinery Platforms
(Sponsor: RUSA-2.0)

CERTIFICATE OF PRESENTATION

This is to certify that ~~Prof./Dr./~~ Mr./~~Mrs./Ms.~~ Sourav Barman

of Chemical Engineering Department, JU, Kolkata *orally presented technical paper titled*

Intensified glucose production through starch hydrolysis in hybrid electromagnetic radiations assisted catalytic packed bed reaeton

in the three-day international seminar held at Chemical Engineering Department, Jadavpur University during December 10-12, 2019.

Prof. Ranjana Chowdhury
(Convener)

Prof. Chiranjib Bhattacharjee
(Nodal Person, RUSA-2)

CERTIFICATE OF PARTICIPATION

International Conference on Chemical Engineering Innovations and Sustainability (ICEIS-2023)

Chemical Engineering Department, Jadavpur University

This is to certify that

Sourav Barman

Jadavpur University, Kolkata, India

Orally presented technical paper entitled "Sustainable ethyl levulinate synthesis from sugarcane bagasse using ternary eutectic solvent under MW-xenon irradiation: Engine performance & emission assessment" in ICEIS-2023 held during 26th-27th February, 2023 at Jadavpur University, Kolkata, India

PROF. RAJAT CHAKRABORTY	PROF. RANJANA CHOWDHURY	PROF. KAJARI KARGUPTA	PROF. PAPITA DAS
Chairman, ICEIS 2023	Joint Conveners, ICEIS 2023		